Optical Property Variability in the Underwater Optical Wireless Channel

Laura J. Johnson

A thesis presented for the degree of

Doctor of Philosophy

School of Engineering

August 2015

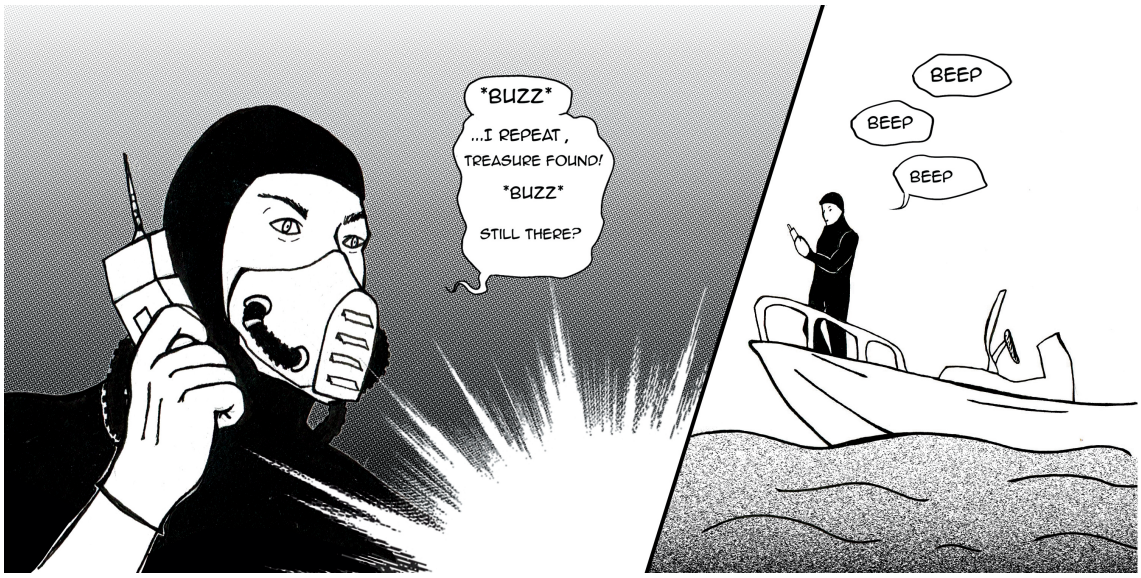

Challenging Underwater Communications by Anna R. Johnson, 2014

Contents

List of Figures

List of Tables

Nomenclature

Acronyms

AOP	apparent optical property
AUV	autonomous underwater vehicle
APD	avalanche photodiode
AWGN	additional white Gaussian noise
BER	bit error rate
BPSK	binary phase shift keying
BR	bit rate
BSF	beam spread function
BW	bandwidth
CDOM	colour dissolved organic material
COST	Cooperation in Science and Technology
CTD	conductivity, temperature, density
DC	direct current
DCM	deep chlorophyll maximum
DPIM	digital pulse interval modulation
EO	electro-optic (modulator)
FOV	field of view
FSK	frequency shift keying
GA	generic algorithm
GMSK	Gaussian minimum shift keying
IOP	inherent optical property
IR	infrared
IrDA	infrared data association

IM/DD	intensity modulated/direct detection
LED	light emitting diode
LD	laser diode
LDPC	low-density parity-check
LOS	line-of-sight
MCML	Monte Carlo mixed-layer
NAP	non-algal particles
OOK	on-off Keying
OFDM	orthogonal frequency division multiplexing
PAT	point-and-tracking
PMT	photomultiplier tube
PPM	pulse position modulation
PSK	phase shift keying
QAM	quadrature amplitude modulation
RF	radio frequency
ROV	remote operated underwater vehicle
RS	Reed-Solomon (coding)
RTE	radiative transfer equation
SNR	signal-to-noise ratio
VSF	volume scattering function

Symbols

a	m^{-1}	absorption coefficient ...
a_{CDOM}	m^{-1}	... of CDOM
a_{CHL}	m^{-1}	... of chlorophyll
a_{NAP}	m^{-1}	... of NAP
a_{PHY}	m^{-1}	... of phytoplankton
a_{W}	m^{-1}	... of pure seawater
a^*_{CDOM}	$\mathrm{m}^2\ \mathrm{mg}^{-1}$	... of CDOM, specific
a^*_{CHL}	$\mathrm{m}^2\ \mathrm{mg}^{-1}$	... of chlorophyll, specific
a^*_{H}	$\mathrm{m}^2\ \mathrm{mg}^{-1}$	... of humic acids, specific
a^*_{F}	$\mathrm{m}^2\ \mathrm{mg}^{-1}$	... of fulvic acids, specific

a^*_{PHY}	$\mathrm{m}^2\ \mathrm{mg}^{-1}$	...of phytoplankton, chlorophyll-specific
a^*_{NAP}	$\mathrm{m}^2\ \mathrm{mg}^{-1}$	...of NAP, carbon-specific
A	-	absorptance
b	m^{-1}	scattering coefficient ...
b_{L}	m^{-1}	...of small particulates
b_{S}	m^{-1}	...of large particulates
b_{W}	m^{-1}	...of pure seawater
b^*_{L}	$\mathrm{m}^2\ \mathrm{mg}^{-1}$	...of small particulates, specific
b^*_{S}	$\mathrm{m}^2\ \mathrm{mg}^{-1}$	...of large particulates, specific
B	-	scatterance
c	m^{-1}	beam attenuation coefficient
C	-	concentration...
C_{CDOM}	$\mathrm{mg\ m}^{-3}$	...of CDOM
C_{CHL}	$\mathrm{mg\ m}^{-3}$	...of chlorophyll
C_{H}	$\mathrm{mg\ m}^{-3}$	...of humic acids
C_{F}	$\mathrm{mg\ m}^{-3}$	...of fulvic acids
C_{NAP}	$\mathrm{mg\ m}^{-3}$	...of NAP
C_{L}	$\mathrm{mg\ m}^{-3}$	...of large particulates
C_{PHY}	$\mathrm{mg\ m}^{-3}$	...of phytoplankton
C_{S}	$\mathrm{mg\ m}^{-3}$	...of small particulates
C_{W}	$\mathrm{mg\ m}^{-3}$	...of pure seawater
$C_{\mathrm{CHL-S}}$	$\mathrm{mg\ m}^{-2}$	...of chlorophyll at the surface
D_R	mm^2	receiver area
E	$\mathrm{W\ m}^{-2}$	irradiance...
E_d	$\mathrm{W\ m}^{-2}$	...downwelling
E_i	$\mathrm{W\ m}^{-2}$	...incident
E_u	$\mathrm{W\ m}^{-2}$	...upwelling
F	-	constant or coefficient ...
F_0	$\mathrm{mg\ m}^{-3}$	...background surface chlorophyll concentration
F_1	-	...specific absorption of chlorophyll factor
F_2	-	...specific absorption of chlorophyll exponent
$F_{\mathrm{L}n}$	-	...large particle haltrin scatter factor
F_N	-	...excess noise factor

F_R	-	... angular radiance factor
$F_{\mathrm{S}n}$	-	... small particle haltrin scatter factor
F_T	mg m^{-2}	... total chlorophyll above background levels
G_R	-	detector current gain
h	-	beam-spread function
H	-	amplitude transfer function
I	W sr^{-1}	radiant intensity ...
I_s	W sr^{-1}	... of scattering
I_{PHY}	W sr^{-1}	... of phytoplankton fluorescence
I	A	current ...
I_{DRK}	A	... multiplied dark
I_{DC}	A	... non-multiplied dark
I_{AMP}	A	... of preamplifier noise
k	nm^{-1}	decay constant ...
k_{F}	nm^{-1}	of fulvic acid ...
k_{H}	nm^{-1}	of fulvic acid ...
K	m^{-1}	diffuse attenuation coefficient ...
K_d	m^{-1}	... downwelling
K_u	m^{-1}	... upwelling
L	W m^{-2} sr^{-1}	radiance ...
$L_{\mathrm{BG-SOL}}$	W m^{-2} sr^{-1}	... of miscellaneous underwater light
$L_{\mathrm{BG-SOL}}$	W m^{-2} sr^{-1}	... of background solar light
M	-	modulation level, M-ary
n	-	real refractive index
P	W	power ...
P_{AMP}	W	... of preamplifier current
P_{BG}	W	... of background light on receiver
P_{DRK}	W	... of dark current in receiver
P_N	W	... noise equivalent
P_R	W	... received
$P_{\mathrm{SHO-BG}}$	W	... of background shot noise
$P_{\mathrm{SHO-T}}$	W	... of signal shot noise
P_N	W	... noise equivalent

P_T	W	... transmitted
r	m	link path length
r_θ	m	radial distance (of beam)
R	-	reflectance
S	-	slope...
S_{CDOM}	nm^{-1}	... of CDOM
S_{NAP}	nm^{-1}	... of NAP
S_{CHL}	m^{-1}	... of chlorophyll with depth
S_R	$\mathrm{A\ W}^{-1}$	receiver sensitivity
t	s	time
T	°C	temperature
V	m^3	volume (of water)
x	m	lateral x coordinate
y	m	lateral y coordinate
z	m	depth coordinate ...
$z_{\max}$	m	... where the DCM occurs
z_∞	m	... where the photic zone ends
β	$\mathrm{m}^{-1}\ \mathrm{sr}^{-1}$	volume scattering function ...
β_{P}	$\mathrm{m}^{-1}\ \mathrm{sr}^{-1}$	... of particulates
β_{W}	$\mathrm{m}^{-1}\ \mathrm{sr}^{-1}$	... of seawater
$\tilde{\beta}$	sr^{-1}	volume phase function ...
$\tilde{\beta}_{\mathrm{S}}$	sr^{-1}	... of small particulates
$\tilde{\beta}_{\mathrm{L}}$	sr^{-1}	... of large particulates
ζ	m	optical depth
ε	J	photon energy
ϵ	psu	salinity, salt concentration
θ	rad	zenith angle ...
θ_R	rad	... of receiver, receiver FOV
θ_T	rad	... of transmitter, beam-width
λ	nm	wavelength ...
λ_0	nm	... reference, sually 440 nm
λ_R	nm	... filtered by optical receiver
μ_{PHY}	-	efficiency of a cell, fluorescence generation

ν	Hz	wave frequency
ρ	kg m^2	pressure
σ	-	standard deviation ...
σ_I	W sr^{-1}	... of scintillation, scintillation index
σ_{CHL}	mg m^{-3}	... of chlorophyll concentration
ϕ	rad^{-1}	azimuthal angle
Φ	W	radiant flux ...
Φ_i	W	... incident
Φ_a	W	... absorbed
Φ_s	W	... scattered
Φ_t	W	... transmitted
ω_0	-	single-scattering albedo

Physical Constants

c	2.998 x 10^8 m s^{-1}	speed of light in a vacuum
h	6.626 x 10^{-34} m^2 kg s^{-1}	Planck's constant
q	1.602 x 10^{-19} C	elementary electronic charge

Metric Prefixes

G	10^9	giga
M	10^6	mega
k	10^3	kilo
m	10^{-3}	milli
μ	10^{-6}	micro
n	10^{-9}	nano

Acknowledgements

I would like to express my gratitude to the Engineering and Physical Sciences Research Council (EPSRC) and Thales Research for sponsorship of the research undertaken. I am grateful for the facilities provided to me by the School of Engineering at the University of Warwick, Thales Research and Thales Underwater Systems.

I wish to send a number of personal thank yous to individuals at Thales: Chris Firth for being the crucial link between Thales and the University of Warwick; Julie Martin, Marcus Palmer, Terry Sharp and others involved in preparations for the outdoor experimentation; attendees of my presentation at Reading, for providing engaging feedback; finally, the team at Waterlip for assistance with the experimental set up and a kind donation of tea. The latter was particularly appreciated in the months spent writing this thesis.

A special thanks to my sister, Anna Johnson, for her input in creating the image *Challenging Underwater Communications*. Her skills in illustration transformed a vague concept into an image I proudly display at the beginning of my thesis.

Lastly, and most importantly, my sincerest gratitude goes towards my supervisors, Prof. Roger J. Green and Dr. Mark S. Leeson, for providing a guiding light – sometimes literally – over the last four years. Their unwavering support, guidance and valuable time have been greatly appreciated. Mark, I thank you for helping to keep my research on the right track. And Roger, as I transition to the next stage of my career, I hope wholeheartedly that you enjoy the final transition of yours.

Declaration

This thesis is submitted in partial fulfilment for the degree of Doctor of Philosophy under the regulations set out by the Graduate School at the University of Warwick. This thesis is solely composed of research completed by Laura J. Johnson, except where stated, under the supervision of Prof. Roger J. Green and Dr. Mark S. Leeson between the dates of September 2011 and August 2015. No part of this work has been previously submitted to any institution for admission to a higher degree.

Laura J. Johnson

August 2015

Associated Publications

Journal

Johnson, L. J., Jasman, F., Green, R. J., & Leeson, M. S. (2014). Underwater visible light communications. *Underwater Technology*, *32(3)*, 167-175.

Johnson, L. J., Green, R. J., & Leeson, M. S. (2014). Underwater optical wireless communications: depth-dependent beam refraction. *Applied Optics*, *53(31)*, 7273-7277.

Johnson, L. J., Green, R. J., & Leeson, M. S. (2013). Underwater optical wireless communications: depth-dependent variations in attenuation. *Applied Optics*, *52(33)*, 7867-7873.
Also selected for *Virtual Journal for Biomedical Optics*, *9(1)*.

Conference

Johnson, L. J., Green, R. J., & Leeson, M. S. (2014). The Impact of Link Orientation in Optical Wireless Communication Systems. In *IEEE/MTS Proceedings of OCEANS 2014, St John's*, (pp.1-7). IEEE/MTS. (Session chaired by Laura J. Johnson)

Johnson, L. J., Green, R. J., & Leeson, M. S. (2014). Hybrid Underwater Opto/Acoustic Link Design. In *16th International Conference on Transparent Optical Networks (ICTON)*, (pp.1-4). IEEE.

Johnson, L. J., Green, R. J., & Leeson, M. S. (2014). A survey of channel models for underwater optical wireless communications. In *2nd International Workshop on Optical Wireless Communications (IWOW)*, (pp. 1-5). IEEE.

Abstract

This thesis details an investigation into the variability of optical properties within the aquatic medium and its consequence for optical wireless communication systems. The principle aim is to aid the optimisation of optical wireless for underwater links through the application of oceanographic light propagation models, where optical property variations that occur within common communication ranges are emphasised. This kind of approach is not typical within the underwater optical wireless community where variability between different natural waters has been considered but, so far, not within a single underwater optical wireless link.

As part of this thesis, relevant underwater optical properties are surveyed and their variability quantified, where the importance of depth-dependent variations are established. A unique model is developed which characterises changing optical attenuation with depth based on two inputs; transmitted wavelength and turbidity at the surface of the water column. From this model, an investigation began into the impact of link location and orientation on link design and in advanced channel models. Select wavelengths are found to perform optimally, these are 410 nm, 490 to 500 nm, 540 nm, and 560 nm and greater; discretisation is attributed to the attenuation-wavelength profile shape and led to the advent of multi-wavelength transmitter designs. Meanwhile, a Monte Carlo modelling scheme, suitable for multi-layered media, predicted discrepancies between the overall attenuation and an average attenuation found by the depth-dependent model. Latterly, such knowledge is implemented in an experimental investigation in which a laser is transmitted down a turbid inland water column, to a maximum depth of 7.5 metres, then reflected back up.

In addition to attenuation, changes in refractive index with depth are considered. With refractive changes occurring from pressure, salinity and temperature gradients, this research recognises that beams transmitted with a vertical component undergo some amount of refraction. Through ray tracing links transmitted at different angles, the maximum distance between a straight-path and the true beam location after propagating 200 metres was 0.3 metres. This is expected to be compensated by the natural widening of the beam.

Chapter 1

Introduction

The oceans, covering two thirds of the Earth's surface, represent one of the ultimate frontiers for exploration, science and technology. In 2014, the high-profile disappearance of civilian aircraft MH370 at sea provided a humbling reminder of how much is yet to be understood about these underwater worlds. A key tool for exploration of the oceans, and other aquatic environments, is the development of remotely operated underwater vehicles (ROV) and autonomous underwater vehicles (AUV) which allow humans to explore and map underwater areas previously undiscovered, without the need to physically travel there. These underwater vehicles characterise areas by way of huge volumes of sensed data. In turn, data is either stored on-board the vehicles, at a significant cost to the battery life, or sent elsewhere underwater via a communication link. At present, the latter is done through tethered optical fibres or wirelessly using acoustic communications.

As explorative technology for the ocean advances, so too does the need for high speed, reliable underwater communication links. With tethered links unsuitable for many applications due to limitations in installation, maintenance and mobility, and acoustic systems inherently lacking the bandwidth to support high speed communications (Stojanovic, 2006), researchers have been motivated to find an alternative technology.

Shortly after the advent of laser technology, it was proposed that light could be used to communicate wirelessly underwater (Wiener & Karp, 1980). However, it was not until the development of powerful blue light emitting diodes (LEDs), coupled with the growth of underwater vehicular technology and the telecommunications industry in general, that research into underwater optical wireless communications really began to gather momentum (Bøtter-Jensen et al., 2000). Since then, optical techniques have accumulated serious consideration as a solution to high speed underwater communications.

1.1 The Underwater Optical Channel

Underwater optical communications are expected to provide high-speed wireless links between AUVs, ROVs, submarines, divers, ships and underwater base stations. In contrast to terrestrial radio frequency (RF) communications, underwater wireless communications are significantly affected by the marine environment and channel noise, and also must cope with limited bandwidth and power resource availability. Underwater communication channels are often seen to display severe attenuation, multi-path effects and frequency dispersion, which collectively make them complex and difficult to control. However, optical wireless has an intrinsic advantage when it comes to underwater applications; water exhibits a band of low electromagnetic absorption within the visible spectrum, particularly at blue/green wavelengths. Either side of this visible window, absorption increases rapidly, as shown in fig. 1.1. The consequence is crucial for the power resource conscious underwater environment; optical links propagate much further than equivalent systems using alternative wavelengths.

The ultimate goal for any communication transmission is to achieve the maximum signal-to-noise ratio (SNR) possible between two nodes of a network. In underwater optical wireless, this means the optical transmission system has to be properly designed in order to provide reliable operation over a range of conditions. The breadth of optical wireless design, coupled with the aforementioned complex underlying communication channel, result in challenging circumstances from which to find an optimal design. Motivation for overcoming these challenges lies in the unique advantages optical wireless has over conventional underwater communication technology, as will be explored in sec. 5.2.4.

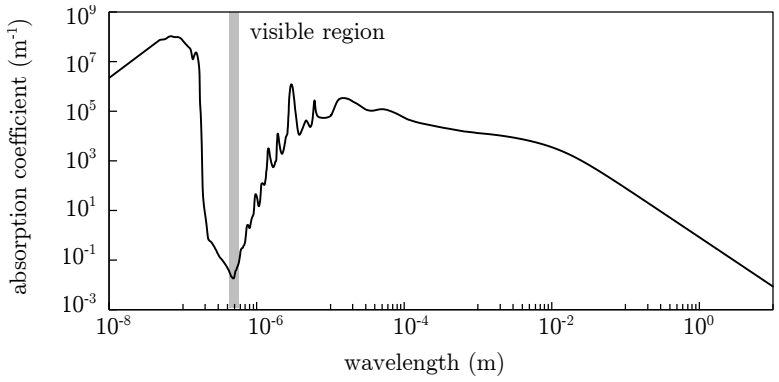

Figure 1.1: Electromagnetic absorption spectrum for pure seawater, based on values in (Pope & Fry, 1997).

1.2 Comparison of Underwater Communication Technology

There are three primary technologies which can be used to communicate wirelessly underwater. The first, most established technology is acoustic communications, responsible for the majority of underwater wireless communications at present. The second technology is RF, represented by wavelengths between 10^{-4} - 10^{8} metres in fig. 1.1, the latter region of low absorption. Although a predominant terrestrial technology, RF has very few underwater applications to date. The final technology is optical wireless. A summary of the three technologies is provided in tab. 1.1.

The main motivation for using optical wireless technology to communicate underwater is to achieve high bandwidths. Unlike acoustics which are inherently limited by frequency dispersion, and RF where bandwidth is regulated, optical links are only indirectly limited through eye safety limits, which dictates the maximum intensity of transmitted light and subsequent channel capacity. At short ranges, optical links have demonstrated the ability to communicate at data rates of up to 1.45 Gb s^{-1} (Nakamura et al., 2015), whilst the best acoustic and RF links are much slower, at 500 kb s^{-1} and 100 Mb s^{-1} respectively (Stojanovic, 1996) (Che et al., 2010). Additional advantages include high efficiency, optical links transmit over three times the number of bits per Joule than the alternative technologies (see tab. 1.1), and high security. The latter is caused by the need to maintain line-of-sight (LOS) between the transmitter and receiver.

Although providing security, the LOS requirement of optical communications is seen as a disadvantage in some applications; both acoustic and RF links can be established without LOS. The greatest challenge for optical wireless, however, is the limited range in comparison with acoustic and RF links. Physical demonstrations of optical wireless have been capped to 200 metres in length (Pontbriand et al., 2008) and, although this is expected to increase as the technology matures, alternative technology boasts ranges in the order of kilometres.

In balance, optical communication is unlikely to replace acoustic technology due to limitations in how far light propagates underwater, but it is a highly regarded complementary technology (Johnson et al., 2014b). Optics are ideal for short-range, high-bandwidth applications, whereas acoustic are suitable in long-range, low-bandwidth situations. Moreover, acoustic propagation is susceptible to changes in the refractive state of the medium, from variations in factors such as temperature and pressure, and acoustic noise. Optical links, on the other hand, are less affected by these, instead noise comes from ambient sunlight and propagation variability through composition and subsequent visibility changes. Consequently, optical wireless communications may be employed in underwater locations unsuitable for acoustic links.

Property	Acoustic	RF	Optical
Range	< 1000 km	< 1 km	< 250 m
Bandwidth	low, inherently limited	low, regulatory limit	high, eye safety limit
Transmission efficiency	8900 bits J^{-1}	9850 bits J^{-1}	30,000 bits J^{-1}
Security	low	medium	high
Susceptibility to medium	sensitive to refractive changes	not sensitive	sensitive to composition changes
Primary noise source	acoustic background noise	interference from other users	ambient background light
Air-sea interface	no	yes, with ease	yes, conditionally

Table 1.1: Comparison of underwater wireless communication technologies. The data is collated from the following sources: for acoustic communications, (Akyildiz et al., 2005), (Stojanovic & Preisig, 2009) and (Stefanov & Stojanovic, 2011); underwater RF (Che et al., 2010) and (Moore, 1967); underwater optical wireless (Smart, 2005), (Cochenour et al., 2007), (Arnon, 2010) and (Farr et al., 2010); and comparative studies (Yusof & Kabir, 2011) and (Gulbahar & Akan, 2012).

1.3 History of Underwater Wireless Communications

A brief history of underwater wireless communications is presented in this section to provide a backdrop for the motivations and aims of this study. What is perhaps most surprising about the history of underwater wireless communications is its relative recency. Early underwater acoustic systems were first demonstrated around the time of World War I, where the use of submarines and underwater mines had a profound influence in their development. In 1919, the first scientific paper on underwater acoustics was published, theoretically describing the refraction of sound waves produced by temperature and salinity gradients in the ocean (Lichte, 1919). As the fundamental understanding of acoustic propagation increased, so too did the necessity to use the technology in warfare; World War II marked the start of extensive research in underwater acoustics.

The development of oceanic optical propagation models began towards the end of the 1950s, leading into the 60s and 70s. Several groups around the world, such as (Duntley, 1971), (Jerlov, 1976) and (Preisendorfer, 1976), developed the instrumentation that was required to measure light propagation and interpreted its consequences for underwater imaging and oceanic oxygen production. With the invention of the laser also occurring in the late 1950s (Schawlow & Townes, 1958), a number of those in defence research envisioned laser-based communication systems

underwater (Karp, 1976) (Wiener & Karp, 1980). By estimating link performance through the recently derived light propagation models, these studies highlighted a series of unique applications for optical wireless, including a strategic satellite-to-submarine link (Kelley et al., 1979). However, due to limitations in existing blue/green laser technology, practical demonstrations of underwater optical wireless did not materialise at this time.

Acoustics remained the dominant technology throughout the 20th century; after World War II, development was driven largely by the Cold War, resulting in advances in the theoretical and practical understanding of underwater acoustics, aided by computer-based techniques. Despite warfare driving technological advances, the applications of underwater acoustics began to diversify, branching into environmental monitoring through sensor networks. The bandwidth requirements of these applications grew in the 1990s, in parallel with a boom in terrestrial wireless trends. As a consequence, by the millennium, both underwater and terrestrial applications were looking for wireless technology that could offer higher bandwidths.

A popular solution to high-bandwidth wireless communication came in the form of optical wireless communications. Developments in transmitter technologies in the early 2000s, especially that of lasers and high power LEDs within the visible spectrum (Bøtter-Jensen et al., 2000), meant the underwater optical systems imagined in the late 1970s became a practical possibility. The revival of underwater optical wireless research was pioneered by studies such as (Smart, 2005) and (Giles & Bankman, 2005) where the new generation of AUVs and ROVs formed the basis of application. The marriage of optical wireless communications with submersible vehicle technology meant that large amounts of information could be collected and sent with minimal human intervention, typically for the purpose of environmental studies, mapping and defence.

Over the past ten years, autonomous submersible technology has advanced significantly, whilst developments in underwater optical wireless have been gradual, with capacity and link length slowly increasing. For the latter, there now exists a small number of commercially available systems, such as the high-bandwidth transceivers in (Ambalux Corporation, 2012) and Bluecomm (Sonardyne, 2014). In spite of this, there are still a lot of fundamental, unanswered questions regarding underwater optical wireless communications links; more detail about these challenges is explored in sec. 1.4. However, for now, acoustic communications remain the dominant underwater technology, as was highlighted by the underwater equipment used in the search and rescue efforts of MH370 in 2014 (Australian Transport Safety Bureau, 2015).

1.4 Motivation and Aims

Underwater communication applications in which the use of optical wireless communication might be beneficial include remote controls in the offshore oil industry, pollution monitoring in environmental systems, collection of scientific data recorded at ocean-bottom stations, disaster detection and early warning, national security and defence (intrusion detection and underwater surveillance), as well as the discovery of new natural resources. Such depth and breadth of application requires unique optical system designs, currently envisioned examples of which are portrayed in fig. 1.2.

There are a number of key research areas in underwater optical wireless communications that require addressing in order to modernise existing commercially available systems into the kinds depicted in fig. 1.2. As highlighted by a recent IEEE Communications Magazine call for papers (Zhang et al., 2014), these challenges include: understanding propagation characteristics of the underwater optical channel and finding an optimal transmission wavelength with variable absorption, scattering and turbulence; the development of high-efficiency laser and LED sources in blue/green wavelengths; methods for single photon detection with receiver design and techniques that maximise the receiver field-of-view (FOV) and reject solar irradiance; and lastly, delay- and disruption-tolerant networking for a highly disconnected data environment. The research in this thesis addresses all these key areas, to an extent. However, the main focus lies in the underwater optical channel and its variability, chosen because of the potential impact of the subsequent knowledge across all underwater optical wireless systems.

The propagation of light underwater is a widely studied subject, mainly due to the

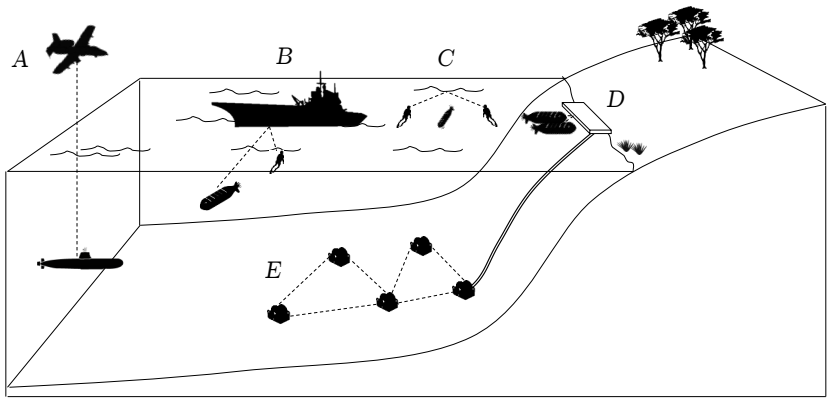

Figure 1.2: Future landscape for underwater optical wireless applications: A is is a satellite-to-submarine link; B is communication between movable transmitters (AUV and diver) and a stationary ship; C is non-LOS between two divers using the water surface to reflect; D is a high-bandwidth, short-range, wide download link for an AUV; and, E is an optical sensor network.

implications it has on natural waters as oxygen-generating ecosystems (Mobley et al., 2014). The productivity of these aquatic environments, as in how much oxygen they produce, depends on the presence of particulate matter in the form of plankton and minerals, in addition to the structure and intensity of solar illumination incident on this particulate matter. Whilst studies of solar illumination provide a good description of ambient lighting for optical wireless communications, productivity has a direct relation to the water composition. Hence, both can be used in determining the propagation of any light beam underwater. In prior underwater optical wireless research, these oceanographic descriptions have only been applied sparingly to optical communication channel models, mainly through simple concepts such as absorption and scattering which will be introduced in sec. 2.4 and sec. 2.5 respectively. The main aim of this research, therefore, is to use oceanographic descriptions to generate a comprehensive understanding of the variability of underwater communication channels, documenting the impact of variability on underwater optical links.

1.5 Outline

The thesis is structured as five main chapters, in addition to an introductory and concluding chapter. A brief summary and the main achievements of each chapter are included here to aid navigation of the thesis.

Ch. 2, *Hydrological Optics*, describes the fundamental physics behind light propagation in aquatic media. The processes of electromagnetic absorption and scattering are explored, detailing the effects from pure seawater and the main constituents of natural waters. The main achievement of this chapter is a comprehensive literature review of oceanographic research in this area.

Ch. 3, *Optical Property Variability*, looks at how the optical properties introduced in ch. 2 vary. Variations across the surface of water bodies are characterised, as well as with depth and with time; collectively these variations are used to form estimates of beam attenuation in mobile underwater optical communication links. The main achievements of this chapter are: a unique model to find the attenuation coefficient with depth based on only locational information; a framework for temporal attenuation variations; and, an introduction to refractive index gradients with depth.

Ch. 4, *Underwater Link Design*, considers the design of underwater optical communication links through governing equations and trade-offs. Particular attention is drawn to technologies which enable the best performance over a wide range of conditions, as described by the variability

studies of ch. 3. The theme of variability is continued in this chapter by surveying underwater-specific channel noise. The main achievements of this chapter are: an investigation detailing how depth-varying attenuation profiles impact links at different geometric orientations; unique multi-wavelength transmitter designs; and, a description of underwater sun/moon light for noise calculations.

Ch. 5, *Channel Modelling*, uses the communication links designed in chapter 4, along with the variability assessment of ch. 3, to generate complex models of optical propagation underwater. The main achievements of this chapter are: a comprehensive survey of modelling schemes; estimations of the average attenuation coefficient over a depth-varying refractive profile using a higher-order pre-compiled model; and, an estimation of the extent that light beams are refractive by a graded oceanic refractive index.

Ch. 6, *Practical Underwater Systems*, surveys previous practical demonstrations of underwater optical wireless to aid the design and demonstration of a unique underwater link. The aim of the designed link is to test optical wireless communications in a variable underwater optical medium, bringing together the knowledge of ch. 2 to ch. 5. The main achievements of this chapter are: a comprehensive survey of previous experimental studies; the design, set-up and execution of a underwater link in a turbid, natural water body; and, experimental results matching the predicted behaviour of the attenuation with depth.

Finally, ch. 7 provides a conclusion and outlook for future work within the subject of optical wireless communications, particularly with regards to optical variability.

Chapter 2

Hydrological Optics

The journey to understanding underwater optical wireless communications begins with the science of hydrological optics which explores how light behaves in natural waters. Such waters, spanning from desert oases to deep oceans, are a concoction of different dissolved and particulate matter. The type and concentration of matter varies considerably, having implications for any light attempting to traverse through underwater environments. Accordingly, by defining these variable natural waters as optical media, the resulting light propagation may be quantified through a series of universal optical properties.

With the aim of surveying the bulk optical properties of natural waters, this chapter builds a picture of the most optically important constituents underwater. Of course, this cannot be done without first assessing how light is described quantitatively, nor without discovering how to describe and measure the optical properties of a medium through which light propagates.

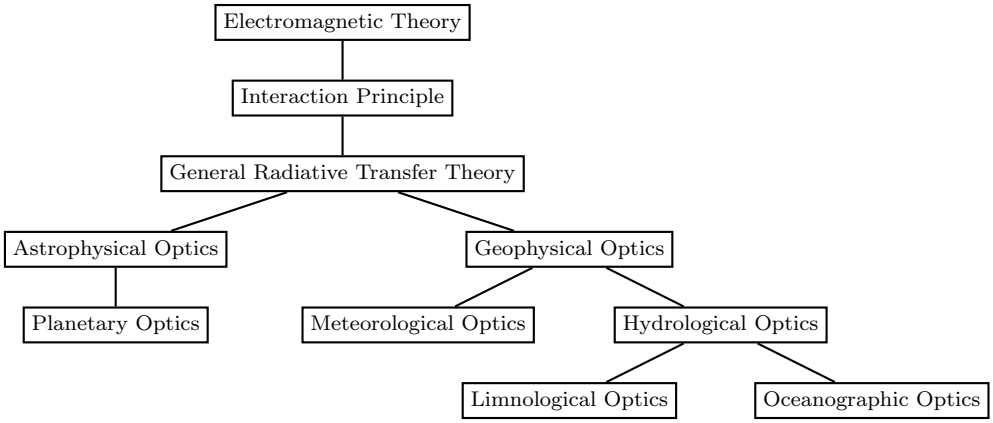

Figure 2.1: The relation between hydrological optics and other branches of optics.

2.1 Light and Energy

Underwater optical wireless communications are concerned with the transmission of visible light through natural waters, where *visible light* refers to radiation in the electromagnetic spectrum between 400 to 700 nm, to which the human eye is sensitive. The science that generically describes the behaviour of light through aquatic media is hydrological optics, consisting of two subfields (fig. 2.1). The first subtype is limnology, used for describing the propagation of light in fresh inland waters; the second, oceanographic optics, predicts behaviours in salty marine waters (Preisendorfer, 1976). Although much of the currently perceived uses of optical wireless are set in oceanic environments, as discussed in sec. 1.4, this study comprehensively addresses both inland and oceanic waters, providing a reference for future limnological and current oceanographic applications.

As fig. 2.1 shows, understanding how light travels through a given medium begins by considering the transmission of energy in an electromagnetic wave using electromagnetic theory. Light is well documented for exhibiting properties both as a wave and as a stream of particles known as photons (Band, 2006). It is through this wave-particle duality that photon properties can coexist with wave properties such as frequency and wavelength. In a vacuum, photons travel and the wave propagates at a constant value of 2.998 x 10^8 m s^{-1}, denoted c, this is related to other wave properties by

$$\lambda = \mathrm{c}/\nu \tag{2.1}$$

where ν is the wave frequency and λ is the wavelength in a vacuum which is commonly given in nm (10^{-9} m). When not in a vacuum, the photon velocity decreases by a factor of $1/n$, where n is the *refractive index* of the new medium through which the light beam is traversing. In air, the refractive

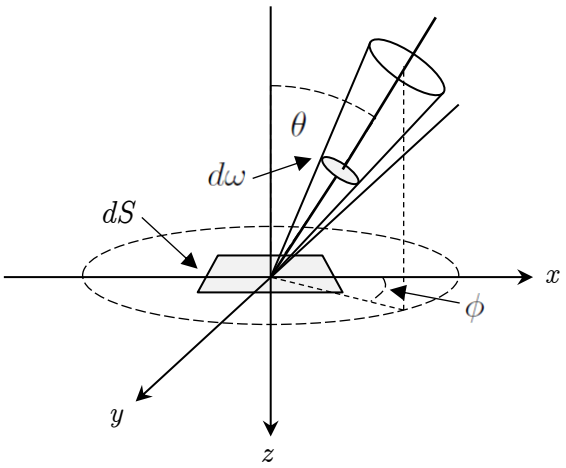

Figure 2.2: Geometry of radiant intensity I, where $d\omega$ is an incremental solid angle, θ and ϕ are zenith and azimuthal angles.

index has a value around 1.001, whilst it is approximately 1.333 for fresh water (Halliday et al., 2010). In seawater, the refractive index is marginally higher than that of fresh water, although can vary considerably more in areas of high pressure and salinity (Austin & Halikas, 1976), as is explored in sec. 3.5. As wave frequency does not change according to the medium, wavelength diminishes with velocity by the relation in eq. 2.1; note that values of wavelength quoted in this text refer to the vacuum wavelength, unless stated otherwise. The energy of each photon, ε, measured in J, is dictated by the wave frequency through the Planck-Einstein relation

$$\varepsilon = h\nu = hc/\lambda \tag{2.2}$$

where h is Planck's constant, equal to 6.63 x 10^{-34} J s. By extending this to consider multiple photons, or full illumination structures, an energy-based description of a light field is formed. Although beyond the scope of this research, there are several texts with discussions of length describing how multiple photon systems are converted into equivalent radiant energies, such as (Band, 2006) and (Sakurai, 2006).

The most basic concept used to define radiation fields by energy is the *radiant flux*, Φ, which represents the flow of radiant energy from a single source, expressed in W. However, a more useful approach is to consider this radiant flux over a unit solid angle, in a specified direction, to find the *radiant intensity*, I. The geometry of this is given in fig. 2.2 and written mathematically in eq. 2.3.

$$I = d\Phi/d\omega \tag{2.3}$$

where I has the units W steradian^{-1}. Radiant intensity represents the field given by a point source to a point in space. However, for this research, a complex source model is needed to provide a more accurate description of the radiant energy field. Thankfully, this is possible by considering the radiant flux not only per unit solid angle but also per unit area of a plane at right angles to the direction of flow, shown as dS in fig. 2.2. The subsequent result is the concept of *radiance*, denoted L, which has the units W m^{-2} steradian^{-1}. A full definition of radiance is given by

$$L(\theta, \phi) = d^2\Phi / dS \, \cos\theta \, d\omega \tag{2.4}$$

where θ and ϕ represent the zenith and azimuthal angles respectively. Radiance can be used to form a description of the behaviour of a specific light beam on a known surface, for example, a laser beam on an underwater telecommunications receiver.

For near-surface underwater communication systems, contributions from sources such as the sun and moon must also be taken into consideration to provide a description of their light fields at certain depths underwater. The concept of *irradiance*, E, is used to express this, defined as the total radiant flux incident on an infinitesimal surface element, such that $E = d\Phi/dS$. In oceanographic optics, irradiance is split into the downwelling irradiance, E_d, found by integrating the radiance in eq. 2.4 over the solid angle of the upper hemisphere, and E_u, the upwelling irradiance. The upwelling and downwelling irradiances are given in eq. 2.5 and eq. 2.6 respectively.

$$E_d = \int_{2\pi} L(\theta, \phi) \cos\theta \, d\omega \tag{2.5}$$

$$E_u = -\int_{-2\pi} L(\theta, \phi) \cos\theta \, d\omega \tag{2.6}$$

both of which are measured in W m^{-2}. These equations respectively portray the light contributions from above and below an underwater plane of interest.

The concepts of radiant flux, radiant intensity, radiation and irradiation appear throughout this text as methods of describing light fields. What has so far been omitted is that all these concepts are wavelength-dependent. The origin of this wavelength dependency is obvious when taking the Planck-Einstein relation (eq. 2.2) into consideration as it shows an inverse relationship between photon energy and wavelength. As optical properties arise from the interaction of these energy fields with a medium, it follows therefore that the optical properties of said medium are also wavelength dependent.

In sec. 2.2, the descriptions of light and energy are explored in terms of their interactions with

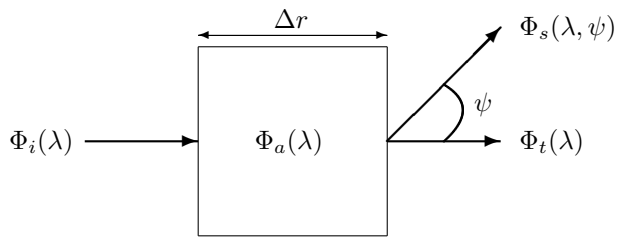

Figure 2.3: Geometry to define inherent optical properties for a volume ΔV, based on radiant flux Φ (Mobley & Mobley, 1994).

the aquatic medium. The concepts introduced in this section will be used in determining a number of defining optical properties for natural waters, subsequently enabling a better understanding of the behaviour of optical communications in a wide variety of underwater applications.

2.2 Optical Properties

As the name would suggest, optical properties are characteristics of a particular medium that describe the interaction between light and said medium. For aquatic media, optical properties are divided into two mutually exclusive groups: inherent and apparent. Inherent properties include optical parameters that depend only on the medium; aquatic media are typically a mix of dissolved and particulate matter, suspended in water. Apparent properties depend on both the medium and geometric structure of illumination, for which a descriptive framework was introduced in sec. 2.1. By considering the interaction between photons and the media they traverse, sec. 2.2.1 and sec. 2.2.2 show how to respectively derive the inherent and apparently properties of interest.

2.2.1 Inherent Optical Properties

When a beam of light is sent through a medium, there are two factors that cause a reduced number of photons to arrive at a location further along the medium. The first possibility is that some photons change direction due to interactions with particles in the medium, this phenomena is known as *scattering*. Alternatively, these interactions could lead to the photon energy being converted into another form, such as heat or chemical, removing photons from the light beam entirely; a process known as *absorption*. Scattering and absorption are combined to give an overall *beam attenuation*. The beam attenuation coefficient, which describes the loss of optical energy per meter, is derived in the following way:

Begin by considering an elemental volume, ΔV, of an aquatic medium such as water, with thickness Δr, as shown in fig. 2.3. The water is illuminated by a collimated beam of monochromatic

light, at a fixed wavelength λ and of radiant flux Φ_i. A certain amount of the incident energy is absorbed by the water, denoted by Φ_a. Another portion of the power will be scattered; the total scattered energy, Φ_s, is the summation of angular scattered energy $\Phi_s(\psi)$, summed over all angles of ψ. The remaining energy, Φ_t, passes through the medium unaffected. Therefore, by conservation of energy, it can be said that

$$\Phi_i(\lambda) = \Phi_a(\lambda) + \Phi_t(\lambda) + \Phi_s(\lambda) \tag{2.7}$$

This energy balance has been restricted to considering only the processes of absorption and elastic scattering. However, molecular physics is also aware of interactions that result in the re-emission of photons at different wavelengths from lower energy states.

From the energies denoted in eq. 2.7, two new parameters are defined. *Absorbance*, A, is the fraction between incident power and absorbed power and whilst *scatterance*, B, refers to the ratio between incident power and scattered power. These are given in eq. 2.8.

$$A(\lambda) \equiv \frac{\Phi_a(\lambda)}{\Phi_i(\lambda)} \qquad\qquad B(\lambda) \equiv \frac{\Phi_s(\lambda)}{\Phi_i(\lambda)} \tag{2.8}$$

Although these coefficients accurately describe the inherent optical properties of an aquatic medium, it is more practical for coefficients to be defined in terms of a unit distance. So, by taking the limit as the medium thickness Δr becomes infinitesimally small, two new coefficients are defined. These are known as the absorption and scattering coefficients, denoted as a and b respectively. The result are given in eq. 2.9.

$$a(\lambda) \equiv \lim_{\Delta r \to 0} \frac{\Delta A(\lambda)}{\Delta r} = \frac{dA(\lambda)}{dr} \qquad\qquad b(\lambda) \equiv \lim_{\Delta r \to 0} \frac{\Delta B(\lambda)}{\Delta r} = \frac{dB(\lambda)}{dr} \tag{2.9}$$

The absorption and scattering coefficients are combined to give the total fraction of energy lost after a unit distance. The beam attenuation coefficient c, which appears in eq. 2.10, is the name given to this summed fractional loss. The unit of distance conventionally used is a metre, giving these coefficients a unit of m^{-1}.

$$c(\lambda) = a(\lambda) + b(\lambda) \tag{2.10}$$

The absorption, scattering and attenuation coefficients are powerful tools for describing a medium optically and, as such, are used extensively throughout this research. These properties

Water Type	a (m^{-1})	b (m^{-1})	c (m^{-1})
Clear ocean	0.114	0.037	0.151
Coastal ocean	0.179	0.220	0.399
Harbour water	0.366	1.829	2.195

Table 2.1: Typical inherent coefficient values at $\lambda = 440$ nm. (Hanson & Radic, 2008).

enable not only a method for defining media but also describe how said media can change optically over a given distance. Moreover, because inherent optical properties are a result of the composition, concentration and morphology, they can be used build a picture of the biological, chemical and geological structure of a particular water body. Indeed, whilst underwater optical communication researchers can utilise the biological, chemical, geological aspects of hydrology in the pursuit of optical properties, these subjects incorporate optics in an equivalent manner. Synergism between these subject areas is found in remote colour sensing of ocean surface composition (Mueller et al., 2003) and bio-geo-optical oceanography (Coble, 2007), amongst other examples.

As hinted upon thus far, physical characteristics of natural waters can vary considerably and therefore so too do the inherent optical coefficients. To introduce the kind of coefficient values relevant for underwater optical communications, tab. 2.1 depicts typical values for the attenuation, absorption and scattering coefficients at different ocean locations, for a wavelength of 440 nm (Hanson & Radic, 2008). Whilst to an optical wireless engineer concerned with the propagation of light through air these numbers may seem high, with absorption in air being typically five orders of magnitude lower (Horvath, 1993), such high absorption is to be expected in a liquid where much more of the photon energy is lost.

The data in tab. 2.1 shows that attenuation is greater in harbours and coastal areas, mainly from a greater loss through scattering; in sec. 2.4 and sec. 2.5, and later in ch. 3, these inherent coefficient values are explored and consolidated extensively. Increased attenuation means it is consequently more challenging to communicate in coastal areas through the use of optical wireless; there is a higher concentration of particulate matter which causes light to scatter more, leading to a surge in the scattering coefficient. This can be particularly detrimental for optical communications as high amounts of scatter have a negative impact on the temporal clarity of underwater communication signals. To emphasise the significance of scattering, another inherent optical property known as

the *single-scattering albedo* is defined (Mullen et al., 2011), as given by eq. 2.11.

$$\omega_0(\lambda) = b(\lambda)/c(\lambda) \tag{2.11}$$

The name single-scattering albedo arises because of the way the absorption and scattering coefficients were derived originally; recall fig. 2.3 where it was assumed that light scattered once is lost forever. In reality, there is a chance for these scattered photons to be re-scattered into the original beam and, in ch. 5, this multi-scattering is considered as a means of paving the way to more complex models of the behaviour of light underwater. For now, a basic understanding of the concepts of absorption and scattering is sufficient for building a comprehensive picture of how and why optical propagation varies underwater.

So far this discussion has omitted a method for finding the total fraction of energy lost by a light beam that has traversed several metres of an aquatic medium, yet this is an imperative concept for constructing optical communication system models. To derive the propagation loss factor, the reduction in radiant flux due to a known attenuation over a distance r is considered. Starting with eq. 2.7, and by defining two new variables, the loss factor in eq. 2.12 is obtained.

$$-\Delta\Phi = c\Phi(r)\Delta r \tag{2.12}$$

where the new variables are the negative change, or reduction, in flux, defined as $-\Delta\Phi = \Phi_a + \Phi_b$ and the continually changing flux with distance, $\Phi(r)$. Integrating eq. 2.12 between a starting location at zero and an end location at r gives the fractional change in flux, or propagation loss factor, for a distance r.

$$\Phi(r)/\Phi_0 = e^{-cr} \tag{2.13}$$

This is known as the Beer-Lambert law (Beer, 1852), a dimensionless loss factor that is often coupled with radiant intensity or irradiation, providing a basic method for determining communication signal loss after a specified distance. This, along with the absorption, scattering and attenuation coefficients and single scattering albedo, forms the basis of more complex light propagation models, as is discussed at length in ch. 5.

2.2.2 Apparent Optical Properties

Whilst the inherent optical properties introduced in sec. 2.2.1 are used primarily for assessing the propagation of underwater optical signals, apparent optical properties characterise the environment through which these signals propagate by providing a description of the background illumination. Accordingly, apparent optical properties are those which depend on both the medium and the geometric structure of illumination, originally conceived due to the difficulties in measuring the inherent optical properties of aquatic media directly (Preisendorfer, 1976). The common apparent coefficients are radiance and irradiance, as introduced in sec. 2.1, and, a new concept discussed in this section, reflectance.

Apparent optical properties can only be formed from regular and stable sources of illumination in order to be a useful descriptor of a body of water. This means, for example, that the downwelling irradiance from sunlight is not technically an apparent property because it changes due to cloud cover and time of day. There are two methods for transforming these temporally varying illumination structures into usable apparent optical properties; either create a ratio of properties which are equally affects by the environment or use a normalised derivative. The latter method creates what is known as the diffuse attenuation coefficient, K, the general form of which is written in eq. 2.14. Notice that to represent the changing illumination field with depth for sunlight, a distance has been introduced here in the form of depth from the water surface, z.

$$K(z,\lambda) = -\frac{1}{E(0,\lambda)}\frac{dE(z,\lambda)}{dz} \tag{2.14}$$

E is the irradiance, which can be downwelling or upwelling (eq. 2.5 and eq. 2.6 respectively). There are a few important factors to note about K functions: they are all directional; they vary greatly near the ocean surface; they are not constant with depth, even with homogeneous water; they can take positive or negative values at boundaries and lastly, deep down in water bodies when the background illumination no longer changes, they become inherent optical properties, written as K_∞ (Mobley et al., 2014). In sec. 4.2, it is shown how these functions are used to form a description of background illumination for noise calculations by considering them as attenuation coefficients in the upwards or downwards directions.

As with attenuation coefficients, the Beer-Lambert law in eq. 2.13 can be applied to diffuse

attenuation coefficients, yielding

$$E_d(z) = E_d(0)e^{-K_d z} \tag{2.15}$$

where $E_d(z)$ and $E_d(0)$ are the downwards irradiances at z metres and 0 respectively, whilst K_d is an averaged diffuse attenuation coefficient over the path. The *optical depth*, denoted ζ, is a measure based on this averaged coefficient, used in water body classification (seen further in sec. 3.2). It describes the natural logarithm of the ratio of incident to transmitted radiant irradiance through the ocean, such that

$$\zeta = K_d z \tag{2.16}$$

Eq. 2.16 shows that ζ can be thought of as an diffuse attenuation-length product. An equivalent inherent attenuation-length product often found in optical wireless research, for example in the work of (Hanson & Radic, 2008) and (Cochenour et al., 2009). Beware that some texts mistakenly refer to this as the *attenuation length*, for example (Cochenour & Mullen, 2011); true attenuation length is a different inherent optical property, defined as the reciprocal of the beam attenuation coefficient, $1/c$.

The final apparent optical property used in generating complex models of underwater optics is the idea of *reflectance*, R, which is simply the radio of downwelling to upwelling irradiance, E_u/E_d. This property reveals how much light, intending to traverse down the water column from the surface, is reflected in the upwards direction. Further details of this apparent optical property and others can be found in (Mobley & Mobley, 1994).

2.3 Optically Significant Constituents

Natural waters are complex physicochemical biological systems with highly variable optical properties, leading to variations in the amount of light absorbed and scattered through them. Such bodies of water are a broth of different constituents, as seen in fig. 2.4 (Mobley et al., 2014), each of which has an optically unique behaviour and each contributing towards the overall bulk optical properties of said water. In this section, detailed knowledge of the optically significant constituents is provided to motivate subsequent studies on the spatial and temporal variations of underwater optical properties.

Natural waters contain a continuum of particle sizes, ranging from individual water molecules,

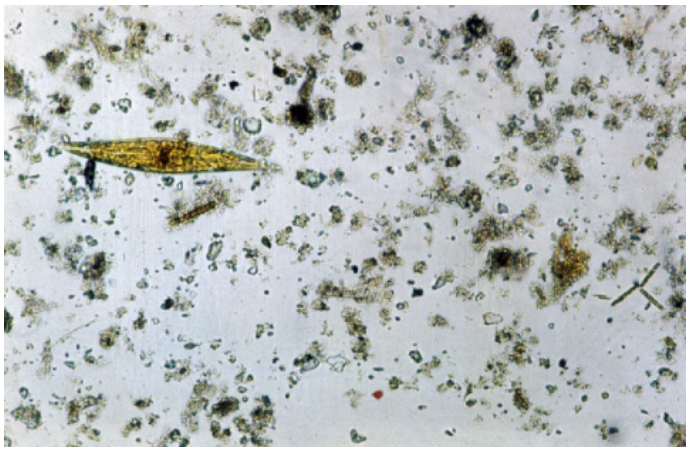

Figure 2.4: Microscopic image of particulates in coastal water, mainly consisting of individual and flocs of inorganic particulates, as well as a large 100 μm long phytoplankton (Mobley et al., 2014)

with diameters around 0.1 nm, to large marine mammals measuring up to 30 metres across. To characterise the optical behaviour of particles at the smaller end of this spectrum, they are split into *dissolved* and suspended or *particulate* components, where particles with a diameter less than 0.4 μm are considered dissolved, corresponding to the minimum visible wavelength. Hence, dissolved particles are those unable to be resolved by microscopy (Mobley, 1995). Both suspended and dissolved matter are further grouped by whether they are of biological or physical origin; organic particulates are created as bacteria, phytoplankton and zooplankton grow and reproduce whilst inorganic particles are created through weathering of terrestrial rocks and soils and from human intervention. Additionally, optical behaviour is influenced by inhomogeneities arising from turbulence-induced refractive index changes and from air bubbles (Sosik, 2005). The information above is summarised in fig. 2.5, where each category is examined in the remainder of this section.

Water

Water is used to refer to either pure water, H_2O, which is seen in artificial or inland water bodies, or pure seawater. The latter is pure water combined with inorganic dissolved particles which take the form of dissolved salts including NaCl, $MgCl_2$, Na_2SO_4, $CaCl_2$ and KCl (Shifrin, 1988). The concentration of dissolved salts is characterised by the *salinity*, S, which for typical ocean conditions is around 35 parts per thousand, albeit varying with latitude and ocean depth.

Organic Dissolved Particles

These are a diverse group of substances, having had over 150 different individual organic substances identified (Riley & Skirrow, 1965). Significantly, most of these substances have limited absorption

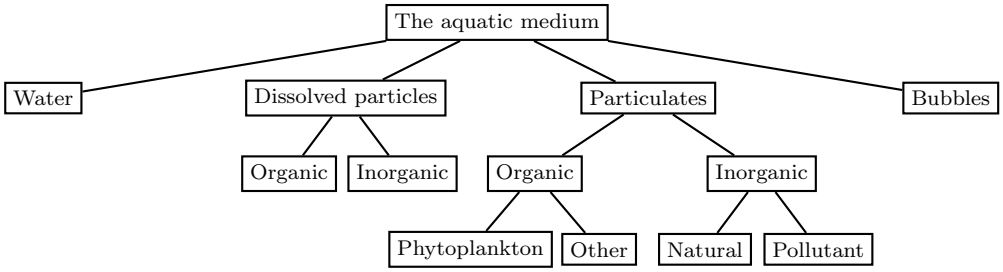

Figure 2.5: Optically significant components of aquatic media, where dissolved particles are considered anything with a diameter less than 0.4 μm.

bands in the visible spectrum. An exception are humic acids, which are a distinct yellow colour, giving rise to the name *colour dissolved organic material* (CDOM). Other names for CDOM include *Gelbstoff*, *gilvin* and *yellow substances* (Bricaud et al., 1981). The main sources of CDOM are broken-down plant tissue and decaying marine matter. When plant tissue decomposes in soil or water the organic matter is broken down to carbon dioxide and inorganic forms of nitrogen, sulphur and phosphorus – the three main nutrients for plant growth. In this process it forms a group of compounds known as the humic substances (Schnitzer, 1978). Humic substances are then defined optically into *fulvic* and *humic* acids. CDOM in natural waters is either a result of the humic substances produced in the water body itself or from fresh water runoff from land; higher concentrations are consequentially found in rivers, lakes and coastal areas.

Phytoplankton

This is a taxonomically diverse group of particulate organic substances, comprising of more than $10,000$ species and taxa (Vesk & Jeffrey, 1977). Phytoplankton develop as plankton and bacteria grow and reproduce; they are photosynthesising, microscopic organisms that form the foundation of the food chain in aquatic media. In terms of concentration, the most important groups of phytoplankton are diatoms, dinoflagellates and coccolithophorids, although many other types of algae are part of phytoplankton. Phytoplankton occur naturally in different sizes (from 0.2 μm to > 1000 μm), shapes (spheroids, cylinders, prolate spheroids and many more), builds (cellulose, silicate or calcium-carbonate cell walls) and with many different physiologies (Shifrin, 1988). Moreover, they contain a large number of different pigments, the most important of them being chlorophyll, thus giving phytoplankton its distinct green colour. As these organisms are photosynthesising, their location varies by light and nutrient availability. Variations occur over time, changing by season and during day-night cycles, and with location, both laterally across a water body and with depth.

Other Organic Particulates

These are non-phytoplankton particles, sometimes referred to as detritus or tripton. This group of particles consists of living organic particles such as bacteria, zooplankon and detrital organic matter. These substances have a limited impact on absorption in the visible spectrum, making them difficult to measure, and subsequently the optical component to receive least attention (Kirk, 1994). Other organic particulates are considered in this research due to their contribution towards the overall scattering profile of aquatic media. As with CDOM, the optically significant components of these particles are humic materials which bind to inorganic particulates to give a yellow-brown colour.

Natural Inorganic Particulates

Natural inorganic particulates include rocks, clays and sands, as well as minerals and metal oxides. These particles enter the aquatic media as wind-blown dust settles on the sea surface, through rivers carry eroded soil to the sea, or as currents re-suspend sediments from the seabed up into the water column. Minerals in particular collide and stick together to form *flocs*, though these are sensitive to turbulent conditions and vary seasonally; more detail about flocs is found in (Boss et al., 2009). Due to the way in which they are extracted from aquatic media, natural inorganic particles tend to be grouped with other organic particulates to form a group of particulates known as *non-algal particles* (NAP) (Mobley et al., 2014).

Pollutants

These occur in different forms, including nutrient pollution from agricultural fertilisers, metals and solvents from industrial waste, and crude oil. Inland waters are mainly affected by point-source pollutants where, in addition to introducing their own unique optical properties, offending pollutants influence the concentration of other dissolved and particulate matter. Dispersed oil droplets are found in seawater from contaminated river inflows, bilge water discharges and as the consequence of oil spills. In additional to impacting on the concentration of organic materials (Zhou & Guo, 2012), oil at the surface causes additional problems for optical links passing the air/water interface (Fingas & Brown, 2014).

Bubbles

In the upper ocean, bubbles are primarily generated by breaking waves and ocean turbulence (Lamarre & Melville, 1991). Depending on the wind speed above the water, bubbles are formed

by different mechanisms: above 7 m s^{-1} a stratus layer of bubbles forms under the sea surface, which continually replenish by frequent wave breaking and subsequent turbulence (Thorpe, 1982) (Crawford & Farmer, 1987); at slower wind speeds waves do not break, bubbles are created by periodic vertical motion of the sea surface. These types of bubbles have the same optical properties as the air above the water body. Other sources of bubbles include phytoplankton photosynthesis and zooplankton respiration (Waaland & Branton, 1969) (Ling & Pao, 1988).

Inhomogenities from Refractive Index Changes

Although not an optical constituent of natural waters, inhomogenities caused by changes in the refractive index have been included here as a factor affecting optical transmission underwater. As shall be seen in sec. 3.5, changes to salinity, pressure and temperature alter the refractive index throughout a body of water. Subsequent refractive index boundaries change the transmission characteristics and direction of light.

2.4 Absorption

The absorption spectra of the optically significant constituents introduced in sec. 2.3 are now examined. Absorption is a highly wavelength dependent process where electromagnetic energy is converted into other forms, typically as heat or chemical. The quantity of energy absorbed depends on wavelength because photon energy is dictated by the wavelength, as in eq. 2.2. Such differences in the quantum energy levels leads to distinct interactions with other molecules. The underlying quantum mechanics are discussed in (Kirk, 1994). Wavelength dependency means that, for a particular water body, there must be some value of wavelength for which the absorption is minimal. These windows of lowered absorption are key to optimising transmission in underwater optical wireless communications.

Absorption plays an important role in all optical communication systems because it potentially causes a large reduction in the number of photons that reach the optical receiver. Communicating underwater, however, optically provides a greater challenge than communicating in air because values of absorption for pure water systems are at least three orders of magnitude higher than in the atmosphere, increasing further in natural water bodies. The overall absorption of natural water bodies is found as the sum of each of the optically significant components multiplied by their concentration:

$$a(\lambda) = \sum_{i=0}^{n} C_i a_i^*(\lambda) \tag{2.17}$$

Absorption of optical constituents shall be denoted in the following way: pure water or seawater as a_{W}; colour dissolved organic material as a_{CDOM}; phytoplankton as a_{PHY}; and non-phytoplankton particulates grouped as NAP, a_{NAP}. Other constituents are not included here due to their limited impact on the absorption spectrum. The optical properties of the aforementioned components are introduced by way of fig. 2.6 (Fujii et al., 2007), which depicts typical absorption spectra for pure water, phytoplankton, NAP and CDOM respectively. Note there are not only differences in the extent of absorption for each case, but more particularly the wavelengths over which highest absorption occurs.

As the overall absorption spectrum of a body of water is defined by superpositioning particular amounts of the individual spectra, as exemplified by fig. 2.7, it can be seen that the aquatic medium has varied optical properties depending on its composition. In ch. 3, the extent and exact causes of overall variations are explored; first, this section deals with identifying variations in individual constituent absorption spectra.

2.4.1 Absorption by Water

Although appearing colourless in small quantities, pure water is a blue liquid. The colour of pure water arises as the absorption coefficient throughout most of the electromagnetic spectrum is high (around 10^4 m^{-1} for infra-red (Prahl, 1998)), significantly lowering for visible light, particularly in the blue/green region of the spectrum. Because the quantity of absorption is so low in this region, there is great disparity in measured values of the absorption coefficient (Kirk, 1994). However, a set of values derived in (Smith & Baker, 1981), which combined their own measurements, previous best measurements and diffuse attenuation coefficients, are widely considered the most accurate for pure natural waters and therefore are used in this research (given in app. A). Note in particular that, as a consequence of high absorption outside the visible region, wavelengths used for atmospheric optical wireless communications such as infra-red and near infra-red are not suitable.

The dissolved salts in pure seawater cause it to have a slightly more complex absorption spectrum than that of pure water, although mostly within the ultra-violet region. In fig. 2.6a the absorption spectrum, a_{W}, has been plotted for the visible region. As with pure water, red wavelengths of 500 nm or higher are greatly attenuated by seawater, leaving primarily blue light

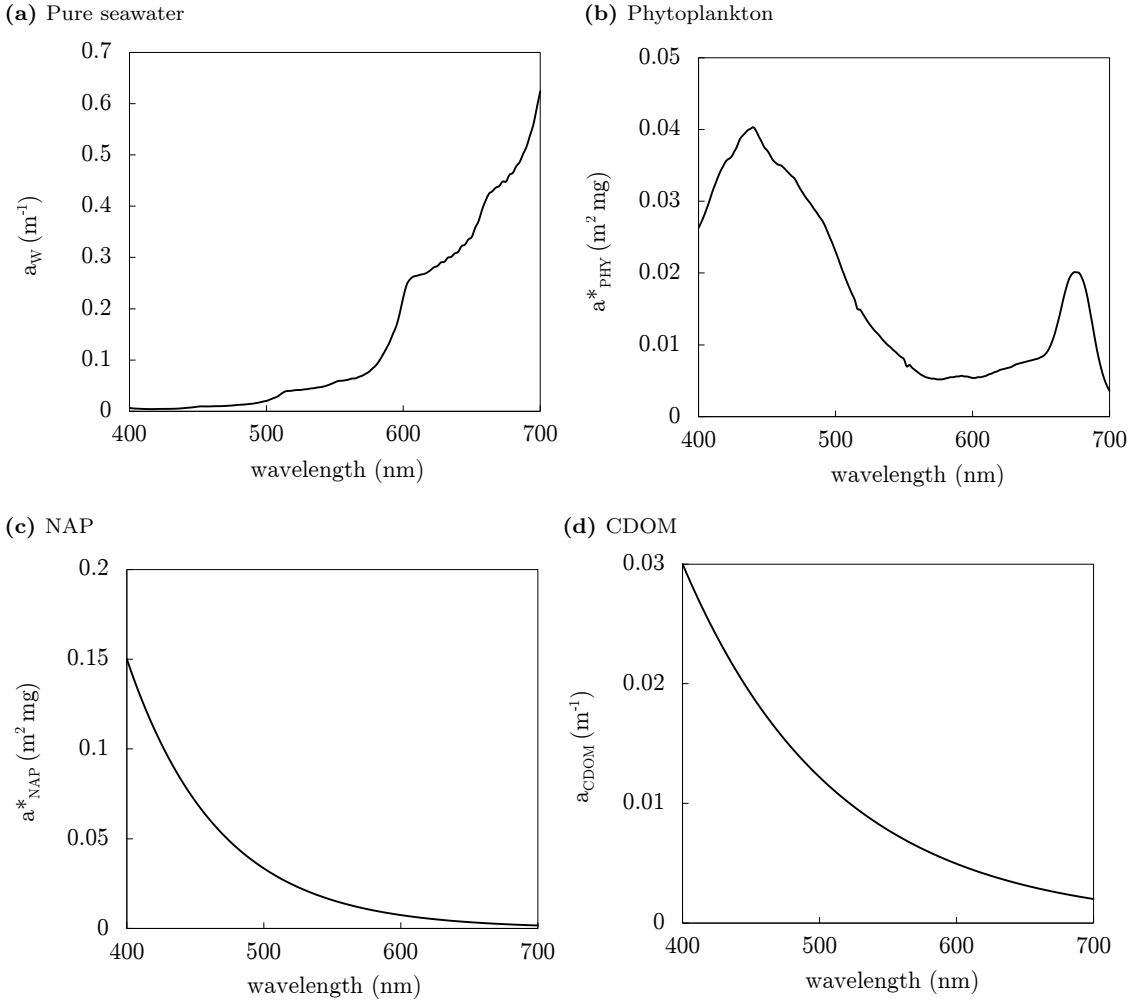

Figure 2.6: Generic absorption spectra for different ocean optical components, where (a) is the absorption coefficient by seawater, (b) is the chlorophyll-specific absorption coefficient by phytoplankton, (c) is the carbon-specific absorption coefficient by NAP, and (d) is the absorption coefficient by NAP, from 400 - 700 nm, edited from (Fujii et al., 2007).

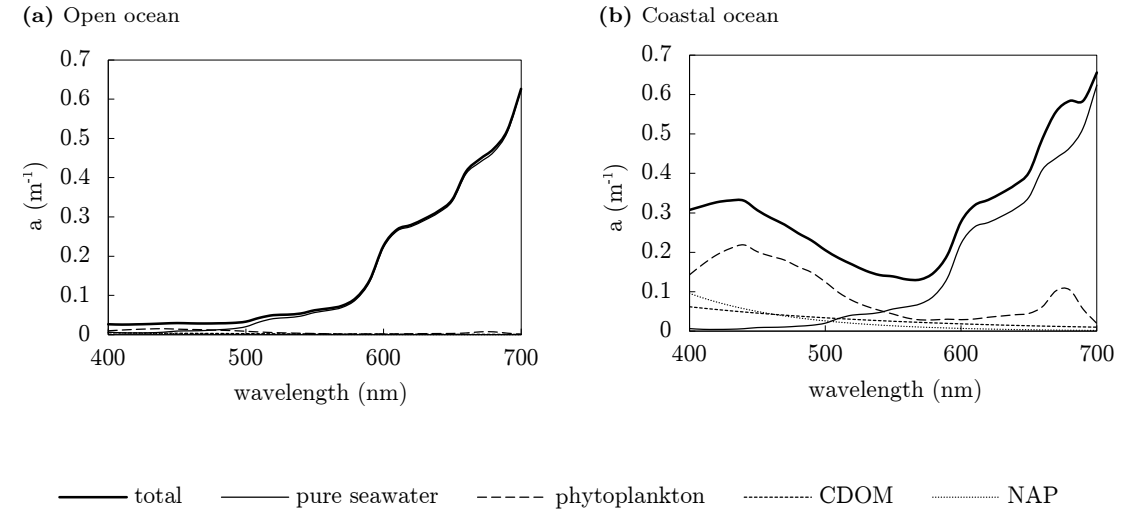

Figure 2.7: Typical combined absorption spectra for different oceanic locations, based on fig. 2.6.

to propagate. This is one of the reasons why open oceans, away from the shore, appear a rich blue colour. Indirect methods have been used to determine a maximum for the water absorption coefficient, given in eq. 2.18 (Smith & Baker, 1981).

$$a_{\mathrm{W}}(\lambda) < K(\lambda) - \frac{b_{\mathrm{W}}(\lambda)}{2} \tag{2.18}$$

Where b_{W} is the scattering coefficient of water and K is the diffuse attenuation coefficient from sec. 2.2.1. This formula is useful in worse case calculations for communication systems.

The absorption spectrum of seawater is fairly consistent regardless of refractive factors, e.g. salinity, temperature, pressure (Pegau & Zaneveld, 1993), though there are inconsistencies in the measurements at shorter wavelengths around the blue part of the spectrum (Shifrin, 1988) (Hale & Querry, 1973) (Kopelevich, 1976), likely due to contamination by CDOM and particulate organic matter (Segelstein, 2011). Research by (Sogandares, 1991) and (Pope & Fry, 1997) is considered up to date (the latter is also given in app. A), providing contamination free data sets of the absorption of pure seawater. According to these data sets, the minimum absorption occurs at a wavelength of 420 nm, rather than in the green region as found in older studies.

When considering eq. 2.17, the seawater concentration can be set to unity for most applications. Exceptions to this are where the seawater is mixed with another significantly present liquid; examples include at estuaries where there is a seawater/freshwater mix and seawater/oil mixes due to pollution.

2.4.2 Absorption by Phytoplankton

Phytoplankton describes a diverse group of species, where the individual spectra vary in magnitude and shape due to the different cellular pigment composition and pigment packaging (Bidigare et al., 1990) (Hoepffner & Sathyendranath, 1991) (Ciotti et al., 2002) (Bricaud et al., 2004). As phytoplankton photosynthesise, they primarily all consist of chlorophylls, resulting in common absorption features for all species, including high absorption in the blue region (around 440 nm) and a further peak in absorption in the red region (670 nm). The presence of other pigments causes broadening of the blue peak and the appearance of an additional absorption maxima, such that the absorption profile, a_{PHY}, has a shape typically as that given in fig. 2.6b. It is these taxa-specific absorption peaks that can be used as an optical detection tool in situ (Millie et al., 2000) as well for development of remote sensing algorithms (Tomlinson et al., 2009).

High absorption in the red and blue regions means that areas of high phytoplankton – usually

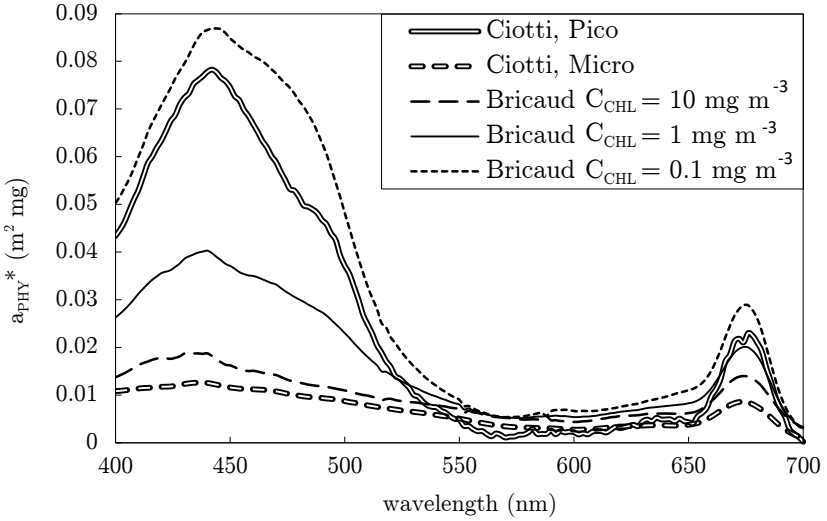

Figure 2.8: The impact of phytoplankton size and concentration: absorption profiles for pico and micro scale phytoplankton (Ciotti et al., 2002) as well as different chlorophyll concentrations C_{CHL} (Bricaud et al., 2004).

defined by high chlorophyll concentration, C_{CHL} – generally appear yellow-green in colour. However, exact absorption by phytoplankton is not a simple sum of absorption coefficients of individual pigments and their concentration, changes in pigment concentration and cell size flatten the specific absorption spectra via the packaging effect (Morel & Bricaud, 1981). As displayed in fig. 2.8, using data from (Ciotti et al., 2002) and (Bricaud et al., 2004), greater concentrations and larger sized phytoplankton give the absorption spectrum less profound peaks in the red and blue regions. The flattening caused by increased concentration can be estimated numerically based on the work of (Bricaud et al., 1995), through the equation

$$a^*_{\mathrm{CHL}}(\lambda) = F_1(\lambda) C_{\mathrm{CHL}}^{F_2(\lambda)} \tag{2.19}$$

where C_{CHL} is the chlorophyll concentration, present in all phytoplankton species, and F_1 and F_2 are numerical constants given in app. B.

The concentration of phytoplankton, and therefore of chlorophyll, varies considerably in natural water bodies as phytoplankton inhabits locations only with sufficient light and nutrients for photosynthesis. As will be seen in ch. 3, in addition to changing its own absorption profile, this variable concentration has a profound effect on the concentrations of other naturally occurring substances such as CDOM and NAP.

2.4.3 Absorption by Colour Dissolved Organic Material

The absorption spectrum of CDOM is dictated by that of the humic and fulvic substances, being the only dissolved organic materials impacting on visible wavelengths. As shown in fig. 2.6d, the spectrum is approximately exponential, where blue-violet wavelengths are highly attenuated so that yellow-red colours become more dominant. The Beer-Lambert law, as given in eq. 2.20, is used to fit the exponential function; the slope S_{CDOM} is estimated by non-linear regression and the wavelength measurement is given in nm.

$$a_{\mathrm{CDOM}}(\lambda) = a_{\mathrm{CDOM}}(\lambda_0)\exp[-S_{\mathrm{CDOM}}(\lambda - \lambda_0)] \tag{2.20}$$

Variations in slope are observed to be between 0.010 - 0.020 nm^{-1} in oceanic conditions, with mean values around 0.014 nm^{-1} (Roesler et al., 1989) (Babin et al., 2003); for inland water bodies the slope is shallower, varying between 0.012 - 0.022 nm^{-1}, with a mean value of 0.018 nm^{-1} (Davies-Colley & Vant, 1987) (Kirk, 1994). The value of the spectral slope is therefore an indicator of CDOM composition, with fulvic terrestrial material having steeper spectral slopes than marine-derived humic material (Carder et al., 1989). As humic and fulvic substances are the two optically significant components of CDOM, the specific absorption spectrum is sometimes rewritten as the contributions from fulvic and humic substances, for example in (Haltrin, 1999), where

$$a^*_{\mathrm{CDOM}}(\lambda) = a^*_{\mathrm{H}}(\lambda) + a^*_{\mathrm{F}}(\lambda) \tag{2.21}$$

Here a^*_{H} and a^*_{F} are the specific absorption coefficients for fulvic and humic fluids respectfully.

Variations in spectral slope have also been attributed to the average size distribution of CDOM particles, where the slope is greater for particles with diameter less than 0.2 μm (Simeon et al., 2003). Following the same logic that was introduced for phytoplankton (sec. 2.4.2), it can be seen that this is because larger particles have a tendency to flatten the absorption profile. Note both total concentration and proportions of CDOM are highly variable.

2.4.4 Absorption by Non-Algal Particles

As NAP incorporates all non-phytoplankton particulates, it is difficult to extract a singular absorption profile for this component. Several methods have been used to derive this, including: direct examination of individual particles using micro-spectrophotometry (Iturriaga & Siegel, 1989); using measurements before and after chemical extraction of phytoplankton (Kishino et al.,

1985); modelling based on an assumed ratio of phytoplankton absorption (Roesler et al., 1989); modelling based on an expected NAP absorption function (Stramski, 1990); and statistical methods based on typical absorption spectra (Morrow et al., 1989). Each of these methods has yielded the same result, an exponentially decaying function which peaks in the blue-violet region:

$$a_{\mathrm{NAP}}(\lambda) = a_{\mathrm{NAP}}(\lambda_0)\exp[-S_{\mathrm{NAP}}(\lambda - \lambda_0)] \tag{2.22}$$

where S_{NAP} is the exponential slope which typically takes values between 0.006 - 0.013 nm^{-1} (Roesler et al., 1989) (Babin et al., 2003), making it a statistically flatter curve than that of CDOM, as can be seen in fig. 2.6c. Research published at a later date is in agreement with previous slope values, estimating the average slope to be 0.012 nm^{-1} (Bowers & Binding, 2006).

Several studies hint at there being a departure from an exponential decay in the form of a bulge in the absorption spectrum between 450 and 550 nm, a feature which has appeared in both inland (Tassan & Ferrari, 1995) and oceanic measurements (Harker, 1997). However, the extent of this deviation is not widely studied or documented.

2.5 Scattering

The second inherent optical property of interest is scattering, a process which causes changes in the direction of electromagnetic energy in an optical beam. These changes occur due to localised non-uniformities in the medium through which the beam passes, this is either from different particles within the medium or variations in the state of the medium itself which result in a varying refractive index.

Scattering is of particular importance to underwater optical wireless systems as it leads to

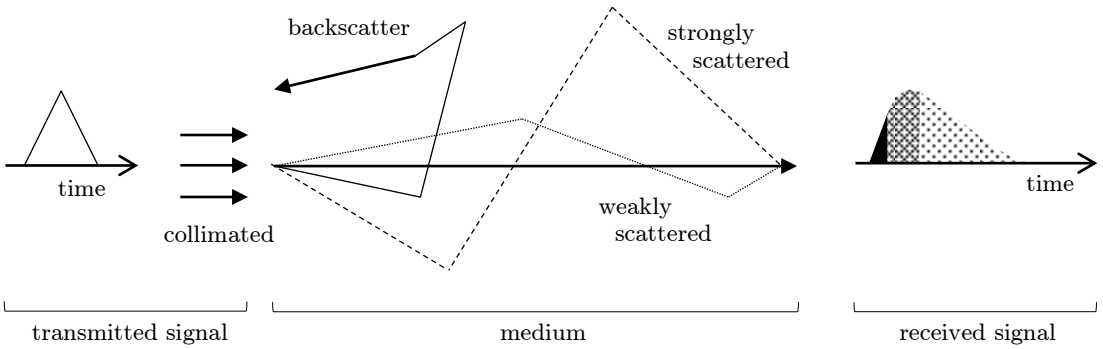

Figure 2.9: The origins of temporal scattering, based on (Stotts, 1978).

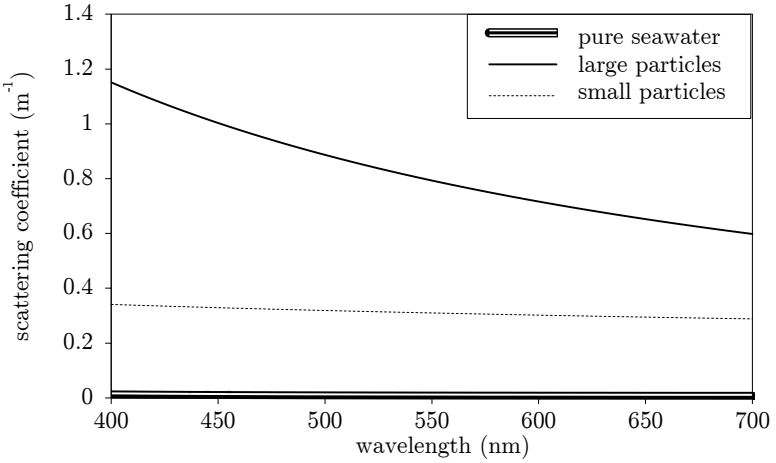

Figure 2.10: Pure seawater and particulate scattering spectra, where small particles are defined as having a diameter < 1 μm. Data from (Haltrin, 1999).

several quality loss mechanisms. First, as photons take alternative paths, the number reaching the receiver is reduced, lowering the detected signal. Second, it causes temporal spreading of the signal, as depicted in fig. 2.9. Temporal spreading occurs when scattered photons are re-scattered back into the beam path, causing them to travel a greater distance than the straight trajectory of unscattered photons. Longer path lengths take a greater time to be travelled and the resulting delay between receiving the two photons can cause inter-symbol interference if the bit rate of the system is not suitably low to accommodate for this temporal spreading. Moreover, for duplex optical systems, backscatter (as shown in fig. 2.9) may be indistinguishable from the return signal if not properly accounted for.

In the visible region, scattering is largely independent of wavelength, depending more on density changes in the aquatic medium, specifically the shape, size and concentration of particulates. Unsurprisingly, smaller particles have a lesser impact, as identified in fig. 2.10, where small particle scatter and that from pure seawater only make up a tiny proportion of the total scatter. Motivated by this, scattering events are physically categorised by the size of the the density fluctuations they cause. Whilst medium inhomogenities in seawater cause small scale fluctuations ($\ll \lambda$), turbulence induced fluctuations are very large ($\gg \lambda$); scattering by organic or inorganic particles ($> \lambda$) lies somewhere between the two extremes (Gawdi, 2006). This section aims to describe the scattering regimes of these each category of scattering event. However, in order to do so, a geometric factor must be introduced into the scattering coefficient.

2.5.1 Volume Scattering Function

The volume scattering function (VSF), β, is defined as the ratio of the intensity of scattered light to the incident irradiance per unit volume; it can also be thought of as a scattering coefficient where the directionality of scatter has been retained. To derive this additional inherent optical property, two assumptions are made about the underwater environment (Jerlov, 1976). First, the aquatic medium is assumed to be isotropic so that its influence on the incident light is the same in all directions and second, that incident light is unpolarised. Once these two assumptions are made, then scattering is azimuthally symmetric and depends only on ψ, the scattering angle depicted in fig. 2.3. The scatterance, introduced originally in eq. 2.8, becomes angularly dependent and is consequentially described as the fraction of incident scattered power through an angle ψ into a solid angle Ω. The VSF is the limit of this as the thickness r and solid angle become infinitesimally small, such that;

$$\beta(\psi,\lambda) \equiv \lim_{\Delta r\to 0}\lim_{\Delta\Omega\to 0}\frac{\Delta B(\psi,\lambda)}{\Delta r\Delta\Omega} \tag{2.23}$$

To convert eq. 2.23 into a more usable form the following is done: the scatterance from eq. 2.8 is substituted in; the spectral scattered power is rewritten as intensity of scattered power multiplied by the solid angle, $\Phi_s(\psi,\lambda) = I_s(\psi,\lambda)\Delta\Omega$; the spectral incident power is split into incident irradiance multiplied over area of incidence $\Phi_i(\lambda) = E_i(\lambda)\Delta A$ and a volume V is introduced where $\Delta V = \Delta r\Delta A$. The VSF consequentially takes the following form

$$\beta(\psi,\lambda) = \frac{1}{E_i(0,\lambda)}\frac{dI_s(\Omega,\lambda)}{dV} \tag{2.24}$$

The definition of the VSF, as the ratio of scattered light intensity to incident irradiance per unit volume, is now more apparent in this form. To give the total scattered power per unit irradiance, i.e. the scattering coefficient, the sum of contributions over all angles is taken.

$$b(\lambda) = \int_{\Xi}\beta(\psi,\lambda)\,d\Omega = 2\pi\int_0^{\pi}\beta(\psi,\lambda)\sin\psi\,d\psi \tag{2.25}$$

Conventionally this equation is split into forward scatter, between angles $0 < \psi < \pi/2$, and back scatter, $\pi/2 < \psi < \pi$ (Mobley & Mobley, 1994); for communication systems, these limits can be adjusted to match the transmitted beam angle and the receiver field-of-view (FOV). In addition to providing information of scattering directionality, the VSF is used to calculate the beam spread

function (BSF) which models how a collimated beam of light spreads due to scattering as it travels through a body of water; this will be revisited in ch. 5. The derivation of the BSF is omitted from this research but a thorough description is found in (Shifrin, 1988).

Another useful concept is the idea of phase function, $\tilde{\beta}$, which is defined as the VSF normalised to the total scattering amount. It provides information about the shape of the VSF regardless of the intensity of the scattered light

$$\tilde{\beta} = \beta / b \tag{2.26}$$

There are several pre-existing models describing underwater phase functions such as the Henyey-Greenstein phase function (Henyey & Greenstein, 1941), Petzold's measurements (Petzold, 1972) and Fournier-Forand (Fournier & Forand, 1994) (Fournier & Jonasz, 1999); these are described in more detail in app. C.

2.5.2 Scattering by Particulates

Particulates such as phytoplankton, CDOM and NAP account for roughly 40 - 80% of the total scattering in turbid aquatic media (Apel, 1987). When photons come into contact with suspended particles, the direction of travel is altered through reflection and refraction at internal and external refractive index boundaries (fig. 2.11). In general, the scatter caused by these particles peaks in the forward direction, suggesting the application of Mie scattering theory (Mobley & Mobley, 1994).

Mie scattering is a solution to Maxwell's equation which describes the scattering of an electromagnetic plane wave by the refractive index boundary of a spherical particle. In the atmosphere, this type of scattering is responsible for the white appearance of clouds where all visible wavelengths are scattered by water droplets. As Mie offers a solution for spherical particles, when applying Mie theory underwater, the assumption is made that particulates in the aquatic medium are spheres of different sizes, instead of the complex shapes. Although this

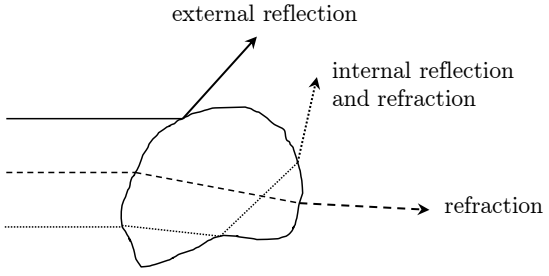

Figure 2.11: Scattering of light by a particulate.

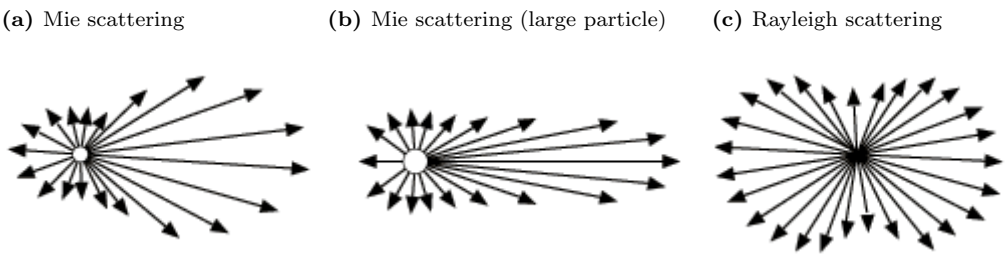

(a) Mie scattering **(b)** Mie scattering (large particle) **(c)** Rayleigh scattering

Figure 2.12: Two-dimensional angular scattering distributions (volume phase functions) for a beam of light moving left to right, interacting with different sized particles. Large particles are defined as those with a diameter greater than 1 μm. Distributions based on figures in (Meyer-Arendt, 1989).

assumption has been attributed to discrepancies between measured and predicted backscatter (Quirantes & Bernard, 2004) (Morel & Ahn, 1991), where Mie provides an underestimation of the total backscatter, it is sufficient for communication system models where forward scatter is of greater significance.

Each particulate size has a unique angular scattering distribution due to the way in which incident light interacts, making an overall distribution difficult to calculate. As there are algorithms for calculating coefficients in single and multi-particle systems (Xu & Gustafson, 2001), optical models are simplified by grouping particulates into crude categories such as *small* and *large* particles. In this research, these crude categories are implemented for simplicity, where small particles are defined as those with a diameter of 1 μm or less, based on (Kopelevich, 1983) and (Haltrin, 1999). Recalling the magnitude of small and large particle scatter shown in fig. 2.11, the typical angular distributions for these groups of particulates is given in fig. 2.12a and fig. 2.12b respectively. Both scattering profiles are dominant in the forward direction with minimal backscatter; larger particles are more highly peaked due to an increased amount of refraction.

Efforts to derive wavelength dependent solutions for angular scattering distributions, or VSFs, led to the development of bio-geo-optical scattering models. Early observations found particulate-rich areas to be less affected by wavelength and that the asymmetry caused by the forward peak reduces at short wavelengths (Morel, 1973). These results were confirmed by mathematical descriptions highlighting the wavelength-to-size ratio (Kopelevich, 1983) (Kopelevich & Mezhericher, 1983), where the distinction between small and large particle scatter was introduced. Further models have included estimations of the size distributions based on the chlorophyll concentration in a particular water body to derive general expressions for wavelength-dependent angular scattering distributions (Morel, 1991) (Haltrin & Kattawar, 1991). This research uses the result found in (Haltrin, 1999) to estimate these distributions as it

provides an amalgamation and update on models presented in previous studies. The scattering coefficient for small and large particulates, which is derived from statistical methods, is quoted as

$$b^*_{\mathrm{L}}(\lambda) = 1.151302 \left(\frac{400}{\lambda}\right)^{1.17} \qquad b^*_{\mathrm{S}}(\lambda) = 0.341074 \left(\frac{400}{\lambda}\right)^{0.3} \tag{2.27}$$

where b^*_{S} and b^*_{L} are the specific scattering coefficients for small and large particles respectively. As shown in fig. 2.10, particulate scattering varies slightly with wavelength being marginally higher in the blue-green region.

Haltrin derived the overall VSF from particulates, here called β_{P}, as

$$\beta_{\mathrm{P}}(\psi, \lambda) = b^*_{\mathrm{S}}(\lambda)\tilde{\beta}_{\mathrm{S}}(\psi)C_{\mathrm{S}} + b^*_{\mathrm{L}}(\lambda)\tilde{\beta}_{\mathrm{L}}(\psi)C_{\mathrm{L}} \tag{2.28}$$

where C_{L} is the concentration of large particulates and C_{S} is the equivalent for small particulates. It is due to these concentrations that areas of high turbidity cause collimated light beams, such as a lasers, to appear as a diffuse source after a short distance. $\tilde{\beta}_{\mathrm{S}}(\psi)$ and $\tilde{\beta}_{\mathrm{L}}(\psi)$ represent phase functions for small and large particulate scattering, which Haltrin gives empirically by as

$$\tilde{\beta}_s(\psi) = 5.6175 \exp\left[\sum_{n=1}^{5} F_{\mathrm{S}n}\psi^{3n/4}\right] \qquad \tilde{\beta}_l(\psi) = 188.38 \exp\left[\sum_{n=1}^{5} F_{\mathrm{L}n}\psi^{3n/4}\right] \tag{2.29}$$

The coefficients $F_{\mathrm{S}n}$ and $F_{\mathrm{L}n}$ are given in tab. 2.2, yielding plots such as those in fig. 2.12. As with results seen previously, these Mie solutions are symmetric through the centre in addition to being azimuthally symmetric and, although both of these scattering regimes are forward dominant, large particles scatter more to small near-forward angles.

The bio-geo-optical models for scattering discussed are useful but generally quite approximate. Reasons for frequent discrepancies between model predictions and measured values of scatter include scattering depending on not only the particulate concentrations, but also the refractive index of those particulates, and poorly parameterised particulate size distributions.

2.5.3 Scattering by Pure Seawater

Random molecular motions and variable concentrations of ions in pure seawater give rise to fluctuations in the density of a given volume, leading to molecular scattering. The typical angular distribution of molecular scattering has equal contributions in forward and backward directions and is found using a small-particle approximation of Mie scattering. The solution to the approximation is given the name Rayleigh scattering, it describes the elastic scattering of

n	$F_{\mathrm{S}n}$	$F_{\mathrm{L}n}$
1	-2.957x10^{-2}	-1.604
2	-2.783x10^{-2}	8.158x10^{-2}
3	1.255x10^{-3}	-2.150x10^{-3}
4	-2.156x10^{-5}	2.419x10^{-5}
5	1.357x10^{-7}	-6.579x10^{-8}

Table 2.2: Haltrin coefficients for eq. 2.29, the volume phase function of particulate scattering, where $F_{\mathrm{S}n}$ are the coefficients for small particulates with a diameter less than 1μm and $F_{\mathrm{L}n}$ are large particulate coefficients (Haltrin, 1999).

light by spheres which are much smaller than the wavelength of light. In the atmosphere, Rayleigh scattering is responsible for making the sky appear blue through the selective scattering of blue/violet wavelengths from air molecules.

In pure seawater, Rayleigh scattering takes the following mathematical form (Morel, 1974)

$$\beta_{\mathrm{W}}(\psi,\lambda) = \beta_{\mathrm{W}}(90^\circ,\lambda_0)(1+0.835\cos^2\psi)\left(\frac{\lambda_0}{\lambda}\right)^{4.32} \tag{2.30}$$

where β_{W} is the VSF of pure seawater, measured in m^{-1} sr^{-1}. The coefficient $\beta_{\mathrm{W}}(90^\circ)$ is given in app. D.1 for a range of wavelengths. The volume phase function corresponding to eq. 2.30 is

$$\tilde{\beta}_{\mathrm{W}} = 0.06225(1+0.835\cos^2\psi) \tag{2.31}$$

which is symmetric about the forward and backward directions, as shown in fig. 2.12c. The remaining part of eq. 2.30 gives the total scattering coefficient for pure seawater

$$b_{\mathrm{W}} = 16.06\,\beta_{\mathrm{W}}(90^\circ,\lambda_0)\left(\frac{\lambda_0}{\lambda}\right)^{4.32} \tag{2.32}$$

for which values are given in app. D.1 for a range of wavelengths. In the visible region, pure seawater scattering remains roughly at a constant level with wavelength, being only slightly higher towards the blue end of the spectrum, as shown by fig. 2.10. This figure also serves as a reminder that the magnitude of pure water scattering coefficient is much less than that of particulate scatter.

The pure seawater and particulate scattering regimes described here include all constituents in the aquatic medium. However, if results from these models were to be compared with real scattering

measurements, a shortfall would be found between the actual and predicted values (Shifrin, 1988). Although this shortfall may be, in part, attributed to inaccuracies in the scattering models, much of the difference comes from additional refractive fluctuation mechanisms such as air bubbles (Mobley & Mobley, 1994) and turbulence (Bogucki et al., 1998). As these scattering mechanisms do not have absorptive equivalents, and absorption usually dominates the attenuation, they are generally omitted from scattering discussions for underwater optical communications. However, for completeness, these aspects have been surveyed in sec. 2.5.4 and sec. 2.5.5.

2.5.4 Scattering by Bubbles

A previous study showed that injecting a significant amount of bubbles into a testing pool causes the measured attenuation coefficient to increase by up to two orders of magnitude (Hagem et al., 2012). Although the bubble density used in this study was many times greater than is found to occur naturally in the ocean, it does indicate that the attenuation can be affected by bubbles. As the absorption coefficient of bubbles is zero and the single-scattering albedo is equal to unity (Zege et al., 2006), this rise in attenuation can be fully attributed to increased scatter.

Over the years, oceanographic research has developed a scattering model for bubbles in the ocean and other water bodies. It was found that each bubble can be optically modelled as a spherical particle of air, permitting the application of Mie scattering theory (Marston, 1979) (Patrick Arnott & Marston, 1988) (Arnott & Marston, 1991). In order to a generate Mie scattering solution for the aquatic medium, estimations of the local air bubble population are required, which is difficult given the temporal nature and a continuous size distribution of bubbles underwater.

Ocean measurements roughly estimate the bubble number density to be between 10^5 - 10^7 m^{-3} in the upper ocean (Zhang et al., 1998). Using this approximation, one study generated a VSF through a range of analytical techniques and measurements (Zhang et al., 2002). Air bubbles of this density were shown to have a negligible contribution to the total scattering (<5%), but accounted for more than 40% of the total backscatter observed in situ. The resulting volume phase function was highly peaked for scattering at large angles and the overall scattering coefficient bared the same wavelength dependency as particulate scatter. Subsequent analytical models of the attenuation coefficient and volume phase function are in agreement with these results (Zege et al., 2006).

Although, as discussed above, bubbles scattering has been estimated to significantly increase backscattering, optical wireless communication links are typically only interested in forward-scatter as this is what will be detected by the receiver. Hence, there is no further inclusion of bubble

scattering in this text.

2.5.5 Scattering by Turbulence

Optical turbulence is the name given when a medium experiences rapid, local changes in refractive index. For atmospheric optical communication systems, turbulence is known to cause irradiance fluctuations, or scintillation, and phase fluctuations (Andrews et al., 1999) (Andrews & Phillips, 2002); the same is expected of underwater optical communications. In aquatic environments, turbulence is found where there are ocean currents, at interfaces between rivers and oceans, or from the movement of large ocean vehicles and animals, making it particularly prevalent in shallow and coastal environments (Hanson & Lasher, 2010).

Unlike atmospheric optical links where humidity and temperature control turbulence, underwater turbulence is attributed mainly to fluctuations in temperature (Bogucki et al., 1998) and salinity (Ata & Baykal, 2014). The statistical variation in refractive index with regards to these factors is expressed through a spatial power spectrum of refractive fluctuation (Nikishov & Nikishov, 2000); derived for homogeneous and isotropic turbulence as a function of the rate of dissipation of turbulent energy, and temperature and salinity fluctuations. Translating this spatial power spectrum into a measurable impact on underwater optical links has recently become a keen area of activity in optical wireless communication research.

Earlier atmospheric studies found that the magnitude of scintillation is proportional to the length scale of turbulence and strength of turbulence regimes (Andrews & Phillips, 2002). Scintillation models are subsequently generated based on the normalised variance of irradiance intensity, or scintillation index, σ_I, as given by

$$\sigma_I^2 = \frac{\langle I^2 \rangle - \langle I \rangle^2}{\langle I \rangle^2} \tag{2.33}$$

where I is the irradiance intensity, as before, and $\langle\ \rangle$ denotes a time average. In a weakly turbulent medium, where $\sigma_I \ll 1$, the scintillation index in eq. 2.33 can also be derived as a log-amplitude correlation function obtained by the Rytov method (Tatarski, 1961) as shown in eq. 2.34.

$$\sigma_I^2 = 4B_\chi(r) \tag{2.34}$$

where B_χ is the log-amplitude correlation function for a scintillation index at the receiver plane of an optical link of path length r.

Investigations into different forms of scintillation index have led to some notable conclusions. One study described the intensity and the coherence characteristics of propagation and showed that underwater turbulence has a significant effect on the beam as compared to atmospheric turbulence (Farwell & Korotkova, 2012), later introducing longitudinal and radial scintillation index components (Korotkova et al., 2012). Another study determined scintillation indices for optical plane and spherical waves, concluding that underwater turbulence effects become significant at path lengths above 5 – 10 metres for a plane wave and at 20 – 25 metres for a spherical wave (Ata & Baykal, 2014), although these lengths are expected to be extended using atmospheric optical communication techniques such as aperture-averaging (Yi et al., 2015).

As scintillation index varies according to the characteristics of the light beam transmitted, the correlations for general-type beams in turbulence have been formulated (Baykal, 2006) and later assessed for use in underwater optical links. Examples of this include: intensity fluctuations of higher order single mode lasers (Baykal, 2014); multi-mode lasers (Baykal, 2015); Gaussian beam lasers (Gerçekcioğlu, 2014) and Gaussian beam arrays (Lu et al., 2015). Moreover, analytical expressions for the log-amplitude correlation function can potentially be used to explore more difficult turbulence regimes (Gudimetla et al., 2012).

A very small number of studies have investigated the phase fluctuations, or temporal impact, of turbulence, most notably the work of (Cochenour, 2013) and (Baykal, 2015). Despite its impact not being fully known, there appears to be an emerging consensus that small-scale temporal changes are not significant to optical wireless links underwater in open ocean locations. It is though that this may be because the scale of scintillation is much lower for water than, for example, air, because the refractive index does not vary to the same extent. It should be noted that, as the research in this thesis is mainly concerned with open ocean locations, scattering from turbulence is assumed to be negligible and hence is omitted from further scattering models.

2.6 Summary

The purpose of this chapter was to build a basic framework of the behaviour of light in varied aquatic media. In order to do so, the significant inherent and apparent optical properties of natural waters have been defined and briefly surveyed. The optical properties and relevant absorption and scattering models of natural constituents – specifically pure seawater and particulates such as phytoplankton, CDOM and NAP – are generally well established, to a degree of accuracy sufficient for the investigation of underwater optical communications. Areas where it may be anticipated that

Quantity	SI units	Symbol
absorption coefficient	m^{-1}	a
scattering coefficient	m^{-1}	b
volume scattering function	$\mathrm{m}^{-1}\mathrm{sr}^{-1}$	β
volume phase function	sr^{-1}	$\tilde{\beta}$
single-scattering albedo	dimensionless	ω_o
refractive index (real part)	dimensionless	n

Table 2.3: Summary of terms, units and symbols for inherent optical properties.

Quantity	SI units	Symbol
diffuse attenuation coefficient	m^{-1}	K
reflectance	dimensionless	R
optical depth	dimensionless	ζ

Table 2.4: Summary of terms, units and symbols for apparent optical properties.

models currently available will undergo improvements as their impact becomes better understood include scattering from bubbles and turbulence, as well as more topical issues such as absorption by pollution.

Tab. 2.3 and tab. 2.4 provide summaries of the terms, units and symbols for the inherent and apparent optical properties that were introduced in this chapter. In ch. 4 and ch. 5 it will be seen how these are used to develop communication and noise channel descriptions, through radiative transfer theory. First, attention is turned to the variability of these inherent and apparent optical properties to establish the range of conditions underwater optical communication systems could potentially be operating in.

Chapter 3

Optical Property Variability

Underwater optical wireless communications are open communication systems, meaning optical links are subject to an uncontrollable and uncertain transmission medium. The resulting optical property variability impacts on communication link range and performance, highlighting the importance of understanding and investigating changes within the aquatic medium.

Optical property variations are categorised into small, local variations, which are generally the result of turbulence, and large-scale variations, arising due to gradual changes in the inherent optical properties. This chapter explores why and when the latter changes occur, with the aim of developing unique models of the variability of optical properties in natural bodies of water.

3.1 Defining Variability

Previously in ch. 2, the optical properties in a generalised aquatic medium were formed, showing the properties to be a result of dissolved and particulate matter present within the medium. Not only does this change single values of the optical properties, such as those tabulated for different ocean locations in tab. 2.1, it has differing impact over the entire spectrum of visible light, though particularly for light in the blue/green part of the spectrum. As a result, the optimum optical communications window changes, as too does the perceived colour of each natural body of water, where fig. 3.1 provides an example of this (Mobley et al., 2014).

Changes to optical properties arise on different size scales, varying by location and over time. Localised changes in the aquatic media are generally the result of turbulence, whether it be from an ocean/inland water interface or from ocean turbulence. However, a discussion of localised variability is not included in this research due to the limited impact of turbulence on underwater optical links, as discussed in ch. 2. Instead, focus is directed towards global or large-scale changes. As with localised variations, global changes occur by location and temporally. Spatial variability comes in the form of differing aquatic environments, such open ocean, coastal oceans and inland water bodies, and with gradually varying optical properties across the surface and with depth. Temporal variability, conversely, is a result of lunar and solar rhythms, where variations occur on a seasonal and day-to-day basis.

The inherent optical properties investigated in this chapter are the attenuation coefficient, which varies as a direct result of the composition, and the refractive index, which was briefly introduced in sec. 2.3 as being controlled by factors such as temperature, salinity and pressure. However, before exploring variability in the attenuation coefficient and refractive index in sec. 3.3

(a) Open ocean

(b) Coastal ocean

Figure 3.1: Varied colour of ocean water due to differing optical properties, as viewed from a research ship, where higher amounts of particulate matter in coastal water cause the region of low attenuation to be shifted towards green wavelengths. Images by D. G. Bowers (Mobley et al., 2014).

Figure 3.2: Example Secchi disk design, based on a description in (Mobley et al., 2014).

and sec. 3.5 respectively, standard historical and modern water classification schemes are introduced to provide an overview of the existing understanding of optical property variability.

3.2 Standard Classification Schemes

Water classification schemes come in an assortment of forms, based on different optical or constituent properties, and exist to characterise the turbidity of natural water bodies. The most successful schemes are visual colour matching methods, Jerlov water types (Jerlov & Nielsen, 1974) and ternary diagrams (Arnone et al., 2004).

Historically, visual classification using a Secchi disk was the first water classification scheme; it uses a submerged black and white disk, such as that shown in fig. 3.2, where the apparent colour of the disk determines the water type. As this is very inaccurate, it was superseded by schemes such as the Forel-Ule scale, which compares the water colour to twenty-two different coloured chemicals. Although visual schemes, in general, are limited by their qualitative nature and preference for determining changes in absorption over scatter, their popularity remains due to their simplicity.

The first quantitative ocean classification scheme was based on the downwelling diffuse attenuation coefficient, an apparent optical property, and is known as Jerlov water types (Jerlov, 1976). The Jerlov classification scheme splits the ocean into two types; open ocean water and coastal or turbid water. Open ocean is then subdivided into five categories, I, IA, IB, II and III, whilst turbid areas are split into groups 1 - 9, representing increasing turbidity. The original scheme refers to the optical transmittance of visible wavelengths, however, the optical transmission can also be displayed as downwelling diffuse attenuation coefficients (Jerlov & Koczy, 1951), see fig. 3.3. Of particular interest is the shape of the diffuse attenuation curves for increasingly turbid areas. The diffuse attenuation coefficient spectrum for open ocean locations closely follows the absorption spectrum of water given in fig. 2.6a as pure seawater is the primary component in these areas. As the turbidity increases, the window of low attenuation is shifted

towards yellow-green wavelengths as the shape changes with spectral contributions from phytoplankton, NAP and CDOM, which were shown in fig. 2.6. The disadvantage of this scheme is inaccuracy; original Jerlov measurements were made using broadband colour filters and the curves obtained with modern spectroradiometers are in some cases in poor agreement (Mobley et al., 2014).

Another classification scheme known as ternary diagrams use inherent optical properties to create a triangle of relative contributions for each of the main optical components of ocean water (Arnone et al., 2004). As with colour matching, this method focuses on variations in absorption. It is the only scheme which is capable of classifying the ocean below a depth of 50 - 200 metres. Although accurate, complexity arises in the measurement of the main optical components, reducing the frequency this classification is used.

A further ocean classification scheme, based on remote sensing, was originally conceived in (Morel & Prieur, 1977) and further refined in (Gordon & Morel, 1983) where, as with Jerlov water types, the ocean is split into two groups, here *Case 1* and *Case 2* waters. In Case 1 waters, it is phytoplankton and its derivative products that play a dominant role in determining optical properties, whilst Case 2 optical properties are highly turbid and a result of the sediments running off continental shelves, from inland waters and other terrestrial run-off. Modern schemes based on Case 1 waters use satellite images that capture the water-leaving irradiances and match the images with quantitative data in the form of the near-surface chlorophyll concentration (Hooker et al., 1992), after correcting for a number of atmospheric effects (Ruddick et al., 2000). In general, chlorophyll concentration plays an important role in dividing natural waters by their turbidity.

Oceanographers use a three-part classification scheme based on chlorophyll concentration to explain the activity of natural waters (Carlson, 1977): *eutrophic* waters are classified as those where the chlorophyll concentration exceeds 20 mg m^{-3}; in *mesotrophic* are waters it is between 2.6 - 20 mg m^{-3}; and *oligotrophic* waters are those with chlorophyll concentrations below 2.6 mg m^{-3}. Whilst oligotrophic waters host very little or no aquatic vegetation and are relatively clear, eutrophic water bodies sustain large quantities of organisms (Smith & Baker, 1978). This generalised scheme, along with those previously mentioned in this section, have been condensed into fig. 3.4, where the respective chlorophyll concentration boundary of each scheme is compared. Where possible, this research states the *water type* description that appears in fig. 3.4.

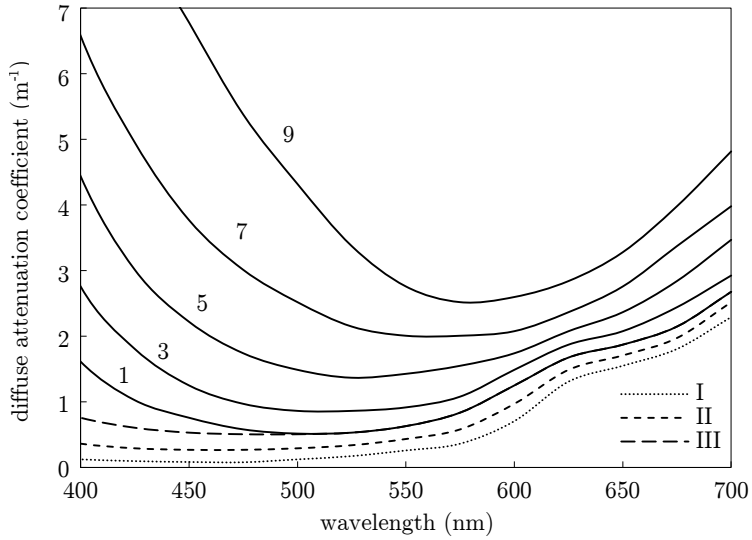

Figure 3.3: Jerlov water types, where open ocean waters are labelled I - III, and turbid areas 1 - 9 (Jerlov & Koczy, 1951).

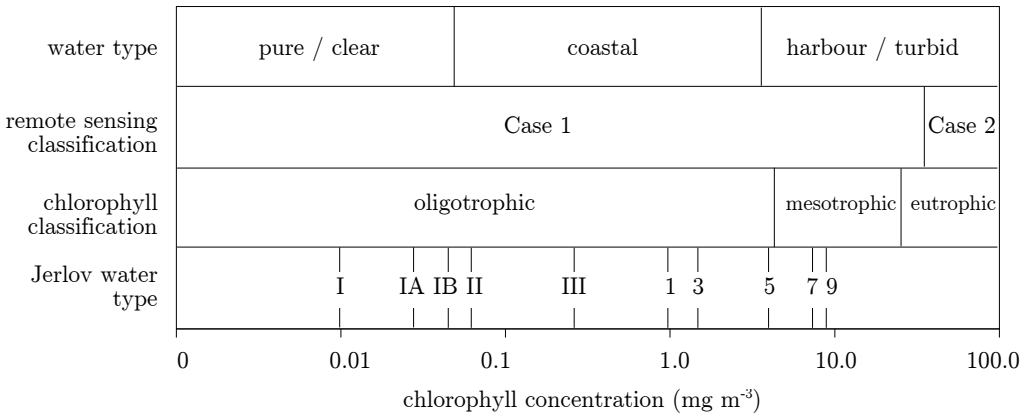

Figure 3.4: Comparison of chlorophyll concentration boundaries for standard classification schemes, where Jerlov water type chlorophyll equivalents are found in tab. 3.1, and remote sensing boundary found in (Morel et al., 2006).

Jerlov water	C_{CHL} (mg m^{-3})	Jerlov water	C_{CHL} (mg m^{-3})
I	0.010 (3 10^{-4})	1	1.00 (0.05)
IA	0.027 (4 10^{-4})	3	1.28 (0.07)
IB	0.037 (0.001)	5	3.95 (0.33)
II	0.044 (0.001)	7	8.4 (1.2)
III	0.177 (0.01)	9	9.1 (1.5)

Table 3.1: Chlorophyll concentrations associated with Jerlov water types I - 9, for fig. 3.4, where standard deviations are given in brackets (Solonenko & Mobley, 2015).

3.3 Attenuation Coefficient Variability

The classification schemes explored in sec. 3.2 highlight the importance of chlorophyll concentration in determining the variability of optical properties in the majority of natural waters. The significance of chlorophyll concentration arises from its ability to to be converted into an equivalent attenuation coefficient through bio-geo-optical models. Bio-geo-optical models are semi-analytical or empirical algorithms that are based on various measured parameters to estimate optical properties. An appropriate model is required for this research to aid assessment of attenuation coefficient variability within the aquatic medium.

A discussion of bio-geo-optical model selection is available in (Brewin et al., 2013), where several algorithms have been assessed against publicly-available in-situ measurements for their accuracy and usability. Properties of a suitable bio-geo-optical model for this research include: being able to accurately describe the absorption and scattering coefficients of pure seawater, phytoplankton, NAP and CDOM, where other constituent coefficients are excluded due to limited impact or insufficient models (see sec. 2.6); being based on a single input parameter, ideally chlorophyll concentration as its behaviour is well understood and documented, for example in depth profiles (Kameda & Matsumura, 1998) and pan-ocean surface data (Mueller, 2000); being able to input different water types, whether turbid inland or clear oceanic water; being computationally simplistic, so that chlorophyll profiles can be translated into attenuation curves with relative swiftness; covering all visible wavelengths from 400 - 700 nm; and being robust to changes in the refractive state of the water. One such model is the Haltrin model (Haltrin, 1999).

The Haltrin model, which was briefly introduced in sec. 2.5.2, describes the concentration, absorption coefficient and scattering coefficient of optical constituents in terms of a single parameter, chlorophyll concentration (Haltrin, 1999). The model was created by combining *in-situ* measurements of inherent optical properties from various researchers and reports, particularly that of (Kopelevich, 1983), and optimising the result until it agreed satisfactorily with establish models. In the absorption part of the model, which is given in equation eq. 3.1, the absorption of CDOM is represented by its fulvic and humic components, previously shown in eq. 2.21. The justification for doing so is to allow the model to be valid for all biologically stable waters, meaning all of Case 1 waters and some of Case 2, where there is not a significantly present inorganic substance such as quartz or sand. However, by observing eq. 3.1, it becomes apparent that absorption contributions from NAP have been entirely omitted, this is likely due to a lack of correlation between chlorophyll and NAP concentrations. The downside of this model,

therefore, is slight underestimation of the absorption coefficient due to the lack of a NAP component.

$$a(\lambda) = a_{\mathrm{W}}(\lambda) + a^*_{\mathrm{CHL}}(\lambda)\left(\frac{C_{\mathrm{CHL}}}{C^*_{\mathrm{CHL}}}\right)^{0.6} + a^*_{\mathrm{F}}C_{\mathrm{F}}\exp\left[-k_{\mathrm{F}}\lambda\right] + a^*_{\mathrm{H}}C_{\mathrm{H}}\exp\left[-k_{\mathrm{H}}\lambda\right] \tag{3.1}$$

Where:

a_{W} is the absorption coefficient of pure seawater (given in app. A);

a^*_{CHL} is the specific absorption coefficient of chlorophyll (given in app. B);

a^*_{F} is the specific absorption coefficients of fulvic acid (given as $a^*_{\mathrm{F}} = 35.96$ m^2 mg^{-1});

a^*_{H} is the specific absorption coefficients humic acid (given as $a^*_{\mathrm{H}} = 18.8$);

C_{CHL} is the total concentration of chlorophyll in mg m^{-3} ($C^*_{\mathrm{CHL}} = 1$ mg m^{-3});

C_{F} is the concentration of fulvic acid (given in eq. 3.3);

C_{H} is the concentration of humic acid (given in eq. 3.3);

k_{F} is the fulvic acid decay constant (given as $k_{\mathrm{F}} = 0.019$ nm^{-1}); and

k_{H} is the humic acid decay constant (given as $k_{\mathrm{H}} = 0.011$ nm^{-1}).

As with absorption, Haltrin derived a one-parameter model for scattering. This unified scattering model only includes contributions from pure seawater and particulate substances only (Haltrin, 1999). The contributions from turbulence- and bubble-induced scattering are omitted as they are assumed to be negligible in less turbid underwater media, as per the discussion in ch. 2.

$$b(\lambda) = b_{\mathrm{W}}(\lambda) + C_{\mathrm{S}}b^*_{\mathrm{S}}(\lambda) + C_{\mathrm{L}}b^*_{\mathrm{L}}(\lambda) \tag{3.2}$$

Where:

b_{W} is the scattering coefficient of pure seawater (given in eq. 2.32);

b^*_{S} is the specific scattering coefficient of small particulates (given in eq. 2.27);

b^*_{L} is the specific scattering coefficient of large particulates (given in eq. 2.27);

C_{S} is the concentration of humic acid (given in eq. 3.3); and

C_{L} is the concentration of humic acid (given in eq. 3.3).

Finally, the concentrations of fulvic and humic acids, as well as small and large particulates, is related to the chlorophyll concentration through the relations

$$\begin{aligned} C_{\mathrm{F}} &= 1.74098\, C_{\mathrm{CHL}} \exp\left[0.12327\, C_{\mathrm{CHL}}\right] \\ C_{\mathrm{H}} &= 1.93340\, C_{\mathrm{CHL}} \exp\left[0.12343\, C_{\mathrm{CHL}}\right] \\ C_{\mathrm{S}} &= 0.01739\, C_{\mathrm{CHL}} \exp\left[0.11631\, C_{\mathrm{CHL}}\right] \\ C_{\mathrm{L}} &= 0.76284\, C_{\mathrm{CHL}} \exp\left[0.03092\, C_{\mathrm{CHL}}\right] \end{aligned} \tag{3.3}$$

where it is noted that the range of chlorophyll concentration the model is valid for is 0 - 12 mg m^{-3}, representing from clear ocean water to moderately turbid inland waters, sufficient for the currently envisioned uses of underwater optical wireless.

A very recent study, (Solonenko & Mobley, 2015), is selected to assess the accuracy of the Haltrin model. In this study, two non-contradictory approaches which describe the relationships between total attenuation, constituent concentrations and diffuse attenuation coefficients were combined to generate a set of inherent optical properties for the original Jerlov diffuse attenuation coefficient measurements. The Haltrin model is one of the two approaches, whilst the second is based on the works of (Morel & Maritorena, 2001), (Morel & Loisel, 1998) and (Bricaud et al., 1998). As matching chlorophyll concentrations were also calculated, these concentrations were inputted into the Haltrin model to yields the plots in fig. 3.5; the results are displayed alongside the values derived by Solonenko and Mobley. It is thought that, as the combined model tested positively against data obtained from numerical simulations, it is likely that this newly-derived model is the most accurate at present. Whilst it could be suggested that the Solonenko and Mobley model be used in future optical property studies, it could also be argued that the unpredictability of natural water bodies casts doubt on the exactness of any modelled optical property value, hence changing the model would be unnecessary.

Regarding fig. 3.5, the two models seem in reasonable agreement, though there are discrepancies at wavelengths towards the extreme ends of the visible spectrum. A possible cause for this may lie in the variable nature of the tabulated chlorophyll concentrations, shown by the standard deviations of tab. 3.1, where the Haltrin models of the averaged chlorophyll concentrations do not necessarily provide the best fit. A further cause becomes apparent by observing profiles where chlorophyll levels are low, as in the Jerlov water types I, II and III in fig. 3.5a. For each of these profiles, the model agreement is strong at longer wavelengths, but the Haltrin model becomes much flatter around 400 - 550 nm. This is likely from an underestimation of the scattering by particulates

(a) Jerlov water types I, II, III

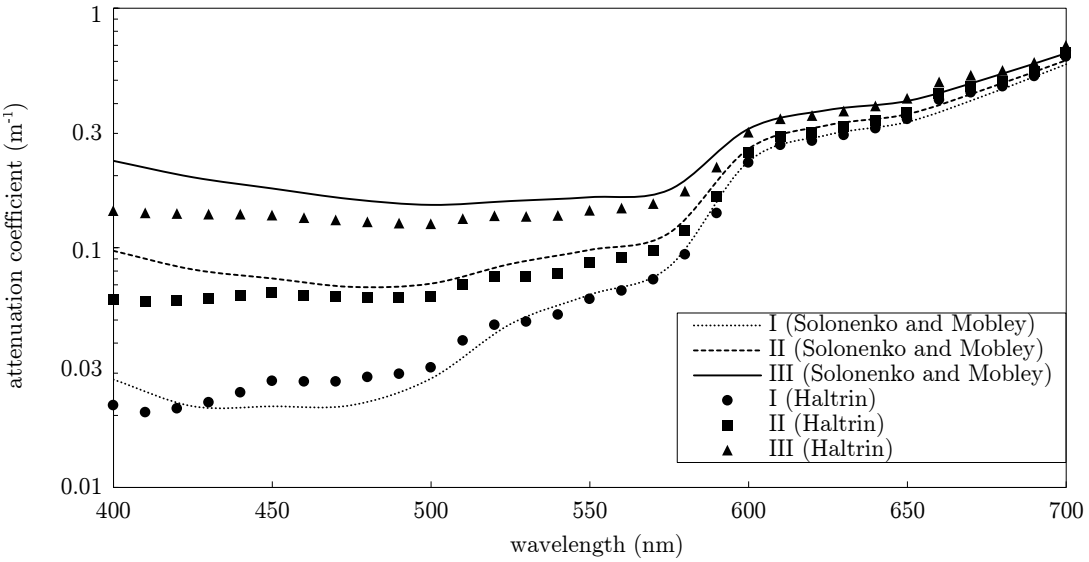

(b) Jerlov water types 1, 3, 7, 9

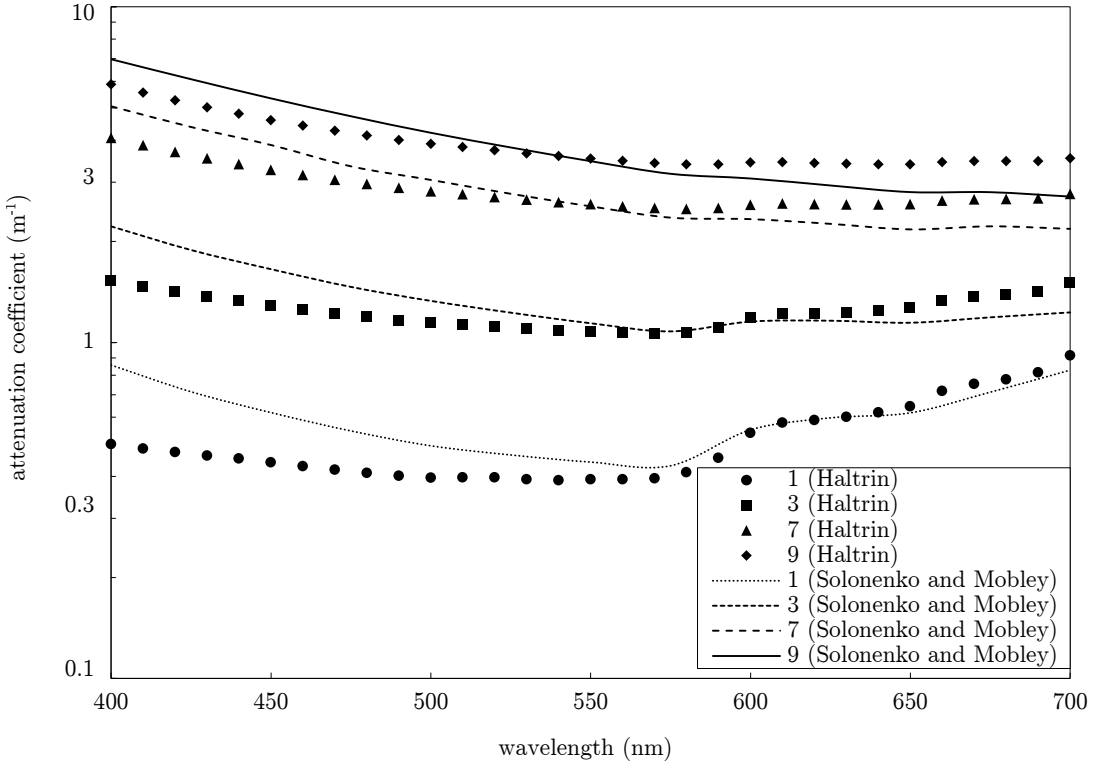

Figure 3.5: Comparison of attenuation coefficient models, where Jerlov inherent optical property equivalents are derived in (Solonenko & Mobley, 2015) and Jerlov profiles using chlorophyll equivalents from tab. 3.1 are derived using (Haltrin, 1999). Jerlov water types I, II and II are included in (a), whilst 1 3 7 and 9 are in (b). Note the profile for 5 is omitted due to issues with the tabulated data in (Solonenko & Mobley, 2015).

in the Haltrin model which considers only small and large particulate sizes, whilst the Solonenko and Mobley model uses a size distribution. For higher chlorophyll profiles, represented by Jerlov water types 1, 3, 7 and 9 in fig. 3.5b, it appears that the Haltrin model overestimates attenuation at wavelengths above 550 nm. This arises due to differences in the way CDOM is considered, particularly with regards to the humic and fulvic decay constants in eq. 3.1, and the equivalent exponent in the Solonenko and Mobley model.

To conclude, despite some inaccuracies, the Haltrin model provides a computationally simplistic method for investigating attenuation coefficient variability through the use of existing chlorophyll concentration variability data. An additional advantage of this model is that it can be applied to both Case 1 and Case 2 waters. In sec. 3.3.1 to sec. 3.3.3, chlorophyll concentration profiles taken at the surface of natural waters, as well as with depth and over time, will be used to generate attenuation coefficient estimates through the Haltrin model introduced here.

3.3.1 Near-Surface Variation

Across the ocean, higher chlorophyll concentrations are observed along the equator, on the coastlines (specifically those that are east-facing) and in high latitude oceans, as shown by fig. 3.6. Typical chlorophyll concentrations for open-ocean fall within the range 0.01 - 4.0 mg m^{-3}, whereas near-shore levels may be up to 60 mg m^{-3} where nutrient run-off from land is a contributing factor. In inland waters, chlorophyll concentration varies from 0.1 mg m^{-3} for clear glacial springs, to well beyond 350 mg m^{-3} in the most eutrophic waters (Kirk, 1994).

By inputting a range of chlorophyll concentrations into the Haltrin model (eq. 3.1 and eq. 3.2), near-surface attenuation profiles such as those demonstrated in fig. 3.5, are formed for a geographically diverse set of natural waters. Recall, however, that the model limits the maximum chlorophyll concentration to 12 mg m^{-3}. In open oceans, the chlorophyll concentration is low, therefore so too are the concentrations of humic and fulvic acid. The subsequent attenuation spectrum is dominated almost entirely by the absorption of pure water which is evident from the shape of the type I profile in fig. 3.5a in comparison to fig. 2.6a. For wavelengths of 500 nm and greater, the attenuation coefficient is almost the same as that of pure water with only a small absorption increase in the blue region. From this it may be deduced that the most ideal transmission wavelengths for optical communication systems in the open ocean is 400 - 500 nm, representing blue/green light; hardware and wavelength optimisation are discussed further in ch. 4.

In coastal regions and the majority of inland waters, the chlorophyll concentration is much

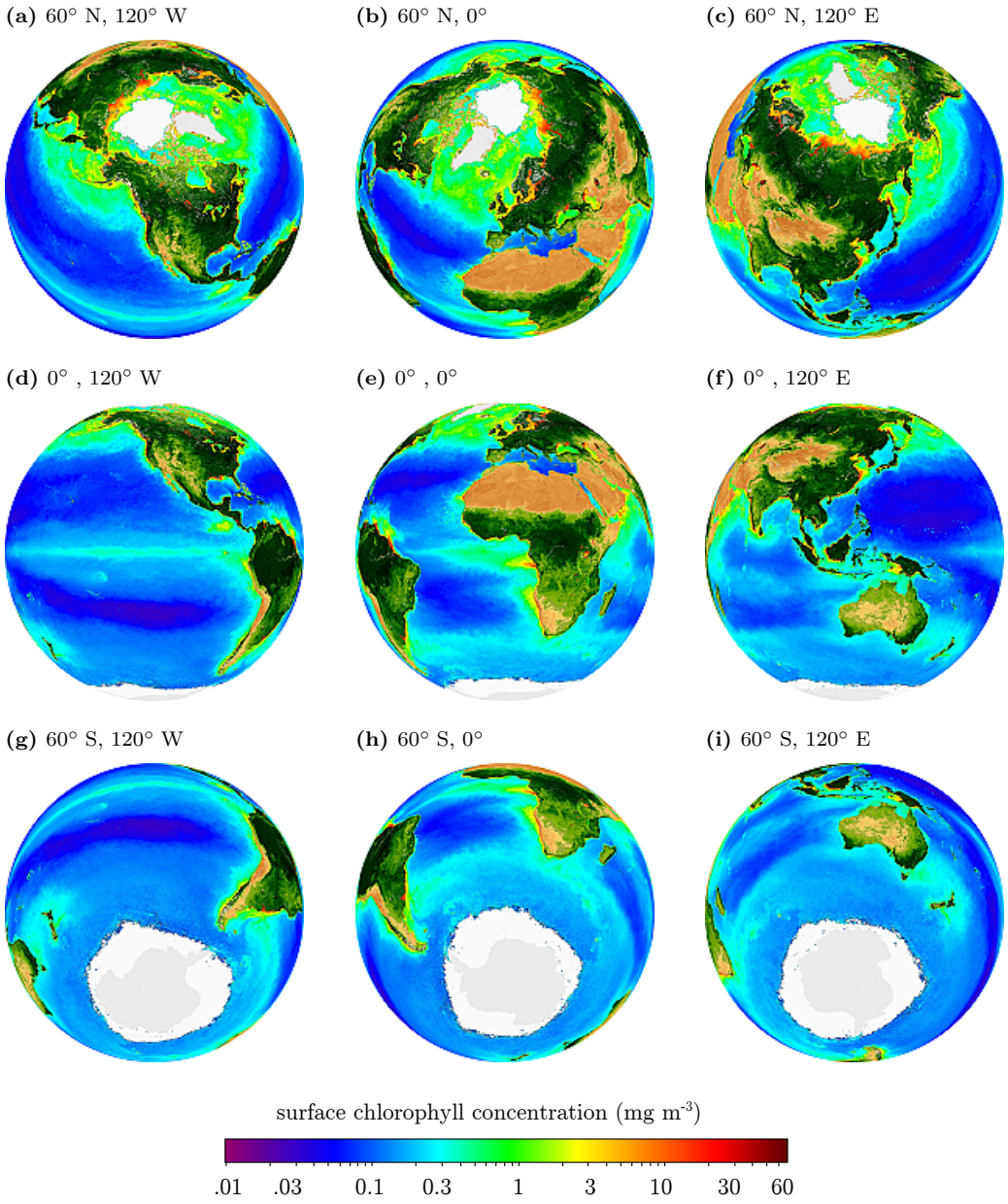

Figure 3.6: Near-surface variation in chlorophyll concentration, where measurements are averaged remote sensing observations based in boreal summer from (SeaWIFs, 2015). The longitude and latitude co-ordinates is given above each image.

higher than that found in open oceans, leading to greater concentrations of particulates. In this case, the total attenuation in shorter wavelengths becomes dominated by particulate absorption and scatter, as in fig. 3.5b, and the ideal transmission wavelength is shifted. The lowest attenuation is experienced in the region between 500 - 570 nm, which means yellow-green light propagates furthest in these aquatic environments. The attenuation induced by scattering is generally much greater than that of absorption; the resulting communication link performance is a direct result of its ability to cope with multi-directional scatter, rather than optimised transmission wavelength selection.

3.3.2 Variation with Depth

The vast majority of existing research in underwater optical wireless communications recognises variation in near-surface attenuation coefficients. However, so far, none have considered variability with depth and the impact it has on optical wireless links at different locations and orientations underwater, despite fluctuations being seemingly extensive (Johnson et al., 2013). Instead of characterising the changing attenuation as a diffuse attenuation coefficient, this research seeks to derive the inherent equivalent through chlorophyll concentration-depth profiles and the Haltrin model, therefore permitting the application of optical wireless modelling.

The concentration of chlorophyll with depth is well documented for natural bodies of water, as is the behaviour of the phytoplankton in which it resides. As phytoplankton are photosynthesising organisms, they inhabit only sections of natural waters that support growth through the availability of sufficient amounts of sunlight and nutrients. In the ocean, the upper area where sunlight propagates is known as the photic zone. This is up to 200 metres deep in clear open ocean waters, 40 metres over continental shelves and 15 metres in coastal waters (Garrison, 2009). The depth distribution of chlorophyll concentration in the photic zone is a skewed Gaussian curve from the surface, given by the following equation (Kameda & Matsumura, 1998)

$$C_{\mathrm{CHL}}(z) = F_0 + S_{\mathrm{CHL}} z + \frac{F_T}{\sigma_{\mathrm{CHL}}\sqrt{2\pi}} \exp\left[\frac{-(z - z_{\max})^2}{2\sigma_{\mathrm{CHL}}^2}\right] \tag{3.4}$$

Where F_0 is the background chlorophyll concentration at surface, S_{CHL} is the vertical gradient of concentration, F_T is the total chlorophyll above background levels, z is the depth and finally, σ_{CHL} is the standard deviation of concentration. The standard deviation is calculated by a further

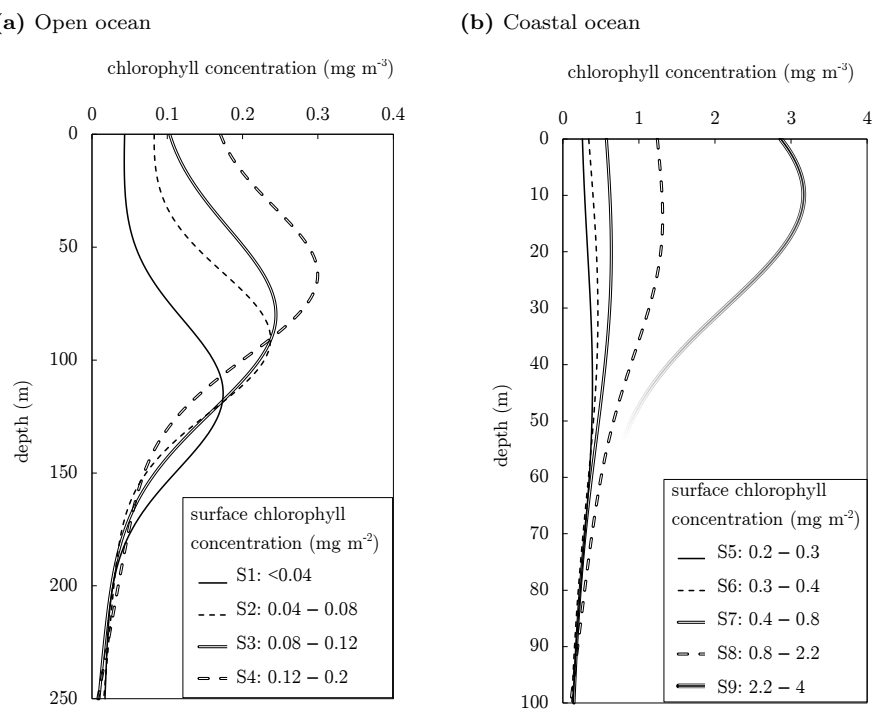

Figure 3.7: Chlorophyll concentration profiles with depth for different surface chlorophyll concentrations. Values are based on eq. 3.4 and eq. 3.5, with parameters taken from app. E. Surface chlorophyll concentrations are catagorised into groups S1-S9, where the profiles displayed are the average profiles for each group.

formula:

$$\sigma_{\mathrm{CHL}} = \frac{F_T}{\sqrt{2\pi\big(C_{\mathrm{CHL}}(z_{\max}) - F_0 - S_{\mathrm{CHL}} z_{\max}\big)}} \tag{3.5}$$

The subsequent chlorophyll distributions typically have a maxima, known as the deep chlorophyll maximum (DCM), between depths of 20 - 50 metres and decay to a negligible level at 50 - 200 metres, depending on the surface chlorophyll concentration. A list of parameters for different surface chlorophyll levels is given in app. E; adapted from data in (Uitz et al., 2006). The resulting chlorophyll-depth profiles are displayed in fig. 3.7. The Gaussian profile shape arises from limited sunlight availability below the DCM and depleted nutrient availability above.

Having quantified the depth dependency of chlorophyll, the Haltrin model is now applied to generate attenuation profiles with depth. Note that the following models are derived in terms of depth z only; for a communication link path of undefined orientation, it is possible to resolve along the direction of the link if lateral changes in the attenuation coefficient are assume to be negligible. The Haltrin models for absorption and scattering, from eq. 3.1 and eq. 3.2 respectively,

are rewritten to include the depth dependency:

$$\begin{aligned} a(\lambda, z) = a_{\mathrm{W}}(\lambda) + a^*_{\mathrm{F}}\, C_{\mathrm{F}}(z) \exp\left[-k_{\mathrm{F}}\lambda\right] + a^*_{\mathrm{H}}\, C_{\mathrm{H}}(z) \exp\left[-k_{\mathrm{H}}\lambda\right] \\ + a^*_{\mathrm{CHL}}(z, \lambda)[C_{\mathrm{CHL}}(z)]^{0.602} \end{aligned} \tag{3.6}$$

$$b(\lambda, z) = b^*_{\mathrm{W}}(\lambda) + b^*_{\mathrm{S}}(\lambda) C_{\mathrm{S}}(z) + b^*_{\mathrm{L}}(\lambda) C_{\mathrm{L}}(z) \tag{3.7}$$

where $C_{\mathrm{F}}(z)$, $C_{\mathrm{H}}(z)$, $C_{\mathrm{S}}(z)$ and $C_{\mathrm{L}}(z)$ are the depth-dependent profiles of fulvic and humic acid and small and large particles from eq. 3.3, now given by

$$\begin{aligned} C_{\mathrm{F}}(z) &= 1.74098\, C_{\mathrm{CHL}}(z) \exp\left[0.12327\, C_{\mathrm{CHL}}(z)\right] \\ C_{\mathrm{H}}(z) &= 1.93340\, C_{\mathrm{CHL}}(z) \exp\left[0.12343\, C_{\mathrm{CHL}}(z)\right] \\ C_{\mathrm{S}}(z) &= 0.01739\, C_{\mathrm{CHL}}(z) \exp\left[0.11631\, C_{\mathrm{CHL}}(z)\right] \\ C_{\mathrm{L}}(z) &= 0.76284\, C_{\mathrm{CHL}}(z) \exp\left[0.03092\, C_{\mathrm{CHL}}(z)\right] \end{aligned} \tag{3.8}$$

and the term for specific chlorophyll absorption in eq. 2.19 becomes

$$a^*_{\mathrm{CHL}}(\lambda, z) = F_1(\lambda) C_{\mathrm{CHL}}(z)^{-F_2(\lambda)} \tag{3.9}$$

By using eq. 3.6 to eq. 3.9, it is possible to fully define the attenuation profile with varying depth and wavelength, based only on the geographic location of the ocean surface nearest the communication system. First, the appropriate S group in app. E must be selected from surface chlorophyll levels at the chosen location, these are available from remote sensing data sets, such as (SeaWIFs, 2015). The chlorophyll profile is then defined using the appropriate Gaussian distribution, which means the chlorophyll-dependent profiles for fulvic and humic acid, and for small and large particles, are all also known. Substituting these profiles into eq. 3.6 to eq. 3.9, for the chosen range of wavelength and depth, gives the absorption and scattering coefficients. Finally, these are combined to give the overall attenuation. This process was used to generate three-dimensional plots for S2, S4, S6 and S8 in fig. 3.8, in addition to nine surface plots in fig. 3.9, representing the attenuation for all nine S groups.

The relationships portrayed in fig. 3.8 and fig. 3.9 are mostly dominated by the absorption spectrum of pure seawater, particularly in areas of low chlorophyll concentration, such as the entirety of the S1 profile and other profiles for large values of z. This can be seen by the sharp increase in attenuation around 550 - 700 nm. Such behaviour is expected as use of the S profiles caps the surface chlorophyll to a relatively modest maximum of 4 mg m^{-2}. The minimum expected

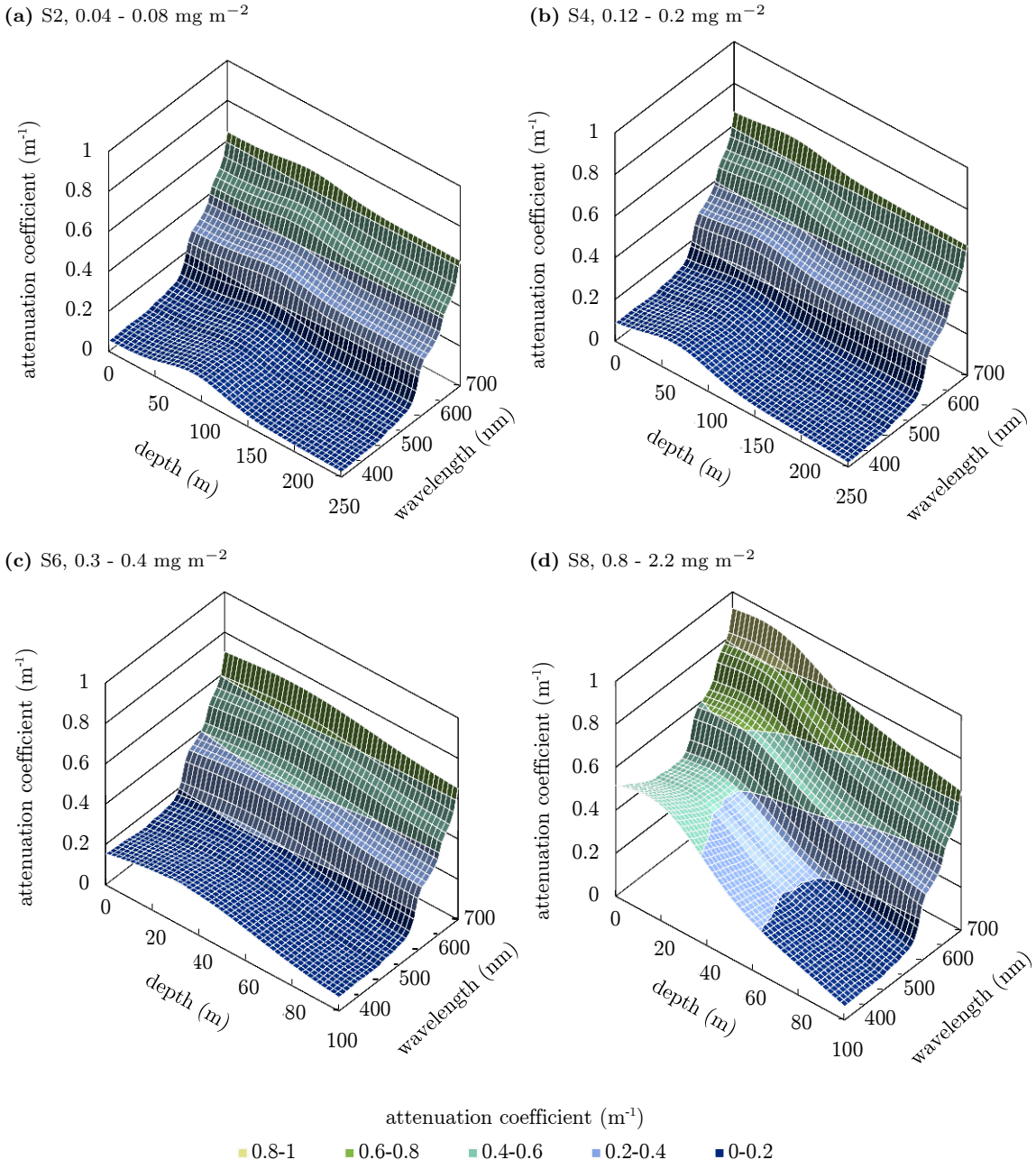

Figure 3.8: Three-dimensional plots of attenuation coefficient variation for the S2, S4, S6 and S8 profiles at depths between 0 - 250 m for S2 and S4 and 0 - 100 m for S6 to S8 and with wavelengths from 400 to 700 nm, where the surface chlorophyll level is given above each figure. Values are estimated using eq. 3.6 to eq. 3.9 inclusive and chlorophyll-depth profiles from app. E.

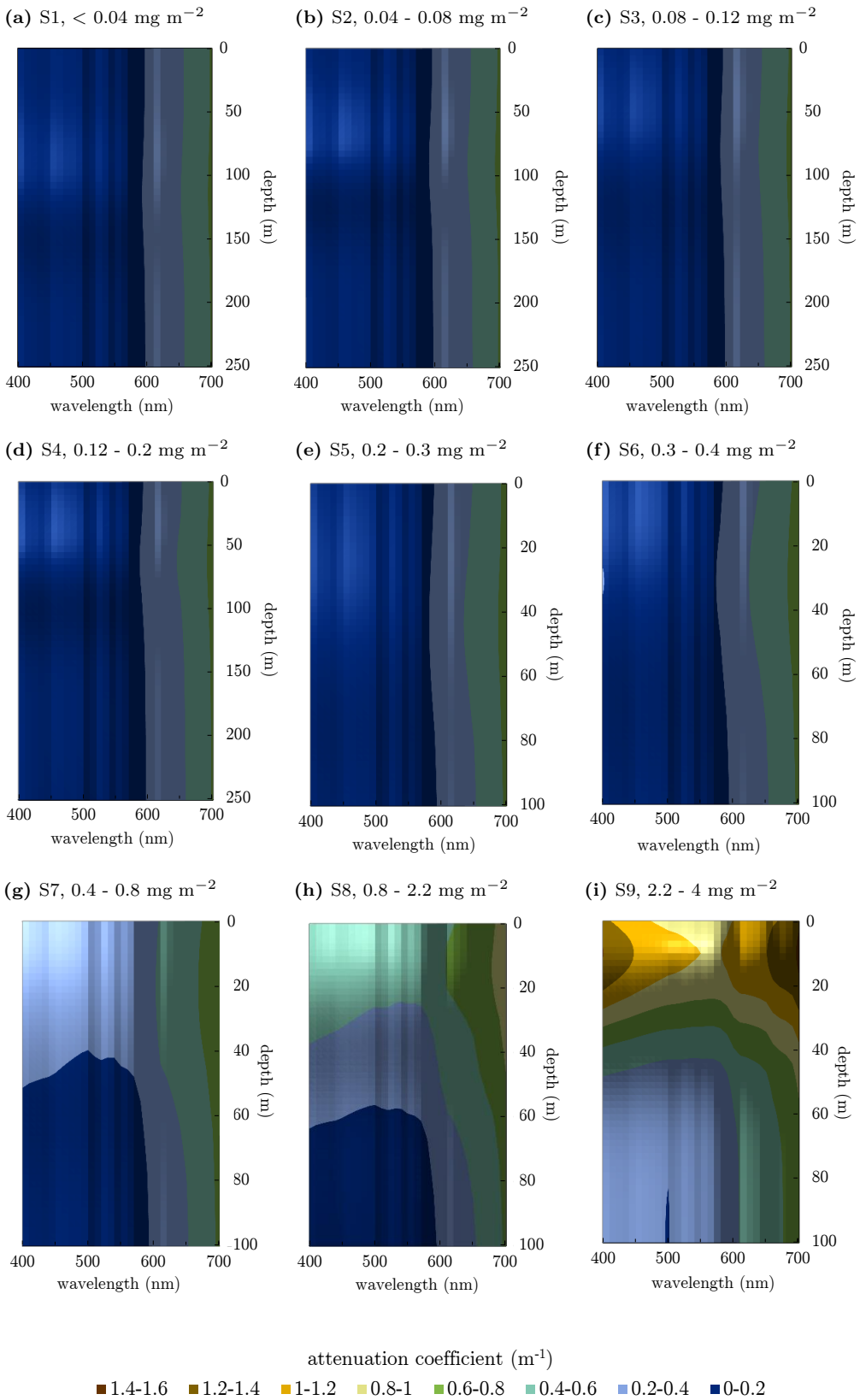

Figure 3.9: Surface plots of attenuation coefficient variation for S1-S9 profiles at depths between 0 - 250 m for S1 to S4 and 0 - 100 m for S5 to S9 and with wavelengths from 400 to 700 nm, where the surface chlorophyll level is given above each figure. Values are estimated using eq. 3.6 to eq. 3.9 inclusive and chlorophyll-depth profiles from app. E.

attenuation coefficient is calculated to be 0.0092 m^{-1}, this attenuation occurs only below z_∞, which is the depth at which the chlorophyll level become negligible; values of z_∞ for each S profile is given in app. E, having originated from (Johnson et al., 2014a). As the surface chlorophyll level increases, the attenuation spectrum deviates from that of pure seawater; scattering contributions raise the attenuation coefficient for blue/green wavelength. This is particularly noticeable at depths around the DCM where greater amounts of scattering occur.

The main distinction between the profiles in fig. 3.8 and fig. 3.9 comes from the chlorophyll surface concentration and the location of the DCM. In the 400 - 500 nm range, where the attenuation profile of chlorophyll are peaked, the depth of the DCM is evident as it leads to a distinct bump in the attenuation profile with depth. For S2 to S8 in fig. 3.8, the attenuation peak can be seen to be occurring at approximately 90, 60, 30 and 15 meters respectively, matching the documented value of z_∞. Optical communication systems operating horizontally at depths around the DCM will experience much greater losses than those in deep oceans or near the surface, this is particularly the case at moderate surface chlorophyll levels, when surface chlorophyll is greater than 0.4 mg m^{-2}. Overall beam attenuation of these links is discussed further in sec. 3.4.

This section concludes with a short discussion of the attenuation-depth profiles of inland waters. Like oceanic waters, chlorophyll concentration in inland waters (excluding eutrophic waters) follows a skewed-Gaussian profile with depth. However, in these inland profiles, the DCM occurs at much shallower depths, typically between 1 - 10 metres (Kirk, 1994). One cause of this is higher surface chlorophyll levels, which means sunlight propagating downwards is more quickly attenuated, limiting the light availability for phytoplankton below; other causes are explored in (Cullen, 1982).

3.3.3 Variation with Time

Temporal variations in chlorophyll concentration are observed seasonally and diurnally, where solar radiant intensity received at the water surface, also known as solar insolation, is the main underlying mechanism controlling variations. Measurements of underwater chlorophyll concentrations inland document it fluctuating over an order of magnitude in a single day (Lorenzen, 1963), whilst fig. 3.10 shows typical seasonal variations, based on remote sensing data (SeaWIFs, 2015). From fig. 3.10, it is apparent that the chlorophyll concentration is lowest in winter and highest in spring and summer, corresponding to high seasonal levels of phytoplankton growth.

To form models of how chlorophyll concentration, and therefore the attenuation coefficient, behaves temporally at a fixed location, there are a number of factors to consider. First, the daily

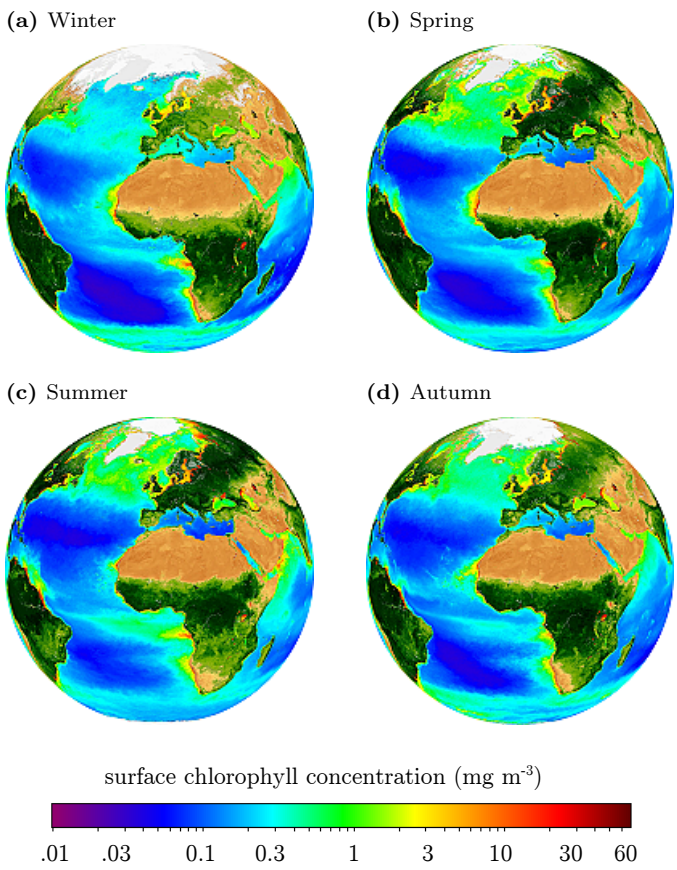

Figure 3.10: Seasonal variation in chlorophyll concentration, where boreal seasons are quoted over each figure, taken at 20° N latitude, 0° longitude, from (SeaWIFs, 2015).

solar insolation at the chosen location must be estimated based on the geometry with respect to the sun. Parameters for this include the solar declination angle, a zenith angle and an hour angle, as well as information regarding the cloud and precipitation (Iqbal, 2012). The solar insolation profile is then related to the concentration of chlorophyll, this is expected to be a fairly linear relationship, with a small time delay between changes in intensity and chlorophyll concentration. Subsequent chlorophyll profiles should be seen to peak around 12 noon, as in (Lorenzen, 1963), subject to weather conditions. Time-dependent chlorophyll profiles are then substituted into the Haltrin model in eq. 3.1 and eq. 3.2, yielding a set of temporally varying attenuation coefficients. Although the model described is not generated as part of this study, this framework exists for future researchers to develop their own temporal variation models for attenuation.

An interesting extension to time-dependent attenuation is to consider what happens to depth-dependent attenuation coefficients over daily and seasonal cycles. During the night, it is found that chlorophyll concentration no longer exhibits a skewed-Gaussian profile with depth (Cullen, 1982). Instead, phytoplankton move down the water column to take advantage of the nutrients available below. Although this behaviour is predictable, its causes are not fully understood, making

it difficult to model. Regardless, it is worth bearing in mind in performance-critical underwater operations involving optical communication at the surface as better communication links may be established in twilight hours.

3.4 Beam Propagation

Suppose engineers were looking to construct an underwater optical wireless communication link with a fixed transmitter station and a movable receiver, for example a diver or AUV. Given the information presented in sec. 3.3 regarding attenuation variability, the question is posed about how variability impacts on a single optical link as the geometry or link orientation changes. Calculation of an overall beam propagation provides the answer; in this chapter, it is defined as the average attenuation coefficient value experienced by the optical beam as it traverses between the transmitter and receiver. By defining the beam propagation in this way, the assumption is made that a beam travelling through a water column where the attenuation coefficient wholly set to the averaged value undergoes the same losses as a beam transmitted through a medium with variable attenuation, though the same overall average. In ch. 5, the validity of this assumption is tested through complex propagation models that take account of multiple-scattering (photons that have strayed from the beam path but then scattered back to be received). Doubt in the validity arises as a high amount of scattering is intuitively thought to have differing overall impact on the beam depending on where in the optical link it occurs, although not apparent in the propagation models introduced thus far.

To provide an example of beam propagation profiles, the link described above is placed in the water column of three different oceanic waters where a fixed distance of 100 metres is assumed between the transmitter and receiver (see fig. 3.11). The surface chlorophyll concentration of the water columns are chosen to be < 0.04 mg m^{-2}, 0.08 - 0.12 mg m^{-2} and 0.3 - 0.4 mg m^{-2} respectively, relating to the chlorophyll profiles S1, S3 and S6 from app. E. For each S profile, the location of the receiver is varied in an arc over 180°, from a horizontal link orientation to a downwards vertical link orientation and then back to the horizontal. The zenith angle, θ, is defined as the angle between a horizontal plane underwater and the communication link direction; for every 5° increment of the zenith angle, an average attenuation coefficient is calculated through the models introduced in sec. 3.3.2. The process is then repeated with the transmitters moved to new depths underwater; depths are fixed to 0, 50 and 100 metres in this example. Note the transmission wavelength has been selected as 490 nm, as per (Johnson et al., 2014a).

Fig. 3.12 shows the results of the aforementioned example. The average attenuation values

are symmetrical about 90° due to the earlier assumption that horizontal attenuation variations are negligible, so that both horizontal directions are being subjected to the same changes in attenuation from the z component. In addition, all profiles are elliptical or semi elliptical, showing that the angle of transmission does cause a change in the attenuation coefficient. The lowest and highest average attenuations for each S profile occur at different locations and orientation depending on the location of the DCM with respect to the optical communication link.

At the ocean surface, fig. 3.12a, lower S profiles have a lesser attenuation in general, with S1 beginning at 0.045 m^{-1} compared to S6 at 1.14 m^{-1}; this is directly due to the level of chlorophyll at the surface. For S1 and S3 profiles transmitted from the surface, the attenuation coefficient gradually increases; this can be seen as the links transmitted closer to the vertical axis have a greater average attenuation coefficient. However, this is not the case for the S6 profile, whose maximum occurs at 40 metres. For this profile, increasing the angle first increases the attenuation coefficient to a peak of 0.16 m^{-1} where transmitted beam reaches the deep chlorophyll maximum. After this it begins to drop to 0.135 m^{-1} as the high levels of particulate and dissolved materials levels drop, meaning that angles towards the vertical are undergo lower attenuation than horizontal links.

At a 50 metre depth, the S6 profile has decreasing attenuation with depth as the DCM has already been passed. S3 slightly increases then decreases meaning the DCM is within the 50 - 150

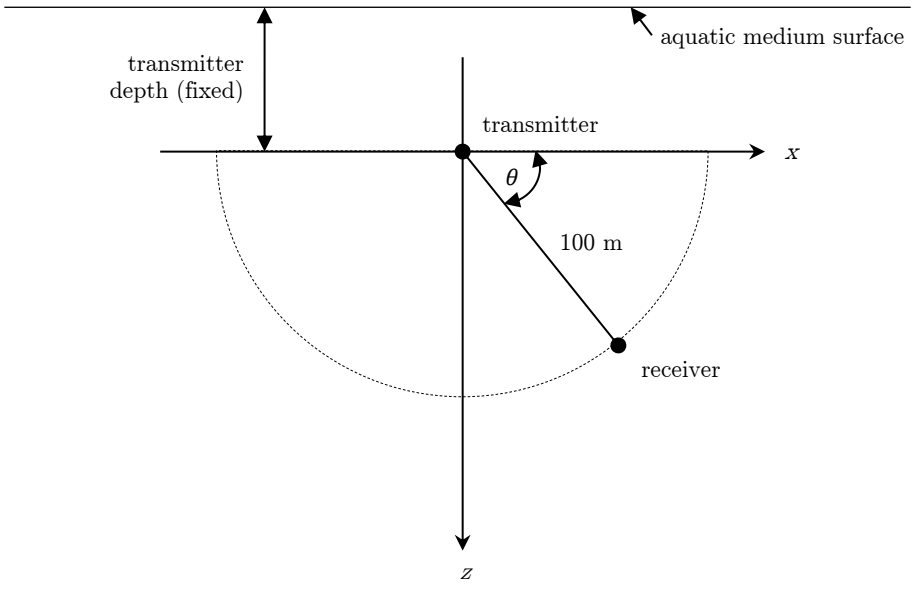

Figure 3.11: Geometry of the fixed-length, variable-orientation underwater communications link used in the beam attenuation investigation in fig. 3.12.

(a) 0 m transmitter depth

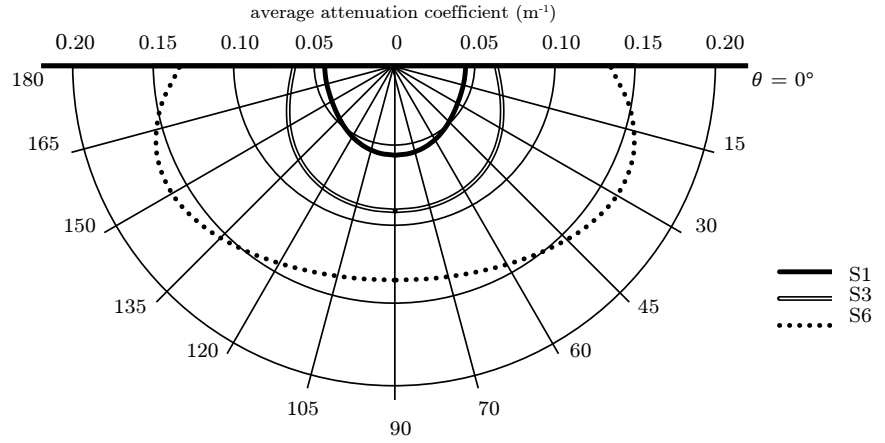

(b) 50 m transmitter depth

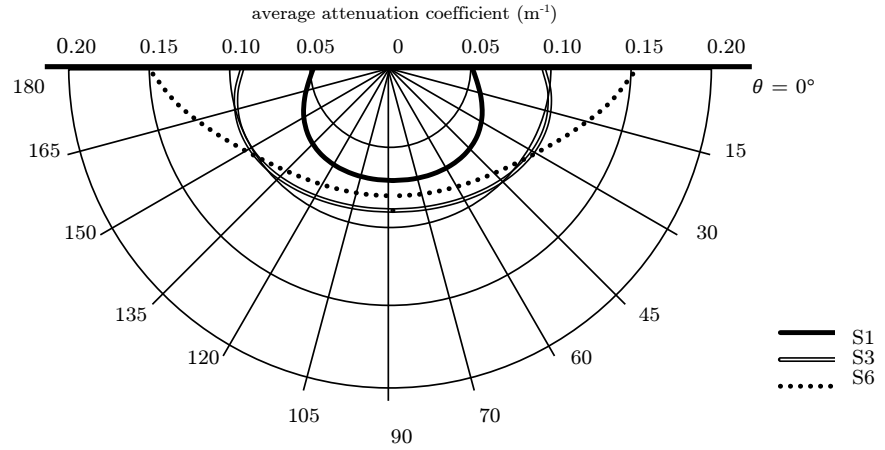

(c) 100 m transmitter depth

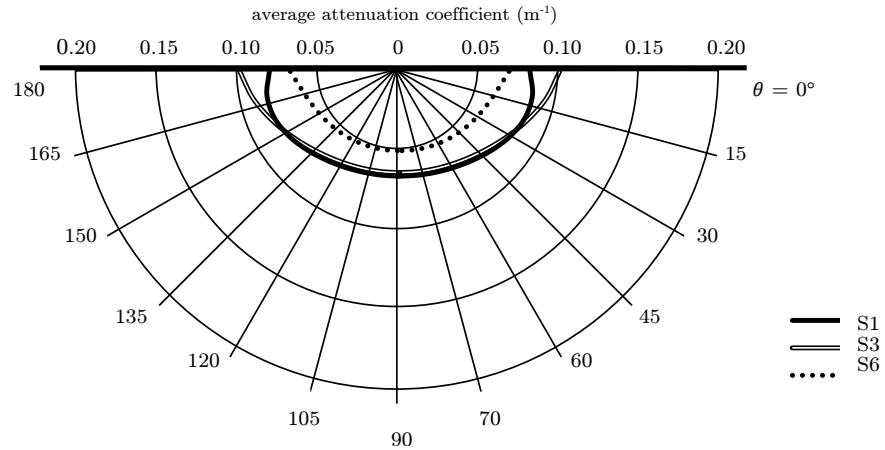

Figure 3.12: Average attenuation coefficient for a 100 metre optical link, in three different oceanic mediums represented by the S1, S3 and S6 profiles, with a fixed transmitter and a movable receiver, where the transmitter is set to three different heights; 0, 50 and 100 m. The zenith angle, θ, is defined as the angle between a horizontal plane underwater and the communication link direction.

metre range. Lastly, at 100 metres, the S3 and S6 profiles both decrease with depth, but S1 takes a similar shape as S3 did at 50 metres because the DCM occurs here. Interesting to note on the 100 metres profile is that the S6 profile has the lowest attenuation overall, this is because the peak occurred further up and chlorophyll levels become negligible by the time it reaches these depths.

To summarise, variations in attenuation have the most impact on signals transmitted horizontally; this is because it is possible to transmit entirely through an extreme attenuation value like those at the DCM. Links that are nearer to the vertical axis, or that have a vertical component, have the possibility of reaching a lower attenuation from these extreme values. Moreover, the longer the optical links are the lower the average attenuation is likely to be as light is transmitted through depths with low turbidity.

3.5 Refractive Index Variability

In addition to the attenuation coefficient, the refractive index plays an important role in the performance of underwater optical wireless communications systems. Controlled laboratory experiments have shown that the extent of scattering by suspended particles and pure seawater molecules matches the theory to a good degree of accuracy (Spinrad et al., 1978). However, scattering of light in true aquatic environments cannot alone be produced by these constituents as measurements by Petzold show that the VSF for real ocean water varies by order of magnitude from the theory (Petzold, 1972). This additional scattering is the result of a varying refractive index, which, as shown in sec. 2.5.4 and sec. 2.5.5, comes in the form of turbulence and subsequent bubble formation.

Although this research will not be surveying the localised refractive changes created by turbulence, recall that scattering in general is a change in photon direction, occurring due to refractive interfaces in the aquatic medium. Where there are gradual refractive gradients in natural waters, such as into the ocean depths, it follows that there will be a gradual change in the direction of light. This is quite significant if the light is, in fact, the beam of an underwater communication system expecting to be received at a specific location. In order to develop models of this scenario, it is necessary to explore the underlying variability of refractive index in aquatic media.

Temperature, salinity and pressure of the medium are factors which vary naturally in aquatic environments and, in addition to the wavelength of incident light, cause the refractive index to change. Austin and Halikas, who surveyed oceanic refractive indices *en masse*, note the extreme

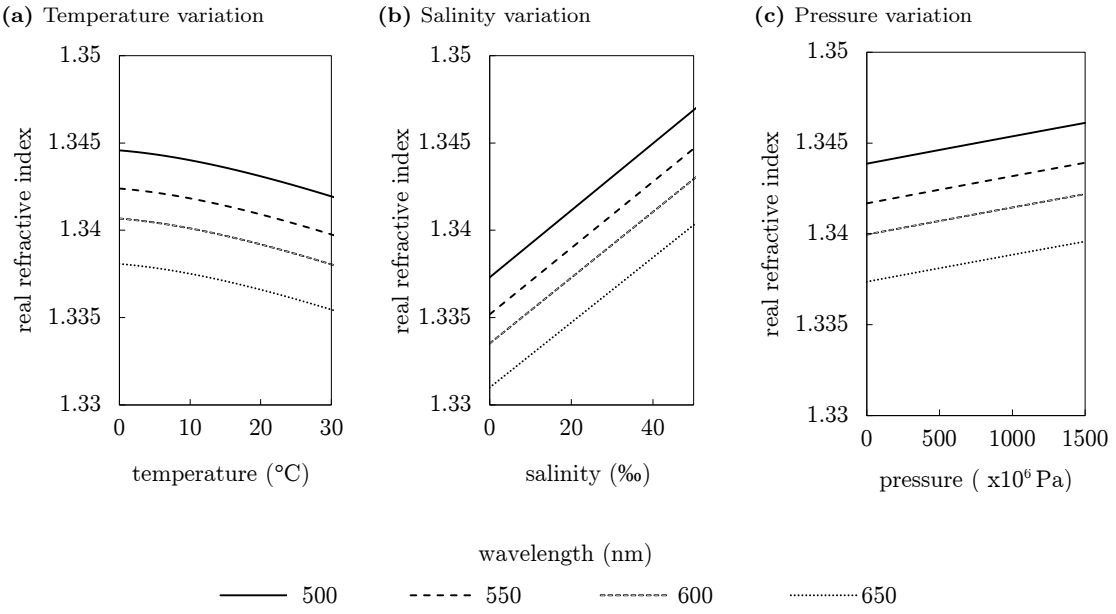

Figure 3.13: Seawater refractive index experiments. $T = 20^oC$, $\lambda = 500$ nm, $\epsilon = 3.5\%$, $\rho = 0$ kg cm^2 unless otherwise stated, where the values are determined from the 27-term algorithm in (Millard & Seaver, 1990).

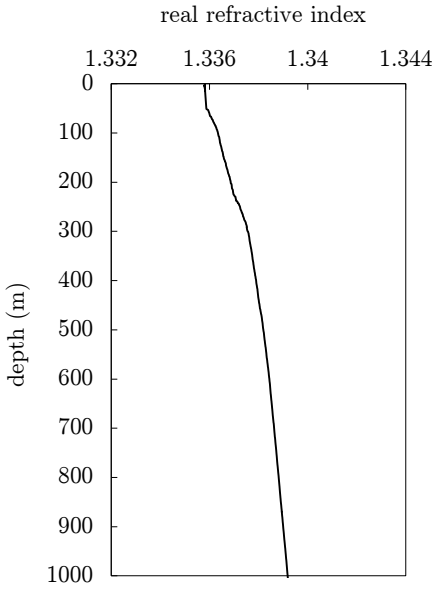

Figure 3.14: Refractive index with depth example, generated using the Pacific Ocean data CTD data set from (Earth Sciences Education, 2013) together with a 27-term algorithm to determine refractive index from salinity, temperature and pressure (Millard & Seaver, 1990).

values of refractive index in oceanic environments to be between 1.32913 and 1.36844 (Austin & Halikas, 1976), where variations occur both laterally and with depth. Changes to the refractive index based on an altering medium state may be calculated through empirical equations or algorithms, such the 27-term algorithm for pure and sea waters developed by Millard (Millard & Seaver, 1990). Using this algorithm, the variation of refractive index due to temperature T, salinity ϵ and pressure ρ is given in fig. 3.13, for a range of wavelengths. Pressure and salinity vary linearly with refractive index whilst wavelength and temperature exhibit more complex behaviours. Considering the total range of each parameter, which represent typical ocean conditions, the index of refraction of seawater is least sensitive to changes in temperature, then salinity, then wavelength and finally most sensitive to changes in pressure.

Gradual changes in refractive index across the ocean surface arise due to temperature fluctuations with latitude or changing salinity with proximity to the shore; both occur over a much greater scale than the present maximum underwater optical communication link distance of 200 metres (Pontbriand et al., 2008). The impact of gradual lateral refractive gradients can therefore be assumed to be negligible. Variability with depth, however, presents an interesting problem. Refractive-depth profiles can be generated by putting measured conductivity, temperature, density (CTD) data through an algorithm such as that in (Millard & Seaver, 1990). An example result, which uses a CTD data set from a low turbidity area of the Pacific ocean (Earth Sciences Education, 2013), is shown in fig. 3.14. Presuming the maximum communication link is around 200 metres in length, there is up a 0.1% difference between the maximum and minimum refractive indices in the optical link. Whilst this may seem low, it is still worth investigating the effects these kind of refractive gradient have on optical communication links due to their prevalence in underwater acoustic communications (Stojanovic, 1996); this discussion continues in sec. 5.4.

3.6 Summary

This chapter set out to understand variations in optical properties, both between and within natural waters. By highlighting the important role chlorophyll concentration plays in determining these properties through a one-parameter model developed by Haltrin, variations in the attenuation spectrum could be characterised. The Haltrin model was extended to establish depth-dependent fluctuations in the attenuation coefficient, whilst also providing a framework for future investigation of temporal attenuation variation. Subsequent averaged attenuation coefficients give a unique

insight into the variable performance of optical communication links where the link orientation or location is not fixed.

Also provided in this chapter are thorough descriptions of different types of natural water. Attenuation in the clearest open oceans is dominated by the absorption of pure seawater, appearing at a minimum between blue-green wavelengths, gradually peaking and then falling with increasing depth down the water column. In highly turbid coastal or inland waters, the effects of particulate scattering are much more profound, shifting the window of low attenuation to yellow-green wavelengths and, in general, peaking very close to the surface. Overall, it is clear that any underwater optical system needs to be carefully designed to suit its environment, regardless of whether it is deep down the water column of the open ocean or close to the surface of particulate-rich inland waters.

Chapter 4

Underwater Link Design

The application of optical wireless communication to aquatic environments is challenging due to the greater extent to which light is attenuated underwater, a challenge further exacerbated by the variable nature of this transmission medium. In this chapter, options for underwater optical wireless link design are considered, where links are optimised to cope with a broad range of underwater conditions including depth and orientation variability. Emphasis is placed on the optical set up, receiver and transmitter design, and modulation scheme selection, to provide an exploration of system trade-offs and optimal component selection.

Following the theme of variability in the aquatic medium, this chapter also surveys and describes changes in medium-specific channel noise, suggesting ways it can be minimised.

4.1 Basic Link Configuration

Underwater optical wireless system design can be considered an extension to traditional free-space optical design where the magnitude of light scattered and absorbed is many times greater. As such, underwater optical link design comprises of familiar aspects: the selection of appropriate transmitter and receiver optics to aid alignment and propagation distance; electronic design to reduce noise; a modulation scheme to reduce errors; and a link configuration suitable for the chosen application (Barry, 1994).

The most basic link configuration for optical wireless is a LOS link, where light is transmitted in a straight line directly towards the receiver, as shown in fig. 4.1a. An adaption to this is the wide-angle LOS link type, where spreading of the optical signal from a wide transmitter FOV relaxes the alignment requirements between the transmitter and receiver. This type of link, which is depicted in fig. 4.1b, is particularly advantageous in mobile platforms as it reduces the need for accurate pointing-and-tracking (PAT) technologies. In underwater optical communications, most existing studies and commercial systems adopt either of these link types due to ease of implementation and higher energy efficiency (Arnon, 2010). However, in a few niche applications, non-LOS links can be implemented, either by exploiting high scattering to transmit past obstacles, as in 4.1c, or by reflecting the transmitted signal from the air/water interface (Arnon & Kedar, 2009).

As with free-space optical communication links, the power at the receiver, P_R, in a LOS underwater link is estimated using eq. 4.1 (Arnon, 2010).

$$P_R = \frac{P_T}{\tan^2(\theta_T)} \frac{e^{-cr}}{4r^2} D_R^2 \cos(\theta_R) \tag{4.1}$$

The term on the left represents transmitter characteristics; P_T is the transmitted power and θ_T is the beam divergence half-angle. The second term is due to the medium where r is the link length and c is the attenuation coefficient. Lastly, the right hand term relates to the receiver, where D_R is the diameter of the receiver aperture and θ_R is the receiver FOV. The associated SNR of this system is

$$\text{SNR} = P_R / P_N \tag{4.2}$$

where P_N is the total noise equivalent power in the system, explored in detail in sec. 4.2.

For a fixed transmitter and receiver the SNR decreases when subjected to increasing link length and attenuation coefficient. Transmitter and receiver design in underwater optical wireless links are

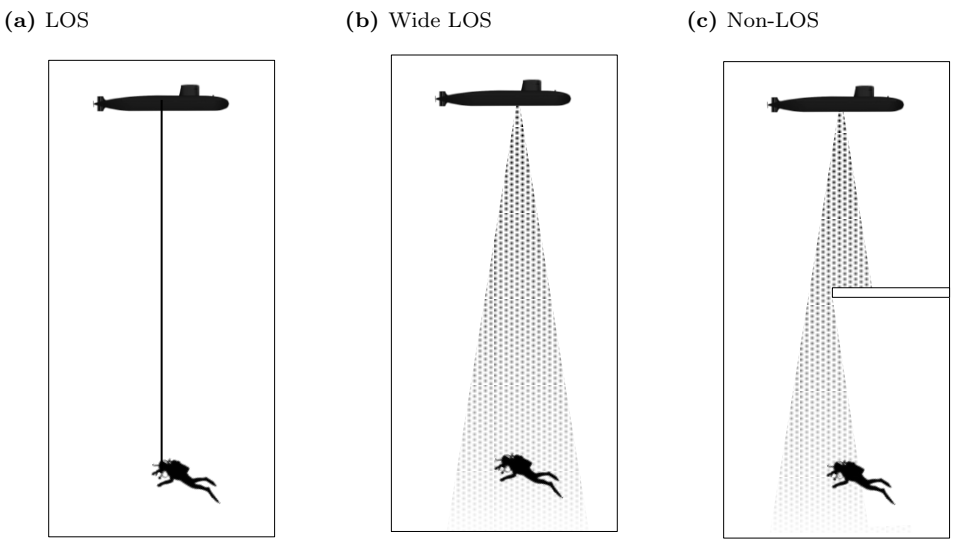

Figure 4.1: Basic communication link configurations for underwater optical wireless communication between a single transmitter, represented by an AUV, and receiver, represented by a diver.

therefore paramount to maximising performance. This is particularly the case in links that have a variable component, whether it be variable in terms of the optical channel or the link requirement.

The remainder of this chapter explores trade-offs in the design of optical wireless links for these kinds of variable underwater environments and systems: in sec. 4.3 transmitter design is assessed, including appropriate optical technology to suit desired beam divergences, compensatory PAT technologies and appropriate wavelength selection; sec. 4.4 looks at maximising the receiver collection FOV whilst minimising the area; and sec. 4.5 briefly surveys modulation schemes. However, first attention is turned to channel noise to form an underwater-specific description of the noise power in eq. 4.2, aiding subsequent system design considerations and channel models.

4.2 Channel Noise

As with all communication systems, underwater optical wireless communications are affected by noise. However, through an understanding of the sources of external and internal noise in these systems, smart communication design may be employed to mitigate and/or limit the extent of noise. For underwater optical links in particular, background light sources can present a significant problem and, as with the channel properties, it will be shown this can be extremely variable in magnitude and impact.

Beginning from the description of the SNR in eq. 4.2, the total noise equivalent power in any

underwater optical wireless systems can be found through (Giles & Bankman, 2005)

$$P_N = \sqrt{P_{\mathrm{SHO-BG}}^2 + P_{\mathrm{SHO-T}}^2 + P_{\mathrm{DRK}}^2 + P_{\mathrm{AMP}}^2} \tag{4.3}$$

where shot noise from background light sources is denoted as $P_{\mathrm{SHO-BG}}$, the signal shot noise is $P_{\mathrm{SHO-T}}$, dark current noise is written P_{DRK} and preamplifier current noise is P_{AMP}; each term is fully defined in app. F. Since there already exists comprehensive literature on general optical wireless noise sources, for example in (Jaruwatanadilok, 2008), this investigation is limited to exploring underwater channel-specific noise sources, as characterised by the background shot noise.

Background shot noise in underwater communication systems mainly originates from ambient sun or moonlight at the receiver; in dark locations, organic processes such as bioluminescence and fluorescence are the main contributors. An estimation of the overall background shot noise is derived (using app. F) from the background noise power P_{BG}, where

$$P_{\mathrm{BG}} = \pi^2 D_R^2 \theta_R^2 \lambda_R (L_{\mathrm{BG-SOL}} + L_{\mathrm{BG-MISC}}) \tag{4.4}$$

The received, perhaps filtered, range of wavelengths is denoted λ_R, the ambient solar radiance, which is discussed in sec. 4.2.1, is denoted $L_{\mathrm{BG-SOL}}$; radiances from other underwater sources are included in the term $L_{\mathrm{BG-MISC}}$ and reviewed in sec. 4.2.2.

4.2.1 Ambient Sunlight

Ambient sunlight causes profound problems when communicating in air but is less significant in natural waters as it only propagates so far down into the water column. Nevertheless, it is considered to be the ultimate limiting noise factor for underwater wireless optical communications (Hodara & Marquedant, 1968). The radiance of solar energy at any point of a natural water body is given through the relation

$$L_{\mathrm{BG-SOL}} = \frac{ERF_R}{\pi} \exp\left[-Kz\right] \tag{4.5}$$

where E, R and K are the AOPs introduced in sec. 2.2.2 and F_R is a constant describing the portion of radiance observed at a specific viewing angle as opposed to a direct viewing angle. Example values, for a wavelength of 532 nm, are $E = 1440$ W m^{-2} and $R = 1.25\%$; F_R is equal to unity at a viewing angle of 180°, or 2.9 when viewed horizontally, or 333 whilst looking up

the water column from a depth of 30 metres (Giles & Bankman, 2005). Values of irradiance, K, depend on the water type, as given in the Jerlov classification scheme of fig. 3.3. It should be noted that, as a consequence of the relation in eq. 4.5, optical receiver designs that try to eliminate a direct beam from the sun are generally unsuccessful at removing noise; sunlight in natural waters is in a diffuse state.

As introduced in sec. 3.3.2, sunlight has a profound effect on the locationality of marine life which in turn dictates how far down the water column solar energy propagates (Brown et al., 1995). To determine at what depths sunlight contributions can be considered negligible, ocean zoning should be considered. The photic zone is the brightest upper region of the ocean where the intensity is at least that necessary for phytoplankton growth. The depth of this region for different ocean types is given in fig. 4.2 from the depth of moonlight intersections with the line labelled III. Below the photic zone is the aphotic zone, here plants do not survive because of insufficient intensities to enable photosynthesis (Meadows, 2013). However, some deep-sea fish have evolved to cope with the low intensities through bioluminescence which has its own impact on received noise, as discussed in sec. 4.2.2. In the aphotic zone, downwelling irradiance is no longer an issue, such low light intensities are indistinguishable from dark current noise across the receiver. Furthermore, at depths below 1500 metres, it becomes much more difficult to design a communication system due to increased pressure on the devices.

4.2.2 Other Light Sources

As mentioned in sec. 4.2.1, lower down the water column, deep-sea fish and other marine life exist that are bioluminescent. Bioluminescence occurs naturally when energy is released by a chemical reaction in the form of photons. Typically bioluminescent transmissions are in the blue region, with wavelengths of 450 - 550 nm, although there are a few cases of far red emissions (Widder et al., 1984). Unsurprisingly, nature designed these transmissions to correspond with the window of low electromagnetic attenuation, making bioluminescence a factor in the design of deep-sea optical wireless applications. Estimations of the spatial location and magnitude of bioluminescent radiation can be estimated through algorithms such as that in (Yi et al., 1992).

Another significant light source in the ocean is fluorescence by photosynthesising phytoplankton, originally omitted from the energy balance model of attenuation in sec. 2.2. Fluroescence is the re-emittance of absorbed light at another wavelength, typically longer, and affects only the photic zone where phytoplankton grows (Babin, 2008). The intensity profile of phytoplankton fluorescence

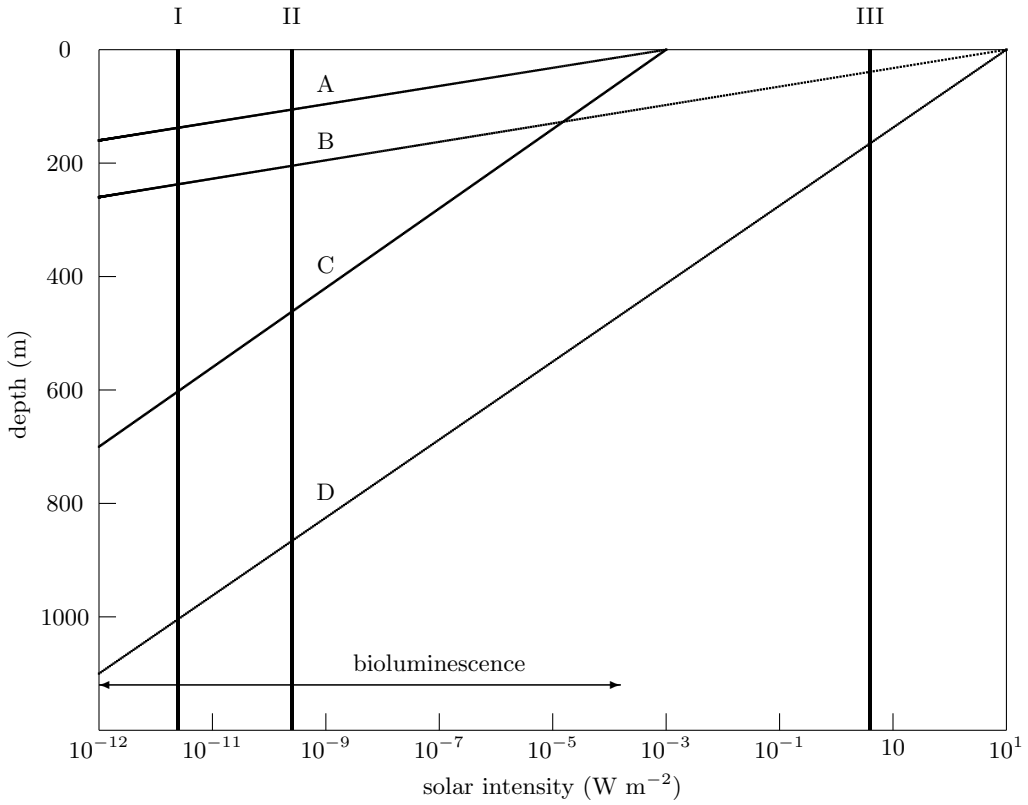

Figure 4.2: Attenuation of light in different water types where: I is minimum intensity for vision by deep-sea fish; II is the minimum intensity for vision by man; and III is the minimum intensity for phytoplankton growth. A and B show moonlight and sunlight in coastal area respectively, C and D are the open ocean equivalent, from (Meadows, 2013).

I_{PHY} can be described with the following equation (Falkowski & Kiefer, 1985):

$$I_{\mathrm{PHY}}(\lambda) = I\mu_{\mathrm{PHY}}\, C_{\mathrm{PHY}}\, a_{\mathrm{PHY}}(\lambda) \tag{4.6}$$

where I is the intensity of light on each phytoplankton cell and μ_{PHY} is the efficiency of the cell or quantum yield of fluorescence; other symbols are as described previously. The intensity profiles of fluroescence are related to the radiance through geometry and because fluorescence is emitted as a longer wavelength, it is possible to eliminate it by limiting the communication system receiver to a narrow spectral range. Note that with bioluminescence and fluorescence occurring at different depths underwater, $L_{\mathrm{BG-MISC}}$ generally has only a single underlying noise mechanism per link.

4.2.3 Obscuration

More often than not, underwater optical wireless links require that line-of-sight is maintained between the transmitter and receiver. However, the chance of beam obscuration underwater is relatively high, certainly higher than the likelihood in air. Light is currently used underwater both

to attract fish, in the case of fishing boats, and to discourage them, as happens around power plant water pipes; it is important to design a transmitter with the latter effect, as described below.

Although each marine species has different preferences regarding which light it is attracted to and repelled by, there are some overruling behaviours (Rich & Longcore, 2005). In general, fish that live in open ocean prefer light of blue/green wavelengths whilst those in freshwater prefer yellow/green wavelengths which, as will be shown in sec. 4.3, are the ideal communication wavelengths in the respective locations. The preferred intensity of fish depends on the background lighting conditions and the time to get used to it, similar to humans. Very bright light in a dark environment causes immediate avoidance reaction until the eyes have adapted; for fish this is typically 30 - 40 minutes as their eyes have to switch between their two receptor types (Rich & Longcore, 2005). This switch is also the trigger for when fish forage in schools, a bright light will cause schooling to increase protection for the fish. After their receptors have adapted, fish are likely to be attracted to the light, as long as it appears constant. Moreover, fish are seen to dislike flashing lights, these also cause an avoidance reaction although the critical frequency, at which a flashing light appears constant to them, is unknown (Rich & Longcore, 2005). In summary, the method for discouraging fish from obstructing communication line-of-sight is to have a seemingly erratic light signal or by changing the transmission wavelength away from the theoretical optimum.

4.3 Transmitter Design

Transmitter sources for optical wireless communications come in the forms of LED and laser technologies, where the latter can be solid-state or laser diodes. Each of these transmitter technologies have undergone huge advances over recent years, with increased output power, better modulation bandwidth, and a greater range of transmission wavelengths available in each case.

LEDs are low-power, lightweight, diffuse sources which generally have a wide divergence angle, capable of easily achieving up to 1 Mb s^{-1} data rates. Solid-state lasers, on the other hand, are high power (> 1 W) and highly directional, with significant disadvantages in terms of power, weight and cost. However, it is worth bearing in mind that the cost associated with cooling this type of laser is lower than that quoted in air, for example in (Green et al., 2008), as the system is submerged in seawater which has an average surface temperature of 3.5 °C (Meadows & Campbell, 1978). The second laser type, laser diodes (LD), are a small size, lower cost and more flexible alternative to solid-state lasers.

None of the three transmitter sources mentioned offers an outright best design for all applications; which technology can be considered optimum is dependent on the architecture of the link in addition to the medium which the link needs to propagate through. In general, solid-state lasers are more suited to long-range applications in open oceans, where the extent of scattering is low. The narrow, highly directional beam results in links above 200 metres (Pontbriand et al., 2008), meaning the greatest challenge with this transmitter type is the implementation of a suitable PAT technology. On the other hand, LEDs are more often associated with short-ranged links, especially those that occur in highly turbid locations or in locations where tracking cannot be implemented. When using LED technology, the aquatic medium causes scattering in multiple directions, increasing the temporal dispersion of the received signal more than that of laser technology. This may ultimately result in the bit rate being lowered. Laser diodes provide for medium-range links between the extremes and in applications where with very high bandwidth requirements ($>$ Gb s^{-1}). Although scattering reduces the range for these links, it is also seen to reduce the alignment requirements (Arnon et al., 2012).

The important characteristics of optical transmitters are the power, beam-divergence angle and wavelength, as per eq. 4.1. Whilst the beam-divergence is generally a result of the technology chosen, maximum power is fixed by eye safety limits or application limits, and wavelength through other criteria. Usually the most appropriate wavelength is selected as the one that experiences the lowest attenuation coefficient throughout the optical link, typically within the 400 - 500 nm region. In this section, depth-dependent attenuation models will be used to see how optical wireless link designers can go about finding the appropriate wavelength for variable ocean-based applications. Note also that alternative wavelengths may be used in diffuse optical links to encourage scattering (Elshimy & Hranilovic, 2011), to be outside of visible solar radiation range (Kedar & Arnon, 2009) or to discourage marine life from swarming the communication system (sec. 4.2.3).

First, the ideal wavelength for horizontal optical wireless links is assessed at different depths throughout the water column and for different surface chlorophyll concentrations. Through the use of the depth-dependent attenuation equations derived in ch. 3, attenuation spectra were calculated at 5 metre depth increments for surface chlorophyll levels between 0 and 0.2 mg m^{-2} (S1 to S4) and at 2 metre increments between 0.2 to 4 mg m^{-2} (S5 to S9). At each depth, the minimum attenuation and the corresponding wavelength were noted, where wavelengths were rounded to the nearest 10 nm. The result for each S profile is plotted in fig. 4.3, where the DCM from app. E has also been plot to show the relationship between the DCM and an increasing ideal wavelength.

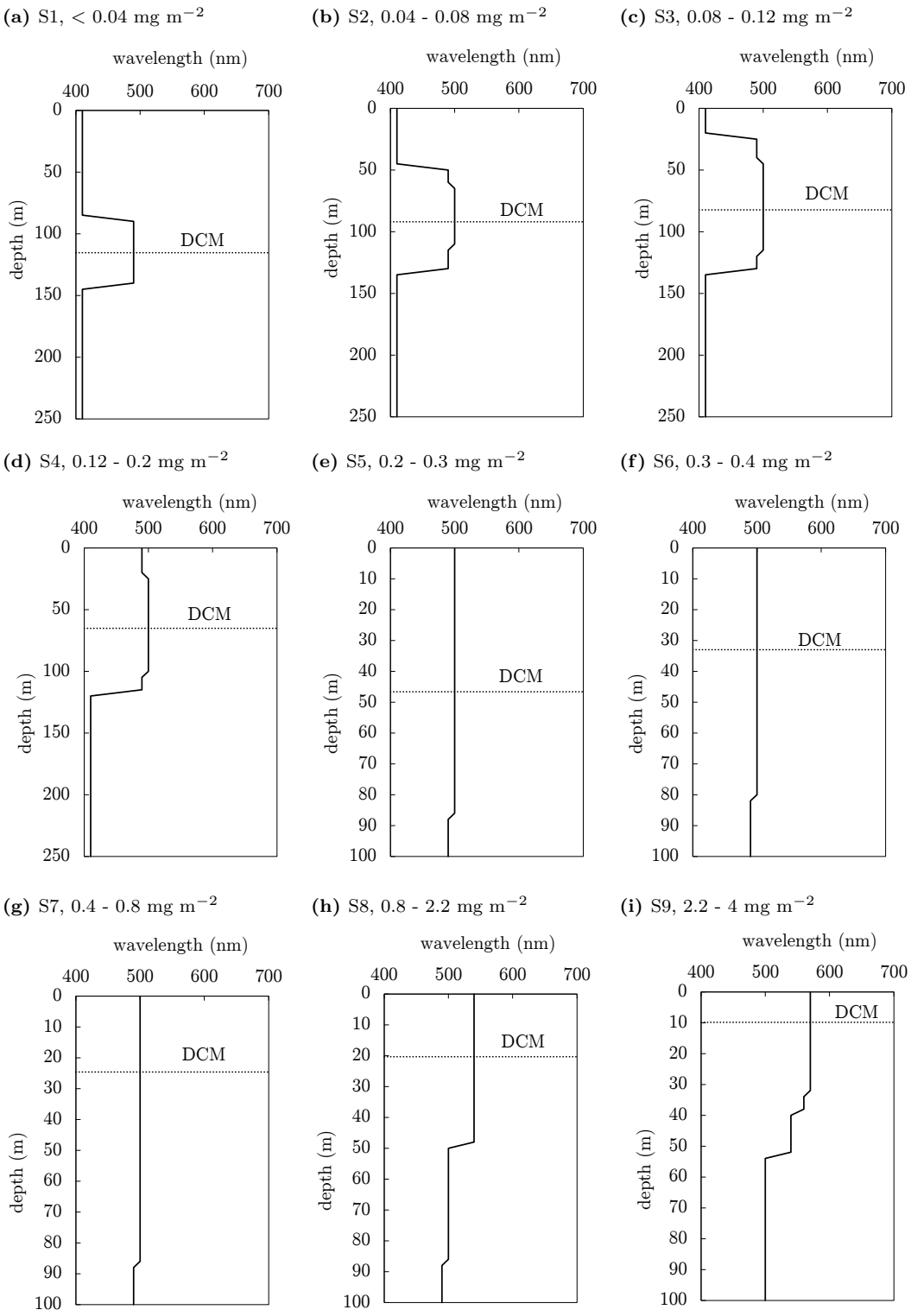

Figure 4.3: Best visible wavelengths for horizontal link any length S1-S9 profiles at depths between 0 - 250 m for S1 to S4 and 0 - 100 m for S5 to S9, where the surface chlorophyll level is given above each figure. Values are estimated using eq. 3.6 to eq. 3.9 inclusive and chlorophyll-depth profiles from app. E.

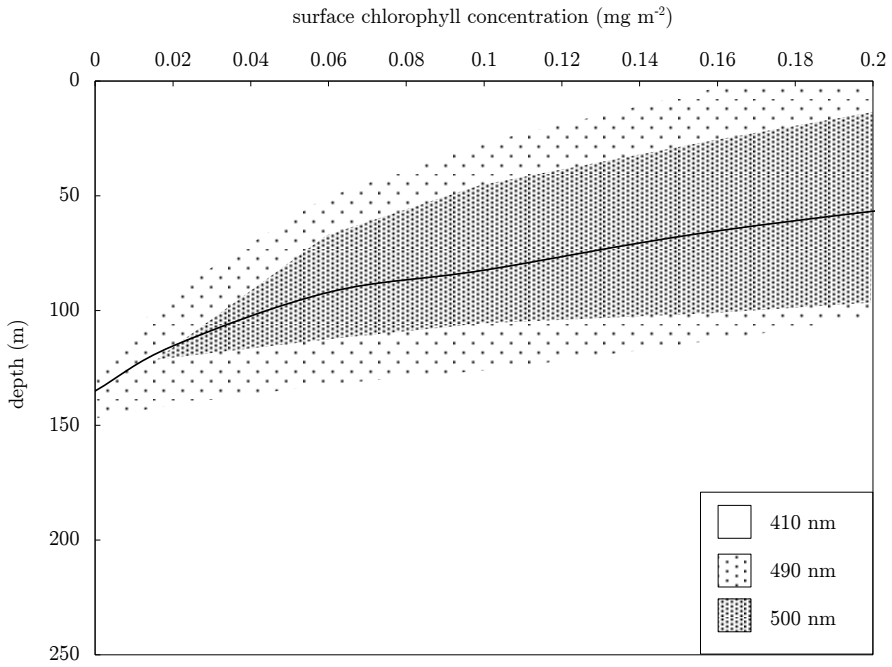

Figure 4.4: An estimation of ideal transmission wavelength with varying depth and surface chlorophyll concentration, calculated with averaged S1 - S4 values and by extrapolating.

The figure shows that, in general, as the chlorophyll concentration increases, the ideal wavelength becomes longer. However, rather interestingly, the relationship is not linear and undergoes some step changes beyond that of the wavelength increment of 10 nm, such as in fig. 4.3a. In fact, the lowest attenuation is seen to stick to certain wavelength increments and distinct groups of wavelengths, these being 410 nm, 490 - 500 nm, 540 nm and 560 nm and longer, caused by the changing shape of the attenuation curve as chlorophyll increases. What happens is instead of there being a single trough in the attenuation that slowly moves to longer wavelengths as the chlorophyll increases, there are several local minimum points along the attenuation profile, as is apparent in fig. 3.5. Increasing the chlorophyll concentration pushes the ideal wavelength towards one of these minimum wavelength points, resulting in discrete wavelengths where the attenuation is found to be lowest.

By extrapolating the average ideal wavelength against depth for each S group between S1 and S4, a plot was formed for selecting the ideal wavelength based on depth and surface chlorophyll concentration, seen in fig. 4.4. Here the importance of the DCM and chlorophyll concentration is apparent with the step change between 410 nm and 490 nm. The 490 nm to 500 nm transition is thought to be gradual, with the small step occurring in fig. 4.4 due to the 10 nm wavelength increments. It was noted that insufficient data existed to form relationships and extrapolate for higher chlorophyll concentrations and wavelengths.

Next, the ideal wavelength for optical wireless links down the water column, or at some angle to the vertical, is explored. From fig. 4.3 it is apparent that the best wavelengths for these links depend on the expected length of the link and the transmitter location, especially in places of high surface chlorophyll. For example, in the S8 profile, the ideal wavelength of a link between 0 to 50 meters is 540 nm, whereas between 0 and 100 meters this wavelength decreases to 500 nm because the chlorophyll levels reduce rapidly at greater depths.

As it has already been shown that ideal transmission wavelength is limited to a few discrete wavelengths, the aim of this analysis is to see how the wavelengths identified fare in links down the water column, or whether choosing an averaged wavelength leads to a lower attenuation coefficient. For the basis of this investigation, the optical communication links determined to find fig. 3.12 are again used, these are 100 metre long links transmitted down the column of S1, S3 and S6 oceanic waters, where the starting depths are taken to be 0, 50 and 100 metres. The average attenuation coefficients at the selected wavelengths for the S1, S3 and S6 profile are documented in app. G in tab G.1. Significantly, the mean wavelength never gives the lowest attenuation, unless it happens to coincide with one of the other wavelengths. This relationship remains true irrespective of depth or surface chlorophyll level. In places of low chlorophyll, such as the 100 - 200 metre depth link on each of the S profiles, the average attenuation coefficient of the link is even much greater using the mean wavelength. Therefore, selecting wavelengths between 410 nm, 490 - 500 nm, 540 nm and 560 nm generally reduces link performance. This result is meaningful when taking into considering previous experimental studies, which are listed in app. I, where it is not uncommon for wavelengths in the range 410 - 490 nm to have been selected inappropriately.

Given what has been discussed, this research proposes three unique transmitter designs to cope with variability in the aquatic medium, as shown in fig. 4.5. The first design (fig. 4.5a) is for long distance, highly directional links in open oceans and is based on laser technology. The transmitter consists of two lasers with wavelengths close to 410 nm and 490 nm and a switching circuit to allow the transmitter to switch between the source devices for transmission. Krypton and Argon gas-ion lasers have wavelengths close to those required, at 416 nm and 501.7 nm respectively (LexelLaser, 2014), though more appropriate would be the use of tuned laser diode. The AlGaInN material allows for laser diodes to be fabricated over a very wide range of wavelengths from ultra-violet, i.e., 380 nm, to the visible wavelengths up to 530nm, whilst waveguide laser diode structures are fabricated to achieve operation with optical powers of > 100 mW in the 400 - 420 nm wavelength range with high reliability (Najda et al., 2013). Frequency-doubled semiconductor lasers offer a different route to achieving blue/green wavelengths; (Gupta, 2014) reported a frequency-doubled

(a) Double laser design

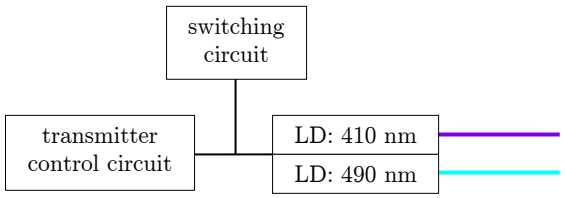

(b) Triple LED design

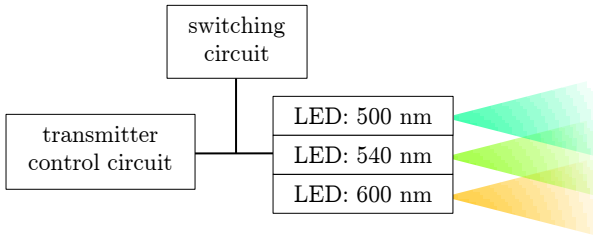

(c) Filtered LED design

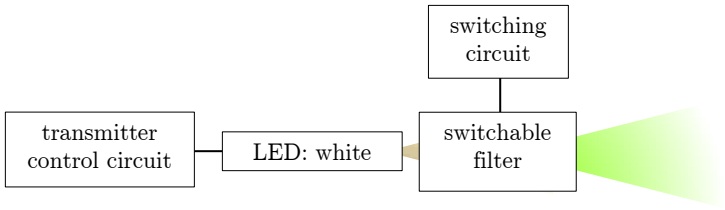

Figure 4.5: Example transmitter designs to cope with optical property variability, based on results derived in sec. 4.3. Only one LED or LD should be active at one time, but all transmitted beams are shown to give an indication of wavelength. Options for optical source technology for the wavelengths depicted is given in sec. 4.3.

semi-conductor laser with tuneable operation between 484 nm and 489 nm, producing 1 W. The latter also may be of interest in the design of covert submarine-to-satellite links as it coincides with a Fraunhofer line, a narrow window of low atmospheric absorption (Hollins et al., 2013)

LED based transmitter designs are suitable for coastal or inland waters, where the presence of particulate matter and scattering extent are much greater. For this reason, longer wavelengths, although still from the discrete values found in fig. 4.3, are selected for three LEDs; 500 nm, 540 nm and 600 nm (fig. 4.5b). The nearest available LEDs to these wavelengths are the Blue Green 505 nm LED, 555 nm Pure Green LED and 592 nm Super Yellow LED (OkSolar, 2015). As with the laser-based design, a switching circuit is added to determine which LED will be powered, where the switching circuit criteria could be determined by test signals or user defined. A more cost effective way to design a transmitter with the same function might be to have a wideband visible source like a single white LED with a switchable filter in front (fig. 4.5c), although this does reduce the efficiency.

In summary, this section has surveyed how variable underwater attenuation affects wavelength selection. With discrete wavelengths and groups of wavelengths identified as optimum values, the design of multi-source transmitters overcomes the challenge of variable high and low turbidity applications.

4.4 Receiver Design

Successful receiver designs in terrestrial optical wireless links include an optical filter, photoreceiver, a preamplifier and sometimes an optical concentrator (Ramirez-Iniguez & Green, 2005). Although requiring the same basic components, underwater optical links benefit from some adjustments: first, the receiver FOV is wide to pick scattered light over a large range of angles; second, filtering techniques are adjusted to reject underwater solar irradiance; third, photoreceivers should be sensitive to the wavelengths highlighted in sec. 4.2. These three points are briefly addressed in this section.

Photoreceivers operating in the visible spectrum come in the form of PIN-photodiodes, photomultiplier tubes (PMT) and avalanche photodiodes (APD). Whilst PIN-photodiodes are attractive due to fast response times ($>$ 1 GHz) and low cost, PMTs and APDs are popular underwater because of high gain and large apertures which allow them to better account for high and variable turbidity. PMTs are favoured in particular through low noise, however obtaining an appropriately high bandwidth ($>$ 350 MHz) in these devices forces either a trade-off with aperture size or a custom design. Improved performance and FOV may be achievable through geometrically diverse photodiode arrays (Simpson et al., 2012).

The use of filtering in underwater optical communications is important because it helps to reduce ambient solar irradiance and radiance from other sources that were seen in sec. 4.2. In addition to removing any direct solar radiation dominating the transmitted beam at the receiver, optical filters also reduce the shot noise from diffused, and temporally variable underwater light. To match the transmitter design in sec. 4.3, unwanted wavelengths should be filtered out, this is anything except 410 nm, 490 - 500 nm, 540 nm and $>$ 560 nm. By moving a switchable filter in front of the photoreceiver, such as the one shown in fig. 4.5c, filtering is selected about one of the aforementioned wavelengths. This design allows the receiver to select and tune into the least attenuated wavelength of a broad optical signal without the need to measure parameters of the water body or change anything at the receiver side.

Notably, shot noise has a tendency to increase with aperture area and receiver FOV, making

it particularly prevalent in medium- to long-ranged underwater links operating without or with minimal PAT techniques. Whilst large FOVs are desirable for collecting widely scattered photons, photons are likely to also be temporally scattered by more adverse channel conditions, leading to a downgrade in link performance. Hence, there is usually trade-off between the receiver FOV and performance, the solution to which is generally unique to the application and turbidity. However, it should be noted that dark areas of the ocean offer a platform for the use of wide collector FOV without much drawback; technologies enabling this range from simple lenses to complex optical concentrators (Ramirez-Iniguez & Green, 2005).

4.5 Modulation Schemes

As with other parts of underwater communication system design, the use of modulation and coding schemes is dependent on the application and subsequent underwater channel of interest. The main defining factor in modulation scheme selection is the received temporal dispersion, which is a result of the channel turbidity and receiver optics.

Applications that better retain temporal clarity, being medium- to long-distance links in relatively clear waters, are able to implement schemes which have shown to be most successful in terrestrial optical wireless, such as pulse position modulation (PPM) (Barry, 1994). A study in the underwater domain comparing modulation schemes in low-turbidity links concluded that M-ary PPM has a power efficiency advantage over on-off keying (OOK) and frequency-shift keying (FSK) (Karp & Gagliardi, 1969), with others claiming PPM to be near optimal (Xu et al., 2011). The downside of this scheme is it requires that the transmitter and receiver are exactly in sync which may be difficult to achieve underwater. It is possible to bypass this using differential PPM (Meihong et al., 2009), but this modulation scheme comes with an unusually large variation in bit rate, therefore potentially violating eye safety laws when used in conjunction with a laser source. Additionally, research is needed to determine at what turbidity PPM becomes unreliable, enabling estimates of the scheme performance for mobile platforms that communicate over a variable channel.

For applications where temporal dispersion is likely, such as short-ranged, diffused links in turbid locations, intensity modulation/direct detection (IM/DD) using OOK offer a simple solution for modulation. However, more complex modulation methods are sometimes used, such as orthogonal frequency division multiplexing (OFDM) and quadrature amplitude modulation (QAM), and have shown to outperform PPM in terms of bit rate; a recent, short range

underwater optical link implementing 16-QAM OFDM demonstrated transmission of 4.8 Gb s^{-1} (Oubei et al., 2015), the highest bit rate seen underwater so far. This study was based on LD technology which is arguably less suited to short-range, dispersive applications. ODFM with LEDs, such as that demonstrated in free-space optical wireless (Tsonev et al., 2014), may be of use for turbid media. However, given the multi-wavelength transmitters introduced in sec. 4.3, wavelength division multiplexing has the potential to offer a better solution to increase bandwidth in areas of high signal dispersivity. Performance using this scheme would be limited to the propagation of the least optimal wavelength, but as there are local minima in the absorption spectrum, and as app. G shows, the difference in attenuation is usually not that large.

In turbid LOS links, receivers must also be capable of differentiating between the incoming signal and backscatter of its own transmitted signal. The implementation of high-frequency intensity modulation has been shown to reduce the impact of backscattered light (Mullen et al., 2007); the diffuse nature of backscattered light gives it a low-pass response which is easily separated from high-frequency signal content.

The bit error rates (BERs) of the two main modulation schemes discussed here, OOK and M-ary PPM, are calculated using eq. 4.7 and eq. 4.8 respectively (Elganimi, 2013). In order to do this, the assumption has been made that the channel is subject to additive white Gaussian noise (AWGN). It is noted that AWGN is generally only suitable in channels where the only impairment to communication is a linear addition of wideband noise with a constant spectral density and Gaussian amplitude distribution. Subsequent models do not account for fading, dispersion, non-linearities from turbulence and medium variability, and other background illumination sources, all of which are particularly prevalent in the underwater channel. Despite this, AWGN is used in this chapter to produce a simple and tractable mathematical model to gain insight into the underlying behaviour of underwater optical wireless system before, in ch. 5, these other phenomena are considered.

$$\mathrm{BER}_{\mathrm{OOK}} = \frac{1}{2}\mathrm{erfc}\left[\frac{\sqrt{\mathrm{SNR}}}{2}\right] \tag{4.7}$$

$$\mathrm{BER}_{\mathrm{M-PPM}} = \frac{1}{2}\mathrm{erfc}\left[\frac{\sqrt{\mathrm{SNR}\ M\ \log_2(M)}}{4}\right] \tag{4.8}$$

Here erfc is the complementary error function, given by eq. 4.9, and M represents the number of

pulse positions. These relations are revisited in sec. 4.6.2 and ch. 6.

$$\mathrm{erfc}(h) = \frac{2}{\sqrt{\pi}} \int_{h}^{\infty} \exp[-t^2] dt \tag{4.9}$$

4.6 Optimal Component Selection

The design of optimal underwater optical wireless systems requires parameters from the optical channel, transmitter, receiver and modulation scheme. Judging the relative merits of each of the optical components can prove difficult, especially when considering the diverse applications and channel conditions underwater. For this reason, there exists several methods for characterising performance as singular numerical values.

The traditional method for comparing link performance, from free-space optical wireless, is through the *bit rate-length* product (Stotts, 1978). However, this measure does not give any indication of the medium; it is generally applied to indoor or clear channels which have very little channel variation. Perhaps a more useful measure for underwater optical wireless therefore is an *attenuation-bit rate-length* product, or alternatively, the *attenuation-length* product for applications where establishing a link is more crucial than data rates. These performances measures will be revisited in ch. 6 when assessing previous experimental studies. Other measures of performance are the SNR, which generally should be kept above 20 dB to provide reliable optical wireless transmission (Ghassemlooy et al., 2012), and the BER.

Typically in communications engineering, desired performance measures and/or applications are selected and components are chosen to best achieve the required link. In underwater optical communications, the variable underwater optical channel and ambient lighting conditions discussed in this research significantly increase the complexity of finding optimal components. For this reason, and to aid the search of optimal components, fig. 4.6 displays a summary of relations between the various performance measures, channel descriptions and link design parameters which have been introduced throughout ch. 3 and ch. 4. The input medium, transmitter, receiver and modulation properties referenced in fig. 4.6 are tabulated in tab. 4.1, where a suggested range is given for each parameter. In contrast to sec. 4.4, wavelength is defined as a transmitter property which determines where in $c(\lambda)$ the attenuation is estimated; in sec. 4.4 wavelength was found through optimisation using the absolute minimal attenuation. Note that for links below the photic zone, the left branch of medium properties can be ignored, this is because P_{BG}, the ambient solar lighting condition, falls to a negligible level below this region.

It is hoped that the information presented in fig. 4.6 and tab. 4.1 assists in the selection of optical components for specific underwater optical wireless applications. However, instead of designing links per application, a more efficient method is to automatically generate optimal solutions from a given number of transmitter, receiver, modulation and environmental options through a suitably selected algorithm. The genetic algorithm (GA), which has previously been used in parameter selection for variable atmospheric channels for optical wireless communications (El Yakzan, 2013), is one such algorithm.

GAs are adaptive, heuristic search algorithms based on the ideas of natural selection. The algorithm evolves through three operators: *selection*, representing to survival of the fittest; *crossover* equating to mating between individuals; and *mutation* which introduces random modifications (Mitchell, 1998). This is repeated until the termination criteria, and best set of solutions, are reached. The framework for creating a successful GA for a dispersive optical wireless channel is provided in (El Yakzan, 2013), which may be adapted to consider the relations summarised in fig. 4.6. Nonetheless, with there being several parameters in the GA to train manually to ensure solution sets converge quickly and accurately, the full formation of an underwater-specific GA would constitute its own thesis. Therefore, the work presented here offers a framework for future research in the underwater communication field.

The advantages of using a GA are: it can solve optimisation problems where parameters have complex, underlying relations, such as those in fig. 4.6; it solves problems with multiple solutions, perhaps not considered in manual design; and can easily be updated as the optical channel becomes better understood. Disadvantages include the time in setting up the correct parameters, in addition to the tendency of the GA to converge on local, rather than global, optimal solutions.

4.6.1 Component Selection Simulation

Although the GA will not be implemented here to find optimal component sets, the purpose of this section is to see how real components fare with respect to the overall performance model generated in fig. 4.6. The reasons for doing this are two-fold: first, it will help to assess the accuracy of the overall performance model, in addition to all associated sub-models and equations; secondly, it will provide information as to which underwater links are most viable and suggests suitable components for use in given applications. The latter point is significant because, as of yet, there has been no research on the capability of optical communication links in depth- and orientation-varying channels.

For the simulation, 64 commercially available transmitters were selected, as per the limitations

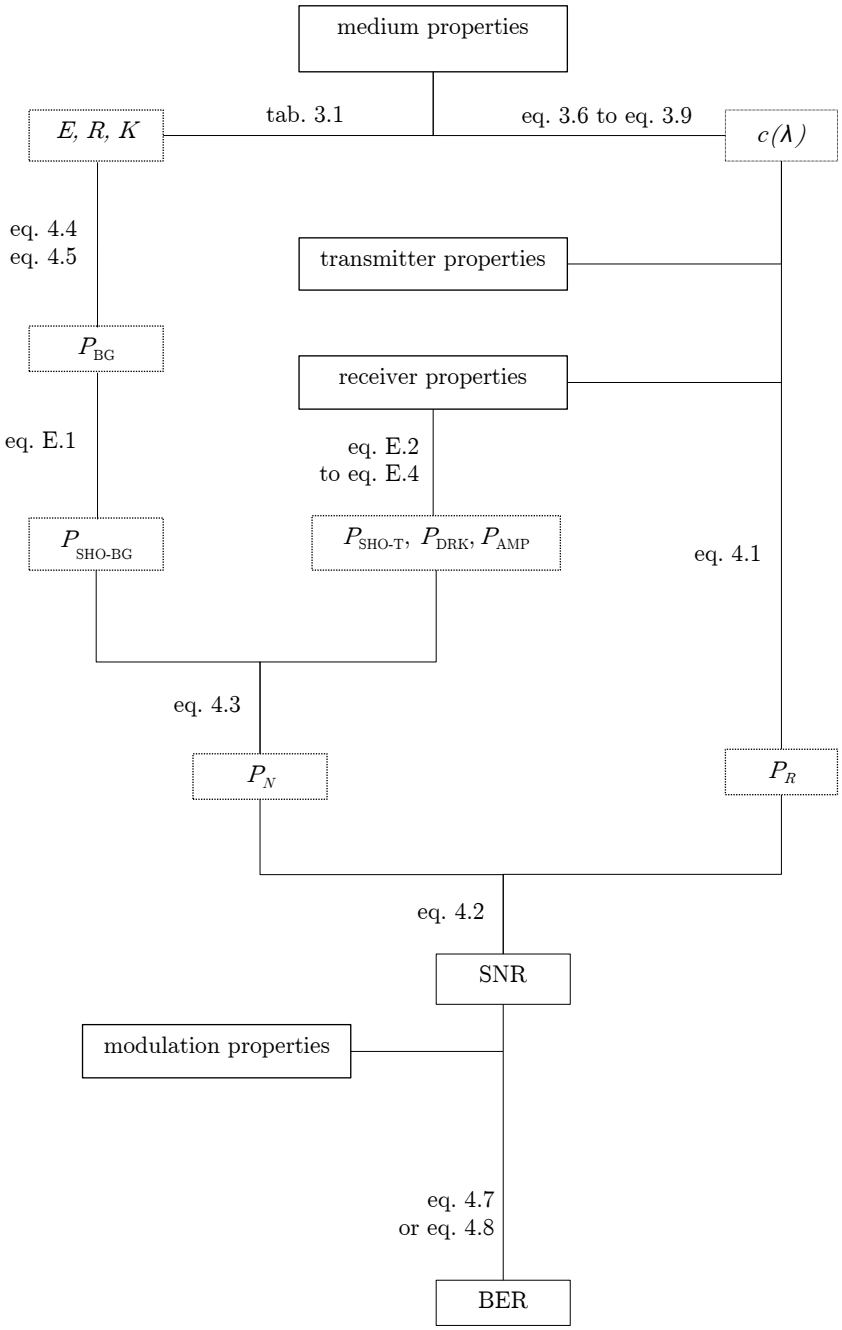

Figure 4.6: Diagram showing the relationships between the performance measures of underwater optical wireless in a variable medium. The measures BER and SNR are related to the input medium, transmitter, receiver and modulation properties, which are given in tab. 4.1.

Input Properties	Typical or Suggested Range
medium properties	
surface chlorophyll concentration, $C_{\mathrm{CHL}}(z=0)$	< 4 mg m^{-2}
starting depth, $z(\mathbf{r}=0)$	$<$ 250 m for S1-S4; $<$ 100 m for S5-S9
ending depth, $z(\mathbf{r}=r)$	$<$ 250 m or S1-S4; $<$ 100 m for S5-S9
link length, r	$<$ 200 m
transmitter properties	
transmitter power, P_T	$<$ 100 mW LD; no limit LED
transmitter wavelength, λ	400 - 700 nm
transmitter beam divergence, θ_T	0.01 - 60° LD, 5 - 60° LED
receiver properties	
receiver area, D_R	0.05 - 100 mm^2
receiver FOV, θ_R	$<$ 180°
receiver gain, G_R	0 - 70 dB
receiver sensitivity, S_R	0.1 - 0.7 A W^{-1}
excess noise factor, F_N	1 for photodiode; $>$ 1 for APD
modulation properties	
modulation bandwidth, BW	dependent on system, higher for LD
modulation type	OOK or PPM
(PPM levels, M)	(limited by temporal dispersion)

Table 4.1: Table of input properties for determining system SNR and BER. Suggested range from: medium properties ch. 3 and (Pontbriand et al., 2008); transmitter ranges from (Keiser, 2003), (Wierer et al., 2013) and (Thorlabs, 2014); receiver from (Thorlabs, 2014) and (Ramirez-Iniguez & Green, 2005).

in tab. 4.1 which state that the transmitter should have a wavelength in the range 400 - 700 nm, with a power up to 100 mW for laser diodes (due to eye safety limits). Further to the selected transmitters are 32 different receiver technologies; a full list of both components is available app. H. These components were chosen as they represent a good range of technologies, including LED and LD transmitters, and several receiver types.

The component selection simulation criteria chosen is simple: for a known underwater location and link length, how many combinations of the aforementioned transmitters and receivers result in an optical communication link with an SNR above 20 dB, using the relations set in fig. 4.6. In the simulation, if a combination is successful, meaning the link has an SNR above 20 dB, the link is marked as a *0* and if unsuccessful, a *1*. These 0s and 1s are subsequently mapped onto a two-dimensional space showing the transmitter options along one axis and the receiver options along the other. The resulting density of the generated space gives an indication as to the viability of communication for that location whilst limiting what type of transmitter or receiver should be implemented. In order to make the results appear more coherent, the transmitter and receiver options are sorted before the simulation commences, where transmitters are listed by from smallest to largest factor of $P_T/\tan^2(\theta_T)$ and receivers by $D_R^2\cos(\theta_R)$, both of which are from eq. 4.1 and listed in app. H.

Two very different underwater locations are chosen for the purpose of this simulation. The first optical link is one of extremely low oceanic turbidity, as such a horizontal link 200 metres down an S1 water column is selected. Importantly, this is below the photic zone, so the overall noise equivalent power, P_N, is determined by the receiver properties, instead of by shot noise from ambient solar radiance. The second optical link is chosen in a highly turbid location where there is a strong presence of ambient solar radiance. For this reason, a horizontal link at 10 metres into the water column of S9 water is selected, approximately corresponding to the DCM of the S9 profile. It is noted that seawater with a surface chlorophyll concentration equal to that of the S9 group (2.2 - 4 mg m^{-2}) comes under the Jerlov classification type 5, for the purpose of estimating $L_{\mathrm{BG-SOL}}$. Links in the two underwater locations are varied in length to find the SNR maps associated with increasing distance between the transmitter and receiver.

The map of successful transmitter/receiver combinations in the first, clearer location is shown in fig. 4.7, for link lengths of 1, 3, 10, 30, 100 and 300 metres, where dark pixels represent an unsuccessful link. This figure shows that, as expected, when the link becomes longer, the number of successful transmitter and receiver combinations becomes fewer due to a drop in the received power P_R. With reference to app. H, the transmitters that have a tendency to perform better

are lasers with wavelengths nearer 410 nm. Lasers that have a high $P_T/\tan^2(\theta_T)$ factor but that are in the 600 - 700 nm range cause banding across the SNR maps, which is particularly visible in fig. 4.7d and fig. 4.7e. Consequentially, although lasers that stray from the ideal wavelength of 410 nm perform better at distance than LEDs due to superior power density, with the maximum transmitter power limited, choosing a transmitter with a wavelength near 410 nm offers the best performance. In terms of receiver technology, the successful combinations generally decreases linearly with link length by decreasing $D_R^2\cos(\theta_R)$ factor, where Si and GaP transimpedance amplified photodetectors with large apertures have a tendency to perform best. However, a single vertical band is present towards the lower $D_R^2\cos(\theta_R)$ end of the SNR maps, it is particularly apparent in fig. 4.7c to fig. 4.7e. This vertical band is the result of a particularly low-noise receiver (PDF10 in app. H), showing low-noise receivers to be a sensible choice in locations of almost no ambient light.

The SNR simulation results of the high turbidity case are shown in fig. 4.8, where ambient solar noise has been ignored in fig. 4.8a to fig. 4.8c, but included in fig. 4.8d to fig. 4.8f to determine its impact. Both 1 metre links in this highly turbid area, in addition to the 1 metre link in fig. 4.7, are similar which seems to suggest that for short-range links transmitter and receiver selection is not important. Whilst this is partly agreeable, sometimes components can be selected on parameters not considered here such as cost, it is more likely there is an misjudgement of the performance based on an underlying flaw in the models used to represent the communication links. In particular, the way in which the model treats scattering events. In fig. 4.6, scattering is included as part of the attenuation coefficient, which assumes that once photons are scattered away, they have been lost forever. However, this is generally not the case, and photons that are scattered multiple times may end up on the receiver, as originally shown in fig. 2.9. Scattering of this type is one of the reasons LEDs are preferred in highly turbid locations, although not apparent from the results of fig. 4.8. For this reason, in ch. 5, the models of propagation and link performance built up thus far are used to pursue more complex modelling schemes which do include multi-scattering.

Referring back to fig. 4.8, it is noted that the appearance of banding is less frequent than with the low turbidity case, due to wavelengths about the centre of the 400 - 700 nm spectrum being most ideal and the attenuation spectrum in general appearing a lot flatter. As expected, where shot noise from ambient solar radiance is included, fig. 4.8d to fig. 4.8f, there is no longer a vertical band from the low-noise receiver since noise in these systems is dominated by ambient shot noise. Therefore, in the high turbidity case, the suitability of certain transmitters and receivers can be acquired from the factors $P_T/\tan^2(\theta_T)$ and $D_R^2\cos(\theta_R)$ respectively. Note that the number of

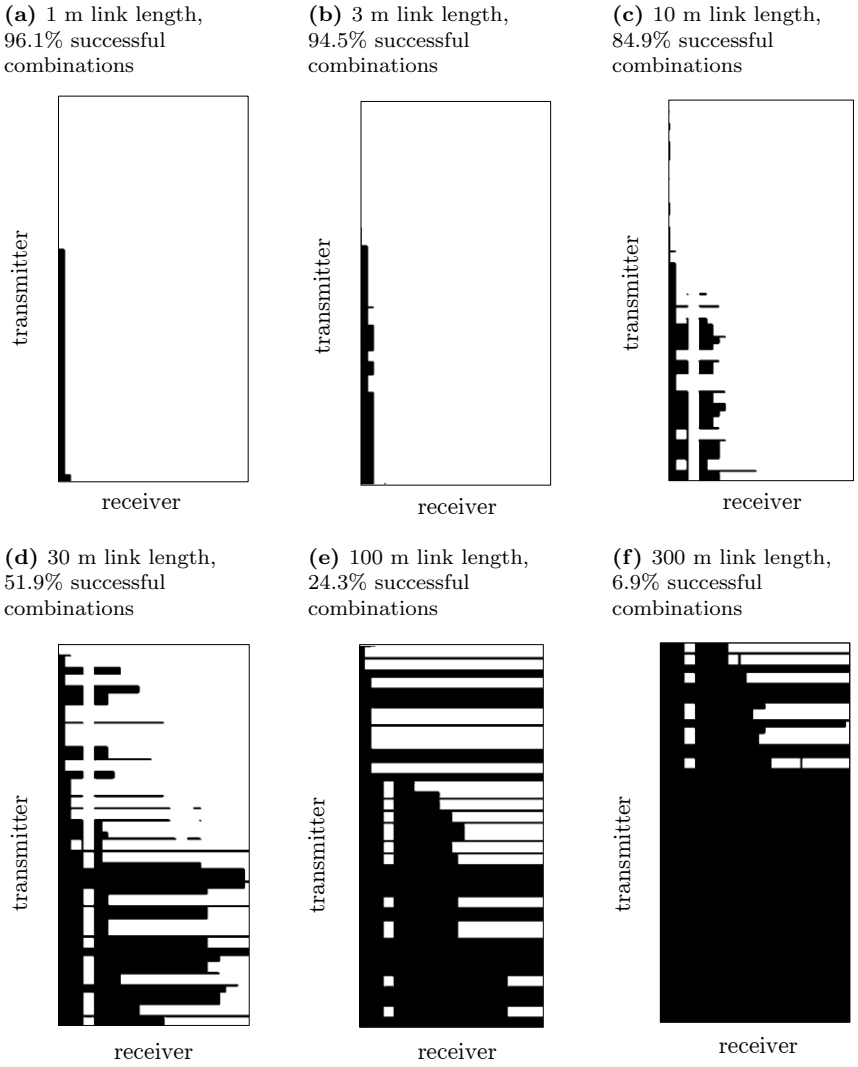

Figure 4.7: Low turbidity case of SNR map of successful and unsuccessful combinations of transmitter and receivers from app. H that achieve an SNR of 20 dB or greater. Communication links are based in S1 type water, 200 m into the water column where ambient solar light is negligible. Black denotes an unsuccessful communication link.

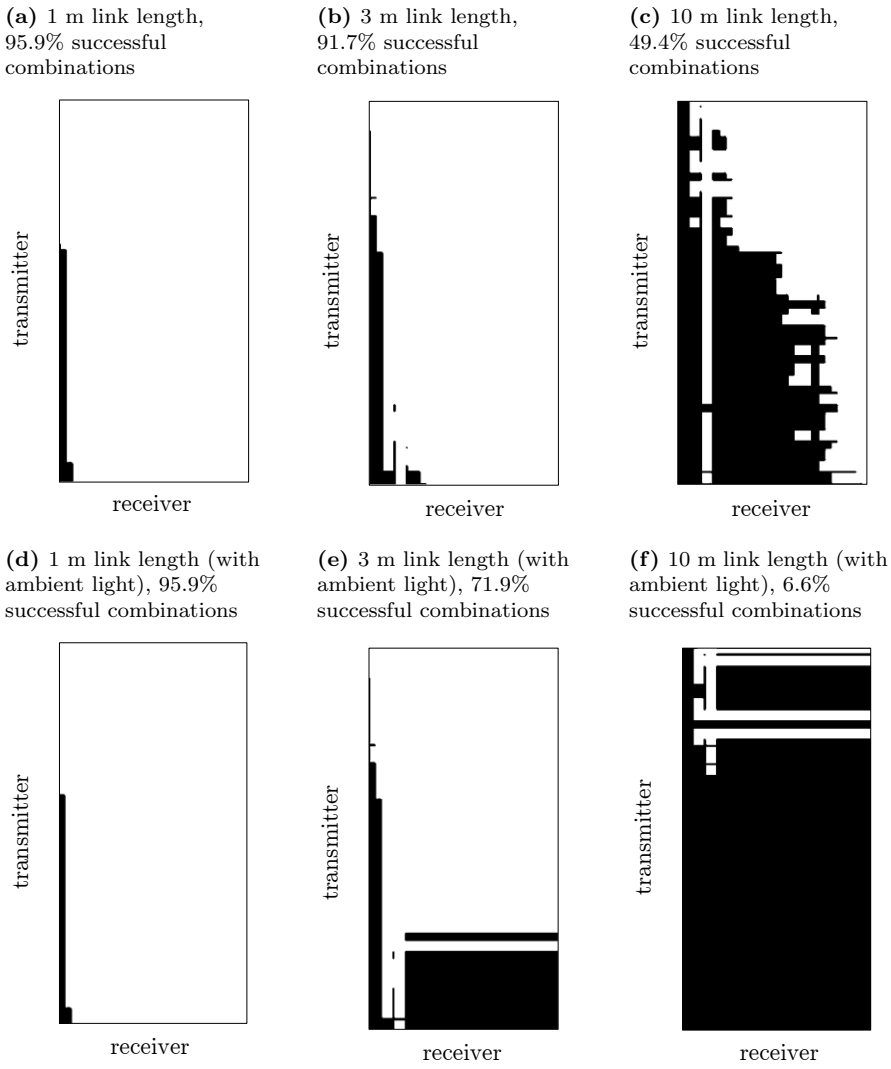

Figure 4.8: High turbidity case of SNR map of successful and unsuccessful combinations of transmitter and receivers from app. H that achieve an SNR of 20 dB or greater. Communication links are based in S9 type water, 10 m into the water column where in (a) - (c) ambient solar light is ignored and in (d) - (e) it is included. Black denotes an unsuccessful communication link.

successful links in the highly turbid location with a 30 metre link length was 0% for both the zero and regular ambient noise simulations.

Although this simulation has provided several interesting conclusions, the simulation, and hence the results, do not properly establish LED and laser technologies in terms of their advantages and disadvantages. One reason this may be the case is that the models introduced do not account for misalignment between the transmitter and receiver. Although it could be added to the existing propagation and performance models, it is likely to be inaccurate whilst the effects of multi-scattering are neglected, particularly underestimating the link capability in turbid underwater media, hence the subsequent study of this area in ch. 5.

4.6.2 Component Performance

Having identified in sec. 4.6.1 which components lead to high SNRs, the BER performance of these components with different modulation schemes is now assessed. As in the previous section, two underwater channels are considered; a low-noise, open ocean location and a turbid coastal location with high amounts of background solar radiation. For both cases, the receiver PDA36A (from app. H) is selected from the SNR simulation, representing a capable but relatively low-cost receiver. This particular choice of receiver also aids a later discussion of the experimental performance, in ch. 6, where the same component is implemented in a practical system. The transmitters for the two cases are selected as per the wavelength requirement, to be LP405-MF80 for the clear ocean case and LP520-MF100 for the turbid case, where details of each component is available in app. H. The subsequent BER performance is given by the relations in fig. 4.6.

For the modulation schemes OOK, 2-PPM and 4-PPM, the BER is calculated with increasing link distance, as displayed in fig. 4.9. This figure shows that the BER increases significantly with link length, though especially for links greater than 100 metres, as in fig. 4.9a. Additionally, the BER is seen to be higher overall in the turbid underwater case, mainly due to lower SNR. In both cases, 2-PPM is seen to perform worse, whilst 4-PPM has a much lower BER in comparison to OOK modulation.

Notably, the BER results from fig. 4.9 are much lower than those seen in other underwater optical wireless studies, such as (Sui et al., 2009) and (Jaruwatanadilok, 2008), by several orders of magnitude. It is thought that this is likely to have been caused by the lack of higher-order effects in the chosen transmission model (Beer-Lambert) and noise model (AWGN), where higher-order effects refer to effects of photons that have undergone more than one scattering event (see ch. 5). Therefore, although the models introduced in this section have provided a preliminary

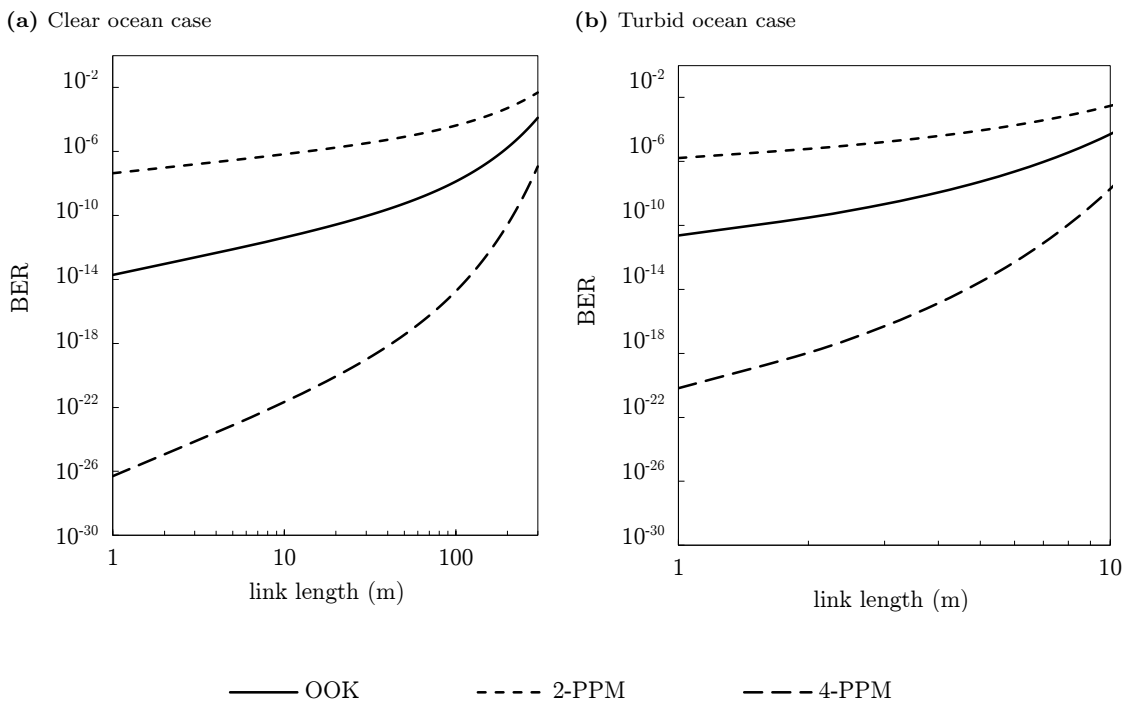

Figure 4.9: BER performance with increasing link length in (a) clear ocean water and (b) turbid water, as described in sec. 4.6.1.

understanding of the optimal components, accurate BER predictions cannot be determined without the use of more descriptive channel and noise models which better simulate the underwater optical channel.

4.7 Summary

This chapter considered options for link design of underwater optical wireless links that have variable locational and directional components. Channel variability between locations was seen to have a two-fold impact; firstly by altering the ideal transmission wavelength according to the minima of the local attenuation profile and secondly, by changing the shot noise conditions through background solar radiance. Unique multi-source transmitter designs were introduced to overcome the former problem. Such solution is particularly appropriate as ideal wavelengths were found to fall into discrete groups, 410 nm, 490 - 500 nm, 540 nm and $>$ 560 nm, regardless of depth or surface turbidity. Meanwhile, the issue of variable noise led to restrictions in the choice of receiver design.

The channel models in this chapter were based on the assumptions of the Beer-Lambert law and AWGN. Whilst these do not account for fading, dispersion, turbulence-induced nonlinearities,

medium variability and underwater background illumination, the combination of these assumptions has provided insight into some of the trade-offs faced in designing underwater optical wireless links over variable optical properties.

Chapter 5

Advanced Channel Modelling

Underwater channel models for optical wireless communications exist to describe the state of light from an LED or LD source after travelling a specified distance through an aquatic medium. Of particular importance are the overall power loss, useful for link budgets and SNR calculations, the spatial distribution of light and the temporal distribution of light. The latter two are found through the radiative transfer equation, an advanced channel model explored throughout this chapter. By selecting an appropriate radiative transfer solution this chapter will begin to explore how the underlying optical property variability affects optical wireless communications.

5.1 The Radiative Transfer Equation

The channel models introduced so far in this thesis have estimated the exponentially decreasing intensity for light beams transmitted underwater and briefly touched on the beams' spatial distribution through the $1/r^2$ term in the LOS link equation, eq. 4.1. The main drawback of these models is their omission of the complexities of multiply scattered photons due to an underlying assumption that photons scattered once are lost. As the aquatic medium is highly scattering, particularly in locations of high chlorophyll and turbidity, using these models to represent the underwater channel can result in high levels of inaccuracy. Advanced channel models for underwater optical wireless communications, on the other hand, do describe the changing intensity, spatial distribution and temporal distribution of light from a source transmitting underwater. By implementing one of the advanced modelling schemes which evaluate scattered light fields, better estimates of the communication characteristics are formed. As has been shown previously in ch. 4, these link performance characteristics are depicted through the SNR and BER, though other factors such as the pointing accuracy and temporal pulse spreading can also be considered.

All optical wireless channel models have humble beginnings; the common features shared by all are the absorption and scattering coefficients. It was these common features which meant that, in ch. 2 and ch. 3, the coefficients and their variability were characterised extensively. Using these coefficients, in the most simplified case, the loss of power in an optical wireless link after a known distance is encapsulated through the Beer-Lambert law of eq. 2.13. The resulting expression describes changing radiant intensity I with distance (previously I_0 at the source) as

$$I(r) = I_0 e^{-cr} \tag{5.1}$$

This is in the same form as the models surveyed so far. It can be seen that by itself, this model is not capable of predicting either spatial nor temporal dispersion and does not consider information about the system configuration, such as the source and receiver FOV. For this, the radiative transfer equation (RTE) must be introduced.

In essence, the RTE describes the energy conservation of an electromagnetic wave that is passing through a medium. It differs from the inherent optical property energy balance in sec. 2.2 by the insertion of an additional energy mechanism in the from of gain due to previously scattered light. The RTE itself exists in both scalar and vector form, the full derivations of which are found in (Van de Hulst, 2012). For the purpose of optical wireless communications, considering the vector

form is advantageous as it provides a model of the temporal dispersion and polarisation state of the light. Therefore, the vector RTE is given in eq. 5.2 (Arnon et al., 2012).

$$\left[\frac{1}{\mathrm{c}}\frac{\partial}{\partial t} + \mathbf{n}.\nabla\right] I(t,\mathbf{r},\mathbf{n}) = \int_{4\pi} \beta(\mathbf{r},\mathbf{n},\mathbf{n}')I(r,\mathbf{n},\mathbf{n}')\,\mathrm{d}\mathbf{n}' - cI(t,\mathbf{r},\mathbf{n}) + E(t,\mathbf{r},\mathbf{n}) \tag{5.2}$$

where t is time, $\mathbf{n}$ is the direction vector, $\mathbf{r}$ is the position vector, ∇ is the divergence operator with respect to r. Other symbols are as described previously: E is an internally propagating source radiance; c is the speed of light; I is the radiant intensity; β is the VSF; and c is the beam attenuation coefficient.

The left hand side of eq. 5.2 represents a change in energy over a differential length. Meanwhile, the right hand side of is formed of three components, which from right to left are; the energy of any internal sources, the main transmission beam extinction losses caused by attenuation and the reintroduction of scattered photons. If the latter component is ignored, then eq. 5.2 essentially becomes a differential form of eq. 5.1. From this, it is clear that this additional term is crucial in determining the temporal and spatial dispersion for underwater optical wireless communication links. However, calculating link performance from the RTE is not straight-forward; the RTE is an integro-differential equation with many variables, making it extremely difficult to solve analytically. Although there exist a number of other methods for solving the RTE, each of these comes with its own associated advantages and disadvantages, as will now be explored in sec. 5.2.

5.2 Solving the Radiative Transfer Equation

Preceding a discussion of RTE solutions, it should be noted that the vector RTE has been investigated for underwater wireless communications in its analytical form, where estimates for VSFs were determined using Mie's solution for typical ocean constituents and size distributions (Jaruwatanadilok, 2008). However, the complexity of this model in what are relatively simple underwater optical channels (no variability, reasonably low scattering) is high. Solutions for channels such those investigated in ch. 3, with depth- and time-dependent variations, would be difficult to conceive using the same method. Sophisticated methods therefore must be employed to solve the RTE for realistic underwater conditions.

The RTE involves solving both an integral and a derivative of the unknown radiance, for known inherent optical properties and boundary conditions. Solutions for this come in three forms: first, exact analytical solutions, which can only be derived for very few geometries; second, approximate

analytical solutions, where assumptions are made to simplify the RTE; last, numerical solutions. These methods are surveyed in sec. 5.2.1 to sec. 5.2.3 respectively.

5.2.1 Exact Analytical Solutions

At present, even simple geometries such as an isotropically emitting point light source in a homogeneous body of water do not have an exact analytical solution (Mobley et al., 2014). However, if the contribution from re-scattered light is ignored – a reasonable assumption for systems that do not rely on the temporal clarity of light, such as very low bit rate signals – and communication is assumed to be occurring in a region where there is no sunlight then, as was mentioned previously, the RTE simplifies to Beer-Lambert law in eq. 5.1. Re-scattered light tends to be neglected in long-ranged communication links because the intensity of the scattered signal is usually less than that of the original signal.

5.2.2 Approximate Analytical Methods

The most common approximate analytical solution is derived by performing a small-angle approximation on the VSF so that $\sin(\theta) \cong \tan(\theta) \cong 1$ and $\cos(\theta) \cong 0$. Such an approximation is valid in the underwater environment as the VSFs for the particulates found in natural waters are highly-peaked in the forward direction, as was previously shown by fig. 2.12. The downside of this simplification is that the temporal information is lost; scattered photons are considered to travel the same distance and in the same time frame as those that have not been scattered. However, it still provides more information about a communication system than the Beer-Lambert law as it gives the radial distribution of light at a given receiver location, also known as the beam-spread function (BSF).

The BSF, denoted as h, is represented through a Fourier-Bessel transform (Wells, 1969), where

$$h(r_\theta, r) = \frac{1}{2\pi} \int_0^\infty H_0(c, r) H_w(v, r) J_0(v r_\theta) v \, \mathrm{d}v \tag{5.3}$$

here r_θ is the radial distance, J_0 is zeroth order Bessel function and H is an amplitude transfer function, where the subscripts 0 and w represent the transmitter source and water respectively. The amplitude transfer function of water is given as (Wells, 1969)

$$H_w(v, r) = \exp\left[-cr + \int_0^r \mathrm{B}\Big(v \frac{r_\theta}{r}\Big) \, \mathrm{d}r_\theta \right] \tag{5.4}$$

where B is the Fourier-Bessel transform of the VSF, $\beta(\theta)$, whilst the amplitude transfer function of a transmitter source is found as the Fourier-Bessel transformation of the radial amplitude of light intensity which is typically Gaussian for laser diodes. This BSF-based modelling scheme has shown to be a good approximation so long as the transmitter FOV is less than 10° (Arnon et al., 2012).

Despite BSF modelling schemes omitting temporal dispersion, it is possible to postulate what it might be by including higher-order effects into the model. Instead of assuming all photons arrive at the receiver at the same time, as with the small-angle approximation, temporal spreading can be estimated statistically and included. Such was done in (Stotts, 1978) where the temporal dispersion, Δt, was estimated to be

$$\Delta t = \frac{r_\theta}{v}\left(\frac{3}{10br_\theta\theta^2}\left[\left(1+\frac{9}{4}br_\theta\theta^2\right)^{1.5}-1\right]-1\right) \tag{5.5}$$

recalling that θ is the azimuthal angle of the VSF.

More advanced approximate analytical models have estimated statistical distributions and values of different aspects of the RTE in eq. 5.2, including multi-path time, the direction vector $\mathbf{n}$ and the position vector $\mathbf{r}$. A survey of these statistical expressions is given in (McLean et al., 1998), though not in the context of underwater optical wireless communications.

5.2.3 Numerical Methods

As finding analytical solutions to the RTE in eq. 5.2 is generally a difficult task, numerical solutions are often preferred, especially in complex aquatic media such as those described in ch. 3. There are three popular numerical techniques for solving RTEs in oceanographic fields (Mobley et al., 1993); Monte Carlo, discrete ordinates and invariant imbedding. The primary differences between each of these schemes are the mathematical techniques implemented to solve the RTE, the treatment of boundary conditions at the water body surface and the resulting computational run time. A list of the advantages and disadvantages of each of these schemes is given in fig. 5.1, which was originally adapted from (Mobley et al., 2014).

The Monte Carlo technique is probabilistic; it finds a solution by sending a single photon at a time through a mathematically described medium. This is iterated over many millions, perhaps billions, of photons until an overall picture is formed of the spatial and temporal distribution of the source at a specified distance away from the transmitter. It relies on knowledge of the inherent optical properties and VSF. Complex media and geometries are easy to program into the model,

Numerical method	Description
Monte Carlo	Based on conceptually simple physics. Completely general; can solve time-dependent and 3D problems with arbitrary geometry. Easy to program. Computed radiances have statistical errors. Computer run times can be extremely slow for complex problems.
Discrete ordinates	Models the medium as a stack of homogeneous layers. Highly mathematical. Difficult to program. Does not handle highly peaked VSFs well. Fast for irradiance calculations and homogeneous water (though can be slow for radiances or if many layers are needed).
Invariant imbedding	Highly mathematical. Difficult to program. Can solve only 1D problems. Includes all orders of multiple scattering. Computed radiances do not have statistical errors. Is extremely fast (run times increase linearly with optical depth).

Table 5.1: Summary of advantages and disadvantages of different numerical methods for solving the RTE, adapted from (Mobley et al., 2014).

the only impact additional complexity has is on the computational run time. As this is the only statistical numerical approach, it is the only one which is prone to statistical errors in the predicted intensities, though these can be reduced by tracing more photons, at the expense of a higher run time.

Discrete ordinate models calculate a solution to the RTE by considering the medium as a stack of homogeneous layers. Layers are divided into a finite number of discrete solid angles and the RTE is solved for each of the solid angles individually. The following layer will use these solutions as boundary conditions for the next set of solutions. The main disadvantage of this method is that it is unable to handle highly-peaked VSFs (like those found in oceanic particulate matter) because of the size of solid angles compared to the region of interest.

Invariant imbedding is a numerical solution based on an analytical estimation. It effectively creates a model by converting the RTE, a two-point boundary value problem, into a regular differential equation with an initial condition. For this reason, it is only capable of solving one-dimensional problems.

5.2.4 Solution Comparison

For the purpose of this research, an appropriate RTE solution is sought from those mentioned in the previous section. As focus has been primarily on variability in the underlying optical properties and noise condition, an appropriate solution is one that is able to accurately implement a channel with variable properties. Particularly, the solution chosen must have the ability to model: attenuation changes with depth, first introduced in sec. 3.3.2; changes of refractive index with depth, mentioned in sec. 3.5; temporal changes, encapsulated by turbulence and daily or seasonal cycles; finally, changes to the background lighting condition from sec. 4.2. In the remainder of this section, the RTE solutions are tested against this specification, criterion at a time.

Varying Composition with Depth

In deep oceans, where the chlorophyll level is near zero, scattering is low and use of the BSF is acceptable because light that is re-scattered towards the receiver will be of low intensity compared to that of light directly received. However, towards the surface of the ocean, scattering and subsequent multi-path effects become very common, so it is important to calculate the temporal dispersion. The RTE and derived numerical solutions are all capable of doing so to a good degree of accuracy, although discrete ordinate methods will begin to fail in areas of extremely high chlorophyll level due to the VSF becoming highly-peaked.

For communication links that have a noticeable change in composition with depth, the inherent optical properties become a function of depth. Working out the power loss with the Beer-Lambert law is done by simply averaging the attenuation coefficient over the communications link, as was implemented in ch. 4; the BSF can also be calculated using averaged values. However, it is not known how accurate this is in comparison with considering a truly varying attenuation coefficient. Having said this, in the form of the RTE given in eq. 5.2, the RTE also does not take account of inherent property changes. If the inherent optical properties in this equation were written in vector form which depends on the position vector $\mathbf{r}$, it would be possible to include attenuation gradients into subsequent numerical models. In this case, Monte Carlo methods offer the best model due to its flexibility. For solutions using discrete ordinates, there will be substantial implications on the run time, as more layers are needed to accurately describe the gradually changing attenuation. In both cases, special consideration needs to be given to the link orientation, the VSF and RTE descriptions and subsequent solutions are better suited to links where the optical property variability is perpendicular to the direction of the beam, i.e. vertical underwater communication links.

Varying Refractive Index with Depth

Changes in the bulk refractive index of the aquatic medium are built into the description of the VSF. For this reason, all models are able to take a depth-varying refractive index into account. However, for communication links which are not perpendicular or in parallel with the changes in depth, modelling the directional impact of these refractive index gradients is not possible. This is because in the derivations of the VSF and RTE, inherent optical property changes are assumed to be over a single dimension only (the direction of photon travel). Links at other orientations underwater, on the other hand, have two simultaneously changing components.

It is noted that light transmitted at an angle through a gradually changing refractive index will slowly deviate from a straight line as it travels through multiple refractive index boundaries, possibly bending a communication link away from the expected receiver location. As the impact of this is potentially significant, depending on the extent of beam deviation, ray tracing methods are used later in this chapter (in sec. 5.4) to estimate the magnitude of the beam deviation under these conditions.

Temporal Variation

Temporal variation comprises of small-scale changes in the aquatic medium from turbulence and larger scale daily and seasonal changes. The latter may be modelled by simply inputting a new set of inherent optical properties describing the medium at a particular point in time. This is not limited to any particular model type.

As the most significant effect of turbulence for a communication system is temporal dispersion, the Beer-Lambert law and BSF are severely limited in their ability to describe a link passing through turbulent waters. In the RTE, turbulence can be modelled as a statistical distribution of scattering strength, vector directions and vector location, as hinted upon in sec. 2.5.5. Monte Carlo methods can readily implement this but the subsequent statistical errors are likely to be significant, considering a statistical solution is being formed from other statistical distributions. It is possible to use invariant imbedding or discrete ordinates, but this is extremely complex and has not yet been attempted by anyone researching underwater optical communications.

Variable Background Lighting Conditions

The contribution from sunlight and other underwater light sources can be modelled in two different ways for a communication system. The first way is as a source of noise, this can be added onto any of the RTE solutions at a later stage, as was done in sec. 4.6. Modelling background light as noise means only the power implications are taken into consideration, it provides no information of spatial or temporal distribution of the background light.

The second method is to consider solar and other background sources to be a secondary, indirect source with their own associated internal radiance. The RTE and subsequent numerical methods take this into account with the final term in eq. 5.2, though Monte Carlo approximations for downwelling irradiance have been noted to be particularly prone to errors (Mueller, 2000). Additionally, if dealing with direct vector RTE solutions, such as in (Jaruwatanadilok, 2008), these background sources are added to the incoherent part of the solution, which turns a usually first order differential equation into something much more difficult to solve. Considering background illumination as a secondary source can also be achieved through the BSF, where the contributions from two BSFs can simply be superimposed on a desired receiver location. The additional light in this case will be modelled as a spatial noise pattern.

Having now surveyed the different modelling schemes against the specification derived by the topics of this research, conclusions about the most suitable scheme may be drawn. Overall, numerical solutions to the RTE seen to provide the most versatility in their description of the

state of a light beam after being transmitted through a known medium by including temporal and spatial distributions of light. Of the three numerical schemes explored here, Monte Carlo was shown to be the most versatile, although it is compromised by slow run time and statistical errors, particularly in the presence of turbulence and downwelling irradiances. Other modelling schemes, such as the BSF and Beer-Lambert law, have shown to be suitable for communication links where temporal information is not required, such as in a long distance link in clear ocean where scattering is minimal. The benefit of using these schemes is their simplicity, however, as was highlighted in sec. 4.6, these schemes are somewhat limited in terms of their consideration for scattered light. For this reason, Monte Carlo methods are chosen as the appropriate advanced channel model for the purpose of this research on optical property variability.

5.3 Monte Carlo Simulations

Many Monte Carlo simulations describing photon transport in natural waters have been reported in oceanographic research, see (Mobley & Mobley, 1994) for examples, with only a handful currently in the context of underwater optical wireless communications. The number of optical communication-based models is further restricted if taking into consideration only LOS and direct links, as opposed to non-LOS (Jasman & Green, 2013) and highly scattered ultra-violet links (Kedar & Arnon, 2009). The remaining Monte Carlo simulations shall now be briefly surveyed in the context of this research.

Early underwater communications-based Monte Carlo simulations in (Hanson & Radic, 2008) were based around a changing frequency modulation and the effects this had on the SNR, rather than variations in the optical channel itself. It was found that at low frequency, increasing the FOV improves the SNR because scattered light does not adversely affect low frequency modulation. However, doing the same as high frequency reduces the SNR different due to temporal effects. It is noted here that temporal effects are more likely to be seen where there are higher particulate concentrations, such as inland and coastal waters or at the DCM. As a result, optical wireless communications underwater either fall into a minimal scattering or multiple scattering regime, dictating the link design. Indeed, subsequent Monte Carlo simulations and experimental confirmation in (Dalgleish et al., 2010) highlight this two-tier approach to underwater link configuration.

Later Monte Carlo simulations are more involved in aspects of the optical channel. For example, in (Gabriel et al., 2011), the authors investigate temporal dispersion over increasingly turbid channels. This study found that, except for highly turbid waters, time dispersion could be

neglected for moderate link distances. A similar conclusion was also made by the Monte Carlo investigation in (Cochenour et al., 2013).

The Monte Carlo simulations mentioned begin to form an understanding of how optical properties determine the link design for underwater optical communications, particularly in terms of their temporal response. However, critically, all of the studies mentioned are based on fixed underwater channels represented by a single attenuation coefficient. As of yet, no research has considered the variability of optical properties within the channel itself and certainly not within the context of advanced Monte Carlo simulations. One reason for this, perhaps, is the complexity behind creating such Monte Carlo simulation with variable underlying inherent optical properties. For this reason, this research investigates how this may be done and builds a foundation from which other researchers may begin to attempt these complex multi-layered Monte Carlo simulations.

One suitable solution for creating Monte Carlo simulations in a variable channel comes in the form of the Monte Carlo Mixed-Layer (MCML) simulation in (Wang et al., 1995). The MCML is a steady-state Monte Carlo model for multi-layered turbid media, based on an infinitely narrow photon beam as the light source. Each layer has its own optical properties including absorption, scattering (and back scattering), anisotropy, which will be introduced shortly, and refractive index. The simulation is three-dimensional, with results stored in an (r_θ, z) array in cylindrical coordinates, representing radial and depth positions. Outputs of the MCML include the radial position and angular dependence of local reflectance and transmittance, in addition to the internal distribution of energy lost to the multi-layered medium. Of particular use for this initial communication-based MCML research is the ability to estimate an overall transmittance of a path to find its reciprocal, the generalised beam attenuation.

The generalised beam attenuation characterises the effective average beam attenuation over an entire LOS link in exact alignment. This differs from the mean beam attenuation coefficient which was calculated in the latter half of ch. 4 as it summarises the energy lost over the entire path, instead of averaging the depth-dependent attenuation changes and expecting no energy implications. As mentioned above, a pre-compiled code enclosed in (Wang et al., 1995) calculates this generalised beam attenuation through the MCML using the following inputs:

- Refractive index, this is taken as a constant with a value of 1.344 (Austin & Halikas, 1976). It is recognised that in actuality the refractive index changes throughout aquatic media, and particularly with ocean depth. However, with no matching refractive data for the depth-dependent profiles, it is better to assume this as a constant.

- Absorption and scattering coefficients, these are found from the adapted Haltrin model in eq. 3.6 to eq. 3.9, from sec. 3.3.2.
- Backscattering ratio, characterised by the Henyey-Greenstein coefficient g, from app. C.
- Anisotropy, also known as the Q factor, is expressed as the ratio of E_u/L_u. Chlorophyll concentration and depth-dependent estimations of this Q factor in the ocean can be found in (Morel et al., 2002), where the value generally lies between 3.8 and 6 in the range of interest.

For this research, the above-mentioned pre-compiled code and inputs have been used to determine a series of generalised beam attenuations for underwater channels with depth-dependent variations. The results obtained for these pre-tests indicated the validity of the MCML model; the generalised attenuation coefficient obtained were similar in value to the average attenuation coefficients. Subsequently, this thesis encloses an exemplary investigation using the MCML.

In the exemplary investigation, the optical communication channels chosen are the same as those used in fig. 3.12, where there are several 100 metre long links transmitted vertically down the column of S1, S3 and S6 oceanic waters, with starting depths of 0, 50 and 100 metres. These were chosen because average values of the attenuation coefficient have already been calculated, as seen in app. G. However, in the MCML case, only the wavelength at which the minimum attenuation occurred will be considered due to the time taken to form the MCML layer inputs.

The MCML generalised attenuation results determined by the MCML pre-compiled code are shown in tab. 5.2. These results show that the MCML-generated beam attenuation is always lower than the value averaged over the same link depth range, the cause of this being the additional re-scattered light term which is present in the RTE in eq. 5.2. The term in the RTE lowers the overall path attenuation by taking into consideration light that had previously been lost after a single scattering event. This is particularly apparent when considering the turbidity of each of the locations in tab. 5.2; in the clear 100 to 200 metre depth link in the S6 profile, the difference between the attenuation coefficients is less than 3%, whilst the most turbid location, the upper region of S6 profile, there is around a 16% difference. Turbid areas with high levels of scattering also have greater amounts of re-scattering light, leading to a more noticeable difference between the mean and MCML attenuation coefficients.

Having seen how the MCML attenuation outputs match up with mean attenuations for a given path, these results are assessed for how accurately they reflect real underwater communication channels. Recalling that inputs of the MCML model investigated here are based on the depth-

	Link range (m)	Wavelength (nm)	Mean c (m^{-1})	MCML c (m^{-1})
	0 - 100	410	0.050011	0.048491
S1	50 - 150	410	0.070626	0.067069
	100 - 200	410	0.061670	0.059820
	0 - 100	490	0.089060	0.081115
S3	50 - 150	490	0.089824	0.081329
	100 - 200	410	0.059353	0.057370
	0 - 100	500	0.131473	0.113327
S6	50 - 150	490	0.081474	0.0748033
	100 - 200	410	0.042341	0.04149418

Table 5.2: Mean attenuation and generalised attenuation from the MCML simulation for vertical 100 metre optical links in the S1, S3 and S6 chlorophyll concentration profiles. Only the optimal wavelengths from app. G are included.

dependent Haltrin model which underestimates attenuation at wavelengths below 470 nm (fig. 3.5), it is expected that these values, although lower than the calculated mean attenuations, are actually an underestimation. However, the extent of this can only be known with validating experimental data. Moreover, at this time, the MCML channel results obtained cannot be used to generate solutions for underwater optical communication systems further than the AWGN models of ch. 4. Significant work is needed to derive a method of convolving a laser (or LED) with the channel in order to find communication performance measures such as the SNR and BER. Therefore, it is suggested that this topic be the main focus of research for those looking to continue research on channel variability in underwater optical wireless communications.

5.4 Refractive Gradient Modelling

In the model assessment of sec. 5.2.4, it was recognised that Monte Carlo simulations could not be used to estimate the effect of large-scale refractive gradients on beam directionality, specifically for links that are neither perpendicular nor parallel to the aquatic media surface. At these orientations, it is possible that the general direction of beams transmitted underwater change as they undergo multiple refractions, through many refractive interfaces. These refractive interfaces arise due to the natural variation in the bulk refractive index of the aquatic medium as it changes with depth,

as was briefly surveyed in sec. 3.5. An equivalent refractive beam divergence is already observed in satellite laser communications, where the atmospheric refractivity gradient means significant PAT correction has to be employed (Abshire & Gardner, 1985). This section considers the extent of the refractive effect for mid-ranged underwater optical communication links. In doing so, it will be determined whether similar correctional techniques must be employed underwater.

Fig. 5.1 introduces the geometry of two underwater optical wireless communication links for the purpose of this investigation. The first path, $\tilde{\mathbf{r}}$, between the transmitter and the expected receiver location $\tilde{R}$ assumes that the refractive index of seawater remains constant throughout the optical link, thus no refraction occurs. On the other hand, path $\mathbf{r}$ takes into account refractive differences, leading to a change in direction from that of path $\tilde{\mathbf{r}}$ and therefore is not received at the expected location. Angle compensation could be employed to counter this; it works by simply changing the transmission angle θ until $\mathbf{r}$ reaches $\tilde{R}$. However, first it is necessary to calculate the extent of divergence caused by the refractive index changes, ensuring compensatory methods are required at all.

There are two techniques for exploring the amount of refraction, namely either by plotting both transmission paths and observing the changes in shape or by calculating the difference in end-point locations for two communication links of equal length, from the refracted and non-refracted paths respectively. The latter technique has been chosen for this study as refractive path changes are

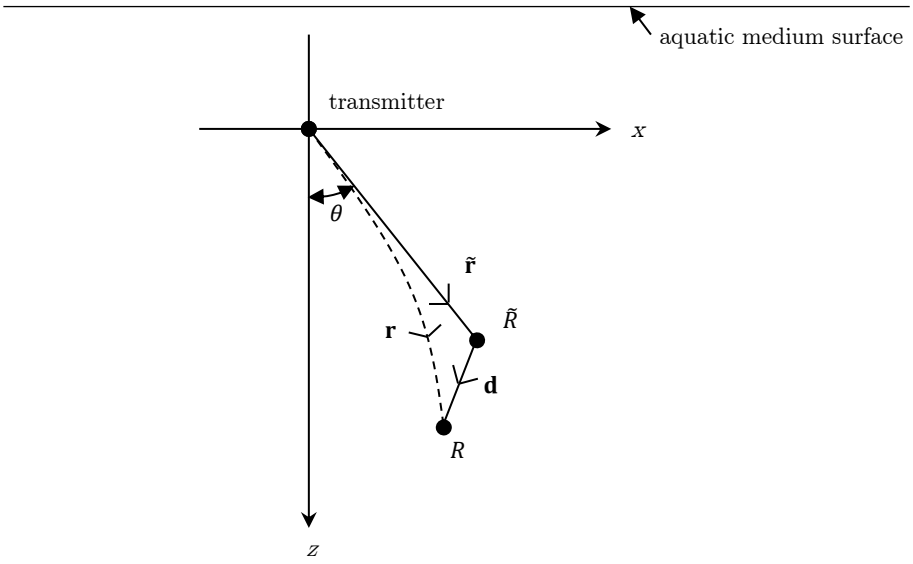

Figure 5.1: Geometry of an underwater communications link, where $\mathbf{r}$ is the path transmitted through a refractive gradient and $\tilde{\mathbf{r}}$ is the same length but with no refractive gradient. Also, $\mathbf{d}$ is the displacement between the two respective receiver points R and $\tilde{R}$.

likely to be small underwater; the natural range of refractive indices and link length of underwater optical communications is several magnitudes lower than experienced in satellite communication links (Austin & Halikas, 1976). The difference, $\mathbf{d}$, between the two end points is found as

$$\mathbf{d} = \mathbf{r} - \tilde{\mathbf{r}} \tag{5.6}$$

Note that $\mathbf{r}$ is the position vector of points on the transmitted beam and therefore can be written in terms of its x, y and z vector components, some of which are shown in fig. 5.1.

In order to calculate the displacement between the end points, the two communication paths, $\mathbf{r}$ and $\tilde{\mathbf{r}}$, must be determined. The unrefracted path is straightforward since it is a straight line whose length depends on the angle and the distance travelled, which will be set to a constant. To find the refracted path, the ray trace equation eq. 5.7 must be solved.

$$\frac{\mathrm{d}}{\mathrm{d}s}\left[n(\mathbf{r})\,\frac{\mathrm{d}\mathbf{r}}{\mathrm{d}s}\right] = \nabla\, n(\mathbf{r}) \tag{5.7}$$

where $n(\mathbf{r})$ is the refractive index distribution along the beam path. This distribution has not been characterised algebraically by any previous studies due to high variability throughout underwater environments. However, a means of calculating it was provided in sec. 3.5, where a real example of refractive index changes with depth was given for the Pacific Ocean in fig. 3.14. Using this Pacific Ocean example, it is possible to solve equation the ray equation in eq. 5.7 to determine the difference in end point locations for the refracted and non-refracted communication links. In order to simplify the Pacific Ocean data for use in a ray tracing algorithm, the refractive profile is estimated using a tenth-order polynomial for depths between 50 and 250 metres, where the transmitter is set at a depth of 50 metres to avoid the complex refractive behaviour above this region. The communication link length is chosen to be 200 metres for initial investigations since refractive beam path divergence should only be noticeable in longer length communication links and this is currently the maximum demonstrated link length (Farr et al., 2010).

The ray equation solution chosen for this research is numerical; it works by transforming the ray equation into a more convenient form which is solved numerically by employing Runge-Kutta techniques (Sharma et al., 1982). Note that, for initial calculations, a point light source is assumed, more complex sources are addressed later in this section. Solutions for the Pacific Ocean location were generated for a range of wavelengths and transmission angles and the results for the horizontal and depth components of displacement $\mathbf{d}$ between the end points R and $\tilde{R}$ are shown in fig. 5.2.

The estimated sizes of the displacements in this figure remain small, under 0.23 metres, especially when compared to the link length. However, these displacements may still be significant depending on the width of the transmitted beam in the communication system.

Fig. 5.2a shows how transmission angle changes the displacement between the expected receiver location and the true refracted path. Beams transmitted at angles near the vertical axis generally have greater displacements as they experience a higher change in refractive index. In addition, the depth displacement component has a tendency to be greater than the horizontal displacement, other than at shallow angles. It is though this is because the refractive change is in this component. In fig. 5.2b, it can be seen that by increasing the wavelength, the displacement becomes greater. This is because a greater wavelength means a higher refractive index, as shown previously in sec. 3.5. It should be noted that the minimum wavelength modelled here is restricted to 500 nm because of limitations in the ray tracing method.

Using the same ray tracing algorithm, this time with a 100 metre link, the overall magnitude of displacement with transmission angle is investigated. The magnitude of displacement between R and $\tilde{R}$ is calculated over a 180° transmission angles range for every 5° increment, again for the Pacific Ocean depth-dependent refractive gradient. The result is plotted in fig. 5.3. As expected, the relationship is symmetrical about 90° because both directions are subjected to the same refractive changes with depth. In this communication link set up, the size of the displacement starts at 0 metres at 0° and 180°, where it is assumed horizontal links are subjected to negligible changes in refractive index. As the transmission angle becomes closer to 90°, the displacement becomes larger as the communication beam is transmitted through a greater refractive index change, peaking at 0.14 metre displacement. However, displacements at this extreme, at 90° exactly, are not important because the beam remains in the line of communication. In fact, the size and FOV if the receiver can, at least in part, account for misalignment when the optical link is transmitted approximately vertically.

The relationships in fig. 5.2 and fig. 5.3 are typical of mid- to long-ranged links in open ocean, where the displacement never seems to exceed more than about 0.3 metres for wavelengths in the visible region, regardless of refractive profile. To put this displacement into context, in order to determine if angle correction techniques are required underwater, the beam divergence transmitter source is taken into account. To do this, the same Pacific Ocean refractive gradient from sec. 3.5 is considered, except this time the source is a narrow-beam laser instead of a point. By comparing the range of locations of the light from the source beyond a 200 metre link against the original end-point displacement for an ideal source, it may be deduced whether refraction compensation

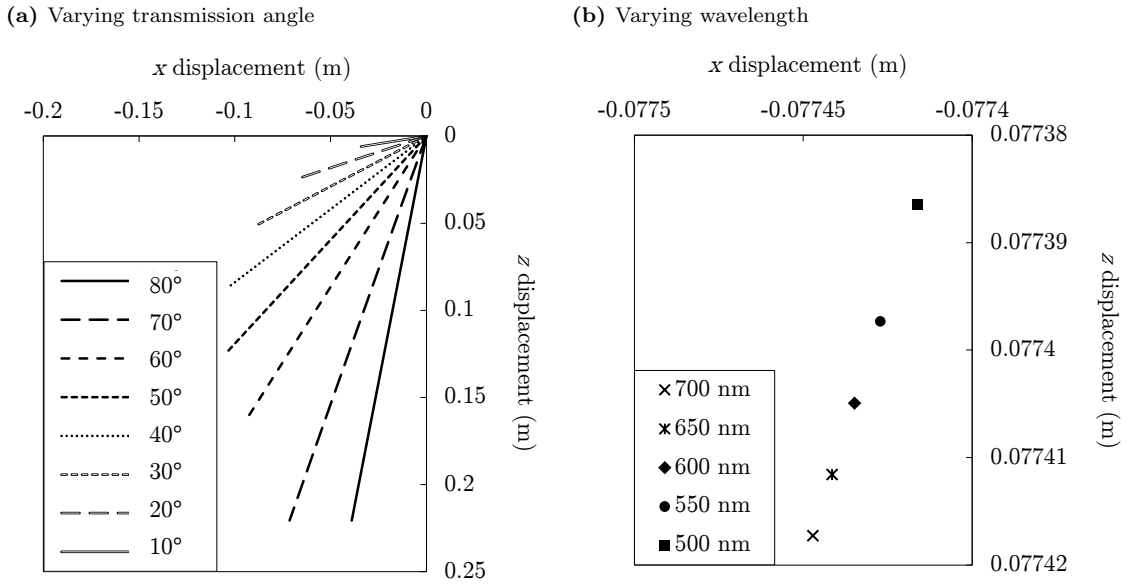

Figure 5.2: Displacement (x and z components thereof) between a regular 200 metre optical wireless link transmitted at an angle θ and one with a depth-varying refractive index gradient, where in (a) the angle of transmission is varied and wavelength fixed to 500 nm, and (b) the angle is fixed to 45° and wavelength varied.

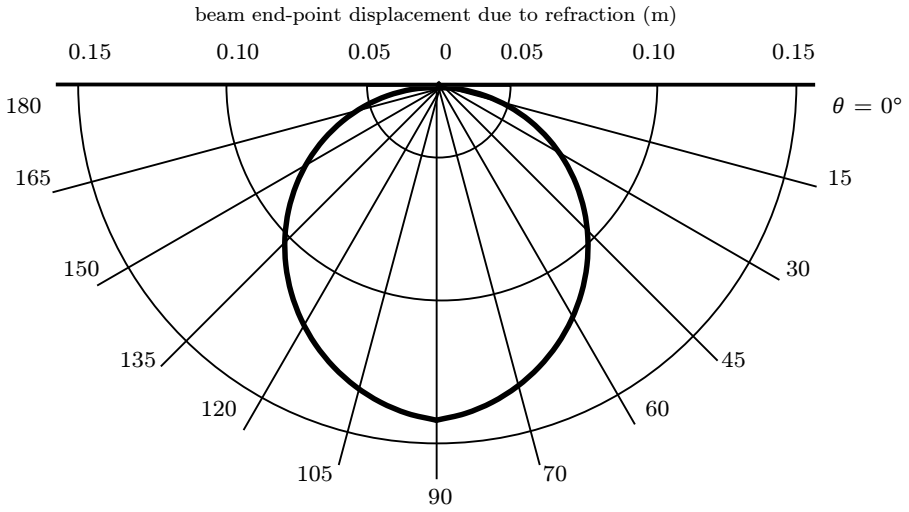

Figure 5.3: Magnitude of displacement with varying orientation between a regular 100 metre optical wireless link transmitted and one with a depth-varying refractive index gradient.

techniques are required underwater.

The laser assumed for this example has a full-angle beam divergence of 1 mrad, or 0.057°, representing the current minimum FOV for commercially available blue/green wavelength, with a uniform distribution to aid simplicity. Solving the ray equation for this source, with the transmission angle set to 15°, 30°, 45°, 60° and 75° respectively, yields fig. 5.4a to fig. 5.4e. After a 200 metre link, the original beam becomes approximately 0.2 metres wide (0.1 metre either side of the original path) thus any link transmitted at an angle above 20° should be outside of the non-refracted path. In practice this angle is slightly smaller as the extreme ends of the beam undergo different refractions due to the angular separation between them; in fig. 5.4a the unrefracted path is shown to lie just outside of the refracted source at 15°. Fig. 5.4 also shows that as the transmission angle increases towards the horizontal, the displacement becomes larger, in agreement with the point source investigation.

Although the narrow-angle beam appears to miss the expected location, what unfortunately cannot be taken into account in these models is the effect of scattering and how that might spread the beam beyond the beam-width modelled here, in order to reach the receiver. Additionally, it is not known how non-uniform beams would impact. It is likely, if both these points are taken into account, that most optical wireless links would be received at the non-refracted receiver location, the issue instead becomes the energy penalty from the pointing error. For example, a 0.5° beam divergence would be over 1.7 metres wide after a 200 metre link, much greater than typical displacements of 0.3 metres, but the power received would be much less. The consequence of this behaviour means it is unlikely that long distance optical wireless communications transmitted at angles near the horizontal will need to have some sort of pointing correction above and beyond standard PAT techniques.

5.5 Summary

A survey of advanced channel modelling schemes has been presented for the underwater optical channel, with reference to variable attenuation, refractive index and background lighting sources. Numerical solutions of the RTE provide the best description of the state of a light beam further along the channel by including temporal and spatial distributions of light. Whilst Monte Carlo in particular provides a versatile methodology, albeit compromised by slow run time and statistical errors. Preliminary results using a multi-layered Monte Carlo scheme found that estimates of overall beam attenuation for a channel with variable attenuation along the beam path are generally

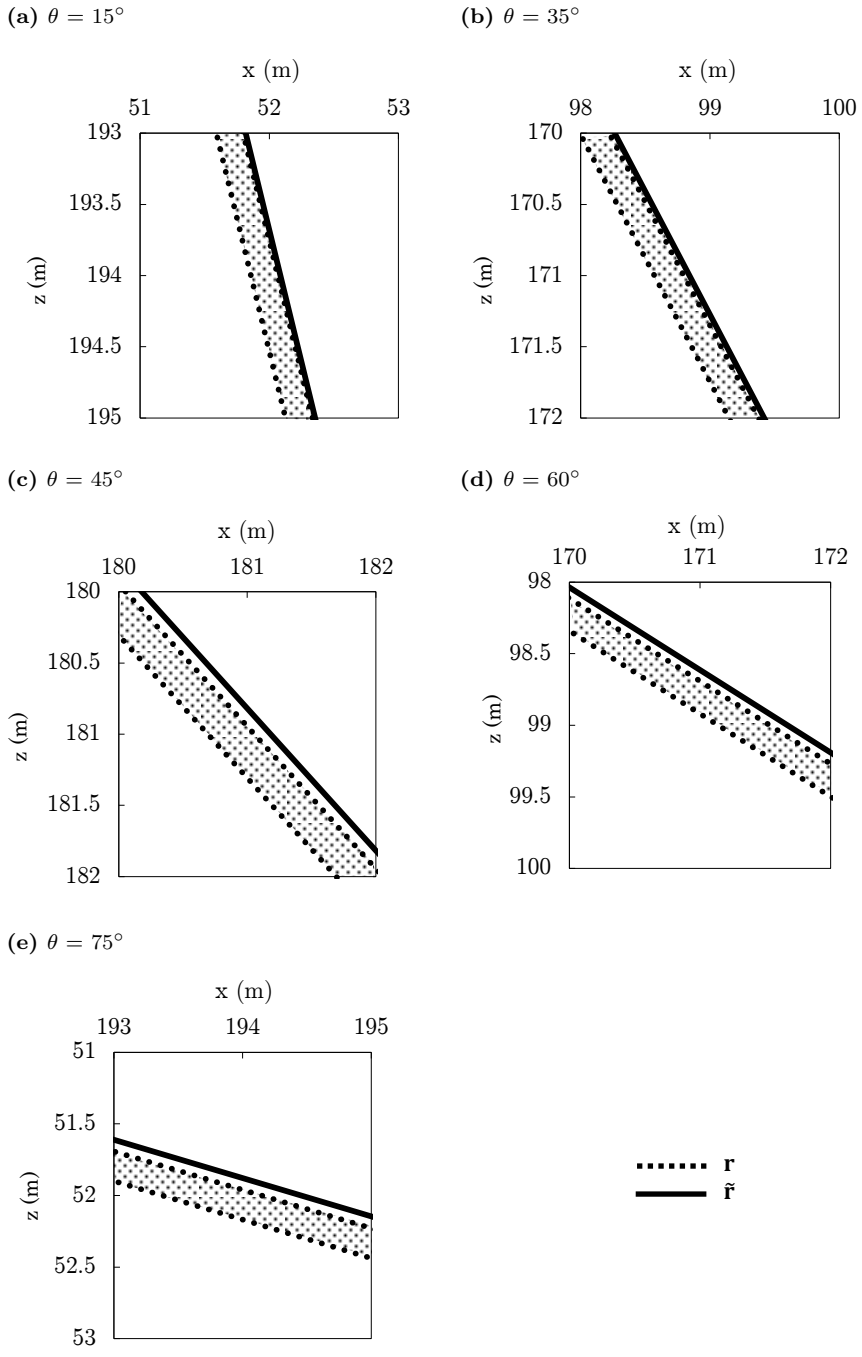

Figure 5.4: Comparing the position of the unrefracted beam against the geometrical extreme of refracted path r for a narrow-beam laser (0.057° full angle beam divergence), for link lengths 200 metres at the transmitted angles between 15° and 75°.

lower than those found by simply averaging over the path. This difference is attributed to an additional term in the underlying model which reintroduces photons previously scattered away; in areas of high scattering, this difference is seen to increase.

In addition, this section attempted to model the beam path divergence effect of refractive index changes with depth. After a 200 metre link, the separation between the expected and actual receiver location were not seen to go beyond 0.3 metres. It is thought that the natural beam-width of the transmitter, combined with the FOV and size of the receiver, in addition to the beam widening through scattering, are likely to compensate for this without the need for additional PAT techniques.

Chapter 6

Practical Underwater Systems

This chapter serves a dual-purpose, the first being to consolidate results presented in the previous chapters of this thesis. To do this, a comprehensive list of experimental demonstrations in underwater optical wireless is formed and used as the basis of a comparison.

The second aim of this chapter is the development and execution of a meaningful practical experiment that aids understanding of optical property variability in natural waters and its impact on underwater optical communication links. By doing so, practical communication system issues surrounding variable underwater optical properties are assessed.

6.1 Previous Experimental Studies

Since the 1990s, there have been numerous practical investigations into the performance of underwater optical wireless communication systems. A summary of these studies, along with notes on their link length, data rate, channel turbidity and transmission technology, is given in app. I. This section offers a discussion of the merits and drawbacks of each experimental set up with respect to the results obtained in this thesis; studies are categorised by their authoring research group.

Woods Hole Oceanographic Institute, USA

Underwater optical wireless links demonstrated by Woods Hole Oceanographic Institute commonly aim to demonstrate long-ranged links, in low-turbidity environments, with data rates in the Mb range. Such communication links offer the most direct comparison with the variable depth-dependent optical transmission described throughout this thesis.

In (Farr et al., 2006), a 10 Mb s^{-1} link was reported spanning 91 metres in clear water using a six blue-green LED transmitter array and a PMT at the receiver. By switching the LED array to a single 470 nm LD, and implementing a spherical concentrator around the PMT, an extended link length of 200 metres was established, though at a lower data rate of 5 Mb s^{-1} (Pontbriand et al., 2008). This is currently the maximum underwater optical wireless link length demonstrated. Later research, again opting for the blue-green LED array, described an optical telemetry system which reported a data rate of 10 Mb s^{-1} at a distance of 108 metres, and 1 Mb s^{-1} for 128 metres (Farr et al., 2010). Here the optical link was paired with acoustic PAT technology; this system would later become commercially available under the name Bluecomm (Sonardyne, 2014).

In the open ocean tests of the experimental set ups described above, each communication link was established as a vertical link far down the water column, thereby indirectly involving channel variability. For this reason, applications for such links are sought nearer the ocean bed than the sea surface (Camilli et al., 2010). In the respective studies, it is not mentioned whether the tests were conducted in daylight, but it is thought that it may be irrelevant as the links were probably positioned below the photic zone. If this is the case, it is also expected that the optical links were tested below the DCM and, as a consequence, the transmitter wavelength selected would be sub-optimal. As shown in sec. 4.3, the ideal wavelength should be closer to 410 nm – or in some cases 490 nm, where the DCM occurs lower down the water column – selecting other wavelengths increases the overall attenuation coefficient, maybe even significantly.

For example, if it is assumed that the vertical link in question is transmitted far down the water column of a section of open ocean water (S1 chlorophyll profile), then the average attenuation at 470 nm would be 0.0313 m^{-1}, whereas it would be 0.0243 m^{-1}, for a wavelength of 410 nm. Using the Beer-Lambert law relation, a transmitter using the latter wavelength of 410 nm and undergoing the same losses as the 200 metre link described by Pontbriant et al. would propagate an estimated 257.6 metres. That is 57.6 metres further than with the 470 nm source used in the study. Hence, the importance of selecting an appropriate wavelength is emphasised.

North Carolina State University, USA

In contrast to the research by Woods Hole Oceanographic Institute are the lightweight, low-power practical underwater optical communication systems developed by North Carolina State University. Their research is mainly concerned with the performance and suitability of a number of modulation and coding schemes for a variety of underwater optical channels. All tests were conducted in water tanks, up to a maximum range 7.7 metres, with turbidity varied by the addition of Maalox Antacid.

The earliest practical study undertaken at North Carolina State University was based on an existing free-space optical communication implementation but used an optically unique transmitter design to create a directable incoherent beam from a single 1 W LED (Chancey, 2005). Several transmitter wavelengths were tested; 475 nm, 505 nm and 525 nm. All wavelengths achieved a data rate of 10 Mb s^{-1} for the length of the water tank, 4.6 metres, where the author extrapolates the potential link distance to be 16 metres. This LED-based transmission was later revisited for two studies on coding schemes, (Simpson et al., 2010) and (Simpson et al., 2012). In the former study, Reed-Solomon (RS) code was implemented to achieve an SNR improvement of 4 - 6 dB for a 5 Mb s^{-1} link in two different optical channels; a turbid 3 metre link with a 0.5 m^{-1} attenuation coefficient and a 7.7 metre link at 0.25 m^{-1}. The latter study compared RS coding, turbo coding, and a low-density parity-check (LDPC), in extreme turbidity – up to a 9 m^{-1} attenuation coefficient – as well as decreased the alignment sensitivity through a unique hexagonal pyramid array for transmitting and receiving components.

The links described in the above LED-based studies appear to have clear practical applications; smaller platforms with compact systems that do not have the volume or energy budget for sophisticated PAT techniques. The practical optical channels described tend to suggest that these platforms are more likely to be used in turbid environments, near the shore or in inland waters, a notion which is supported by the selected transmission wavelengths. In these shorter ranged links, the optical property variability is negligible, at least as far as the models

introduced by this thesis are concerned, though variability in the ambient lighting conditions will be more noticeable.

North Carolina State University also conducted a number of practical studies based on 405 - 410 nm LDs. The first study using this transmission source received signals using a PMT in conjunction with a variable gain amplifier to throughput a 1 Mb s^{-1} data rate (Cox, 2008). Using the same set up but with a computer for post-processing, this optical link achieved a 0.5 BER at 6.5 dB SNR, 10^{-1} at 8.5 dB, 10^{-2} at 12 dB, 10^{-3} at 16 dB and 10^{-4} at 19 dB (Cox et al., 2008). Interestingly, SNR variations were simulated by changing the overall turbidity of the tank meaning that, even though the link was only 3.66 metres in length, the experiment depicted the equivalent losses of a medium-range link in an open ocean channel. Having said this, it still does not account for the optical property variability of real aquatic environments. A step was taken in a subsequent study to better model realistic environments through the inclusion of turbulence by means of bubbles injected onto the beam path (Simpson et al., 2009). In this case, performance was increased through spatial diversity, where the implementation of a two-transmitter and two-receiver design reduced errors by a factor of 10.

Massachusetts Institute of Technology, USA

In balance to studies mentioned thus far, practical Massachusetts Institute of Technology research is based around the development of a medium-range (around 50 metres) optical modem system coined AquaOptical (Doniec et al., 2009) and its successor AquaOptical II (Doniec & Rus, 2010). Early versions of the AquaOptical system were based on transmission from a single 470 or 532 nm LED (Doniec et al., 2009), where it was later extended to an array of six LEDs. In a test pool, the latter achieved a 30 metre link at 1.2 Mb s^{-1}; however, its performance dramatically decreased in harbour tests, where a data rate of 600 kb s^{-1} was maintained for only 7 metres. It is possible that such a drop in performance is, in part, the result of an inappropriate wavelength selection, and that transmission over a longer distance may have been possible if transmitting at a wavelength closer to 600 nm. It should be noted that at this range, the depth-dependent variability of optical properties from the Haltrin-based models can be ignored.

AquaOptical II relaxed the alignment condition of AquaOptical through the use of an 18 LED array with a total transmitted power of 20 W; the losses caused by a 15° pointing alignment error were measured to be only 1.8 dB for link lengths between 10 and 50 metres in a test pool (Doniec & Rus, 2010). A subsequent study found the system capable of up to 8 Mb s^{-1} for a range of 50 metres, again in extremely clear conditions (Doniec et al., 2013).

University of Genoa, Italy

The research group at the University of Genoa devised a similarly omnidirectional transmitter, with 12 blue LEDs arranged in a circle, each with an optical power of 15 - 20 mW (Anguita et al., 2009) (Anguita et al., 2010). A further transmitter comprising of 18 LEDs was proposed in the shape of a octahedron (Anguita et al., 2011). The receiver consisted of APD with an area of 1 mm^2 and an amplifier with automatic gain control. Using 4-PPM and 16-PPM, a data rate of 100 kb s^{-1} was reported to clear a distance of 1.8 metres in a test tank of low water turbidity.

Cooperation in Science and Technology, Europe

A Cooperation in Science and Technology (COST) action to increase understanding in optical wireless communications led a number of European research institutes to investigate underwater optical wireless (COST, 2011). Of those, several undertook experimental studies, with familiar omnidirectional, multi-LED optical links demonstrated in by (Destrez et al., 2012) and (Cossu et al., 2013). The latter of these two demonstrated the highest data rate for an LED based system, establishing a 58 Mb s^{-1} link over 2 metres of a test tank in ambient sunlight.

Whilst the study in (Rosenkrantz & Arnon, 2014) did not establish a communication system, the transmission of five 3 W LEDs of different wavelength was investigated in a highly turbid harbour. Significantly, measurements for this were taken as the transmitter, which comprised of five individual, uniquely coloured LEDs, was lowered into the natural harbour water. As a consequence, these results take account of depth variations in the attenuation coefficient; the brightest source after a distance of 17 metres was noted to be the red 635 nm LED, coinciding with what this study expects for a highly turbid environment (specifically, wavelengths > 560 nm).

Defence and Military Sectors, Worldwide

A small group based at the Naval Air Warfare Centre, USA, extensively explored the impact of high water turbidity on underwater optical wireless links. However, as with other studies, the turbidity was generated by the addition of Maalox Antacid; in sec. 2.5 additional factors were explained, such as ocean turbulence, which mean there can be significant differences between the scattering observed in closed experiments and from real ocean data. A data rate of 1 Mb s^{-1} was reported in a pure water and Maalox solution that had an attenuation coefficient 3.0 m^{-1}, representing a turbid coastal harbour (Cochenour et al., 2006). This data rate was improved a year later to 5 Mb s^{-1} by use of QAM (Cochenour et al., 2007). QAM is a suitable choice of modulation scheme due to the likelihood of temporal dispersion reducing the effectiveness of schemes such as PPM.

Subsequent studies using a 532 nm LD transmitter and PMT at the receiver looked to characterise different aspects of the turbid underwater channel: first was an experimental confirmation of the BSF models introduced in sec. 5.2.2 (Cochenour et al., 2009); following was an exploration of non-LOS channels (Cochenour & Mullen, 2011); finally, measurements were observed of the temporal dispersion in highly turbid media (Cochenour, 2013).

It is expected that other defence bodies have an active interest in underwater optical wireless but knowledge of these studies and their results is outside the public domain.

Commercial, Worldwide

Ambalux Corporation designed and manufactures an optical modem with a maximum data rate of 10 Mb s^{-1} with transmission distances of up to 40 metres claimed (Ambalux Corporation, 2012). This is a high power system requiring power to be provided externally, where the transmitter consumes 36 W; the receiver, 7.2 W. In (Baiden et al., 2009), the Ambalux Corporation modem was used to perform two tests; one in an inland lake and another in a testing pool. In the former, a data rate of 9.69 Mb s^{-1} was achieved over a distance of 11 metres. In the pool, this distance increased to 21 metres. Although, at this range, optical property variability can begin to matter, it should be noted that this optical modem was not designed for depths greater than approximately 60 metres, as pressure below this depth becomes too great for the vessel and window. As a consequence, depth-dependent attenuation variability is unlikely to be an issue for this modem in open ocean environments.

The commercial system that was developed from Woods Hole Oceanographic Institute technology, Bluecomm (Sonardyne, 2014), was tested in (Fasham & Dunn, 2015). The manufacturer claims a 20 Mb s^{-1} data rate is possible at a transmission length of 100 metres; the study reported that this link had successfully been established in open ocean waters, possibly far down the water column, although this information was not reported.

Other, Worldwide

With reference to app. I, it is apparent that there are many practical studies of underwater optical wireless that are yet to be reviewed, particularly with regards to studies in the period before the year 2005 and after 2013. Here, achievements of interest to this research are highlighted.

The earliest experimental studies in underwater optical wireless communications used highly specialised, high-cost, high-powered equipment, such as in (Snow et al., 1992) and (Bales & Chrissostomidis, 1995), where both set ups achieved data rates within the metabyte range. Such

data rates would not be surpassed until 2008, where a 1 Gb s^{-1} link was established over a 2 metre water filled pipe (Hanson & Radic, 2008). This link adopted a 7 mW, 532 nm LD transmitter along with an APD at the receiver. Similar performance was obtained in a more recent study, where a 405 nm LD was used in conjunction with a 16-QAM IM/DD-OFDM modulation scheme (Mizukoshi et al., 2014). The results in this thesis suggests the combination of the wavelength and modulation scheme selected in this link are counterintuitive; 405 nm is an ideal wavelength for an open ocean channel with very little turbidity, yet QAM and OFDM are typically associated with turbid locations exhibiting some extent of temporal dispersion. It is thought this combination could have been implemented in order just to maximise the potential data rate. This idea is supported by a subsequent transmission using the same optical link but modulated with 16-QAM IM/DD-OFDM which achieved the current maximum data rate of 4.8 Gb s^{-1} maintained over a distance of 5.4 metres (Oubei et al., 2015).

An alternative branch of experimental configuration considered portable, low-cost systems which were triggered by the advance of infra-red data association (IrDA) standards for infrared communications in air. In one study, the IrDA physical layer was adapted for underwater environments and achieved 14.4 kb s^{-1} over 2.7 m (Tivey et al., 2000). The transmitter consisted of 22 LEDs and used a transceiver of dimensions 5 cm by 10 cm; a system which was considered to be too large with too poor a data rate (Schill et al., 2004). This system had a wide-angle FOV of 120°, making system alignment trivial and removing the need for PAT techniques. A smaller transceiver was designed in (Tian et al., 2013) which showed to be capable of transmitting over 25 metres of pure water at 38.4 kb s^{-1}. In general, these low-cost, portable optical communication systems do not transmit far enough to be impacted by depth-dependent optical property variability, at least in the turbidity range assessed by this research.

6.2 Analysis of Previous Studies

Having briefly surveyed the experimental studies of underwater optical wireless in sec. 6.1 this section looks to analyse link performance and component selection *en masse*. By doing this, general comments will be drawn about results obtained in previous chapters of this thesis, as well as provide motivation for a subsequent optical property variability experiment.

To begin, performance characteristics for the optical communication links are reviewed. In sec. 4.6 the *attenuation-bit rate-length* and *attenuation-length* products were said to be a useful measure for determining the performance of an underwater optical wireless link. Calculating

the latter of these products for the studies in app. I where sufficient information is given, and plotting this against the maximum data rate established, yields fig. 6.1. This figure shows that the majority of studies are within the Mb data rate range; moreover, only links within this range have propagated through adverse media or over larger distances. Links devised either side of this peak in attenuation-length product exist either as super portable technologies or data rates orders of magnitude greater. This is likely due to limitations in existing technology and understanding of the media.

From fig. 6.1, the joint highest attenuation-length product estimated was 12, coming from two studies transmitting 100 metres in clear water, (Camilli et al., 2010) and (Fasham & Dunn, 2015). Both these studies are actually the same underlying Woods Hole Oceanographic Institute, or Bluecomm, design comprising of a directed array of 470 nm LEDs. The second highest attenuation-length product is 9.15 and comes in the form of a highly attenuating (2.5 m^{-1} attenuation coefficient) short range (3.66 metres) link (Cox et al., 2008). Using simple channel models, the SNR penalty of the links described would be similar, when high turbidity is a substitute for greater link lengths. However, in ch. 5, high turbidity media were found to have secondary impacts such as temporal dispersion and multiple-scattering, thus reducing the analogousness between distance and turbidity. This is important to consider in subsequent experimental designs where devising a link with a high attenuation-length product would be desirable.

Following on from the performance analysis, the component selection in previous experimental studies is now assessed. As this research is involved primarily in optimisation of the transmitter source wavelength through an understanding of the underlying channel, the assessment will be limited to this aspect. The transmitter wavelengths selected for use in practical underwater optical wireless demonstrations, in addition to their number of occurrences, are detailed in fig. 6.2. This figure shows that, in general, wavelengths between 400 and 550 nm are most often implemented, representing the blue/green part of the visible spectrum. This may be due to a blanket application of wavelengths which are commonly believed to be optimum based on the absorption spectrum of pure water in fig. 1.1. However, as was shown in sec. 4.3, variable attenuation modelling results found ideal wavelengths to fall into discrete groups – 410 nm, 490 - 500 nm, 540 nm and > 560 nm – regardless of location and orientation. Consequentially, studies with wavelengths lying outside of these discrete groups have a reduced performance. Furthermore, by observing the information presented in app. I, it appears that source wavelength selection within the recommended groups is haphazard, with transmitter wavelength corresponding to the medium turbidity in very few cases;

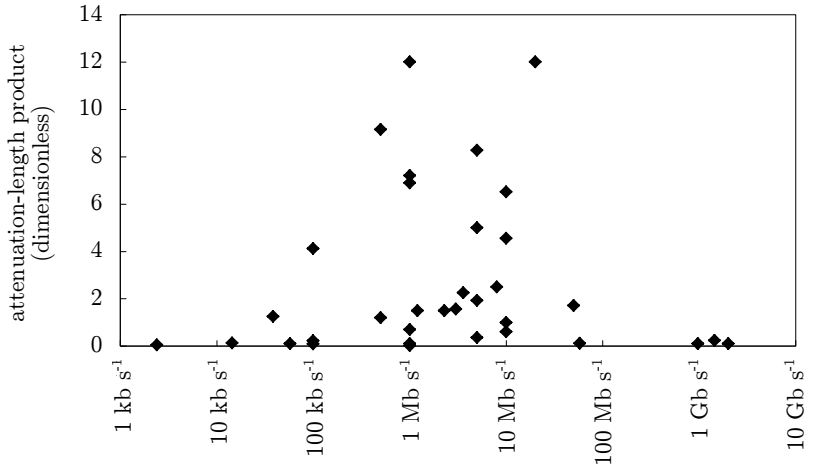

Figure 6.1: Attenuation-length product versus data rate achieved in experimental studies of underwater optical wireless communications, from app. I. Each study is represented by a single dot based on best performance. Where attenuation has not been stated, the attenuation coefficient of the Pure group is assumed to be 0.05, Clear is 0.12, Coastal is 0.5 and Turbid/Inland is 2 m^{-1}.

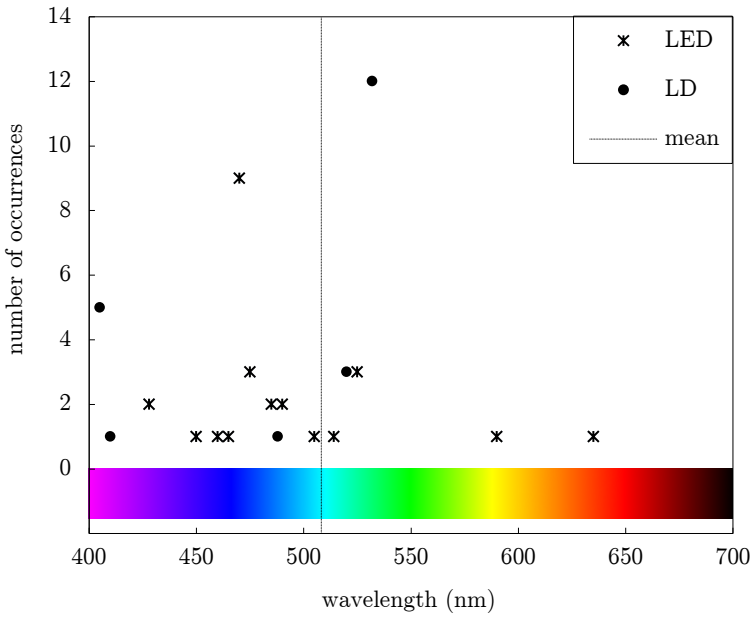

Figure 6.2: The number of transmitter wavelength occurrences over all underwater optical wireless practical demonstrations details in app. I.

for example, in the Woods Hole Oceanographic Institute case as described in sec. 6.1. This raises an important point about the lack of transmitter wavelength optimisation for specific experimental applications.

Having looked at the link performance and transmitter wavelength selection of previous experimental studies, requirements of a novel experimental study are beginning to form. In the next section, these aims are consolidated so that a suitable link may be designed.

6.3 Optical Variability Experiment

6.3.1 Motivation and Aims

As shown by sec. 6.1 and sec. 6.2, the experimental investigations of underwater optical wireless communications explore a range of turbidities through raising or lowering the attenuation coefficient, with some studies even indirectly including depth derivative optical property variation. No study, however, has looked specifically at the variable attenuation over a single optical link, or even considered it a possibility; moreover, prevalent attenuation coefficient values for underlying models are often based on surface or averaged coefficients which were shown to be inaccurate in ch. 3 and ch. 6 respectively. For these reasons, optical variability becomes the principal aim of an experimental investigation in this research.

One of the simpler and most suitable methods to investigate optical property variability is to assess optical communication link propagation down a water column, through increasing depths. The reasons why this particular locational variation is chosen is two-fold: first, chlorophyll-based attenuation models for depth variations have already been derived sec. 3.3.2 of this research; second, that those models show that, by increasing optical link penetration even a few metres into the ocean, there should be a noticeable change in the attenuation coefficient, particularly in turbid locations with high surface chlorophyll levels. The latter point is of particular importance as lateral and temporal variations are on too large a scale to be captured reliably by a small-scale experimental investigation, as well as not having underlying models describing the expected behaviour yet. On the topic of channel modelling, the beam deviations models caused by refractive index gradients with depth in sec. 5.4 also need to be validated by experimental data. The problem in this case is that the scale and location of the optical link required is beyond the practical possibilities of this study.

With regards to depth-dependent attenuation variations, these can only be tested in natural water bodies, where there will be changes in the chlorophyll concentration with depth. Ideally,

coastal oceans or turbid harbours are the best locations to undertake this research due to turbidity changes being near the surface; subsequent length requirement of the optical link are low. Additionally, propagation models already exist for these locations. However, issues with these types of locations are oceanic currents and turbulence, in addition to freshwater interfaces at harbours. Although these factors do not increase absorption a great deal, the attenuation will be greater than predicted due to increased amounts of scattering (see sec. 2.5), leading to greater temporal and spatial dispersion. If these optical links want to retain equivalency a with low-turbidity long-range link, this additional scattering source should be reduced.

A compromise is offered by performing the experiment down the water column in still inland waters. Although the values of attenuation are likely to be higher than those found in coastal and harbour waters, this location should reveal the principle of a changing attenuation coefficient with depth. Though, it should be noted that the surface-chlorophyll level is likely to be greater than the range modelled in ch. 3. Due to generally high turbidity in static inland waters, typically with attenuation of 1 m^{-1} (Kirk, 1994), the link length will be severely limited but will show significant variability within several metres down the water column. In order to assess how equivalent these low-turbulence links would be to long-range optical links with similar SNR penalties, the spatial dispersion should be characterised. This is achieved by transmitting using a laser of a known initial spatial profile, such as a Gaussian beam. Doing so will also provide an insight into the higher-order scattering models introduced back in ch. 5.

Additionally, the analysis of previous experimental performance in sec. 6.2 raised two important points for subsequent experimental designs. The first was to establish a link in which the attenuation-length product is high; a high product is regarded in respect to previous studies as values of 10 or greater. Essentially, what this shows is that communication was established even though the irradiance lost through the *cr* factor in the Beer-Lambert law (eq. 5.1) is large. It is noted from app. I that the furthest inland link established so far is 5.8 metres, based in ambient daylight conditions (Vasilescu et al., 2005); a subsequent experimental set up should also aim to surpass this. The second point raised by previous experimental studies is the importance of selecting an appropriate transmitter wavelength. This will be done as part of the experimental design.

To conclude this section, a list is compiled summarising the aims of a novel underwater optical wireless practical assessment:

- Assess the variability of the attenuation coefficient in a natural body of water by looking at attenuation of a signal through the water column.

- Look at spatial dispersion with varying attenuation coefficient, reinforcing higher-order scattering models and the attenuation curve with depth.
- Design a link to propagate for a greater length than 5.8 metres in inland waters, based in diffused daylight, that also achieves a high (> 10) attenuation-length product.

6.3.2 Design and Methodology

A suitable experimental set up and methodology are sought to satisfy the aims introduced in the previous section. Aspects of the communication system to consider are: the inland water body upon which to base the tests; geometric design of the link, where the majority should traverse a vertical water column; transmitter wavelength and source type; modulation scheme and modulation optics; receiver design. The latter three options will be selected in conjunction with information in ch. 4.

To begin, the inland water body is introduced. Access was granted to a waterlogged quarry and testing facility based in the UK. The height of the water in the quarry varies annually between 8 to 15 metres, where the height was over 10 metres at the time of testing. Positioned on top of the water is a large floating pontoon with access to the water body underneath through a 0.25 by 0.75 metre gap. Although this set-up reduces the ambient sunlight from directly above the communication system test location, diffused sunlight illuminates the upper section of water regardless. In fig. 6.3 a photograph is presented of the water-leaving irradiance coming from upwelling scattered sunlight; illumination across the section is not constant due to the geometry of the pontoon. This image highlights that the chlorophyll concentration near the surface is likely to be high as the irradiance is well within the green part of the spectrum.

As the experimental set up is under the geometric constraints imposed by the testing facility, thought needs to be given as to how best to establish a vertical communication link. One possibility is to have a near-surface transmitter and a receiver in the water (or, of course, vice versa), where the distance between them is varied. Such method requires time investing in waterproofing optical components and a further method for lowering one side of the link that ensures alignment is maintained. A better method would be to keep all communications equipment above the waterline and use mirror structure positioned underwater to reflect the beam, as seen in fig. 6.4. It is hoped that, as the water body is mostly static, the will be little movement in the water surface. Using this method, the beam propagates the vertical path twice, highlighting and conferring any attenuation changes with depth. It should be noted that to achieve a directional link geometry

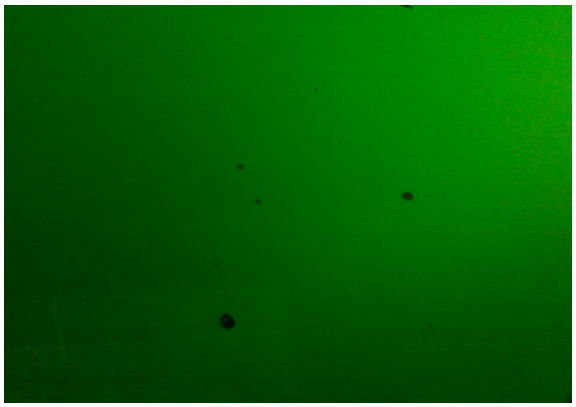

Figure 6.3: Photograph of the inland water body used for experiments. Light is the water-leaving irradiance from scattered sunlight; black spots are shadows from large particulates in or floating on the surface of the water.

such as that in fig. 6.4, a LD should be used at the transmitter with strict safety controls. The likely high scattering coefficient of this water body would cause a beam transmitted from an LED to become hard to distinguish from its reflection, as well as any reflections from various interfaces and backscattered light.

In the practical set up, the mirrors II and III in fig. 6.4 must be exactly at right angles to each other to ensure the beam reflects back at the angle it was transmitted. This is achieved by designing a fixed mirror housing and, as long as the mirrors are at 90° to each other, misalignment of the mirror housing would be trivial in at least one plane. Two different three-dimensional mirror housing designs based on maintaining the mirrors at right angles are shown in fig. 6.5a and fig. 6.5b. In the first case, alignment of the mirror housing is trivial in both x and y planes; in the latter, only one of these planes. Preference is given to the design in fig. 6.5b for this study because it requires flat mirrors only; cone-shaped mirror surfaces need high-cost, specialist equipment to produce. In the one-plane alignment design, the plane which is not aligned can be controlled by two variable-length ropes which also hold the weighted mirror housing in place and allow it to be lowered into the water column.

Based on the mirror housing design and the frame needed to suspend it from, dimensions can be formed for fig. 6.4, as noted in the figure description. The total underwater path length r and the depth z are related by

$$r = 2z + 0.3 \tag{6.1}$$

measured in metres. When $z = 0$, the mirror box is placed slightly below the water surface (within

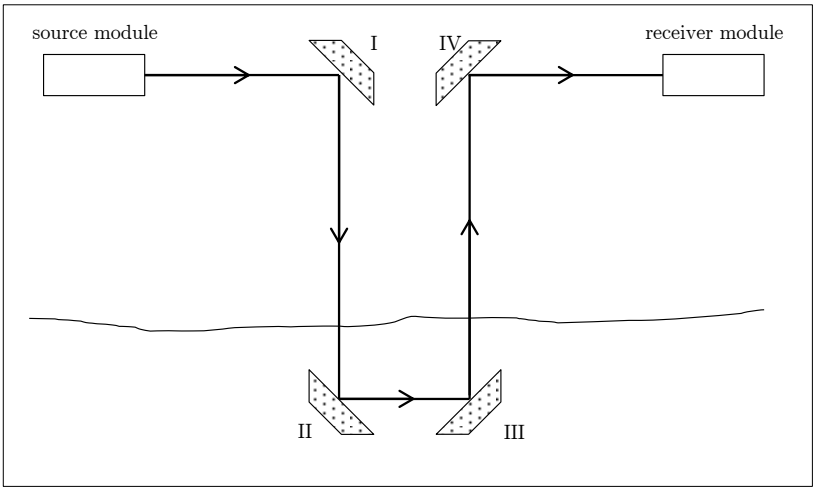

Figure 6.4: Geometrical design of the optical property variability with depth experiment. Dotted components represent mirrors. In the real experiment distances were as follows: source to I 0.3 m; I to II 0.5 m; II to III 0.3 m; III to IV 0.5 m and IV to receiver 0.3 m.

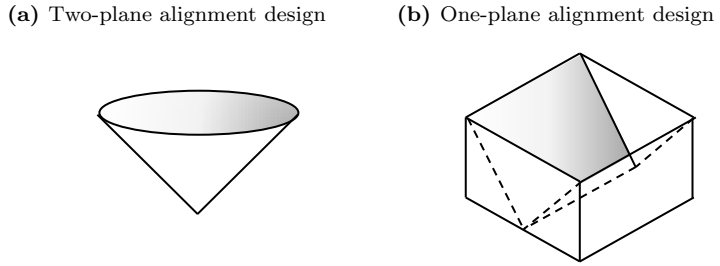

Figure 6.5: Design of a mirror housing that allows for automatic alignment of the return signal by use of mirrors placed 90° to each other. The inside surface in both cases are mirrors.

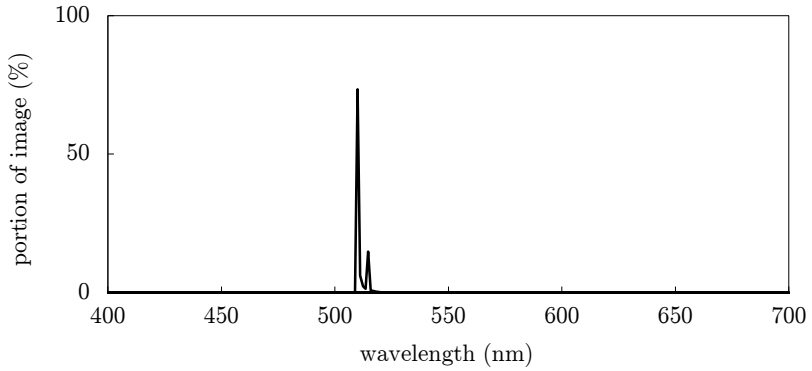

Figure 6.6: Frequency analysis of fig. 6.3 after removing the intensity gradient, revealing the best propagation wavelength for this body of water.

0.01 metres of the surface), and the underwater propagation distance between the mirrors II and III is 0.3 metres, hence the link length is 0.3 metres at the minimum depth. By defining it this way, the losses caused by the initial mirror I, as well as at the air/water interface, may be ignored.

In terms of selecting a suitable transmitter, the need for a directional LD was already highlighted but a suitable wavelength remains to be chosen. As attenuation-profiles for the water body of interest are not available and require specialist instruments to measure, an estimate for the best wavelength may be found through the water-leaving irradiance in fig. 6.3. The water-leaving irradiance is the result of near-surface attenuation which is a valid for this experiment as the link shall be transmitting from the surface; this may not be the case lower down the water column due to changes in the attenuation profile. Frequency analysis was performed on the image in fig. 6.3, the result of which is shown in fig. 6.6. A large peak is seen to occur around 510 - 515 nm; rather coincidentally, this peak occurs close to the mean wavelength used in previous experimental studies (fig. 6.2), raising further questions about the suitability of the wavelengths chosen. With reference to fig. 6.2, the closest existing LD wavelength to the peak are 514 and 532 nm. Preference was given to the latter wavelength as a Photop 532 nm solid-state laser was already in possession. This laser has a variable power output with a maximum of 100 mW, which was tested to be temporally stable between 70 and 100 mW, but also offers the correct average output power below these values (Photop, 2012). With the in-built modulation bandwidth of the laser being only 10 kHz, an external electro-optic (EO) modulator, also already in possession, is implemented, increasing the modulation bandwidth to 50 kHz.

At the receiver module, two technologies are required to detect the communication signal and spatial profile respectively. To detect and amplify the incoming communication signal, a suitable pre-built transmitter is chosen with help from the component simulation in fig. 4.8. This simulation found combinations of receiver and transmitter that resulted in an SNR of 20 dB or greater for a highly turbid, depth-variable channel with high ambient sunlight, making it applicable to the chosen experimental channel. Of the successful receivers, the Thorlabs PDA36A, a switchable gain detector, is selected for the purpose of this experiment, offering sufficient bandwidth (< 17 MHz, according to gain setting), sensitivity (0.3 A W^{-1} at 532 nm) and a relatively large detector area (13 mm^2) (Thorlabs, 2015). To capture the spatial light profile at the receiver, a CMOS camera with known gain settings is implemented.

To conclude this section, the experimental methodology is reviewed. Following system alignment and pre-tests determining the losses at various interfaces and mirrors, a two-part test is performed. The first part assesses the vertical attenuation characteristics by looking at changes

to the modulation depth of a 50 kHz sine wave (this being the maximum achievable bandwidth of the set up) as the link length is extended over greater depths down the water column. The result is recorded through a digital oscilloscope and saved on a personal computer. This will be done at every 0.25 metres down the water column until the link can no longer be detected, where the large-size increment is chosen due to the perceived difficulty in aligning the mirror housing at each depth. In the second part of the experiment, images will be taken of the spatial profile of the beam incoming to the receiver, again at every 0.25 metres. Processing of these latter results will occur after the testing concludes. In both cases, repeatability may be effected by time constraints and weather conditions, where the latter impacts on the stillness of the water surface and background ambient lighting.

6.3.3 Results

The experiment was performed over two-and-a-half days in May 2015 using the equipment, methodology and inland location described in sec. 6.3.2. The first half-day was dedicating to setting up and pre-tests which found exact distances between each component as well as the losses at the system interfaces. Subsequent data have been adjusted to take account of these losses. In addition, the experimental design was altered slightly to include heavier weights underneath the mirror housing and additional alignment ropes, as shown in fig. 6.7. The purpose of this was to reduce oscillations in the mirror housing. Vertical attenuation characterising tests and spatial imaging each spanned a day; harsh weather conditions were present for the latter.

Vertical Attenuation Characterisation

For vertical attenuation characterisation tests, the modulation depth and intensity were recorded every 0.25 metres until the beam reached a depth of 2.5 metres (representing a total underwater link length of 5.3 metres). At this depth, the signal became too small to reliably find, align and record measurements. Because the gain of the receiver at these depths needed to be high, and the bandwidth of the Thorlabs PDA36A reduces to 12.5 kHz at its maximum gain setting of 70 dB (Thorlabs, 2015), the frequency of the transmitted sine wave was reduced to 10 kHz for the duration of the test. For this test, an additional large (0.15 metre diameter) collection lens was put in front of the receiver module to concentrate the beam spread from the underwater medium.

Vertical attenuation characterisation tests were repeated twice over the morning and afternoon of a single day. The averaged receiver modulation depth values are shown in fig. 6.8. As per the Beer-Lambert law, the modulation depth and received intensity should decrease exponentially with

increasing link length. However, by observing the attempted exponential fit in fig. 6.8, it becomes apparent that the data only approximately follows an exponential curve, with outliers seen near the surface as well as a general deviation from the exponential curve deeper down in the water column. While this could be, in part, due to experimental errors since the number of repeats is low, it is more likely this is from an underlying change in the underwater optical channel. To investigate these channel variations further, the average received intensity with depth, which is larger than the modulation depth and therefore more accurate, is shown in fig. 6.9 and fig. 6.10.

Fig. 6.9 shows the received power against communication link depth, where the Beer-Lambert results at fixed attenuation coefficients of 0.9, 1.3 and 1.7 m^{-1} are also depicted. In this figure, the

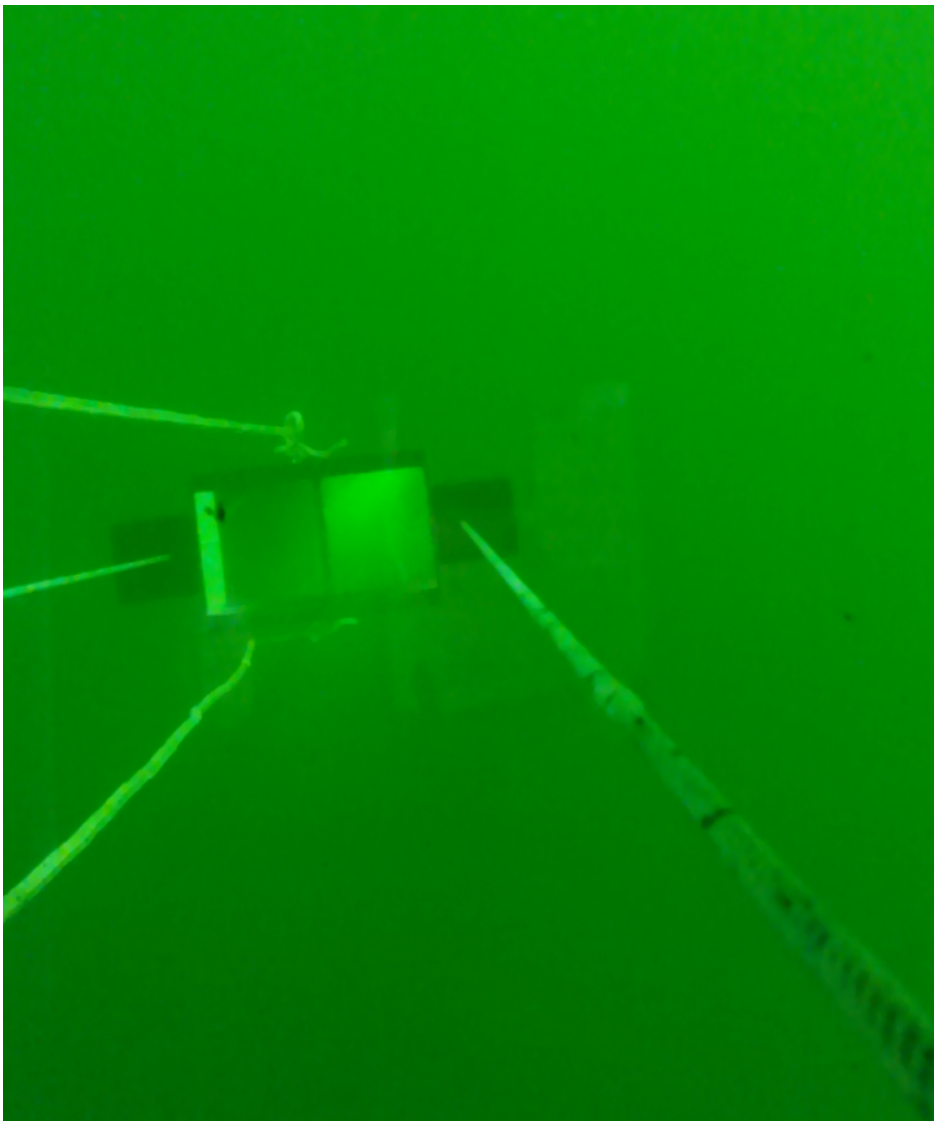

Figure 6.7: Photograph of the mirror housing suspended 3 metres underwater with only background illumination from diffused sunlight. Two additional ropes are seen either side of the box for fine alignment. Slight reflection is seen in the image from the water surface.

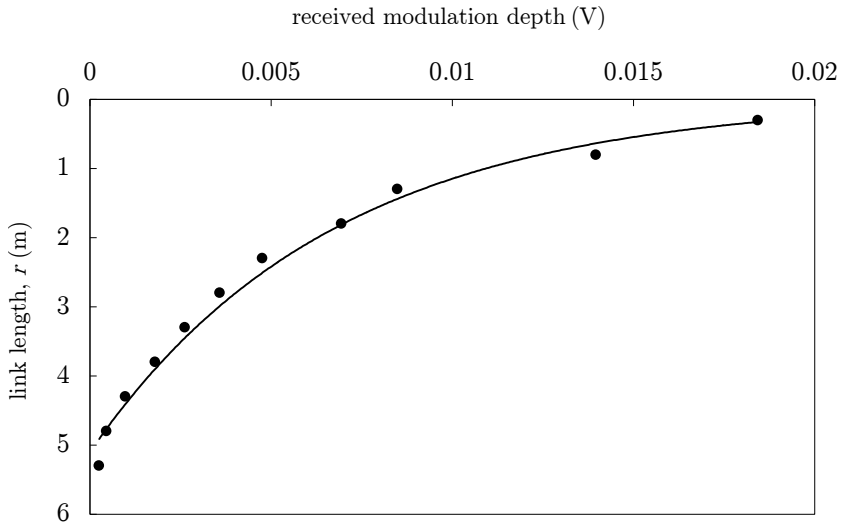

Figure 6.8: Experimental modulation depth with increasing link length down a vertically-aligned optical wireless communication link in a turbid environment for a 10 kHz sine wave. Path length is related to depth by $r = 2z + 0.3$.

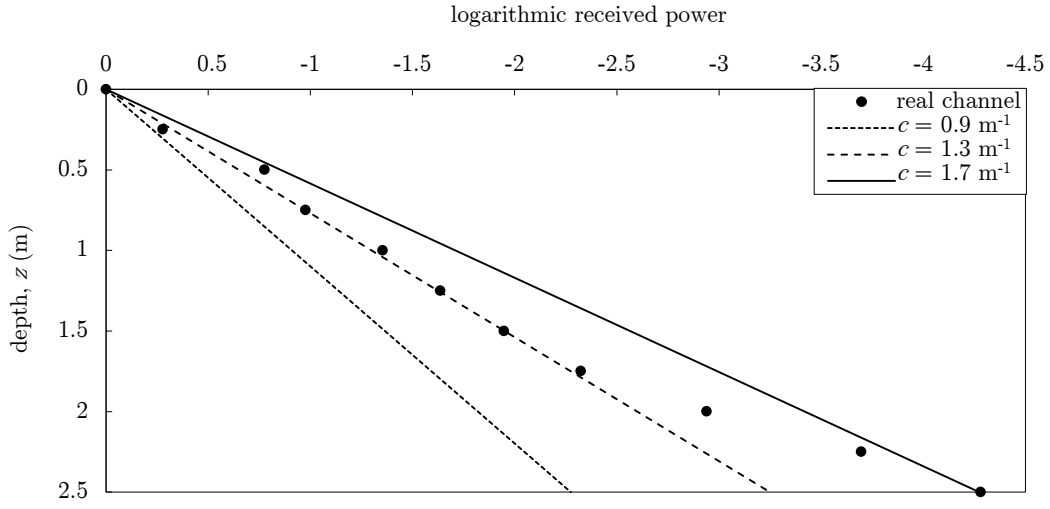

Figure 6.9: Vertical attenuation characterisation test result; depth against average attenuation coefficient is compared against Beer-Lambert law results with nearby attenuation coefficients.

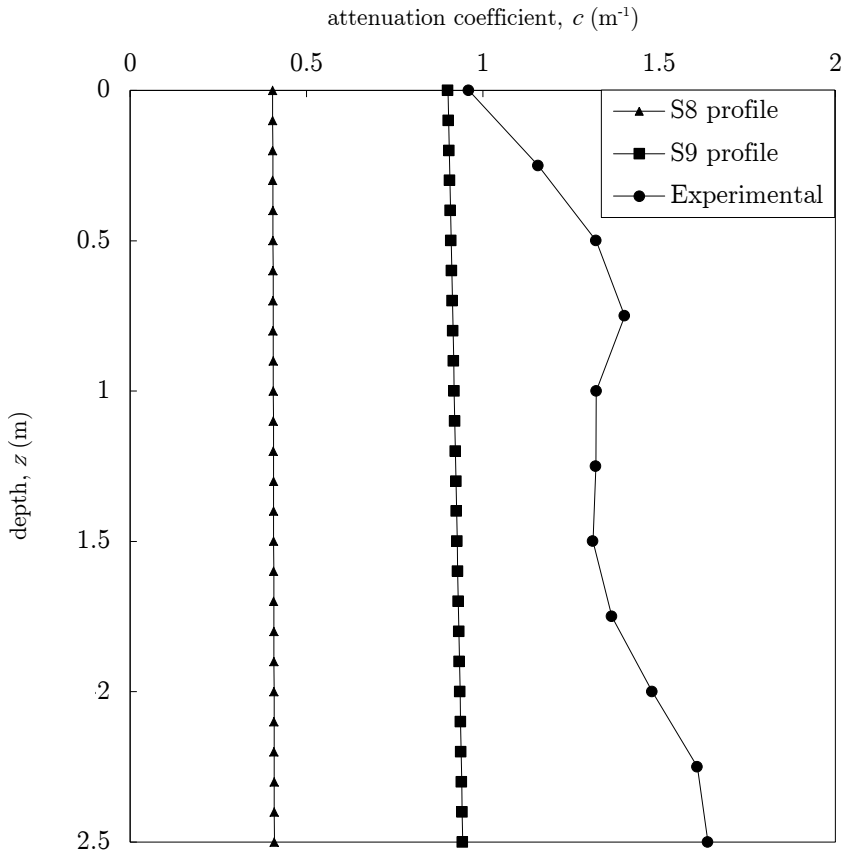

Figure 6.10: Experimentally defined attenuation coefficient varying with depth, based on a Beer-Lambert law relation, compared with the high-chlorophyll Gaussian depth-dependent attenuation profiles derived in sec. 3.3.2.

variation in attenuation coefficient is much clearer than as seen in fig. 6.9. For shallow propagation depths, the received power is measured to follow the decay of a communication link of attenuation coefficient around 1.3 m^{-1}. At the 1.75 metre depth increment, attenuation begins to increase, eventually settling at a value of 1.7 m^{-1} at a depth of 2.5 metres, after which the link could not be established. This initial increase in attenuation coefficient is reminiscent of the Gaussian attenuation-depth profiles derived in sec. 3.3.2; yet, with changes already occurring at 1.75 metres depth, the DCM is likely to be higher up the water column than the high-chlorophyll S9 profile. The reason for this is the high chlorophyll concentration in the chosen static inland water body.

The shape of the attenuation curve with depth can be extracted from the results in fig. 6.9 through the Beer-Lambert relation to yield fig. 6.10; included in this figure are the S8 and S9 attenuation-depth profiles from sec. 3.3.2. Attenuation is seen to initially increase from 0.95 to 1.4 m^{-1} between a 0 and 1.25 metre depth. It is thought this initial peak could be from NAP, particulates from land run-off floating near the surface. These particulates are not seen in open ocean waters, which is why initial peaks such as this do not appear in the S8 and S9 attenuation-depth profiles. Another reason these profiles might omit an initial peak is due to the level of detail in the models; the underlying chlorophyll-concentration in (Uitz et al., 2006) are skewed Gaussians spanning several hundred metres, so resolution to a few metres is unlikely to be overly accurate. It should be noted that, in terms of deriving the attenuation of a link, near-surface inaccuracy only presents a problem in short links or links transmitting horizontally near to the surface.

After the initial local maxima in the experimental data of fig. 6.9, the attenuation coefficient begins to increase again around 1.75 metres depth. This is a reasonable depth for the attenuation to begin a Gaussian peak in high-chlorophyll inland waters, according to (Kirk, 1994). However, as the data is only recorded down to a depth of 2.5 metres, the equivalent attenuation-depth coefficients (see app. E) cannot be found for this water body using them. For this, measures the peak intensity of spatial distribution provides the answer.

Spatial Distribution

Images of the spatial distribution of the transmitted beam were recorded with increasing propagation depth, where progress was impeded by variable weather conditions. Spatial beam distributions were depicted only every 0.5 metres, though down to a depth of 7.5 metres, at which point the transmitted beam was no longer detectable by the CMOS camera. It should be noted that if a communication link would be established at this point, it would be a 15.3 metre link in a highly turbid, variable underwater environment. However, a link longer than 2.5 metres

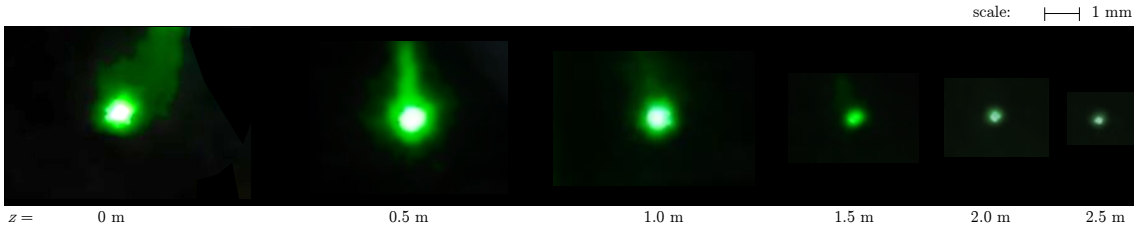

Figure 6.11: Examples of spatial profile images from the 0 to 2.5 metre depth range. Elongation of the beam in one direction is due to multiple reflections.

was not possible for two reasons: first, manual alignment, particularly in adverse weather conditions, became increasingly difficult at greater depths; second, the EO modulator caused a spatial interference pattern on the beam so was removed for this test. Both of these points shall be discussed further in sec. 6.3.4.

Pre-tests showed the chosen laser to have a Gaussian profile with a diameter of approximately 1 mm; the beam divergence was too small to measure accurately for the link range of interest, so it is assumed this is 1 mrad (0.057°) as per the data sheet (Photop, 2012). Using this data for the link path noted in fig. 6.4 reveals an estimated beam width at the $z = 0$ position, which has been used subsequently to scale fig. 6.11. This figure shows examples of the spatial profile images in the 0 to 2.5 metre depth range. As expected, the incoming beam reduces in size and intensity as the mirror housing is moved further down the water column. However, there are also two artefacts apparent in the images; elongation in one direction and saturation around the beam centre. Elongation of the spatial profile occurs at near-surface depths because of multiple reflections of the beam, these are too weak to be detected in links transmitting to greater depths, more details of this are available in sec. 6.3.4. Meanwhile, saturation is the result of the beam intensity at those points being greater than the camera is able to detect, even with minimal gain settings. Due to the latter, the input LD power is incremented, though all results have been adjusted to take account of this.

To transform recorded images such as those in fig. 6.11 into two-dimensional spatial profiles, five cross-sections are taken through the centre of the spatial distribution and averaged. The cross-sections are drawn manually to avoid the multiply-reflected beams as far as possible and are aligned together using the central peak. Background levels are then adjusted to take account of the camera gain setting and background lighting conditions. The results of this are shown in fig. 6.12 to fig. 6.13.

Fig. 6.12 and fig. 6.13 show the spatial light distribution of the beam at increasing propagation depths, as viewed from the receiver location in fig. 6.7. All received intensities, or powers, are normalised by the peak power recorded at $z = 0$, enabling a later analysis of the attenuation in the

(a) 0 - 2.5 metre link depth

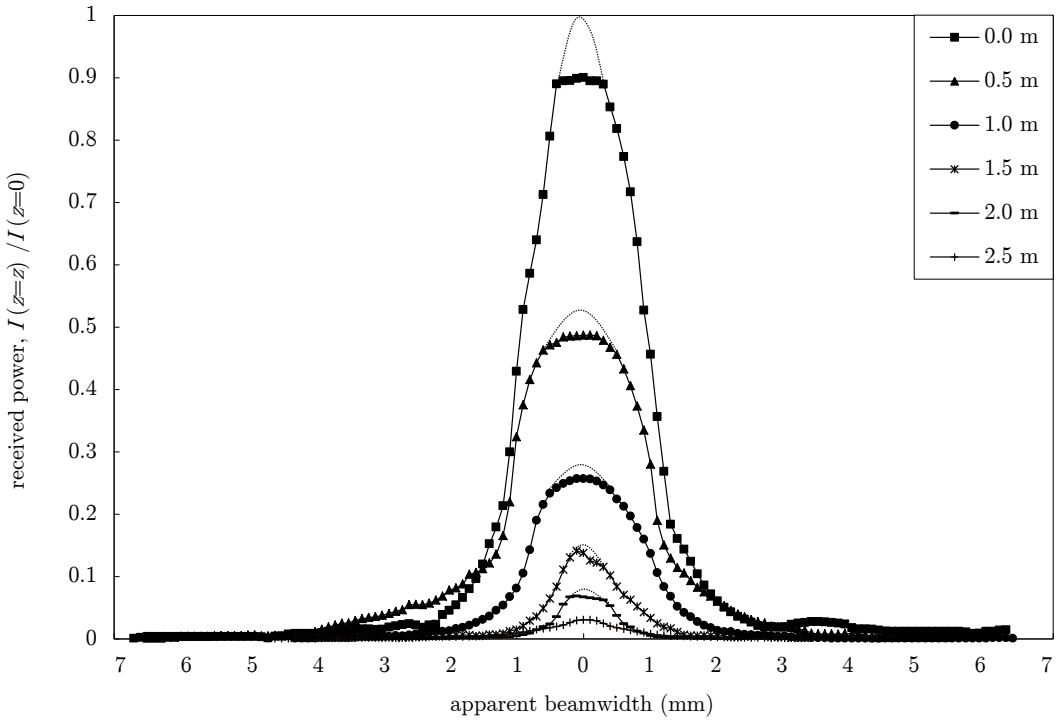

(b) 3 - 5.5 metre link depth

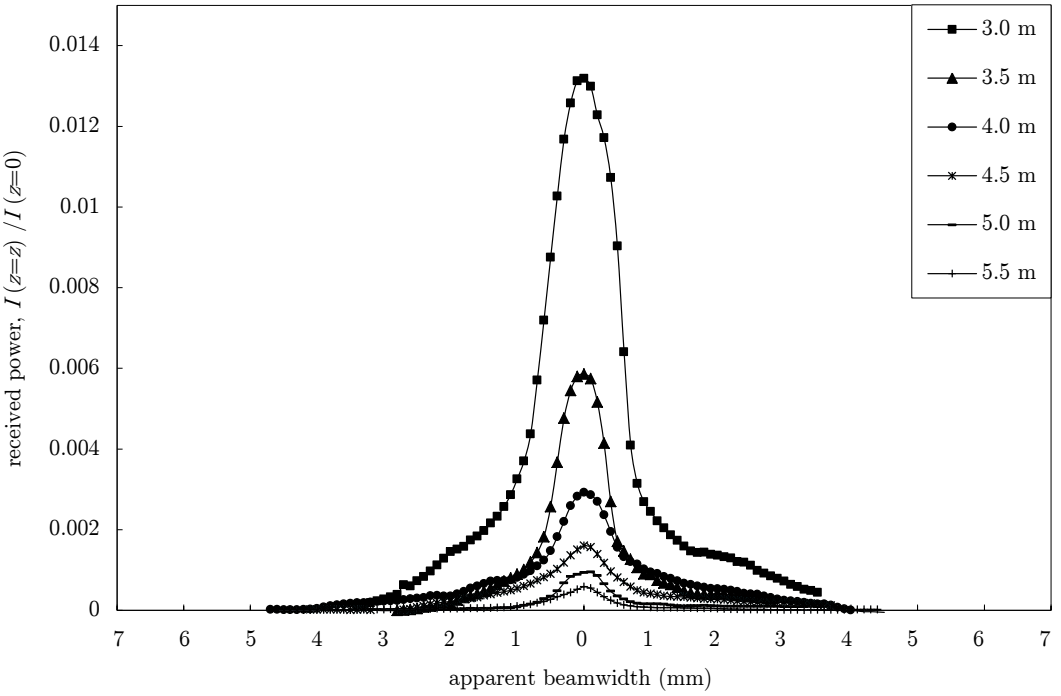

Figure 6.12: Apparent spatial light distribution of the beam after propagating to a range of depths between 0 - 5.5 metres. In (a) additional Gaussian profiles are estimated where the camera saturated, represented by dotted lines.

(a) 6 - 7 metre link depth

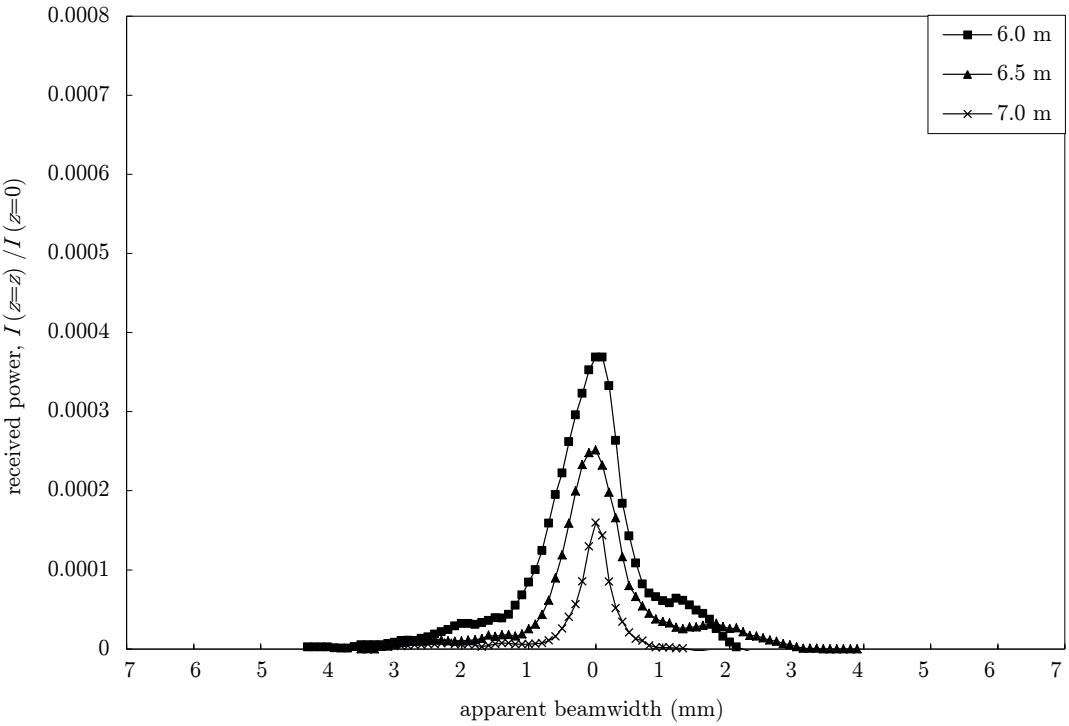

(b) 7.5 - 8 metre link depth

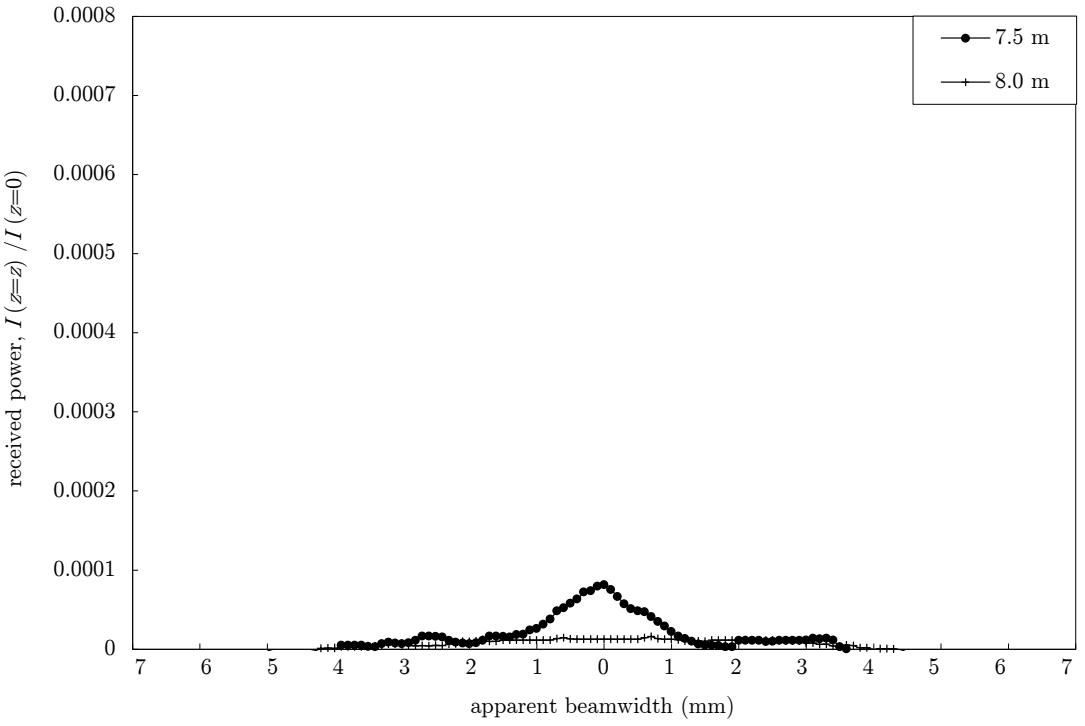

Figure 6.13: Apparent spatial light distribution of the beam after propagating to a range of depths between 6 - 8 metres.

link. Additionally, in fig. 6.12a, Gaussian curves were fit above the data points to represent the expected curve had the camera not saturated. It should be noted that saturation only occurred in the range 0 to 2.0 metres, as can be seen in fig. 6.11.

From these figures, the overall intensities clearly decrease rapidly with link propagation depth; for example, at a depth of 5 metres, representing a total link length of 10.3 metres, the maximum received power is 0.6% of that originally received at a depth of 0 metres. Although the beamwidths become generally narrower in terms of their apparent size at the receiver, the beams actually widen relative to their intensity and propagation distance. This would be expected since the beam becomes flatter and wider with distance due to geometric spreading as well as scattering from the underwater medium. In addition, it is expected that at areas of high attenuation, specifically where there is a larger amount of loss due to increased chlorophyll, there would also be a noticeable increase in the beam width due to more particulate scattering. However, no obvious link has been found relating the beam width to the loss in intensity. It could be that terrestrial particulates are impacting the scattering behaviour or that the increased attenuation is mostly the result of higher absorption in high-chlorophyll regions. Regardless of the reason, the scattering extent and subsequent beamwidth is not seen to follow an underlying chlorophyll concentration.

Although these will be revisited in sec. 6.3.4, there are two notable aspects of the results in fig. 6.12 and fig. 6.13 which have not been mentioned. First and foremost the lack of symmetry in some of the profiles; asymmetry in the spatial light distributions of the 0 and 6 metre depths, among others, is attributed to multiple beam reflections where it has not be possible to entirely omit the surplus beams. Multiple reflections are also possibly responsible for the width of the 7.5 metre distribution in fig. 6.13b, though the intensity levels are also almost undetectable in this case. Next, the deeper propagating spatial profiles have more of a spiked appearance as opposed to a Gaussian distribution, this is likely down to the pixel density of the camera at these points in addition to a change of general profile shape through scattering.

6.3.4 Analysis of Results

Having seen the results for both vertical link characterisation and spatial distribution tests, this section compares them with each other and against previously modelled data in addition to drawing general comments about their reliability.

To begin, the attenuation-depth distribution of the vertical link and spatial experiment results are compared. The peak intensity of each profile in the latter is considered in order to generate estimates of the attenuation coefficient throughout the water body. As with the vertical attenuation

characterisation test, this is done at each depth increment to find a variable attenuation coefficient; the results of both tests are compared in fig. 6.14. The two profiles are in reasonable agreement in terms of their numerical values, with some shape discrepancies between links propagated to depths in the range 0 to 1.5 metres. This difference is likely due to the precipitation and winds that occurred whilst performing the spatial part of the test; near-surface attenuation has averaged out as particulates are better mixed in this upper region. Although the near-surface attenuation behaviour means the spatially derived profile still does not follow a Gaussian chlorophyll-concentration type curve, it does support the theory that particulates from terrestrial run-off were impacting the near-surface attenuation coefficient. Ignoring this upper local increase in attenuation, it is possible to fit a Gaussian to the attenuation-depth curve of this inland water body, as shown in fig. 6.15. However, translating this into the equivalent coefficient to those derived for open and coastal waters in app. E is not possible through the models derived in this research. The formation of a method with which to do this is suggested for future study.

Although the result in fig. 6.15 is beyond the range of the chlorophyll-concentrations depicted

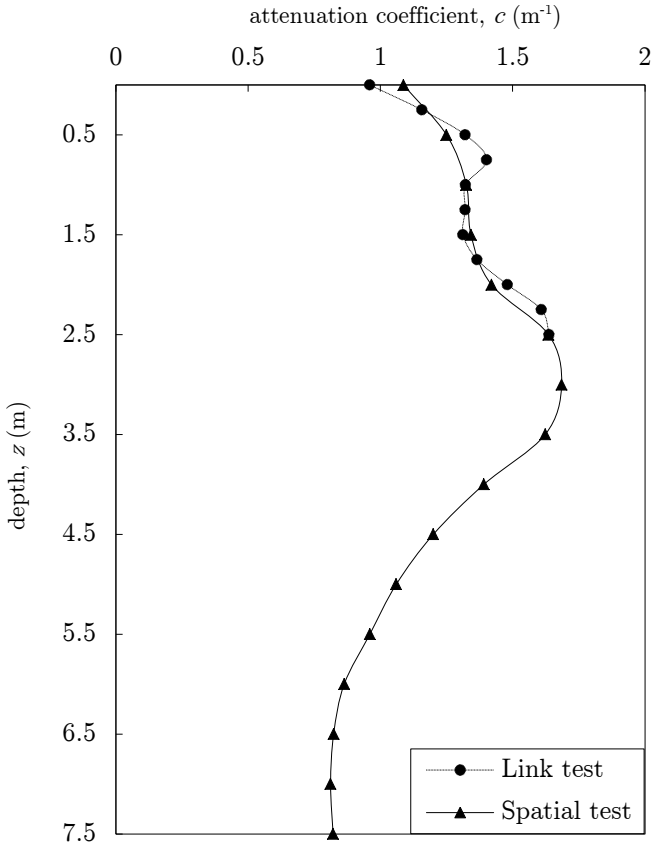

Figure 6.14: Estimated attenuation coefficient with depth for a turbid inland water body based on the vertical link characterisation and spatial profile tests.

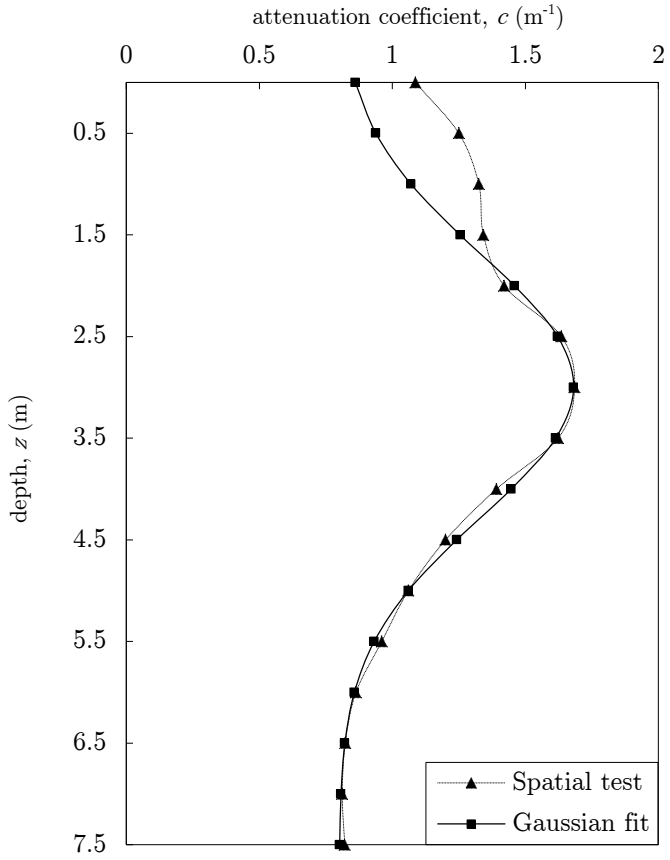

Figure 6.15: Fitting a skewed Gaussian distribution to the estimated attenuation coefficient found in the spatial profile tests.

by the S1-S9 profiles in app. E, it does show that the attenuation-depth profile has an underlying skewed Gaussian distribution. This is significant as it supports the validity of the attenuation-depth models generated in ch. 3 and established throughout the subsequent chapters of this thesis. It also raises the point that, for inland bodies of water, there are factors other than the chlorophyll-concentration to consider, such as particulates from terrestrial run-off. In the experimental inland example tested in this research, these additional particulates fortunately only affect the first 1.5 metres of the attenuation-depth profile; however, in particularly turbid case 2 waters, it is likely that the attenuation-depth curve deviates much further from the Gaussian chlorophyll-dependent profiles. For this reason, it is suggested that the attenuation-depth models derived in this research be applied to oceanic environments only.

Presently, the accuracy of the obtained experimental results is assessed through a survey of experimental issues. Issues faced included: alignment, the EO modulator and its spatial interference pattern, multiple-reflections and environmental issues. In app. J a photographic documentary depicts several of these issues.

Alignment Issues

As shown by fig. 6.7, two additional ropes were added to the mirror housing to aid alignment of the mirrors. Alignment issues were the primary reason the vertical attenuation characterisation experiment was limited to depths of 2.5 metres; oscillations of the mirror housing, in addition to changes in the water surface and general movements of the pontoon affecting the rig holding experimental equipment meant that LOS was difficult to maintain. For this reason, it is expected that the vertical characterisation data recorded includes inaccuracies resulting from this issue.

EO Modulator Issues

The EO modulator caused an isogyre spatial interference pattern on the transmitted beam as shown in fig. J.1 in app. J. For the vertical attenuation profiling experiment this meant the beam at the receiver had to be collected and focused large lens at the receiver. For the spatial distribution testing, the component was removed from the beam path, giving the beam its source Gaussian distribution.

Environment Issues

Environment issues refer to the weather conditions at the time the data was taken. For initial set-up and the vertical attenuation characterisation test, weather conditions were clear and the surface of the water still. However, for spatial testing, there was significant wind and precipitation outside the covered pontoon. Most noticeably, this caused variable background ambient light levels as seen in fig. J.2 in app. J. This affected the recorded image for depths below approximately 2.5 metres, which is the depth where the mirror housing was no longer shadowed by the pontoon. The variable, diffused sunlight was filtered out for the presented results.

Multiple Reflection Issues

The air/water and water/air interfaces in the link, as well as the four mirrors, caused the initial beam to have several reflections, as shown in fig. J.3 of app. J. For this reason, the communication link was purposefully misaligned; without misalignment, the initial reflection from the water surface in constructive interference the originally transmitted beam damaged the polarising film on the outer side of the EO modulator. Despite the misalignment, some multiply-reflected beam artefacts remained in several of the spatial intensity profiles, as previously mentioned. From pre-tests, the power lost by the pair of medium interfaces was found to be 9.6%, which is considerable but was account for by basing measurements on an initial $z = 0$ value. However, this initial

measurement does not account for any variation in the initial conditions which are likely due to surface movements.

To conclude, the original experimental aims from sec. 6.3.1 are reviewed. The principal aim was to assess variability of the attenuation coefficient with depth. This has been completed successfully, where the attenuation-depth profile was seen to follow similar Gaussian to those modelled in ch. 3 once particulates from terrestrial run-off had been ignored. In terms of the second aim to reinforce higher order scattering models, this was challenging due to the lack of obvious relationship between the perceived particulate concentration and the beam spreading. It is thought this may be because of the aforementioned particulates or due to increased attenuation inducing absorption over scattering. The third and final aim was to transmit over 5.8 metres and achieve an attenuation-length product greater than 10. Although the communication link developed was only a maximum of 5.3 metres (equivalent to a 2.5 metre mirror housing depth), the spatial testing saw the transmitted beam detectable up to 15.3 metres (7.5 metre depth). In the latter case, the attenuation-length product was 19.5, far exceeding the original aim.

6.4 Summary

In this chapter, previous experimental studies of underwater optical wireless were surveyed and used to generate three aims for a novel investigation on optical channel variability: to assess the change in attenuation coefficient with depth in a natural water body, to determine the scattering of the aforementioned channel through the spatial profile and to achieve the highest attenuation-length product. To satisfy these aims, the experimental set up summarised in fig. 6.16 was devised.

Most notably from the results, the attenuation-depth curve of a turbid inland water body was seen to follow a skewed Gaussian, reinforcing the chlorophyll-concentration based models established throughout this research. It is thought that if there existed a method to translate this profile into a set of Haltrin coefficients (app. E) then all case 1 and low turbidity case 2 waters could be depicted through this model. Moreover, it opens the possibility to build a smart underwater optical communication system that learns its environment and is subsequently able to predict the attenuation curve over a path of varying orientation and location, adapting accordingly. However, such is the work of future researchers; it is now time to bring this research to its conclusion.

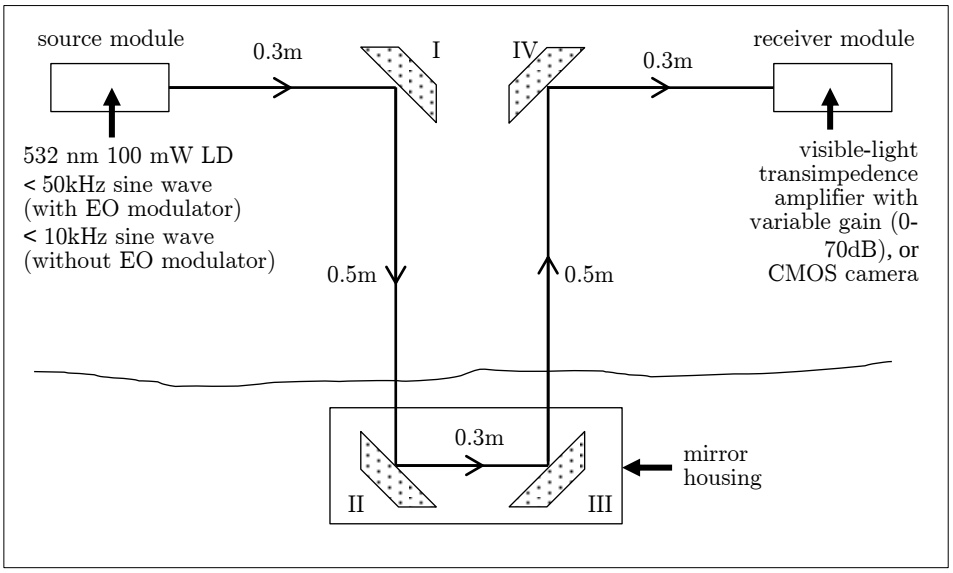

Figure 6.16: Summary of the real vertical characterisation and spatial experimental set-up where the mirror housing is adjusted to increase link length.

Chapter 7

Conclusion

The mystery surrounding the underwater world has led to a boom in its exploration, with high speed communications at the forefront of the requirements for new submersible technology. As this study draws to an end, reflections are made upon the variable aspect of the optical properties of this vast unknown, as have been explored throughout this study. Further, this chapter addresses how these ever changing properties have impacted on the design and performance of underwater optical wireless communication systems.

To bring this thesis to a close, several aspects are highlighted for further research for those with continued interest in optical property variability in the underwater optical wireless channel.

7.1 Conclusion

The principal aim of this research was to investigate variability in the optical properties of natural waters to determine its impact on the performance of underwater optical wireless communications. As a result of this knowledge, subsequent communication system configurations would be better optimised for the underwater optical channel. Furthermore, the underwater optical channel model would itself be updated, bridging the gap between existing optical communication propagation models and the extensive oceanographic models of underwater light transport.

What initially set this research apart from previous studies is that optical property variations were assumed to occur within a single optical wireless link; in previous studies, turbidity is assumed to be constant throughout the optical link, though differences between links are considered. It was for this reason that emphasis was placed on optical property variations existing on a scale comparable to a 200 metre optical link, the longest underwater optical wireless communication link demonstrated to date. A literature review of underwater optical properties, in addition to a quantitative analysis of their variability, highlighted the attenuation coefficient and refractive index as befitting foundations for a study on optical property variability.

The main achievement of this research was the development of a unique model to characterise variability of the attenuation coefficient with depth. The model was based on a bio-optical model that derived attenuation from the chlorophyll concentration and chlorophyll-depth profiles which took the form of skewed Gaussian curves with depth. The subsequent attenuation-depth profiles were seen to exhibit a similar skewed Gaussian form, peaking underwater at the DCM, where link performance was a result of the link's geometric relation to the DCM. Significant variations in attenuation were found for links transmitted from a fixed location, over a set distance, where the transmission angles were varied (fig. 3.12). Observations of this kind are novel in the field of underwater optical wireless communications. Meanwhile, the attenuation-depth profiles themselves were reinforced by an experimental characterisation of the attenuation coefficient with depth, in ch 6. As the model suggested, the attenuation coefficient for the waterlogged quarry where the experiment took place followed a skewed Gaussian distribution with depth, though only after particulates from terrestrial run-off had been account for. It is these particulates, grouped as NAP, that mean the derived models are better suited to describing oceanic optical channels. Despite being currently only applicable to oceanic channels, the attenuation-depth model represents a substantial contribution, giving those within the field of underwater optical communications a simple method for estimating the attenuation coefficient for all oceanic links, regardless of link

orientation, and requiring only information of the link location.

A valuable attribute of the attenuation-depth model derived is that it is independent of transmission wavelength. Whilst this makes the model applicable to any source transmitting in the visible spectrum, it also means an optimum wavelength can be found for any underwater optical wireless link. This is useful for researchers and communication engineers looking to design links for predetermined applications. Such method offers a significant contrast from the wavelength selection of previous experimental studies which is best described as haphazard; although wavelengths within the blue/green spectrum were chosen, in very few cases did the wavelength coincide with the optimum wavelength of the channel. In ch. 4, by surveying a large range of optical links – surface chlorophyll concentrations from 0 to 4 mg m^{-3} and at depths between 0 and 250 metres – select wavelengths were found to performed optimally. These wavelengths were 410 nm, 490 to 500 nm, 540 nm, and 560 nm and greater, rounded to the nearest 10 nm. The discretisation present in the optimal wavelength is attributed to the attenuation-wavelength profile shape and subsequently led to the advent of multi-wavelength transmitter designs in ch. 4. It is thought that with these transmitters, future smart communication systems shall be capable of selecting an appropriate wavelength based on their environment.

Two means of using the calculated attenuation coefficient profiles to find communication performance were introduced by this research. The first, in ch. 4, offered a set of link equations based on the Beer-Lambert law and an AGWN assumption, therefore excluding fading, dispersion and optical property variability within the path. A higher order model, the MCML in ch. 5, subsequently addressed these areas. MCML results found the average attenuation coefficient calculated from the attenuation-depth profiles to slightly overestimate the overall beam path attenuation. This disparity was associated with an additional contribution of re-scattered light in the MCML model. Interestingly, in terms of the experimental results, the initial Beer-Lambert model described the propagation sufficiently. In this case, unaccounted experimental losses may have counteracted the transmission gain from re-scattered light and the location meant the extent of turbulence was reduced.

The second optical property explored in this research was the refractive index. Variations with depth were considered in ch. 3; their impact determined in ch. 5. Unlike attenuation coefficient variations which alter the power received, refractive index variability was found to affect the directional properties of underwater optical communication links. Ray tracing revealed that, after propagating upwards of 200 metres through a refractive gradient generated by

pressure, salinity and temperature changes, a beam transmitted over a range of angles refracted from a straight path by up to 0.3 metres. Whether the transmitted beam could be detected at a receiver positioned conventionally in LOS with the transmitter depends on the transmitted FOV, the receiver size, the extent of scattering in the channel and the geometric relation of the beam with respects to the refractive gradient. By introducing the idea of refractive displacement in underwater optical wireless communications and providing a method to quantify it, this research highlights a new dimension to the aforementioned aspects of link design.

In summary, this research has shown the significance of optical property variability within the beam paths of singular underwater optical wireless communication links, where there had previously assumed to be none. The implications of this extend to all case 1 waters, regardless of link depth, link orientation or water turbidity. Based on this, it is anticipated that future technological advances in underwater optical wireless communications will involve learning from and adapting accordingly to their environment. The results showcased here offer a strong foundation from which this is possible.

7.2 Future Research

Throughout this research, several aspects have been recommended as potential areas of further study. By highlighting these areas, this section provides an outlook of the future landscape of underwater optical wireless communications.

Initially, this study set out with the aim of applying oceanographic descriptions of underwater light transport to optical wireless communications to better understand its variability. Whilst the research presented has made a sizable contribution, there is still a considerable gap between oceanographers' understanding of natural waters as propagation media and optical wireless channel models. To address this, the depth-dependent attenuation coefficient models derived here could be extended in several ways:

Chlorophyll-Concentration Range

The Haltrin model which forms the basis of the depth-dependent attenuation model is valid for chlorophyll-concentration ranges between 0 - 12 mg m^{-3} but depth-dependent chlorophyll profiles are limited to 0 - 4 mg^{-3}. Consequently, natural waters with chlorophyll concentrations in the range 4 - 12 mg^{-3} can readily be described by the depth-dependent model; the inland water body used for experimental purposes a prime example of this. However, such descriptions require the

formation of a method in which the chlorophyll profile coefficients (app. E) may be extracted from an attenuation-depth profile. If the aforementioned method is realised and programmed into an AUV then there exists the possibility of creating a smart underwater communication system that learns from and adapts to its environment. As sec. 3.4 showed, this would be particularly advantageous in a communication link with variable underwater orientation and location.

Lateral Variability

Optical variability characterisation has been mainly limited to quantifying changes in the attenuation coefficient with depth since lateral variability, or variability across the ocean surface, is on too great a scale to be noticeable by even the longest underwater optical link. Be that as it may, there are situations in which lateral changes occur within the scale of an optical wireless link; at the sea/freshwater interfaces in coastal regions or in open ocean locations affected by pollution, such as near an oil spillage.

Temporal Variability

In sec. 3.3.3, a framework to determine temporal attenuation changes was introduced, detailing the likely required inputs. This framework requires embellishing so that it may be added to depth-dependent and lateral-dependent attenuation models to create model which describes all underwater optical property variability. Such model would be applicable to all oceanic communication propagation, regardless of time, location and link orientation.

It is noted that small-scale temporal variability in the form of turbulence has not been included; prior research suggests that the temporal impact of turbulence on the open ocean links, which are characterised in this thesis using depth-dependent attenuation models, is not significant. This also means that first-order models of optical propagation in these locations should be of reasonable accuracy. However, the temporal consequence of turbulence in highly turbid areas is still unknown and could form the basis for future model amendments.

Constituents of Natural Waters

Recalling the derivation of the attenuation-depth profiles in ch 3, the constituents considered were restricted to pure water, phytoplankton and CDOM; others were detailed in sec. 2.3. Although models based on these three constituents are sufficient for oceanic case 1 waters, experimental results highlighted inaccuracies caused by the missing NAP component for inland and case 2 waters. As the NAP concentration cannot be related to the chlorophyll concentration, additional

inputs are required to model the attenuation variability caused by it.

In addition to the attenuation variability model appendages described above, in sec. 3.3 it was found that the model itself could be adapted. Instead basing optical property variability on the Haltrin model in (Haltrin, 1999), an updated bio-optical model could be used (Solonenko & Mobley, 2015); it was shown to be more accurate, particularly towards either end of the visible spectrum. Unfortunately, the application of this model is not included here as it post-dates much of the research. Having said this, one advantage of having a Haltrin-based attenuation model is that it is applicable to both case 1 and case 2 waters. As well as the underlying optical property variability, improvements can be found in the way in which optical properties are used to determine the communication performance. By finding a method to convolve known transmitter beams to the MCML results, aspects such as the SNR and BER can be estimated for a channel with variable optical properties.

The final part of this study with significant capacity for further research is the practical aspect. Having assessed the vertical attenuation coefficient variability in an inland water body, this should be extended to open and coastal oceans to further validate the attenuation-depth model. A practical system may also be designed in these locations to explore the extent of beam refraction over a variable refractive index gradient. The collective results would be of particular interest for optical links propagating over a variable orientation or location, such as the link between a base station and a moving AUV, as a means of estimating link performance.

Future practical uses of the research presented here are found through the projected landscape for underwater optical wireless envisioned in fig. 1.2. It is thought that with additional investigations of the air/water interface interaction, the attenuation-depth models derived could be used as part of the models describing a full air-to-sea link. Meanwhile, in terms of AUV technology, the presented research has the potential to be implemented towards the design of a new generation of smart underwater communication systems capable of understanding and adapting to optical property variability in the underwater optical wireless channel.

Appendices

Appendix A

Pure Water Absorption Spectrum

λ (nm)	a_W (m^{-1})	λ (nm)	a_W (m^{-1})	λ (nm)	a_W (m^{-1})
400	0.0171	500	0.0257	600	0.244
410	0.0162	510	0.0357	610	0.289
420	0.0153	520	0.0477	620	0.309
430	0.0144	530	0.0507	630	0.319
440	0.0145	540	0.0558	640	0.329
450	0.0145	550	0.0638	650	0.349
460	0.0156	560	0.0708	660	0.4
470	0.0156	570	0.0799	670	0.43
480	0.0176	580	0.108	680	0.45
490	0.0196	590	0.157	690	0.5

Table A.1: Pure natural water absorption spectrum (natural pure water without added salts) in the visible region, from (Smith & Baker, 1981).

λ (nm)	a_{W} (m^{-1})	λ (nm)	a_{W} (m^{-1})	λ (nm)	a_{W} (m^{-1})
400	0.00663	500	0.0204	600	0.2224
402.5	0.00579	502.5	0.0228	602.5	0.247
405	0.0053	505	0.0256	605	0.2577
407.5	0.00503	507.5	0.028	607.5	0.2629
410	0.00473	510	0.0325	610	0.2644
412.5	0.00452	512.5	0.0372	612.5	0.2665
415	0.00444	515	0.0396	615	0.2678
417.5	0.00442	517.5	0.0399	617.5	0.2707
420	0.00454	520	0.0409	620	0.2755
422.5	0.00474	522.5	0.0416	622.5	0.281
425	0.00478	525	0.0417	625	0.2834
427.5	0.00482	527.5	0.0428	627.5	0.2904
430	0.00495	530	0.0434	630	0.2916
432.5	0.00504	532.5	0.0447	632.5	0.2995
435	0.0053	535	0.0452	635	0.3012
437.5	0.0058	537.5	0.0466	637.5	0.3077
440	0.00635	540	0.0474	640	0.3108
442.5	0.00696	542.5	0.0489	642.5	0.322
445	0.00751	545	0.0511	645	0.325
447.5	0.0083	547.5	0.0537	647.5	0.335
450	0.00922	550	0.0565	650	0.34
452.5	0.00969	552.5	0.0593	652.5	0.358
455	0.00962	555	0.0596	655	0.371
457.5	0.00957	557.5	0.0606	657.5	0.393
460	0.00979	560	0.0619	660	0.41
462.5	0.01005	562.5	0.064	662.5	0.424
465	0.01011	565	0.0642	665	0.429
467.5	0.0102	567.5	0.0672	667.5	0.436
470	0.0106	570	0.0695	670	0.439
472.5	0.0109	572.5	0.0733	672.5	0.448
475	0.0114	575	0.0772	675	0.448

477.5	0.0121	577.5	0.0836	677.5	0.461
480	0.0127	580	0.0896	680	0.465
482.5	0.0131	582.5	0.0989	682.5	0.478
485	0.0136	585	0.11	685	0.486
487.5	0.0144	587.5	0.122	687.5	0.502
490	0.015	590	0.1351	690	0.516
492.5	0.0162	592.5	0.1516	692.5	0.538
495	0.0173	595	0.1672	695	0.559
497.5	0.0191	597.5	0.1925	697.5	0.592

Table A.2: Pure seawater absorption spectrum (pure water with added salts) in the visible region, from (Pope & Fry, 1997).

Appendix B

Specific Absorption of Chlorophyll

λ (nm)	F_1	F_2	λ (nm)	F_1	F_2
400	0.0263	0.282	550	0.0080	0.052
410	0.0313	0.283	560	0.0062	0.016
420	0.0356	0.299	570	0.0053	0.005
430	0.0386	0.314	580	0.0053	0.035
440	0.0403	0.332	590	0.0056	0.073
450	0.0371	0.359	600	0.0054	0.092
460	0.0350	0.365	610	0.0057	0.071
470	0.0332	0.368	620	0.0065	0.064
480	0.0301	0.377	630	0.0071	0.078
490	0.0274	0.361	640	0.0077	0.098
500	0.0230	0.321	650	0.0083	0.124
510	0.0180	0.260	660	0.0115	0.121
520	0.0143	0.196	670	0.0189	0.149
530	0.0117	0.139	680	0.0182	0.155
540	0.0097	0.090	690	0.0083	0.086
550	0.0080	0.052	700	0.0030	0.034

Table B.1: F_1 and F_2 factors in eq. 2.19 and eq. 3.9 to calculate the specific absorption coefficient of chlorophyll for visible wavelengths, from (Bricaud et al., 1995).

Appendix C

Phase Scattering Functions

Here is a summary of the three common phase scattering functions for underwater light propagation; the Henyey-Greenstein function, Pezold's measurements and the Fournier-Forand function.

The *Henyey-Greenstein phase function* (Henyey & Greenstein, 1941), $\tilde{\beta}_{\mathrm{HG}}$, was the first analytical phase function devised, initially used to describe the directional light scatter of interstellar dust clouds. It is based on the parameter g which can be adjusted to control the relative amounts of forward and backward scattering in $\tilde{\beta}_{\mathrm{HG}}$; $g = 0$ corresponds to isotropic scattering, whilst $g \rightarrow 1$ gives a highly peaked forward scattering function. The Henyey-Greenstein phase function equation is given as

$$\tilde{\beta}_{\mathrm{HG}}(g,\theta) \equiv \frac{1}{4\pi} \frac{1-g^2}{(1+g^2-2g\cos\theta)^{3/2}} \tag{C.1}$$

This can be integrated over θ from $\pi/2$ to π to obtain the backscatter coefficient

$$B_{\mathrm{HG}} = \frac{1-g}{2g}\left[\frac{1+g}{\sqrt{1+g^2}} - 1\right] \tag{C.2}$$

Due to its mathematical simplicity, the Henyey-Greenstein phase function is widely used in many fields, including oceanography. However, because $\tilde{\beta}_{\mathrm{HG}}$ is based on interstellar dust scatter observations and scattering particulates in aquatic media are quite different in terms of their physical properties, other more accurate functions have subsequently been derived.

Pezold's measurements, which are found in (Petzold, 1972), are another set of phase scattering functions. The measurements were derived using two instruments, one for VSF measurements at very small angles ($\theta = 0.172$, 0.344, and 0.688°) and one for angles between 10° and 170° , to obtain

VSF measurements over almost the full range of scattering angles. Petzold's report describes his instruments and their calibration and validation, with data tabulated from very clear, productive coastal and turbid harbour waters. Pezold's measurements are seen to better represent the shape of the forward peak in the phase scattering function for oceanic particulates, in comparison with Henyey-Greenstein functions.

Unlike Pezold's measurements, the *Fournier-Forand* phase scattering function is an approximate analytical form of the phase function for particulates in the ocean and other aqueous environments (Fournier & Forand, 1994). It is assumed in this model that particulates have a hyperbolic particle size distribution, with each particle scattering according to the anomalous diffraction approximation of the exact Mie theory. The form of the resulting analytical equation is more complex than the Henyey-Greenstein function and for this reason is not included in this text, however, it is available in (Fournier & Jonasz, 1999).

The Fournier-Forand analytical model is the most accurate at reproducing the shapes of ocean phase functions, especially at very small angles. However, it should be noted that there is some discrepancy between the measured and modelled data at wavelengths near 180°, though this may be due in part to instrumental error. In any case, Fournier-Forand phase functions currently give the best fits to measurements of any analytical model developed so far. For this reason, they are now commonplace in numerical simulations, having replaced other analytic models for most underwater simulations.

Appendix D

Rayleigh Scattering Coefficients

λ (nm)	$\beta_{\mathrm{W}}(90°)\ 10^{-4}$ ($\mathrm{m}^{-1}\ \mathrm{sr}^{-1}$)	$b_{\mathrm{W}}\ 10^{-4}$ (m^{-1})
350	8.41	134.5
375	6.24	99.8
400	4.72	75.5
425	3.63	58.1
450	2.84	45.4
475	2.25	35.9
500	1.80	28.8
525	1.46	23.3
550	1.21	19.3
575	1.01	16.2
600	0.88	14.1

Table D.1: Wavelength dependent Rayleigh scattering coefficients for pure seawater, where the volume scattering coefficient $\beta_{\mathrm{W}}(90°)$ is from (Morel, 1974) and the scattering coefficient is calculated from eq. 2.32

.

Appendix E

Chlorophyll-Depth S Profiles

	$C_{\mathrm{CHL-S}}$ (mg m^{-2})	F_0 (mg m^{-3})	S_{CHL} 10^{-3} (mg m^{-2})	F_T (mg)	$z_{\max}$ (m)	$C_{\mathrm{CHL}}(z_{\max})$ (mg m^{-2})	z_∞ (m)
S1	< 0.04	0.0429	-0.103	11.87	115.4	0.708	415.5
S2	0.04 - 0.08	0.0805	-0.260	13.89	92.01	1.055	309.6
S3	0.08 - 0.12	0.0792	-0.280	19.08	82.36	1.485	282.2
S4	0.12 - 0.2	0.143	-0.539	15.95	65.28	1.326	264.2
S5	0.2 - 0.3	0.207	-1.03	15.35	46.61	1.557	200.7
S6	0.3 - 0.4	0.160	-0.705	24.72	33.03	3.323	226.8
S7	0.4 - 0.8	0.329	-1.94	25.21	24.59	3.816	169.1
S8	0.8 - 2.2	1.01	-9.03	20.31	20.38	4.556	111.5
S9	2.2 - 4	0.555	0	130.6	9.87	136.5	-

Table E.1: Gaussian parameter values for the chlorophyll concentration of the ocean with depth, where profiles S1 - S9 represent increasing surface chlorophyll. Adapted from (Johnson et al., 2013), which is based on original observations in (Uitz et al., 2006).

Appendix F

Noise Calculations

Underwater optical wireless communication noise relations, based on (Giles & Bankman, 2005) and (Jaruwatanadilok, 2008).

$$P_{\mathrm{SHO-BG}} = \frac{\sqrt{\pi q S_R P_{\mathrm{BG}}\ \mathrm{BW} F_N}}{S_R} \tag{F.1}$$

$$P_{\mathrm{SHO-T}} = \frac{\sqrt{\pi q S_R P_T\ \mathrm{BW} F_N}}{S_R} \tag{F.2}$$

$$P_{\mathrm{DRK}} = \frac{\sqrt{\pi (q \mathrm{I}_{\mathrm{DRK}} G_R^2 F_N + q \mathrm{I}_{\mathrm{DC}})\ \mathrm{BW}}}{S_R G_R} \tag{F.3}$$

$$P_{\mathrm{AMP}} = \frac{\mathrm{I}_{\mathrm{AMP}} \sqrt{\pi\ \mathrm{BW}}}{\sqrt{2} S_R G_R} \tag{F.4}$$

BW	bandwidth (Hz)
$\mathrm{I}_{\mathrm{DRK}}$	multiplied dark current (A)
I_{DC}	non-multiplied dark current, also DC (A)
$\mathrm{I}_{\mathrm{AMP}}$	preamplifier current noise density (A)
F_N	excess noise factor = 1 for photodiode, > 1 for avalanche photodiode.
G_R	detector current gain
P_{BG}	ambient optical power on detector (W)
P_T	transmitted power (W)
q	electronic charge (1.602 x 10^{-19} C)
S_R	radiant sensitivity of the detector (A W^{-1}),

Appendix G

Average Vertical Link Attenuation

		410 nm	490 nm	500 nm	mean
	z (m)		average c (m^{-1})		
	0 - 100	**0.050011**	0.054053	0.054905	0.050913
S1	50 - 150	**0.070626**	0.070714	0.071127	0.074515
	100 - 200	**0.061670**	0.063503	0.064128	0.064951
	0 - 100	0.093209	0.089060	0.089082	0.089933
S3	50 - 150	0.094157	**0.089824**	0.089832	0.090713
	100 - 200	**0.059353**	0.061608	0.062299	0.062882
	0 - 100	0.146781	0.132246	**0.131473**	**0.131473**
S6	50 - 150	0.083889	**0.081474**	0.817072	0.084682
	100 - 200	**0.042341**	0.047800	0.048843	**0.042341**

Table G.1: Average attenuation of three vertical 100 metre optical links in a water column with the S1, S3 and S6 chlorophyll concentration profiles from app. E, for wavelengths at 410 nm, 490 nm, 500 nm and a mean wavelength calculated as the average of the optimal wavelength taken at each depth increment. Wavelengths are rounded to the nearest 10 nm. Minimum attenuation at each depth range, for each S profile, given in bold.

Appendix H

Transmitter and Receiver Component List

Transmitter	Type	λ (nm)	P_T (mW)	θ_T (°)	$P_T/\tan^2(\theta_T)$
LED631E	LED	635	4	20	0.07484
LED591E	LED	590	2	10	0.1595
LPS-675-FC	LD	670	2.5	8	0.3137
LED525E	LED	525	2.6	7.5	0.3718
L635P5	LD	635	5	8	0.6275
HL6312G	LD	635	5	8	0.6275
L637P5	LD	637	5	8	0.6275
L650P007	LD	650	7	9	0.6917
LED528EHP	LED	525	7	9	0.6917
LED630E	LED	639	7.2	7.5	1.030
HL6320G	LD	635	10	8	1.255
HL6358MG	LD	639	10	8	1.255
HL6748MG	LD	670	10	8	1.255
HL6714G	LD	670	10	8	1.255
HL6322G	LD	635	15	8	1.882
HL6756MG	LD	670	15	8	1.882
L405P20	LD	405	20	8.5	2.220
LED465E	LED	465	20	8	2.510

L638P040	LD	638	40	10	3.189
HL6362MG	LD	640	40	10	3.189
L658P040	LD	658	40	10	3.189
LED405E	LED	405	10	5	3.238
HL6323MG	LD	639	30	8.5	3.329
HL6501MG	LD	658	30	8.5	3.329
HL6738MG	LD	690	30	8.5	3.329
L658P050	LD	658	50	10	3.986
HL6544FM	LD	660	50	10	3.986
L488P060MLD	LD	488	60	10	4.784
HL6364DG	LD	642	60	10	4.784
HL6750MG	LD	685	50	9	4.941
DL5146-101S	LD	405	40	8	5.020
HL6366DG	LD	642	80	10	6.378
L520P50	LD	520	45	7	7.399
PL520	LD	520	50	7	8.221
HL63163DG	LD	633	100	8.5	11.10
PL450B	LD	450	80	7.5	11.44
HL63142DG	LD	637	100	8	12.55
LED470L	LED	470	170	7	27.95
LED635L	LED	635	170	7	27.95
DJ532-10	LD	532	10	0.69	170.9
DJ532-40	LD	532	40	0.68	703.8
LPS-635-FC	LD	635	2.5	0.1	2034
LPS-PM635-FC	LD	635	2.5	0.1	2034
LP473-SF6	LD	473	6	0.1	4882
LPS-660-FC	LD	658	7.5	0.1	6103
LPM-635-SMA	LD	635	8	0.1	6510
LP635-SF8	LD	635	8	0.1	6510
LP405-SF10	LD	405	10	0.1	8137
LP450-SF15	LD	450	15	0.1	12206
LP520-SF15	LD	520	15	0.1	12206
LP685-SF15	LD	685	15	0.1	12206

LP406-SF20	LD	406	20	0.1	16274
LP488-SF20	LD	488	20	0.1	16274
LP642-SF20	LD	642	20	0.1	16274
LP642-PF20	LD	642	20	0.1	16274
LP660-SF20	LD	658	20	0.1	16274
LPM-660-SMA	LD	658	22.5	0.1	18309
LP405-SF30	LD	405	30	0.1	24412
LP660-SF40	LD	658	40	0.1	32549
LP660-SF60	LD	658	60	0.1	48823
LP405-MF70	LD	405	70	0.1	56961
LP637-SF70	LD	637	70	0.1	56961
LP405-MF80	LD	405	80	0.1	65098
LP520-MF100	LD	520	100	0.1	81372

Table H.1: List of available transmitter sources from (Thorlabs, 2014).

Receiver	Type	P_N (W)	D_R (mm^2)	θ_R (°)	$D_R \cos(\theta_R)$
FPD310-FV	Si PIN RF	$3.00\ 10^{-08}$	0.13	30	$8.403\ 10^{-08}$
FPD510-FV	Si PIN RF	$6.00\ 10^{-09}$	0.13	30	$8.403\ 10^{-08}$
APD210	Si avalanche	$4.00\ 10^{-10}$	0.39	30	$8.206\ 10^{-07}$
PDA8A	Si transimpedance	$6.50\ 10^{-12}$	0.50	30	$1.330\ 10^{-06}$
PDA10A	Si transimpedance	$3.50\ 10^{-11}$	0.80	30	$3.405\ 10^{-06}$
PDF10	Si transimpedance	$1.40\ 10^{-15}$	1.20	30	$7.662\ 10^{-06}$
APD120A2	Si avalanche	$2.10\ 10^{-10}$	3.14	60	$3.032\ 10^{-05}$
APD120A	Si avalanche	$2.00\ 10^{-10}$	3.14	60	$3.032\ 10^{-05}$
PDA25K (0 dB)	GaP transimpedence	$3.00\ 10^{-10}$	4.80	60	$7.078\ 10^{-05}$
PDA25K (10 dB)	GaP transimpedence	$1.00\ 10^{-10}$	4.80	60	$7.078\ 10^{-05}$
PDA25K (20 dB)	GaP transimpedence	$4.00\ 10^{-11}$	4.80	60	$7.078\ 10^{-05}$
PDA25K (30 dB)	GaP transimpedence	$2.00\ 10^{-11}$	4.80	60	$7.078\ 10^{-05}$
PDA25K (40 dB)	GaP transimpedence	$1.60\ 10^{-11}$	4.80	60	$7.078\ 10^{-05}$
PDA25K (50 dB)	GaP transimpedence	$1.70\ 10^{-11}$	4.80	60	$7.078\ 10^{-05}$
PDA25K (60 dB)	GaP transimpedence	$1.00\ 10^{-11}$	4.80	60	$7.078\ 10^{-05}$
PDA25K (70 dB)	GaP transimpedence	$7.00\ 10^{-12}$	4.80	60	$7.078\ 10^{-05}$

PDA36A (0 dB)	Si transimpedance	$2.91\ 10^{-11}$	13.00	60	$5.192\ 10^{-04}$
PDA36A (10 dB)	Si transimpedance	$7.52\ 10^{-12}$	13.00	60	$5.192\ 10^{-04}$
PDA36A (20 dB)	Si transimpedance	$2.34\ 10^{-12}$	13.00	60	$5.192\ 10^{-04}$
PDA36A (30 dB)	Si transimpedance	$1.21\ 10^{-12}$	13.00	60	$5.192\ 10^{-04}$
PDA36A (40 dB)	Si transimpedance	$5.93\ 10^{-13}$	13.00	60	$5.192\ 10^{-04}$
PDA36A (50 dB)	Si transimpedance	$7.94\ 10^{-13}$	13.00	60	$5.192\ 10^{-04}$
PDA36A (60 dB)	Si transimpedance	$1.43\ 10^{-12}$	13.00	60	$5.192\ 10^{-04}$
PDA36A (70 dB)	Si transimpedance	$2.10\ 10^{-12}$	13.00	60	$5.192\ 10^{-04}$
PDA100A (0 dB)	Si transimpedance	$2.70\ 10^{-11}$	100.00	60	$3.072\ 10^{-02}$
PDA100A (10 dB)	Si transimpedance	$1.10\ 10^{-11}$	100.00	60	$3.072\ 10^{-02}$
PDA100A (20 dB)	Si transimpedance	$8.91\ 10^{-12}$	100.00	60	$3.072\ 10^{-02}$
PDA100A (30 dB)	Si transimpedance	$4.65\ 10^{-12}$	100.00	60	$3.072\ 10^{-02}$
PDA100A (40 dB)	Si transimpedance	$3.55\ 10^{-12}$	100.00	60	$3.072\ 10^{-02}$
PDA100A (50 dB)	Si transimpedance	$2.42\ 10^{-12}$	100.00	60	$3.072\ 10^{-02}$
PDA100A (60 dB)	Si transimpedance	$1.22\ 10^{-12}$	100.00	60	$3.072\ 10^{-02}$
PDA100A (70 dB)	Si transimpedance	$9.73\ 10^{-13}$	100.00	60	$3.072\ 10^{-02}$

Table H.2: List of available pre-built receivers from (Thorlabs, 2014).

Appendix I

Previous Experimental Studies

A comprehensive list of all experimental studies on underwater optical wireless to date is compiled in tab. I.1. Additional notes for this table are available below.

[1] Maximum range stated where several link distances are established.

[2] Maximum data rate stated where several data rates are established.

[3] Where the exact attenuation coefficient has not been stated, the environments are categorised into the following; Pure is pure water (usually found in test tanks), Clear is open ocean waters, Coastal is coastal water, Turbid is turbid harbours, and Inland is river or lake water. This relates to the classification comparison in fig. 3.4. The attenuation of the respective groups is assumed to be; 0.05 m s^{-1} for Pure, 0.12 m s^{-1} for Clear, 0.5 m s^{-1} for Coastal and 2 m^{-1} for Turbid/Inland.

[4] Source type, rated power and wavelength are noted, where possible. In some cases, the wavelength is given as a colour, e.g. *blue*, as per its originating study. Modulations schemes are mentioned where the study uses a scheme other than OOK including several schemes not previously surveyed by this research; phase-shift keying (PSK), binary PSK (BPSK), digital pulse interval modulation (DPIM) and Gaussian minimum-shift keying (GMSK). Moreover, Reed-Solomon (RS), turbo and b are all communication coding schemes.

Year	Reference	Range [1]	Data Rate [2]	Environment, c [3]	Notes [4]
1992	(Snow et al., 1992)	9 m	< 50 Mb s^{-1}	Coastal, < 0.19 m^{-1}	150 mW 514 nm LD, 15 mW 532 nm LD
1995	(Bales & Chrissostomidis, 1995)	20 m	< 10 Mb s^{-1}	Pure, < 0.05 m^{-1}	30 mW 660 nm LED, 1 mW 450 nm LED
2004	(Tivey et al., 2000)	2.7 m	14.4 kb s^{-1}	Pure	IrDA, infrared LED, omnidirectional
2004	(Schill et al., 2004)	2 m	57.6 kb s^{-1}	Pure	IrDA, 3 W 460 nm 490 nm 520 nm LEDs
2005	(Chancey, 2005)	4.6 m	10 Mb s^{-1}	Pure	1 W 475 nm 505 nm 525 nm LEDs
2005	(Farr et al., 2006)	91 m	10 Mb s^{-1}	Pure	6 470 nm LED, PMT
2005	(Vasilescu et al., 2005)	5.8 m	100 kb s^{-1}	Inland, 0.71 m^{-1}	700 mW 532 nm LED
2006	(Cochenour et al., 2006)	3 m	1 Mb s^{-1}	Turbid, < 2.4 m^{-1}	3 W 532 nm LD, BPSK
2006	(Chen et al., 2006)	50 m		Pure	532 nm LD, 256-PPM
2007	(Cochenour et al., 2007)	3.6 m	5 Mb s^{-1}	Turbid, 2.3 m^{-1}	3W 532 nm LD, M-PSK, M-QAM
2008	(Hanson & Radic, 2008)	2 m	1 Gb s^{-1}	Clear, < 0.12 m^{-1}	532 nm LD
2008	(Pontbriand et al., 2008)	200 m	5 Mb s^{-1}	Clear, 0.025 m^{-1}	470 nm 660 nm LD transmissometer
2008	(Cox, 2008)		1 Mb s^{-1}	Clear	405 nm 635 nm LDs, PMT
2008	(Cox et al., 2008)	3.66 m	500 kb s^{-1}	Turbid, < 2.5 m^{-1}	405 nm LD, PMT, RS coding
2009	(Doniec et al., 2009)	30 m	1.2 Mb s^{-1}	Pure	500 mW 470 nm 530 nm LEDs, DPIM

2009	(Cochenour et al., 2009)	3.68 m		Turbid, < 3.2 m^{-1}	532 nm LD, PMT, BSF characterisation
2009	(Simpson et al., 2009)	0.6 m	500 kb s^{-1}	Turbid	Parallel 405 nm LD, bubbles, turbulence
2009	(Anguita et al., 2009)	1.9 m	100 kb s^{-1}	Clear	Blue LED, 4-PPM, 16-PPM
2009	(Baiden et al., 2009)	3.26 m	10 Mb s^{-1}	Inland	Blue LED array, duplex, omnidirectional
2009	(Lu et al., 2009)	10 m		Clear	120 mW 520 nm LED, low ambient
2010	(Brundage, 2010)	13 m	3 Mb s^{-1}	Clear	4.8 W 465 nm LED array
2010	(Simpson et al., 2010)	3 m	5 Mb s^{-1}	Turbid, < 0.5 m^{-1}	3 W 470 nm 525 nm white LEDs, RS coding
2010	(Simpson et al., 2010)	7.7 m	5 Mb s^{-1}	Coastal, 0.25 m^{-1}	3 W 470 nm 525 nm white LEDs, RS coding
2010	(Farr et al., 2010)	138 m	> 1 Mb s^{-1}	Clear, 0.05 m^{-1}	15-20 W blue-green LED array, acoustic alignment
2010	(Camilli et al., 2010)	100 m	1 Mb s^{-1}	Clear	Blue-green LED array, omnidirectional
2010	(Doniec & Rus, 2010)	50 m	< 2.28 Mb s^{-1}	Pure, 0.03 m^{-1}	18 470 nm LED array, DPIM
2011	(Anguita et al., 2010)	2 m		Pure	12 428 nm LED, omnidirectional
2011	(Cochenour & Mullen, 2011)	7.6 m		Turbid, < 3.7	532 nm LD, PMT, NLOS
2011	(Cox et al., 2011)	3.66 m	1 Mb s^{-1}	Coastal, < 0.19 m^{-1}	30 mW 410 nm LD, duplex, GMSK
2011	(Anguita et al., 2011)	1.8 m	100 kb s^{-1}	Pure	18 428 nm LED array, 4-PPM, 16-PPM
2011	(Hagem et al., 2011)	1.1 m	2.4 kb s^{-1}	Pure	1.5 mW 520 nm LD, FSK, bubbles, wearable

2012	(Simpson et al., 2012)	3.66 m		Turbid, < 9 m^{-1}	7 LEDs, RS coding, turbo coding, LDPC, omnidirectional
2012	(Dy & Gustilo, 2012)	0.58 m	1 Mb s^{-1}	Pure	7 Blue LED array, air/water interface
2012	(Destrez et al., 2012)	2.1 m	1 Mb s^{-1}	Pure	12 470 nm LED array, omnidirectional
2013	(Doniec et al., 2013)	< 50 m	8 Mb s^{-1}	Pure	18 470 nm LED array, 18-b coding
2013	(Cossu et al., 2013)	2.5 m	58 Mb s^{-1}	Pure	14 470 nm LED array, PMT, sunlight
2013	(Tian et al., 2013)	25 m	< 38.4 kb s^{-1}	Pure	500 mW 485 nm LED, small size
2013	(Gabriel et al., 2013)	3.5 m		Coastal, 0.43 m^{-1}	4.6 W 528 nm LED, misalignment
2013	(Cochenour, 2013)	7.6 m		Turbid, < 2.31 m^{-1}	4 W 532 nm LD, PMT, misalignment, temporal
2014	(Islam & Faruque, 2014)		2.5 Mb s^{-1}	Clear	Green LD, orthogonal OOK, turbulence
2014	(Sun et al., 2014)	4.5 m	3.6 Mb s^{-1}	Coastal	50 mW 488 nm LD, Mach-Zender, PMT
2014	(Rosenkrantz & Arnon, 2014)	< 17 m		Turbid	3 W 950 nm 635 nm 590 nm 532 nm 482 nm LEDs
2014	(Mizukoshi et al., 2014)	2 m	968 Mb s^{-1}	Pure	405 nm LD,16-QAM IM/DD-OFDM
2015	(Fasham & Dunn, 2015)	100 m	20 Mb s^{-1}	Clear	Blue LED array, PMT, sunlight
2015	(Nakamura et al., 2015)	4.8 m	1.45 Gb s^{-1}	Pure	405 nm LD, 64-QAM IM/DD-OFDM
2015	(Oubei et al., 2015)	5.4 m	4.8 Gb s^{-1}	Pure	405 nm LD,16-QAM IM/DD-OFDM

Table I.1: Bit rates, link length, turbidity and transmission technology of previous experiments in underwater optical communications.

Appendix J

Photographic Documentary of Experimental Issues

(a) Isogyre A

(b) Isogyre B

(c) Real spatial profile

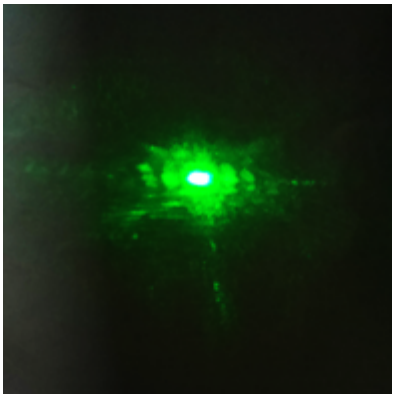

Figure J.1: EO modulator isogyre intensity interference pattern, where (a) and (b) are from the user manual at (Thorlabs, 2015) and (c) is a photograph from the experimental set up.

(a) Bright sunlight

(b) Sun behind clouds

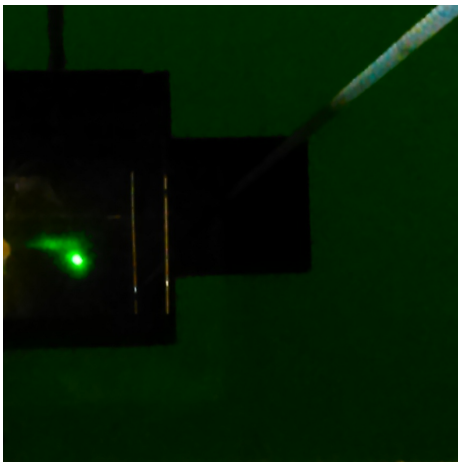

Figure J.2: Images of the experimental set up showing the effect of upwelling sunlight on the received signal.

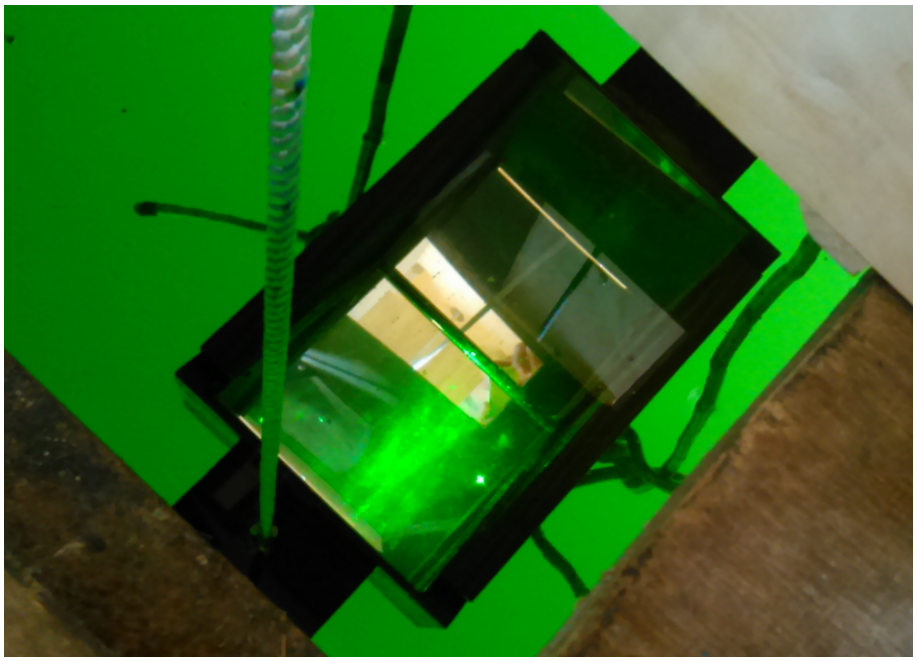

Figure J.3: Image of the experimental set up showing multiple reflections on the mirror.

Glossary

This section has been restricted to the unfamiliar optical oceanography terms that appear in this text. Note that some descriptions are based on those in (Mobley et al., 2014).

absorptance	The fraction of incident power that is absorbed within a volume of a substance, for a given wavelength.
absorption	The process of radiant energy being converted to non-radiant energy, for example, to thermal, chemical, vibrational, or rotational energy of a molecule. Absorption results in the disappearance of photons from a transmitted beam path.
absorption coefficient	The absorptance per unit distance for a photons travelling through a medium. Defined per metre for aquatic media.
aphotic zone	The portion of the ocean where downwelling sunlight is insufficient for phytoplankton and plants to photosynthesise.
apparent optical property	An optical quantity that depends on the inherent optical properties of an aquatic body as well as weakly on the external environment (for example, sun angle or surface waves). Apparent optical properties are either ratios of radiometric quantities or depth derivatives of radiometric quantities; radiometric variables themselves (radiance, irradiance, etc.) are not apparent optical properties.

attenuation coefficient The limit of the ratio of absorptance plus scatterance to the distance of photon travel as the distance becomes infinitesimally small. Equal to the sum of the absorption and scattering coefficients. Defined per metre.

back scattering Scattering at angles greater than 90° relative to the incident or original transmitted beam direction.

Beer-Lambert law The law which states that radiation travelling in a certain direction in a medium with scattering and absorption exponentially attenuated with distance travelled.

bio-geo-optical model A class of analytical and numerical models that parameterise the absorption and scattering properties of natural water constituents (phytoplankton, colour dissolved organic material, non-algal particles) in terms of the concentrations of those constituents (such as chlorophyll concentration) or other parameters.

bioluminescence Light produced by living underwater organisms via a conversion of chemical energy to radiant energy.

case 1 water Natural waters in which the absorption and scattering properties are determined primarily by phytoplankon and their degradation products (non-algal particles and colour dissolved organic material). Subsequent inherent optical properties can be parameterised by the chlorophyll concentration.

case 2 water Natural waters in which the absorption and scattering properties are significantly influenced by mineral particles or colour dissolved organic material not derived from phytoplankton (instead from terrestrial runoff, etc.). Consequentially, inherent optical properties do not correlate well with chlorophyll concentration.

chlorophyll The chemical compounds occurring in plants that enables radiant energy to be converted to chemical energy by the process of photosynthesis.

coastal water This refers to water situated over continental shelves. Generally, but not always, comes under the definition of case 1 waters.

coloured dissolved organic material High molecular weight organic compounds (humic and fulvic acids) formed from the decomposition of plant tissue; they strongly absorb light at the blue end of the spectrum with a further peak in the red, giving water a yellow colour at high concentrations. Also called yellow matter, gilvin or Gelbstoff.

deep chlorophyll maximum The depth in the water column where the highest concentration of chlorophyll occurs; generally a balance between sunlight availability and nutrients availability.

diffuse attenuation coefficients Apparent optical properties; the negative of the derivative with respect to depth of the natural logarithm of a radiometric variable (for example, radiance, downwelling or upwelling irradiance). Defined per metre.

photic zone The upper region of a water body in which significant phytoplankton photosynthesis can take place.

eutrophic water Water with high phytoplankton biomass; chlorophyll concentration exceeds 10 mg m^{-3}.

fluorescence An inelastic scattering process where photons are absorbed by a molecule and shortly thereafter another photon of greater wavelength is emitted.

fulvic substance High molecular weight organic compounds resulting from plant decay, especially phytoplankton; one component of coloured dissolved organic matter.

Haltrin model A one-parameter bio-optical model for the absorption and scattering coefficients, derived by Haltrin for Case 1 and some Case 2 waters, based on the chlorophyll concentration.

Henyey-Greenstein phase function An analytical model for phase scattering functions that parameterises the shape of the phase function via an asymmetry parameter. Based on atmospheric optics so can be inaccurate.

humic substance High molecular weight organic compounds resulting from plant decay, especially terrestrial plants; see coloured dissolved organic matter.

inherent optical property In optical oceanography, any optical quantity that depends only on the properties of the water and is independent of the ambient light field is an inherent optical property. The absorption coefficient and the volume scattering function are the fundamental inherent optical properties.

inland waters Natural waters which are not situated in or around the ocean. These waters which are turbid in nature, coming under the definition of Case 2 waters.

intensity The radiant spectral power in a given direction per unit solid angle per unit wavelength interval. Intensity is used to describe the light emitted by point sources.

irradiance The radiant power per unit area per unit wavelength interval. Commonly used irradiances are the downwelling and upwelling irradiance.

isotropic An adjective meaning equal in all directions or independent of direction. An isotropic medium distribution has the same inherent optical properties in every direction, whereas isotropic scattering means light is scattered equally in all directions.

Jerlov water type A water clarity classification scheme based on the downwelling diffuse attenuation coefficient just below the sea surface.

Maalox Antacid An agent which is mixed with water to create similar scattering and absorption coefficients to oceanic waters. Used frequently in experimental test tanks.

mesotrophic water Water with moderate concentrations of phytoplankton biomass; chlorophyll concentration ranges between 0.5 and 10 mg m^{-3}.

Mie scattering An exact solution of Maxwell's equations that describes the scattering of electromagnetic waves, such as visible light, by homogeneous spheres of any size. Use of the theory requires knowledge of the refractive index of the sphere relative to the surrounding medium and the ratio of the sphere's circumference to the wavelength of light in the medium. Mie scattering is peaked in the forward direction.

Monte Carlo Algorithms that use probability theory and random numbers to simulate a large number of photons propagating through a medium. Come with associated probabilistic errors.

multiple-scattering Photons which have undergone several scattering events before being received. In simple propagation models such as the Beer-Lambert law, these photons are ignored.

non-algal particles The particulate decomposition or disintegration products of plankton, including dead cells, cell fragments, faecal pellets, shells, and skeletons. Sometimes considered to include inorganic mineral particles.

oligotrophic water Water with low phytoplankton biomass, typical in many open ocean regions; chlorophyll concentration is below 0.5 mg m^{-3}.

open ocean Ocean water that is away in the seaward direction from continental shelves; mostly always Case 1 water with low turbidity.

phase function The ratio of the volume scattering function to the scattering coefficient such that the integral of the phase function over all directions is unity.

photosynthesis The formation of carbohydrates from carbon dioxide and water in the presence of chlorophyll. Utilises radiant energy to releasing oxygen.

phytoplankton Small, usually single-cell, organisms living in oxygenated environments. They are photosynthetic, meaning they are pigmented, containing chlorophyll and use sunlight in the manufacture of oxygen.

pure water An aquatic body containing only water or, exceptionally, water with some inorganic mineral compounds such as salts. Used generally to describe the water of testing tank facilities in underwater optical communications.

radiance The radiant power in a beam per unit solid angle, per unit area perpendicular to the beam, per unit wavelength interval. Radiance is the fundamental radiometric quantity from which all others can be derived.

radiative transfer equation A linear integro-differential equation that expresses conservation of energy in terms of the radiance. The radiative transfer equation describes the rate of change with distance of the radiance in a collimated beam with a specified location, direction, and wavelength; the equation accounts for all losses (due to absorption and scattering out of the beam) and gains (by emission or scattering into the beam).

Rayleigh scattering A mathematical model that describes elastic scattering by very small particles (at least small relative to the wavelength of the light being scattered); it is characterised by a volume scattering function that depends inversely with the fourth power of the wavelength and has forward-backward directional symmetry.

refraction The change in direction of a light beam when crossing an interface between two media that have different real indices of refraction; see refractive index.

refractive index The ratio of the speed of light in a vacuum to its speed in a material medium; governs how light is refracted when crossing an interface between materials with different refraction indices.

scatterance The fraction of incident power at a given wavelength that is scattered within a volume of a substance.

scattering coefficient The scatterance per unit distance of photons traveling in a medium. Derived as the limit of the ratio of the scatterance to the distance of photon travel as the distance becomes infinitesimally small. Defined per metre.

specific The adjective used to express a quantity per unit mass or unit concentration.

turbidity A measure of the degree to which the water loses its transparency from the presence of suspended particulates. The more total suspended solids in the water, the higher the turbidity. Related directly to the chlorophyll concentration in Case 1 waters.

turbulence The chaotic flow of a liquid or gaseous medium which results in scintillation in a transmitted optical beam.

volume scattering function The ratio of the scattered intensity to the incident irradiance per unit volume. The volume scattering function describes both the angular pattern of the light scattered from an incident direction and the magnitude of scattering. The integral of the volume scattering function over all directions (all solid angles) is the scattering coefficient. The volume scattering function can be written as the product of the phase function and the scattering coefficient.

References

Abshire, J. B. & Gardner, C. S. (1985). Atmospheric refractivity corrections in satellite laser ranging. *IEEE Transactions on Geoscience and Remote Sensing*, (4), 414–425.

Akyildiz, I. F., Pompili, D., & Melodia, T. (2005). Underwater acoustic sensor networks: research challenges. *Ad hoc networks*, *3*(3), 257–279.

Ambalux Corporation (2012). High-bandwidth underwater transceiver. *http://www.ambalux.com*. [Accessed 16/09/12].

Andrews, L. C. & Phillips, R. L. (2002). Impact of scintillation on laser communication systems: recent advances in modeling. In *International Symposium on Optical Science and Technology*, (pp. 23–34). International Society for Optics and Photonics.

Andrews, L. C., Phillips, R. L., Hopen, C. Y., & Al-Habash, M. (1999). Theory of optical scintillation. *Journal of the Optical Society of America A*, *16*(6), 1417–1429.

Anguita, D., Brizzolara, D., & Parodi, G. (2009). Building an underwater wireless sensor network based on optical: Communication: Research challenges and current results. In *International Conference on Sensor Technologies and Applications*, (pp. 476–479). IEEE.

Anguita, D., Brizzolara, D., & Parodi, G. (2010). VHDL modules and circuits for underwater optical wireless communication systems. *WSEAS Transactions on Communications*, *9*(9), 525–552.

Anguita, D., Brizzolara, D., Parodi, G., & Hu, Q. (2011). Optical wireless underwater communication for auv: Preliminary simulation and experimental results. In *IEEE/MTS Proceedings of OCEANS 2011, Santander*, (pp. 1–5). IEEE/MTS.

Apel, J. R. (1987). *Principles of ocean physics*, volume 38. Academic Press.

Arnon, S. (2010). Underwater optical wireless communication network. *Optical Engineering*, *49*(1), 015001.

Arnon, S., Barry, J., Karagiannidis, G., Schober, R., & Uysal, M. (2012). *Advanced optical wireless communication systems*. Cambridge University Press.

Arnon, S. & Kedar, D. (2009). Non-line-of-sight underwater optical wireless communication network. *Journal of the Optical Society of America A*, *26*(3), 530–539.

Arnone, R., Wood, A., & Gould, R. (2004). Science box: The evolution of optical water mass classification. *Oceanography*, *17*(2), 14–15.

Arnott, W. P. & Marston, P. L. (1991). Unfolded optical glory of spheroids: backscattering of laser light from freely rising spheroidal air bubbles in water. *Applied Optics*, *30*(24), 3429–3442.

Ata, Y. & Baykal, Y. (2014). Scintillations of optical plane and spherical waves in underwater turbulence. *Journal of the Optical Society of America A*, *31*(7), 1552–1556.

Austin, R. W. & Halikas, G. (1976). The index of refraction of seawater. Technical report, Scripps Institute of Oceanography, University of California, USA.

Australian Transport Safety Bureau (2015). MH370: Sonar Contacts. *Australian Government*.

Babin, M. (2008). Phytoplankton fluorescence: theory, current literature and in situ measurement. *Real-time coastal observing systems for marine ecosystem dynamics and harmful algal blooms. UNESCO*, 237–280.

Babin, M., Morel, A., Fournier-Sicre, V., Fell, F., & Stramski, D. (2003). Light scattering properties of marine particles in coastal and open ocean waters as related to the particle mass concentration. *Limnology and Oceanography*, *48*(2), 843–859.

Babin, M., Stramski, D., Ferrari, G. M., Claustre, H., Bricaud, A., Obolensky, G., & Hoepffner, N. (2003). Variations in the light absorption coefficients of phytoplankton, nonalgal particles, and dissolved organic matter in coastal waters around europe. *Journal of Geophysical Research: Oceans (1978–2012)*, *108*(C7).

Baiden, G., Bissiri, Y., & Masoti, A. (2009). Paving the way for a future underwater omni-directional wireless optical communication systems. *Ocean Engineering*, *36*(9), 633–640.

Bales, J. W. & Chrissostomidis, C. (1995). High-bandwidth, low-power, short-range optical communication underwater. In *International Symposium on Unmanned Untethered Submersible Technology*, (pp. 406–415). University of New Hampshire.

Band, Y. B. (2006). *Light and matter: electromagnetism, optics, spectroscopy and lasers*, volume 1. John Wiley & Sons.

Barry, J. R. (1994). *Wireless infrared communications*. Springer.

Baykal, Y. (2006). Formulation of correlations for general-type beams in atmospheric turbulence. *Journal of the Optical Society of America A*, *23*(4), 889–893.

Baykal, Y. (2014). Scintillations of higher-order laser beams in non-kolmogorov medium. *Optics Letters*, *39*(7), 2160–2163.

Baykal, Y. (2015). Intensity fluctuations of multimode laser beams in underwater medium. *Journal of the Optical Society of America A*, *32*, 593.

Beer, A. (1852). Determination of the absorption of red light in colored liquids. *Annalen der Physik und Chemie*, *86*, 78–88. [German].

Bidigare, R. R., Ondrusek, M. E., Morrow, J. H., & Kiefer, D. A. (1990). In-vivo absorption properties of algal pigments. In *Proceedings of Ocean Optics X*, (pp. 290–302). International Society for Optics and Photonics.

Bogucki, D. J., Domaradzki, J. A., Stramski, D., & Zaneveld, J. R. (1998). Comparison of near-forward light scattering on oceanic turbulence and particles. *Applied Optics*, *37*(21), 4669–4677.

Boss, E., Slade, W., & Hill, P. (2009). Effect of particulate aggregation in aquatic environments on the beam attenuation and its utility as a proxy for particulate mass. *Optics Express*, *17*(11), 9408–9420.

Bøtter-Jensen, L., Bulur, E., Duller, G., & Murray, A. (2000). Advances in luminescence instrument systems. *Radiation Measurements*, *32*(5), 523–528.

Bowers, D. & Binding, C. (2006). The optical properties of mineral suspended particles: A review and synthesis. *Estuarine, Coastal and Shelf Science*, *67*(1), 219–230.

Brewin, R. J., Sathyendranath, S., Müller, D., Brockmann, C., Deschamps, P.-Y., Devred, E., Doerffer, R., Fomferra, N., Franz, B., Grant, M., et al. (2013). The ocean colour climate change initiative: Iii. a round-robin comparison on in-water bio-optical algorithms. *Remote Sensing of Environment*.

Bricaud, A., Babin, M., Morel, A., & Claustre, H. (1995). Variability in the chlorophyll-specific absorption coefficients of natural phytoplankton: Analysis and parameterization. *Journal of Geophysical Research: Oceans (1978–2012)*, *100*(C7), 13321–13332.

Bricaud, A., Claustre, H., Ras, J., & Oubelkheir, K. (2004). Natural variability of phytoplanktonic absorption in oceanic waters: Influence of the size structure of algal populations. *Journal of Geophysical Research: Oceans (1978–2012)*, *109*(C11).

Bricaud, A., Morel, A., Babin, M., Allali, K., & Claustre, H. (1998). Variations of light absorption by suspended particles with chlorophyll a concentration in oceanic (case 1) waters: Analysis and implications for bio-optical models. *Journal of Geophysical Research: Oceans (1978–2012)*, *103*(C13), 31033–31044.

Bricaud, A., Morel, A., Prieur, L., et al. (1981). Absorption by dissolved organic matter of the sea (yellow substance) in the uv and visible domains. *Limnology and Oceanography*, *26*(1), 43–53.

Brown, E., Colling, A., Park, D., Phillips, J., Rothery, D., & Wright, J. (1995). *Seawater: its composition, properties and behaviour*. Butterworth-Heinemann.

Brundage, H. (2010). Designing a wireless underwater optical communication system. Master's thesis, Massachusetts Institute of Technology, USA.

Camilli, R., Bowen, A., & Farr, N. (2010). Bright blue: Advanced technologies for marine environmental monitoring and offshore energy. In *IEEE/MTS Proceedings of OCEANS 2010, Sydney*, (pp. 1–7). IEEE/MTS.

Carder, K. L., Steward, R. G., Harvey, G. R., & Ortner, P. B. (1989). Marine humic and fulvic acids: Their effects on remote sensing of ocean chlorophyll. *Limnology and Oceanography*, *34*(1), 68–81.

Carlson, R. E. (1977). A trophic state index for lakes. *Limnology and Oceanography*, *22*(2), 361–369.

Chancey, M. A. (2005). Short range underwater optical communication links.

Che, X., Wells, I., Dickers, G., Kear, P., & Gong, X. (2010). Re-evaluation of RF electromagnetic communication in underwater sensor networks. *IEEE Communications Magazine*, *48*(12), 143–151.

Chen, M., Zhou, S., & Li, T. (2006). The implementation of PPM in underwater laser communication system. In *International Conference on Communications, Circuits and Systems Proceedings*, volume 3, (pp. 1901–1903). IEEE.

Ciotti, A. M., Lewis, M. R., & Cullen, J. J. (2002). Assessment of the relationships between dominant cell size in natural phytoplankton communities and the spectral shape of the absorption coefficient. *Limnology and Oceanography*, *47*(2), 404–417.

Coble, P. G. (2007). Marine optical biogeochemistry: the chemistry of ocean color. *Chemical Reviews*, *107*(2), 402–418.

Cochenour, B. & Mullen, L. (2011). Channel response measurements for diffuse non-line-of-sight (NLOS) optical communication links underwater. In *IEEE/MTS Proceedings of OCEANS 2011, Waikoloa*, (pp. 1–5). IEEE/MTS.

Cochenour, B., Mullen, L., & Laux, A. (2007). *Phase coherent digital communications for wireless optical links in turbid underwater environments*. IEEE/MTS.

Cochenour, B., Mullen, L., Laux, A., & Curran, T. (2006). Effects of multiple scattering on the implementation of an underwater wireless optical communications link. In *IEEE/MTS Proceedings of OCEANS 2006, Boston*, (pp. 1–4). IEEE/MTS.

Cochenour, B., Mullen, L., & Muth, J. (2013). Temporal response of the underwater optical channel for high-bandwidth wireless laser communications. *IEEE Journal of Oceanic Engineering*, *38*(4), 730–742.

Cochenour, B. M. (2013). *Experimental measurements of temporal dispersion for underwater laser communications and imaging*. PhD thesis, North Carolina State University, USA.

Cochenour, B. M., Mullen, L. J., & Laux, A. E. (2009). Characterization of the beam-spread function for underwater wireless optical communications links. *IEEE Journal of Oceanic Engineering*, *33*(4), 513–521.

Cossu, G., Corsini, R., Khalid, A., Balestrino, S., Coppelli, A., Caiti, A., & Ciaramella, E. (2013). Experimental demonstration of high speed underwater visible light communications. In *International Workshop on Optical Wireless Communications (IWOW)*, (pp. 11–15). IEEE.

COST (2011). IC1101 Optical Wireless Communications – An Emerging Technology. *http://www.cost.eu/*. [Accessed 10/10/11].

Cox, W. C. (2008). A 1 Mbps underwater communication system using a 405 nm laser diode and photomultiplier tube. Master's thesis, North Carolina State University, USA.

Cox, W. C., Simpson, J. A., Domizioli, C. P., Muth, J. F., & Hughes, B. L. (2008). An underwater optical communication system implementing reed-solomon channel coding. In *IEEE/MTS Proceedings of OCEANS 2008, Quebec City*, (pp. 1–6). IEEE/MTS.

Cox, W. C., Simpson, J. A., & Muth, J. F. (2011). Underwater optical communication using software defined radio over LED and laser based links. In *IEEE Military Communications Conference (MILCOM)*, (pp. 2057–2062). IEEE.

Crawford, G. & Farmer, D. (1987). On the spatial distribution of ocean bubbles. *Journal of Geophysical Research: Oceans (1978–2012)*, *92*(C8), 8231–8243.

Cullen, J. J. (1982). The deep chlorophyll maximum: comparing vertical profiles of chlorophyll a. *Canadian Journal of Fisheries and Aquatic Sciences*, *39*(5), 791–803.

Dalgleish, F. R., Caimi, F. M., Vuorenkoski, A. K., Britton, W. B., Ramos, B., Giddings, T. E., Shirron, J. J., & Mazel, C. H. (2010). Efficient laser pulse dispersion codes for turbid undersea imaging and communications applications. In *SPIE Defense, Security and Sensing*, (pp. 76780I). International Society for Optics and Photonics.

Davies-Colley, R. & Vant, W. (1987). Absorption of light by yellow substance in freshwater lakes. *Limnology and Oceanography*, *32*(2), 416–425.

Destrez, A., Toffano, Z., & Leon, P. (2012). Underwater high bit-rate optical free-space communication system. In *International Workshop on Optical Wireless Communications (IWOW)*, (pp. 1–3).

Doniec, M., Angermann, M., & Rus, D. (2013). An end-to-end signal strength model for underwater optical communications. *IEEE Journal of Oceanic Engineering*, *38*(4), 743–757.

Doniec, M. & Rus, D. (2010). Bidirectional optical communication with aquaoptical II. In *IEEE International Conference on Communication Systems (ICCS)*, (pp. 390–394). IEEE.

Doniec, M., Vasilescu, I., Chitre, M., Detweiler, C., Hoffmann-Kuhnt, M., & Rus, D. (2009). Aquaoptical: A lightweight device for high-rate long-range underwater point-to-point communication. In *IEEE/MTS Proceedings of OCEANS 2009, Biloxi*, (pp. 1–6). IEEE/MTS.

Duntley, S. Q. (1971). Underwater lighting by submerged lasers and incandescent sources. Technical report, DTIC Document.

Dy, H. C. & Gustilo, R. C. (2012). Characterization of signal response for surface water movements in underwater optical wireless communications. In *TENCON IEEE Region 10 Conference*, (pp. 1–6). IEEE.

Earth Sciences Education (2013). Enduring resources for earth sciences education, tropical pacific ctd data at 1 meter intervals. *http://earthref.org/ERDA/861/*. [Accessed 01/07/2014].

El Yakzan, A. (2013). *Performance prediction, parameter selection, and channel adaptation in the line-of-sight outdoors optical wireless channels using intelligent systems*. PhD thesis, University of Warwick, UK.

Elganimi, T. Y. (2013). Performance comparison between OOK, PPM and PAM modulation schemes for free space optical (FSO) communication systems: analytical study. *International Journal Computer Applications*, *79*(11), 22–27.

Elshimy, M. A. & Hranilovic, S. (2011). Non-line-of-sight single-scatter propagation model for noncoplanar geometries. *Journal of the Optical Society of America A*, *28*(3), 420–428.

Falkowski, P. & Kiefer, D. A. (1985). Chlorophyll a fluorescence in phytoplankton: relationship to photosynthesis and biomass. *Journal of Plankton Research*, *7*(5), 715–731.

Farr, N., Bowen, A., Ware, J., Pontbriand, C., & Tivey, M. (2010). An integrated, underwater optical/acoustic communications system. In *IEEE/MTS Proceedings of OCEANS 2010, Sydney*, (pp. 1–6). IEEE/MTS.

Farr, N., Chave, A., Freitag, L., Preisig, J., White, S., Yoerger, D., & Titterton, P. (2006). Optical modem technology for seafloor observatories. In *IEEE/MTS Proceedings of OCEANS 2006, Boston*, (pp. 928–934). IEEE/MTS.

Farwell, N. & Korotkova, O. (2012). Intensity and coherence properties of light in oceanic turbulence. *Optics Communications*, *285*(6), 872–875.

Fasham, S. & Dunn, S. (2015). Developments in subsea wireless communications. In *Underwater Technology*, (pp. 1–5). IEEE.

Fingas, M. & Brown, C. (2014). Review of oil spill remote sensing. *Marine Pollution Bulletin*, *83*(1), 9–23.

Fournier, G. R. & Forand, J. L. (1994). Analytic phase function for ocean water. In *Proceedings of Ocean Optics XII*, (pp. 194–201). International Society for Optics and Photonics.

Fournier, G. R. & Jonasz, M. (1999). Computer-based underwater imaging analysis. In *SPIE International Symposium on Optical Science, Engineering, and Instrumentation*, (pp. 62–70). International Society for Optics and Photonics.

Fujii, á., Boss, E., Chai, F., et al. (2007). The value of adding optics to ecosystem models: a case study. *Biogeosciences Discussions*, *4*(3), 1585–1631.

Gabriel, C., Khalighi, M.-A., Bourennane, S., Leon, P., & Rigaud, V. (2011). Channel modeling for underwater optical communication. In *IEEE GLOBECOM Workshop*, (pp. 833–837). IEEE.

Gabriel, C., Khalighi, M.-A., Bourennane, S., Léon, P., & Rigaud, V. (2013). Misalignment considerations in point-to-point underwater wireless optical links. In *IEEE/MTS Proceedings of OCEANS 2013, Bergen*, (pp. 1–5). IEEE/MTS.

Garrison, T. (2009). *Oceanography: an invitation to marine science*. Cengage Learning.

Gawdi, Y. J. (2006). Underwater free space optics. Master's thesis, North Carolina State University, USA.

Gerçekcioğlu, H. (2014). Bit error rate of focused gaussian beams in weak oceanic turbulence. *Journal of the Optical Society of America A*, *31*(9), 1963–1968.

Ghassemlooy, Z., Popoola, W., & Rajbhandari, S. (2012). *Optical wireless communications: system and channel modelling with Matlab®*. CRC Press.

Giles, J. W. & Bankman, I. N. (2005). Underwater optical communications systems. part 2: basic design considerations. In *IEEE Military Communications Conference (MILCOM)*, (pp. 1700–1705). IEEE.

Gordon, H. R. & Morel, A. Y. (1983). *Remote assessment of ocean color for interpretation of satellite visible imagery: A review*, volume 4. American Geophysical Union.

Green, R., Leeson, M., Joshi, H., & Higging, M. (2008). Underwater optical communications: Prospects and opportunities. Technical report, QinetiQ. [Draft].

Gudimetla, V., Holmes, R. B., & Riker, J. F. (2012). Analytical expressions for the log-amplitude correlation function for plane wave propagation in anisotropic non-kolmogorov refractive turbulence. *Journal of the Optical Society of America A*, *29*(12), 2622–2627.

Gulbahar, B. & Akan, O. B. (2012). A communication theoretical modeling and analysis of underwater magneto-inductive wireless channels. *IEEE Transactions on Wireless Communications*, *11*(9), 3326–3334.

Gupta, S. (2014). Spectral transmission studies of ocean water under different sea conditions. *Defence Science Journal*, *34*(1), 19–28.

Hagem, R. M., Thiel, D. V., Keefe, S. G., Wixted, A., & Fickenscher, T. (2011). Low-cost short-range wireless optical FSK modem for swimmers feedback. In *IEEE Proceedings of Sensors*, (pp. 258–261). IEEE.

Hagem, R. M., Thiel, D. V., O'Keefe, S. G., & Fickenscher, T. (2012). The effect of air bubbles on an underwater optical communications system for wireless sensor network applications. *Microwave and Optical Technology Letters*, *54*(3), 729–732.

Hale, G. M. & Querry, M. R. (1973). Optical constants of water in the 200-nm to 200-μm wavelength region. *Applied Optics*, *12*(3), 555–563.

Halliday, D., Resnick, R., & Walker, J. (2010). *Fundamentals of physics extended*, volume 1. John Wiley & Sons.

Haltrin, V. & Kattawar, G. (1991). *Light fields with Raman scattering and fluorescence in sea water*. PhD thesis, Texas A&M University, Department of Physics.

Haltrin, V. I. (1999). Chlorophyll-based model of seawater optical properties. *Applied Optics*, *38*(33), 6826–6832.

Hanson, F. & Lasher, M. (2010). Effects of underwater turbulence on laser beam propagation and coupling into single-mode optical fiber. *Applied Optics*, *49*(16), 3224–3230.

Hanson, F. & Radic, S. (2008). High bandwidth underwater optical communication. *Applied Optics*, *47*(2), 277–283.

Harker, G. E. L. (1997). *A comparison between the optical measurements made in the field and in the laboratory, and the development of an optical model*. PhD thesis, University of Wales, UK.

Henyey, L. G. & Greenstein, J. L. (1941). Diffuse radiation in the galaxy. *The Astrophysical Journal*, *93*, 70–83.

Hodara, H. & Marquedant, R. (1968). The signal/noise ratio concept in underwater optics. *Applied Optics*, *7*(3), 527–534.

Hoepffner, N. & Sathyendranath, S. (1991). Effect of pigment composition on absorption properties of phytoplankton. *Marine Ecology Progress Series*, *73*(1), 0–23.

Hollins, R., Rudge, A., & Bennett, S. (2013). Technologies for blue-green underwater optical communications. In *SPIE Security+ Defence*, (pp. 88990F). International Society for Optics and Photonics.

Hooker, S. B., Firestone, E. R., Esaias, W. E., Feldman, G. C., Gregg, W. W., & McClain, C. R. (1992). Seawifs technical report series. volume 1: An overview of seawifs and ocean color.

Horvath, H. (1993). Atmospheric light absorption—a review. *Atmospheric environment. Part A. General Topics*, *27*(3), 293–317.

Iqbal, M. (2012). *An introduction to solar radiation*. Elsevier.

Islam, Z. & Faruque, S. (2014). Experimental investigation of underwater turbulence effect on BER for orthogonal OOK modulation. In *IEEE International Conference on Electro/Information Technology (EIT)*, (pp. 608–611). IEEE.

Iturriaga, R. & Siegel, D. A. (1989). Microphotometric characterization of phytoplankton and detrital absorption properties in the sargasso sea. *Limnology and Oceanography*, *34*(8), 1706–1726.

Jaruwatanadilok, S. (2008). Underwater wireless optical communication channel modeling and performance evaluation using vector radiative transfer theory. *IEEE Journal on Selected Areas in Communications*, *26*(9), 1620–1627.

Jasman, F. & Green, R. J. (2013). Monte Carlo simulation for underwater optical wireless communications. In *2nd International Workshop on Optical Wireless Communications (IWOW)*, (pp. 113–117). IEEE.

Jerlov, N. G. (1976). *Marine optics*. Elsevier.

Jerlov, N. G. & Koczy, F. F. (1951). *Photographic measurements of daylight in deep water*. Elanders Boktr.

Jerlov, N. G. & Nielsen, E. S. (1974). *Optical aspects of oceanography*, volume 12. Academic Press.

Johnson, L. J., Green, R. J., & Leeson, M. (2014a). The impact of orientation on an underwater optical wireless communication system. In *IEEE/MTS Proceedings of OCEANS 2014, St. John's*, (pp. 1–7). IEEE/MTS.

Johnson, L. J., Green, R. J., & Leeson, M. S. (2013). Underwater optical wireless communications: depth dependent variations in attenuation. *Applied Optics*, *52*(33), 7867–7873.

Johnson, L. J., Green, R. J., & Leeson, M. S. (2014b). Hybrid underwater optical/acoustic link design. In *16th International Conference on Transparent Optical Networks (ICTON)*, (pp. 1–4). IEEE.

Kameda, T. & Matsumura, S. (1998). Chlorophyll biomass off sanriku, northwestern pacific, estimated by ocean color and temperature scanner (OCTS) and a vertical distribution model. *Journal of Oceanography*, *54*(5), 509–516.

Karp, S. (1976). Optical communications between underwater and above surface (satellite) terminals. *IEEE Transactions on Communications*, *24*(1), 66–81.

Karp, S. & Gagliardi, R. M. (1969). The design of a pulse-position modulated optical communication system. *IEEE Transactions on Communication Technology*, *17*(6), 670–676.

Kedar, D. & Arnon, S. (2009). Subsea ultraviolet solar-blind broadband free-space optics communication. *Optical Engineering*, *48*(4), 046001.

Keiser, G. (2003). *Optical fiber communications*. Wiley Online Library.

Kelley, K., Stotts, L., Mooradian, G., & Anderson, R. (1979). Strategic blue-green optical communications program plan. investment strategy toward an optical solution for satellite-to-submarine information transfer. Technical report, DTIC Document.

Kirk, J. T. O. (1994). *Light and photosynthesis in aquatic ecosystems*. Cambridge university press.

Kishino, M., Takahashi, M., Okami, N., & Ichimura, S. (1985). Estimation of the spectral absorption coefficients of phytoplankton in the sea. *Bulletin of Marine Science*, *37*(2), 634–642.

Kopelevich, O. & Mezhericher, E. (1983). Calculation of the spectral characteristics of light scattering by sea water. *Izvestiya. Atmospheric and Oceanic Physics*, *19*(2), 144–148.

Kopelevich, O. V. (1976). Optical properties of pure water in the 250-600-nm range. *Optics and Spectroscopy*, *41*, 391–392.

Kopelevich, O. V. (1983). Small-parametric model of the optical properties of seawater.

Korotkova, O., Farwell, N., & Shchepakina, E. (2012). Light scintillation in oceanic turbulence. *Waves in Random and Complex Media*, *22*(2), 260–266.

Lamarre, E. & Melville, W. (1991). Air entrainment and dissipation in breaking waves. *Nature*, *351*(6326), 469–472.

LexelLaser (2014). *http://www.lexellaser.com*. [Accessed 27/08/13].

Lichte, H. (1919). On the influence of horizontal temperature layers in sea water on the range of underwater sound signals. *Physikalische Zeitschrift*, *17*, 385–389. [German].

Ling, S. & Pao, H. (1988). Study of micro-bubbles in the north sea. In *Sea Surface Sound* (pp. 197–210). Springer.

Lorenzen, C. J. (1963). Diurnal variation in photosynthetic activity of natural phytoplankton populations. *Limnology and Oceanography*, *8*(1), 56–62.

Lu, F., Lee, S., Mounzer, J., & Schurgers, C. (2009). Low-cost medium-range optical underwater modem: short paper. In *Proceedings of 4th ACM International Workshop on Underwater Networks*, (pp.1̃1). ACM.

Lu, L., Zhang, P., Fan, C., & Qiao, C. (2015). Influence of oceanic turbulence on propagation of a radial gaussian beam array. *Optics Express*, *23*(3), 2827–2836.

Marston, P. L. (1979). Critical angle scattering by a bubble: physical-optics approximation and observations. *Journal of the Optical Society of America A*, *69*(9), 1205–1211.

McLean, J. W., Freeman, J. D., & Walker, R. E. (1998). Beam spread function with time dispersion. *Applied Optics*, *37*(21), 4701–4711.

Meadows, P. S. (2013). *An introduction to marine science*. Springer Science & Business Media.

Meadows, P. S. & Campbell, J. I. (1978). *An introduction to marine science*. Blackie Glasgow and London.

Meihong, S., Xinsheng, Y., & Zhangguo, Z. (2009). The modified PPM modulation for underwater wireless optical communication. In *International Conference on Communication Software and Networks (ICCSN)*, (pp. 173–177). IEEE.

Meyer-Arendt, J. R. (1989). *Introduction to classical and modern optics*, volume 1. Englewood Cliffs: Prentice-Hall.

Millard, R. & Seaver, G. (1990). An index of refraction algorithm for seawater over temperature, pressure, salinity, density, and wavelength. *Deep Sea Research Part A. Oceanographic Research Papers*, *37*(12), 1909–1926.

Millie, D. F., Moline, M. A., & Schofield, O. (2000). Optical discrimination of a phytoplankton species in natural mixed populations. *Biological Sciences*, 135.

Mitchell, M. (1998). *An introduction to genetic algorithms*. MIT press.

Mizukoshi, I., Kazuhiko, N., & Hanawa, M. (2014). Underwater optical wireless transmission of 405 nm, 968 Mbit/s optical IM/DD-OFDM signals. In *OptoElectronics and Communication Conference on Optical Fibre Technology*, (pp. 216–217).

Mobley, C., Boss, E., & Roesler, C. (2014). *Ocean optics web book*. http://www.oceanopticsbook.info. [Accessed 10/12/14].

Mobley, C. D. (1995). The optical properties of water. *Handbook of Optics*, *2*.

Mobley, C. D., Gentili, B., Gordon, H. R., Jin, Z., Kattawar, G. W., Morel, A., Reinersman, P., Stamnes, K., & Stavn, R. H. (1993). Comparison of numerical models for computing underwater light fields. *Applied Optics*, *32*(36), 7484–7504.

Mobley, C. D. & Mobley, C. D. (1994). *Light and water: Radiative transfer in natural waters*, volume 592. Academic Press.

Moore, R. K. (1967). Radio communication in the sea. *IEEE Spectrum*, *4*(11), 42–51.

Morel, A. (1973). Diffusion de la lumiere par les eaux de mer. résultats expérimentaux et approche théorique. *Optics of the Sea*, *61*, 3–1.

Morel, A. (1974). Optical properties of pure water and pure sea water. *Optical Aspects of Oceanography*, *1*, 1–24.

Morel, A. (1991). Light and marine photosynthesis: a spectral model with geochemical and climatological implications. *Progress in Oceanography*, *26*(3), 263–306.

Morel, A. & Ahn, Y.-H. (1991). Optics of heterotrophic nanoflagellates and ciliates: A tentative assessment of their scattering role in oceanic waters compared to those of bacterial and algal cells. *Journal of Marine Research*, *49*(1), 177–202.

Morel, A., Antoine, D., & Gentili, B. (2002). Bidirectional reflectance of oceanic waters: accounting for raman emission and varying particle scattering phase function. *Applied Optics*, *41*(30), 6289–6306.

Morel, A. & Bricaud, A. (1981). Theoretical results concerning light absorption in a discrete medium, and application to specific absorption of phytoplankton. *Deep Sea Research Part A. Oceanographic Research Papers*, *28*(11), 1375–1393.

Morel, A., Gentili, B., Chami, M., & Ras, J. (2006). Bio-optical properties of high chlorophyll case 1 waters and of yellow-substance-dominated case 2 waters. *Deep Sea Research Part I: Oceanographic Research Papers*, *53*(9), 1439–1459.

Morel, A. & Loisel, H. (1998). Apparent optical properties of oceanic water: dependence on the molecular scattering contribution. *Applied Optics*, *37*(21), 4765–4776.

Morel, A. & Maritorena, S. (2001). Bio-optical properties of oceanic waters: A reappraisal. *Journal of Geophysical Research: Oceans (1978–2012)*, *106*(C4), 7163–7180.

Morel, A. & Prieur, L. (1977). Analysis of variations in ocean color. *Limnology and Oceanography*, *22*(4), 709–722.

Morrow, J., Chamberlin, W., & Kiefer, D. (1989). A two-component description of spectral absorption by marine particles. *Limnology and Oceanography*, *34*(8), 1500–1509.

Mueller, J. L. (2000). SeaWiFS algorithm for the diffuse attenuation coefficient, K (490), using water-leaving radiances at 490 and 555 nm. *SeaWiFS postlaunch calibration and validation analyses*, *3*(11), 24–27.

Mueller, J. L., Bidigare, R., Trees, C., Balch, W., Dore, J., Drapeau, D., Karl, D., Van Heukelem, L., & Perl, J. (2003). Ocean optics protocols for satellite ocean color sensor validation, revision 5, volume

v: Biogeochemical and bio-optical measurements and data analysis protocols. *NASA Technical Memo*, *211621*, 36.

Mullen, L., Alley, D., & Cochenour, B. (2011). Investigation of the effect of scattering agent and scattering albedo on modulated light propagation in water. *Applied Optics*, *50*(10), 1396–1404.

Mullen, L., Laux, A., Cochenour, B., Zege, E. P., Katsev, I. L., & Prikhach, A. S. (2007). Demodulation techniques for the amplitude modulated laser imager. *Applied Optics*, *46*(30), 7374–7383.

Najda, S., Perlin, P., Suski, T., Marona, L., Boćkowski, M., Leszczyński, M., Wisniewski, P., Czernecki, R., Kucharski, R., Targowski, G., et al. (2013). Advances in algainn laser diode technology for defence applications. In *SPIE Security+ Defence*, (pp. 88990B). International Society for Optics and Photonics.

Nakamura, K., Mizukoshi, I., & Hanawa, M. (2015). Optical wireless transmission of 405 nm, 1.45 Gbit/s optical IM/DD-OFDM signals through a 4.8 m underwater channel. *Optics Express*, *23*(2), 1558–1566.

Nikishov, V. & Nikishov, V. (2000). Spectrum of turbulent fluctuations of the sea-water refraction index. *International Journal of Fluid Mechanics Research*, *27*(1).

OkSolar (2015). *http://www.oksolar.com/led*. [Accessed 21/03/2015].

Oubei, H. M., Duran, J. R., Janjua, B., Wang, H.-Y., Tsai, C.-T., Chi, Y.-C., Ng, T. K., Kuo, H.-C., He, J.-H., Alouini, M.-S., Lin, G.-R., & Ooi, B. S. (2015). 4.8 Gbit/s 16-QAM-OFDM transmission based on compact 450- nm laser for underwater wireless optical communication. *Applied Optics*, *In press*.

Patrick Arnott, W. & Marston, P. L. (1988). Optical glory of small freely rising gas bubbles in water: observed and computed cross-polarized backscattering patterns. *Journal of the Optical Society of America A*, *5*(4), 496–506.

Pegau, W. & Zaneveld, J. R. (1993). Temperature-dependent absorption of water in the red and near-infrared portions of the spectrum. *Limnology and Oceanography*, *38*(1), 188–192.

Petzold, T. J. (1972). Volume scattering functions for selected ocean waters. Technical report, DTIC Document.

Photop (2012). *Photop DPGL-2100, a 532 nm, 100 mW temperature stablized DPSS laser*. Photop Technologies.

Pontbriand, C., Farr, N., Ware, J., Preisig, J., & Popenoe, H. (2008). Diffuse high-bandwidth optical communications. In *IEEE/MTS Proceedings of OCEANS 2008, Quebec City*, (pp. 1–4). IEEE/MTS.

Pope, R. M. & Fry, E. S. (1997). Absorption spectrum (380–700 nm) of pure water. ii. integrating cavity measurements. *Applied Optics*, *36*(33), 8710–8723.

Prahl, S. (1998). Optical absorption of water. *Oregon Medical Laser Center*, *11*.

Preisendorfer, R. W. (1976). Hydrologic optics. volume 2. foundations. Technical report, Honolulu: US Dept. of Commerce, National Oceanic and Atmospheric Administration, environmental Research Laboratories.

Quirantes, A. & Bernard, S. (2004). Light scattering by marine algae: two-layer spherical and nonspherical models. *Journal of Quantitative Spectroscopy and Radiative Transfer*, *89*(1), 311–321.

Ramirez-Iniguez, R. & Green, R. (2005). Optical antenna design for indoor optical wireless communication systems. *International Journal of Communication Systems*, *18*(3), 229–245.

Rich, C. & Longcore, T. (2005). *Ecological consequences of artificial night lighting*. Island Press.

Riley, J. P. & Skirrow, G. (1965). *Chemical Oceanography*. London.

Roesler, C. S., Perry, M. J., & Carder, K. L. (1989). Modeling in situ phytoplankton absorption from total absorption spectra in productive inland marine waters. *Limnology and Oceanography*, *34*(8), 1510–1523.

Rosenkrantz, E. & Arnon, S. (2014). Optimum LED wavelength for underwater optical wireless communication at turbid water. In *SPIE Optical Engineering+ Applications*, (pp. 922413). International Society for Optics and Photonics.

Ruddick, K. G., Ovidio, F., & Rijkeboer, M. (2000). Atmospheric correction of SeaWiFS imagery for turbid coastal and inland waters. *Applied Optics*, *39*(6), 897–912.

Sakurai, J. J. (2006). *Advanced quantum mechanics*. Pearson Education India.

Schawlow, A. L. & Townes, C. H. (1958). Infrared and optical masers. *Physical Review*, *112*(6), 1940.

Schill, F., Zimmer, U. R., & Trumpf, J. (2004). Visible spectrum optical communication and distance sensing for underwater applications. In *Proceedings of ACRA*, volume 2004, (pp. 1–8).

Schnitzer, M. (1978). Humic substances: chemistry and reactions. *Developments in Soil Science*, *8*, 1–64.

SeaWIFs (2015). *http://oceancolor.gsfc.nasa.gov/SeaWiFS*. [Accessed 06/06/2015].

Segelstein, D. J. (2011). *The complex refractive index of water*. PhD thesis, University of Missouri.

Sharma, A., Kumar, D. V., & Ghatak, A. K. (1982). Tracing rays through graded-index media: a new method. *Applied Optics*, *21*(6), 984–987.

Shifrin, K. (1988). *Physical optics of ocean water*. Springer.

Simeon, J., Roesler, C., Pegau, W. S., & Dupouy, C. (2003). Sources of spatial variability in light absorbing components along an equatorial transect from 165 e to 150 w. *Journal of Geophysical Research: Oceans (1978–2012)*, *108*(C10).

Simpson, J., Hughes, B. L., Muth, J. F., et al. (2012). Smart transmitters and receivers for underwater free-space optical communication. *IEEE Journal on Selected Areas in Communications*, *30*(5), 964–974.

Simpson, J. A., Cox, W. C., Krier, J. R., Cochenour, B., Hughes, B. L., & Muth, J. F. (2010). 5 Mbps optical wireless communication with error correction coding for underwater sensor nodes. In *IEEE/MTS Proceedings of OCEANS 2010, Seattle*, (pp. 1–4). IEEE.

Simpson, J. A., Hughes, B. L., & Muth, J. F. (2009). A spatial diversity system to measure optical fading in an underwater communications channel. In *IEEE/MTS Proceedings of OCEANS 2009, Biloxi*, (pp. 1–6).

Smart, J. (2005). Underwater optical communications systems part 1: variability of water optical parameters. In *IEEE Military Communications Conference (MILCOM)*, (pp. 1140–1146). IEEE.

Smith, R. C. & Baker, K. S. (1978). Optical classification of natural waters. *Limnology and Oceanography*, *23*(2), 260–267.

Smith, R. C. & Baker, K. S. (1981). Optical properties of the clearest natural waters (200–800 nm). *Applied Optics*, *20*(2), 177–184.

Snow, J. B., Flatley, J. P., Freeman, D. E., Landry, M. A., Lindstrom, C. E., Longacre, J. R., & Schwartz, J. A. (1992). Underwater propagation of high-data-rate laser communications pulses. In *Proceedings of SPIE, San Diego*, (pp. 419–427). International Society for Optics and Photonics.

Sogandares, F. M. (1991). *The spectral absorption of pure water*. PhD thesis, Texas A&M University, USA.

Solonenko, M. G. & Mobley, C. D. (2015). Inherent optical properties of jerlov water types. *Applied Optics*, *54*(17), 5392–5401.

Sonardyne (2014). Bluecomm underwater optical modem. *http://www.sonardyne.com*. [Accessed 13/07/14].

Sosik, H. M. (2005). Characterizing seawater constituents from optical properties. *Real-time observation systems for ecosystem dynamics and harmful algal blooms. UNESCO*.

Spinrad, R. W., Zaneveld, J. R. V., & Pak, H. (1978). Volume scattering function of suspended particulate matter at near-forward angles: a comparison of experimental and theoretical values. *Applied Optics*, *17*(7), 1125–1130.

Stefanov, A. & Stojanovic, M. (2011). Design and performance analysis of underwater acoustic networks. *IEEE Journal on Selected Areas in Communications*, *29*(10), 2012–2021.

Stojanovic, M. (1996). Recent advances in high-speed underwater acoustic communications. *IEEE Journal of Oceanic Engineering*, *21*(2), 125–136.

Stojanovic, M. (2006). Underwater wireless communications: Current achievements and research challenges. *IEEE Oceanic Engineering Society Newsletter*, *41*(2), 1–5.

Stojanovic, M. & Preisig, J. (2009). Underwater acoustic communication channels: Propagation models and statistical characterization. *IEEE Communications Magazine*, *47*(1), 84–89.

Stotts, L. (1978). Closed form expression for optical pulse broadening in multiple-scattering media. *Applied Optics*, *17*(4), 504–505.

Stramski, D. (1990). Artifacts in measuring absorption spectra of phytoplankton collected on a filter. *Limnology and Oceanography*, *35*(8), 1804–1809.

Sui, M., Yu, X., & Zhang, F. (2009). The evaluation of modulation techniques for underwater wireless optical communications. In *International Conference on Communication Software and Networks (ICCSN)*, (pp. 138–142). IEEE.

Sun, M., Zheng, B., Zhao, L., & Yu, J. (2014). Paying a way of the ROV equipped with a function of underwater laser communication. In *IEEE/MTS Proceedings of OCEANS 2014, Taipei*, (pp. 1–4). IEEE/MTS.

Tassan, S. & Ferrari, G. M. (1995). An alternative approach to absorption measurements of aquatic particles retained on filters. *Limnology and Oceanography*, *40*(8), 1358–1368.

Tatarski, V. (1961). *Wave propagation in a turbulent medium*. Dover.

Thorlabs (2014). *https://www.thorlabs.com*. [Accessed 18/12/2014].

Thorlabs (2015). *PDA36A(-EC) Si Switchable Gain Detector*. Thorlabs.

Thorpe, S. (1982). On the clouds of bubbles formed by breaking wind-waves in deep water, and their role in air–sea gas transfer. *Philosophical Transactions of the Royal Society of London. Series A, Mathematical and Physical Sciences*, 155–210.

Tian, B., Zhang, F., & Tan, X. (2013). Design and development of an LED-based optical communication system for autonomous underwater robots. In *IEEE/ASME International Conference on Advanced Intelligent Mechatronics (AIM)*, (pp. 1558–1563). IEEE/ASME.

Tivey, M., Fucile, P., & Sichel, E. (2000). A low power, low cost, underwater optical communication system. *Ridge*, *1*, 27–29.

Tomlinson, M., Wynne, T., & Stumpf, R. (2009). An evaluation of remote sensing techniques for enhanced detection of the toxic dinoflagellate, karenia brevis. *Remote Sensing of Environment*, *113*(3), 598–609.

Tsonev, D., Chun, H., Rajbhandari, S., McKendry, J. J., Videv, S., Gu, E., Haji, M., Watson, S., Kelly, A. E., Faulkner, G., et al. (2014). A 3-Gb/s single-LED OFDM-based wireless VLC link using a gallium nitride. *IEEE Photonics Technology Letters*, *26*(7), 637–640.

Uitz, J., Claustre, H., Morel, A., & Hooker, S. B. (2006). Vertical distribution of phytoplankton communities in open ocean: An assessment based on surface chlorophyll. *Journal of Geophysical Research: Oceans (1978–2012)*, *111*(C8).

Van de Hulst, H. C. (2012). *Multiple light scattering: tables, formulas, and applications*, volume 1. Elsevier.

Vasilescu, I., Kotay, K., Rus, D., Dunbabin, M., & Corke, P. (2005). Data collection, storage, and retrieval with an underwater sensor network. In *Proceedings of the International Conference on Embedded Networked Sensor Systems*, (pp. 154–165). ACM.

Vesk, M. & Jeffrey, S. (1977). Effect of blue-green light on photosynthetic pigments and chloroplast structure in unicelluar marine algae from six classes. *Journal of Phycology*, *13*(3), 280–288.

Waaland, J. R. & Branton, D. (1969). Gas vacuole development in a blue-green alga. *Science*, *163*(3873), 1339–1341.

Wang, L., Jacques, S. L., & Zheng, L. (1995). MCML– monte carlo modeling of light transport in multi-layered tissues. *Computer Methods and Programs in Biomedicine*, *47*(2), 131–146.

Wells, W. H. (1969). Loss of resolution in water as a result of multiple small-angle scattering. *Journal of the Optical Society of America A*, *59*(6), 686–691.

Widder, E. A., Latz, M. I., Herring, P. J., & Case, J. F. (1984). Far red bioluminescence from two deep-sea fishes. *Science*, *225*(4661), 512–514.

Wiener, T. & Karp, S. (1980). The role of blue/green laser systems in strategic submarine communications. *IEEE Transactions on Communications*, *28*(9), 1602–1607.

Wierer, J. J., Tsao, J. Y., & Sizov, D. S. (2013). Comparison between blue lasers and light-emitting diodes for future solid-state lighting. *Laser & Photonics Reviews*, *7*(6), 963–993.

Xu, T., Jiang, B., Wen, D., & Shi, Y. (2011). Design of a wireless laser communication system based on PPM technique. In *International Conference on Electrical and Control Engineering (ICECE)*, (pp. 4427–4430). IEEE.

Xu, Y.-l. & Gustafson, B. Å. (2001). A generalized multiparticle mie-solution: further experimental verification. *Journal of Quantitative Spectroscopy and Radiative Transfer*, *70*(4), 395–419.

Yi, H., Sanchez, R., & McCormick, N. J. (1992). Bioluminescence estimation from ocean in situ irradiances. *Applied Optics*, *31*(6), 822–830.

Yi, X., Li, Z., & Liu, Z. (2015). Underwater optical communication performance for laser beam propagation through weak oceanic turbulence. *Applied Optics*, *54*(6), 1273–1278.

Yusof, M. A. B. & Kabir, S. (2011). Underwater communication systems: A review. In *Proceedings of Progress In Electromagnetics Research Symposium*, (pp. 803–807).

Zege, E. P., Katsev, I. L., Prikhach, A. S., Gilbert, G., & Witherspoon, N. (2006). Simple model of the optical characteristics of bubbles and sediments in seawater of the surf zone. *Applied Optics*, *45*(25), 6577–6585.

Zhang, X., Cui, J.-H., Das, S., Gerla, M., & Chitre, M. (2014). Call for papers. Underwater Wireless Communications and Networks: Theory and Applications. *IEEE Communications Magazine*.

Zhang, X., Lewis, M., & Johnson, B. (1998). Influence of bubbles on scattering of light in the ocean. *Applied Optics*, *37*(27), 6525–6536.

Zhang, X., Lewis, M., Lee, M., Johnson, B., & Korotaev, G. (2002). The volume scattering function of natural bubble populations. *Limnology and Oceanography*, *47*(5), 1273–1282.

Zhou, Z. & Guo, L. (2012). Evolution of the optical properties of seawater influenced by the deepwater horizon oil spill in the gulf of mexico. *Environmental Research Letters*, *7*(2), 025301.